# Combining stellar structure and evolution models with multi-dimensional hydrodynamic simulations

**Andreas Christ Sølvsten Jørgensen**


München 2019

# Combining stellar structure and evolution models with multi-dimensional hydrodynamic simulations

**Andreas Christ Sølvsten Jørgensen**

Dissertation
an der Fakultät der Physik
der Ludwig–Maximilians–Universität
München

vorgelegt von
Andreas Christ Sølvsten Jørgensen
aus Fredericia, Dänemark

München, den 23. August 2019

Erstgutachter: Professor Dr. Achim Weiss
Zweitgutachter: Professor Dr. Jochen Weller
Tag der mündlichen Prüfung: 23.10.2019

# Contents

# List of Figures

# List of Tables

# Zusammenfassung

Die vorliegende Dissertation widmet sich einer verbesserten Darstellung von hydrodynamischen Prozessen in eindimensionalen (1D) Modellen zur Beschreibung der Struktur und Entwicklung von Sternen. 1D Modelle bilden das Rückgrat des theoretischen Verständnisses von Sternen und sind aufgrund ihres geringen Rechenaufwands von unschätzbarem Wert für die Interpretation von Beobachtungen. Fast alle Bereiche der Astrophysik bauen darüber hinaus direkt oder indirekt auf einem detaillierten Verständnis der inneren Struktur und der Entwicklung von Sternen auf. Damit spielen realistischere Sternenmodelle eine entscheidende Rolle im Bestreben, den Kosmos besser zu verstehen. Aus diesem Grund erstelle ich in dieser Arbeit 1D Sternenmodelle, die eine physikalisch verbesserte Darstellung verschiedener konvektiver Grenzschichten ergeben, und ich untersuche, wie sich diese verbesserte theoretische Modellierung auf die stellaren Eigenschaften auswirkt.

Die Energie, die durch Kernfusion im Inneren von Sternen erzeugt wird, wird durch Strahlung, Wärmediffusion und Konvektion an die Oberfläche transportiert. Wegen der inhärent dreidimensionalen (3D) Natur von superadiabatischen turbulenten Strömungen sowie der komplexen Dynamik des Strahlungsfeldes im photosphärischen Übergangsbereich greift man zur theoretischen Modellierung des Energietransportes in 1D Sternenmodellen üblicherweise auf vereinfachte Parametrisierungen zurück. Vergleiche mit Beobachtungen zeigen jedoch, dass diese Vorgehensweise für Sterne mit konvektiven Hüllen eine unzureichende Darstellung der äußeren Schichten zur Folge hat. Die Sonne ist ein prominentes Beispiel für einen solchen Stern. Insbesondere die Oberflächenschwingungen von Sternen mit konvektiven Hüllen deuten offenkundig auf diese Modellmängel hin, da die vorhergesagten seismischen Eigenschaften systematisch von den Beobachtungen abweichen. Das beschriebene Modelldefizit hat jedoch noch weitere Folgen: Die Berechnung von Sternenmodellen läuft auf die Lösung gekoppelter Differentialgleichungen hinaus. Die unvollständige Darstellung der äußersten superadiabatischen Schichten liefert daher fehlerhafte Randbedingungen für die zugrundeliegenden Differentialgleichungen, welches den vorausgesagten Entwicklungsweg beeinflusst.

Während 1D Modelle die Physik der Oberflächenregion nicht verlässlich beschreiben können, zeichnen 3D strahlungs-hydrodynamische (RHD) Simulationen von stellaren Hüllen ein realistischeres Bild. Diese 3D Simulationen beschränken sich jedoch auf die Oberflächenregion: Die ganzheitliche Berechnung der Struktur und Entwicklung eines Sterns, die für 1D Modelle möglich ist, steht derzeit außer Reichweite.

Trotz des enormen Rechenaufwands, der auch mit 3D Simulationen von Hüllen verbunden ist, stehen seit Kurzem umfangreiche Datenbanken mit solchen Simulationen zur Verfügung.

Indem ich die äußeren Schichten von 1D Sternenmodellen durch gemittelte 3D Hüllen ersetze, bin ich in der Lage, 1D Modelle zu konstruieren, die die Vorzüge der hinzugezogenen 3D RHD Simulationen korrekt widerspiegeln. Das dazu benötigte Interpolationsverfahren sowie die Substitutionsmethoden wurden im Zusammenhang mit der vorliegenden Arbeit entwickelt. Durch die Verknüpfung von 1D mit 3D Modellen erreiche ich eine deutlich verbesserte Übereinstimmung mit seismischen Sonnenbeobachtungen. Zugleich stelle ich durch immer komplexere Verfahren stufenweise sicher, dass die innere Struktur der Modelle mit den verbesserten äußeren Schichten im Einklang steht. Durch Vergleiche mit Beobachtungen von kühlen Hauptreihensternen wird aufgezeigt, dass die entwickelten Methoden eine leistungsstarke Weiterentwicklung des Standardverfahrens darstellen. Diese Arbeit enthält somit nicht nur eine Zusammenfassung der Methodenentwicklung und -Validierung, sondern auch Anwendungen auf Daten.

Des Weiteren wende ich mich den unteren Schichten von konvektiven Hüllen zu: Basierend auf Parametrisierungen von multidimensionalen hydrodynamischen Simulationen, untersuche ich den Einfluss verschiedener zusätzlicher Mischungsprozesse in der unteren Randzone. Obwohl die untersuchten Implementierungen allein nicht ausreichen, um alle Beobachtungseinschränkungen zu erfüllen, veranschaulicht die Studie, wie 1D Sternenmodelle durch die Verwendung multidimensionaler hydrodynamischer Simulationen profitieren können.

Qualitativ hochwertige Beobachtungen zeigen, kurz gesagt, mehrere Mängel an Standard 1D Sternenmodellen auf. Diese Arbeit stellt verschiedene Methoden vor, um diesen Modellmängeln entgegenzutreten, und wendet diese Methoden an, um zu einem besseren Verständnis von kühlen Sternen beizutragen.

# Abstract

This thesis is devoted to an improved description of hydrodynamic processes in one-dimensional (1D) models of stellar structures and their evolution. Due to their low computational cost, 1D models are the backbone of the theoretical understanding of stars and are invaluable for interpreting observations. Furthermore, nearly all astrophysical findings — from cosmology to exoplanet research — rely directly or indirectly on a detailed understanding of stellar structures and their evolution. Thus, improvements of state-of-the-art stellar models are essential for the pursuit of obtaining a better understanding of the cosmos. For this reason, in this thesis, I construct 1D stellar models that give a physically more realistic depiction of different convective boundary layers, and I investigate how the improved theoretical modelling affects stellar properties.

Energy is generated at the centre of stars by nuclear fusion and is subsequently transported to the stellar surface by radiation, conduction, and convection. Proper modelling of stellar interiors, therefore, requires a realistic depiction of hydrodynamic processes such as turbulence. However, this is a notoriously challenging task, owing to the inherently three-dimensional (3D) nature of superadiabatic, turbulent flows and the complex dynamics of the radiation field in the photospheric transition region. As a result, 1D stellar models resort to simplified parameterizations of convection.

For stars with convective envelopes, this approach turns out to be especially problematic. The present-day Sun is a prominent example of such a star. In particular, the surface oscillations of stars with convective envelopes highlight this model deficiency. Thus, the predicted seismic properties deviate systematically from observations. Yet the described model deficiency has further consequences: computing stellar models amounts to solving a set of coupled differential equations. The incomplete depiction of the outermost superadiabatic layers, therefore, provides erroneous boundary conditions for the underlying differential equations, which affects the predicted evolution.

While 1D models cannot reliably describe the physics of the surface layers, 3D radiative hydrodynamic (RHD) simulations of stellar envelopes draw a more realistic picture. However, these simulations are limited to the surface region: comprehensive 3D models of stellar structures and their entire evolution are currently out of reach.

Despite the considerable computational costs that are likewise associated with 3D simulations of stellar envelopes, extensive grids of such simulations have recently become available. In this thesis, I thus make use of such grids of 3D simulations to improve 1D stellar models. By replacing the outer layers of 1D stellar models with averaged 3D envelopes, I construct 1D models that reliably mimic the underlying 3D RHD simulations. The required

interpolation scheme, as well as the substitution methods, were developed in connection with the present work. These methods are gradually refined and extended throughout the thesis. The resulting solar models show near-perfect agreement with seismic observations. Moreover, comparisons with observations of other low-mass stars show that the developed methods constitute a powerful improvement of the standard procedure. Not only does this thesis hence contain a summary of method development and method validation, but also applications to data.

I furthermore investigate the impact of additional mixing processes at the lower boundary of convective envelopes. I do this by employing different parameterizations that build on multi-dimensional hydrodynamic simulations. Among other reasons to include such processes, additional mixing is needed to explain the higher-than-predicted depletion of lithium at stellar surfaces. Although the investigated mixing schemes are, on their own, insufficient to meet all observational constraints, the study illustrates how 1D stellar models can benefit from multi-dimensional hydrodynamic simulations.

In summary, high-quality observations reveal several shortcomings of standard 1D stellar models. This thesis presents various methods to overcome these model deficiencies and applies these methods to observational data, contributing to a better understanding of cool stars.

# Chapter 1

# Introduction

The focus of this thesis is turbulent convection and mixing processes in low-mass stars. My research is devoted to an improved theoretical description of these hydrodynamic processes in numerical stellar models. Gaining a thorough theoretical depiction of stars is key to a better understanding of the cosmos, as nearly every field of astrophysics relies on the predictions of stellar physics. For this reason, I both improve the modelling of different physical processes and evaluate the ramifications of these improvements for the predicted properties of stars.

The determination of stellar properties relies on comparisons between theoretical predictions and observations. Accurate numerical stellar models are thus the backbone of stellar physics and play a crucial role when characterizing stars. Conversely, any in-depth analysis of stellar observations may potentially reveal shortcomings of stellar models, leading to new physical insights. In other words, theoretical models must keep pace with observations. However, prevailing model inadequacies related to the depiction of magneto-hydrodynamic (MHD) processes have haunted stellar physics for decades. This is because theoretical models often resort to a simplified treatment of MHD processes, although a proper understanding of such phenomena is essential to describe stellar structures and their evolution. The resulting systematic errors draw model predictions into question. This makes it imperative to develop more sophisticated theoretical models and is the motivation for the present work.

Indeed, several shortcomings of state-of-the-art stellar models are related to the simplified treatment of MHD processes. For instance, the role of magnetic fields is either neglected or taken into account in an ad hoc manner since magnetic fields are expensive to compute, interact with other processes, such as rotation, and are not fully understood, anyway (e.g. Solanki et al., 2006). Another example relates to something as fundamental as energy transport: stars are self-gravitating spheres of plasma that are powered by nuclear fusion processes throughout most of their lifetime. The energy is transported from the reaction sites to the surface via radiation, conduction, or convection. The crux is that standard stellar models employ a naive depiction of convective boundary layers, skewing vital model predictions. This latter issue is the focus of this thesis.

The reason stellar evolution codes do not correctly depict MHD processes is manyfold. First, many MHD phenomena, such as turbulent convection, take place on timescales that

are short compared to the timescales that govern the overall evolution of stars. Stellar evolution codes are tuned to compute the life cycle of stars at low computational cost rather than to resolve MHD processes on the relevant timescales. Secondly, stellar evolution codes compute stellar structures, under the assumption of spherical symmetry. As a result, the obtained stellar structures are one-dimensional (1D). However, the nature of many MHD processes is intrinsically multi-dimensional. While 1D stellar evolution codes do not correctly depict MHD processes, it stands to reason that two- (2D) and three-dimensional (3D) simulations must, therefore, paint a more realistic picture. Indeed, although such multi-dimensional simulations have their own numerical issues, they are undoubtedly superior to their 1D counterparts at depicting MHD processes. This advantage, however, comes at a price: multi-dimensional MHD simulations are extremely computationally expensive, They are, therefore, local rather than global simulations. They neither cover the entire volume of the star in question, nor do they evaluate structural changes over long timescales. In other words, 1D stellar models resort to simplifying approximations in order to depict the entire stellar structure over aeons, while multi-dimensional MHD simulations reliably recover the physics at play but cannot give the same holistic picture. In this thesis, I combine 1D stellar models with multi-dimensional MHD simulations in order to take advantage of the virtues of both approaches.

As mentioned above, this thesis specifically deals with issues related to convective boundary layers: I have developed upon the physical description of mixing processes and turbulent convection in state-of-the-art 1D stellar evolution codes. The implemented modifications of the convective treatment are derived from multi-dimensional radiative hydrodynamic (RHD) and MHD simulations. The resulting numerical models are compared to observations to evaluate their predictive power. Based on these comparisons, I show that the achieved modified depiction of convection significantly improves the agreement between model predictions and data.

In particular, I address the outermost layers of stars with convective envelopes. In this transition region, the energy goes from being fully carried by convection in the nearly-adiabatic interior to being entirely carried by radiation in the vastness of outer space. This happens as convection gradually becomes too inefficient for convective elements to transport the entire luminosity of the star. These near-surface layers are said to be superadiabatic (cf. Kippenhahn et al., 2012). Furthermore, in the uppermost part of this transition region, the gas becomes optically thin, and the diffusion approximation for radiative transport that applies in the stellar interior breaks down. The escaping photons carry away entropy, leading to a characteristic entropy jump near the photosphere. None of the described features of superadiabatic surface layers is well captured by standard 1D stellar models. 3D simulations, on the other hand, lead to a more realistic depiction of the underlying physics, reproducing phenomena, such as stellar granulation (e.g. Magic and Asplund, 2014), and recovering observables, such as stellar spectra (e.g. Chiavassa et al., 2018).

In addition, I investigate the lower boundary of convective envelopes. This constitutes another transition region that is not well-understood. Naively, the transition between the convective and radiative zones would be expected to be rather abrupt. However, observations point towards additional mixing processes beyond the boundary of convective

regions. In this thesis, I address several parameterizations that aim to take this into account based on 2D and 3D simulations of convection.

When comparing models to data, I draw upon both spectroscopic constraints and results from asteroseismology, i.e. the study of stellar pulsations (cf. Leighton, 1960; Ulrich, 1970; Aerts et al., 2010; Chaplin and Miglio, 2013). In short, the surfaces of stars oscillate with characteristic frequencies. From these frequencies, it is possible to infer stellar properties because the oscillations are determined by the stellar interior structure. In solar-like stars, these oscillations are due to propagating sound waves. In the same way as standing waves in the pipes of an organ carry information about the instrument, the resonances of stars reveal much about their acoustic properties. Much like in the case of an ultrasound scan of a fetus or the analysis of Earthquakes, sound is thus used to gain information that would be otherwise inaccessible (Aerts et al., 2010). As a result, the detailed information that can be extracted from stellar oscillations gives a unique insight into stellar structures, and high-quality data from asteroseismic surveys, such as the CoRoT and *Kepler* space mission (cf. Baglin et al., 2009; Borucki et al., 2010), have provided precise stellar parameter estimates (e.g. Christensen-Dalsgaard et al., 2010; Silva Aguirre et al., 2013; Lebreton and Goupil, 2014).

The detailed structure of stars depends dramatically on different properties, such as their mass and their evolutionary stage. Some stars have radii that exceed the distance between the Earth and the Sun, while other stars have been found to have a radius comparable to Jupiter (cf. red dwarf, e.g. OGLE-TR-122b, see Pont et al. 2005). The surface temperatures of stars likewise vary significantly: while the surface temperatures of some stars reach tens of thousands of Kelvin, the surface temperatures of other stars barely exceed one thousand Kelvin, which is comparable to the temperature of lava ejected from volcanic vents. Within this broad range of stars, stars that are similar to the Sun, i.e. low-mass stars that burn hydrogen into helium at their centre, are of particular interest. This is because solar-like hosts are the main focus of surveys, such as the *Kepler* mission, that hunt for Earth-like planets. Due to the availability of high-quality data and the scientific significance of such stars, solar-like stars are likewise the focus of the present thesis.

Solar-like stars have convective envelopes and hence particularly suffer from any simplified treatment of turbulent convection. Not only does an improper depiction of the outermost layers affect the predicted seismic properties of stars, but this deficiency alters the entire structure and evolution. As illustrated above, the accuracy of stellar models for solar-like stars plays a vital role in cutting-edge science — including exoplanet research (e.g. Lundkvist et al., 2018). This makes the improvements of the stellar structure models presented in this thesis relevant to a broad range of astrophysical applications and illustrates how these improvements may contribute to a better understanding of the cosmos.

## 1.1 Overview of the Content of this Thesis

Chapters 2 and 3 give a brief introduction to stellar structures and their evolution as well as to asteroseismology. The purpose of these chapters is to give the reader the necessary

theoretical background to interpret the results and evaluate the methods presented in this thesis.

Chapters 4-10 constitute the main body of this thesis. I address the surface layers of stars with convective envelopes as well as the transition region between the convective envelope of such stars and their radiative interior. State-of-the-art stellar models are unable to depict either of these regions correctly, which manifests itself in the predicted seismic properties, the predicted surface abundances, and even in the predicted evolution tracks. While Chapter 4 addresses the lower convective boundary, Chapters 5-10 present two methods that aim to overcome the inadequate depiction of the upper convective boundary.

Note that the text in Chapters 4-10 has to a large extent been extracted from publications of my work, including Jørgensen et al. (2017), Jørgensen et al. (2018), Jørgensen and Weiss (2018), Jørgensen and Weiss (2019), and Jørgensen et al. (2019). In the introduction of each of these chapters, the relevant papers and my contributions to the presented work are, therefore, explicitly stated.

Chapter 11 summarizes the main conclusions of the thesis. Chapter 12 discusses possible future applications and extensions of the presented framework. The acronyms, abbreviations, and terminology that is used in this thesis are listed in Appendix A.

Below, I give a summary of the thesis, highlighting the main results in order to give the reader a comprehensive overview.

### 1.1.1 The Lower Convective Boundary

Chapter 4 illustrates how information extracted from multi-dimensional hydrodynamic simulations can be utilized to improve stellar models by addressing potential additional mixing processes at the lower boundary of the convective envelope of the present-day Sun.

Observations of solar oscillations reveal a prominent shortcoming of stellar structure models: the actual sound speed in the Sun differs significantly from model predictions at the lower boundary of the convective envelope. This is known as tachocline anomaly. Furthermore, standard solar models cannot explain the low abundance of lithium at the solar surface. Both issues can be addressed by including additional mixing processes, so-called overshooting, beyond the convective boundary (e.g. Schlattl et al., 1997). Overshooting changes the chemical composition and hence the sound speed profile and transports lithium to hotter layers, where it is efficiently depleted.

Suitable parameterizations of overshooting can be inferred from multi-dimensional simulations of convection (cf. Pratt et al., 2017). I implemented different parameterizations of diffusive overshooting into the Garching Stellar Evolution Code (GARSTEC, Weiss and Schlattl 2008) and investigated the consequences for the sound speed profile and lithium depletion. The analysis presented in Chapter 4 leads to the conclusion that diffusive overshooting is, on its own, insufficient to solve the discrepancies between the stellar models and observations, when addressing both problems in tandem. In other words, the discussed diffusive overshooting schemes do not encompass all the relevant physics. This is an intriguing result since some of these prescriptions are commonly used in 1D stellar models.

### 1.1.2 The Upper Convective Boundary

While Chapter 4 presents a self-contained analysis of processes at the lower convective boundary, Chapters 5-10 constitute a continuous body of work and depict the gradual development of different methods that address with the upper convective boundary.

A critical shortcoming of stellar structure models is the use of simplified parameterizations of superadiabatic convection. This ad hoc treatment of superadiabatic convection means that the surface layers are not modelled correctly for stars with convective envelopes. The present-day Sun is a prominent example. Addressing this issue is the main focus of this thesis.

Stellar models are computed by solving a set of coupled differential equations, for which a simplified depiction of the outermost layers provides improper boundary conditions. Consequently, a simplified treatment of superadiabatic convection affects the entire structure of stellar models. As discussed in Chapter 8, this even affects the predicted evolution tracks and hence the global model parameters. Moreover, simplified outer boundary layers pose a challenge for asteroseismology by introducing a systematic frequency shift, known as the structural surface effect (cf. Chapter 3 and e.g. Brown, 1984; Christensen-Dalsgaard et al., 1988b). This frequency shift necessitates an empirical correction of the model frequencies, when comparing to data, and leads to systematic errors in the inferred stellar properties (cf. Chapter 7 and e.g. Ball and Gizon, 2017; Nsamba et al., 2018a).

In my research, I have extracted information from 3D RHD simulations of stellar envelopes in order to improve the physics of the outermost layers of 1D structure models. The resulting stellar models are yet another example of how multi-dimensional hydrodynamic simulations can be used to improve the predictions of stellar evolution codes.

#### 1.1.2.1 Dealing with 3D Simulations

Only a limited number of 3D simulations are available (e.g. Magic et al., 2013a; Trampedach et al., 2013), and such simulations are computationally expensive. Until recently, the use of 3D simulations to improve 1D models was, therefore, limited to a few cases, including the present-day Sun. To overcome this limitation, I developed and tested an interpolation scheme that recovers the structure of 3D simulations with high accuracy for any combination of effective temperature, surface gravity and chemical composition. Specifically, since the aim is to improve 1D stellar models, the interpolated temporal and spatial average stratifications of 3D simulations suffice. I will refer to these average structures as $\langle 3D \rangle$-envelopes. A detailed discussion of this interpolation scheme is given in Chapter 5. Note that the averaging is itself a source for potential errors — taking the average over different physical parameters leads to different structures (Magic and Weiss, 2016).

With my interpolation scheme, it has become possible to explore a broad range of stellar parameters (mass, age, composition). Indeed, in combination with 1D stellar evolution codes, the interpolated $\langle 3D \rangle$-envelopes are shown to be able to contribute to the interpretation of high-quality asteroseismic data. Two different approaches aimed at fusing 1D stellar models with 3D simulations are summarized below.

#### 1.1.2.2 Post-Evolutionary Patching

As a first step on the way to address the improper surface layers of stars with convective envelopes, I substituted the outermost layers of stellar models with interpolated ⟨3D⟩-envelopes at a given evolutionary stage without altering the evolution or adjusting the interior structure. In other words, any corrections to the stellar envelope structure are made during the post-processing. This method is known as patching: after all, the idea is to patch up for the errors made throughout the evolution, when determining the properties of the final model.

I have implemented and validated my own patching criteria and procedure based on requirements such as hydrostatic equilibrium and the aim to reduce discontinuities at the base of the appended ⟨3D⟩-envelope. I have applied the method to study *Kepler* stars as well as the present-day Sun by comparing to data. My patching procedure strongly improves the predicted stellar oscillation frequencies. Furthermore, I have used my procedure to examine and validate empirical surface correction relations that are usually employed to address the surface effect. The obtained results clearly favour certain surface correction relations and hence demonstrate how patching can function as a valuable diagnostic tool. The method and the obtained results are summarized in Chapters 6 and 7. The presented analysis highlights both the advantages and drawbacks that are connected with patching, showing how patching can be used as a valuable diagnostic tool, and pointing towards the inconsistencies between 1D and 3D simulations. By uncovering these inconsistencies, Chapters 6 and 7 delineate how to further advance the fusion of 1D and 3D simulations.

#### 1.1.2.3 Coupling 1D Stellar Models with 3D Envelopes

Although patching corrects the structure of the final model, it does not correct for the use of a simplified treatment of convection throughout the computed evolution. I have, therefore, developed a method that employs interpolated ⟨3D⟩-envelopes to set the outer boundary conditions of 1D stellar models iteratively at every time-step of the evolution. The boundary conditions are supplied far below the photosphere. Beyond the outer boundary of the 1D models, the interpolated ⟨3D⟩-envelopes are appended. This means that the simplified parameterizations of turbulent convection are no longer needed to describe the envelope: such prescriptions have been replaced by a realistic superadiabatic layer that is coupled to the nearly-adiabatic deeper regions of the convective envelope at every time-step during the evolution.

This coupling of 1D and 3D simulations was successfully implemented in the GARSTEC. The computed outermost layers reliably mimic the average structure of 3D simulations, as discussed in Chapter 8, where the method is presented in detail. As a result, the procedure largely corrects for the structural surface effect. The new boundary layers also affect the evolution tracks, leading to higher effective temperatures of red giants, and shifting the point in the Hertzsprung-Russel diagram, at which stars leave the main sequence.

The method has also been applied in asteroseismic analyses of solar-like stars in the *Kepler* field and to Alpha Centauri A and B. In the case of Alpha Centauri, we mapped

the posterior probability distribution for different stellar parameters, using a Markov Chain Monte Carlo approach. The results and method are presented and discussed in Chapter 9.

The bulk movement of a convective fluid contributes with additional pressure, the so-called turbulent pressure. I have improved the treatment of turbulent pressure in 1D models, such as to mimic the predictions from 3D simulations. By including a realistic treatment of turbulent pressure, the structural surface effect has been fully corrected for, as discussed in Chapter 10.

# Chapter 2

# Stellar Structure and Evolution

The present chapter gives a brief introduction to basic concepts of stellar physics and summarizes key aspects of the numerical procedures that are employed to model the interior structure and life of stars. In later chapters, I will frequently draw and build upon the nomenclature and theory that is introduced below. I have written this chapter based mostly on Christensen-Dalsgaard (2008b) and Kippenhahn et al. (2012), to which I refer for further details.

All models that are presented in this thesis have been computed using the Garching Stellar Evolution Code, GARSTEC (cf. Weiss and Schlattl, 2008), and this chapter hence contains some code specific details.

## 2.1 Introduction

Stars are self-gravitating spheres of hot gas[1]. Throughout most of their lifetime, stars are powered by thermonuclear fusion reactions that provide the necessary pressure for the stars to avoid gravitational collapse. The energy that is produced by fusion is transported to the stellar surface via radiation, conduction, or convection and is then radiated into the vastness of space. To a first approximation, stars radiate as black bodies. Actual stellar spectra, however, reveal a myriad of spectral lines based on which it is possible to determine the composition of the surface layers (Grevesse and Noels, 1993; Grevesse and Sauval, 1998; Asplund et al., 2009). As discussed in Chapter 3, a detailed study of variations in the emitted flux even allows inferring the deeper stellar interior through the seismic properties of stars.

The gas in stars can be treated as a continuous fluid. Building upon this notion, a theoretical description of stellar interiors and their evolution emerges by putting together hydrodynamics and nuclear physics.

[1] A large proportion of the gas in stars is not neutral but consists of ions and electrons. In other words, to a large extent, stars are actually made of plasma. However, following the terminology used by most authors (e.g. Christensen-Dalsgaard, 2008b; Kippenhahn et al., 2012), I uniformly refer to the matter in stars as being a gas, irrespectively of its degree of ionization.

Section 2.2 introduces a set of simplifying assumptions that allow depicting stellar structures and their evolution as a series of one-dimensional snapshots by solving five coupled differential equations. These equations are stated in Section 2.3, while Section 2.4 discusses how to solve them.

Throughout this thesis, I will frequently return to the present-day Sun as an invaluable benchmark case for stellar modelling. Section 2.5 gives a detailed description of how to compute reliable solar models. Finally, having summarized the basic concepts of stellar modelling, I briefly outline the life cycle of stars in Section 2.6.

## 2.2 Simplifying Assumptions

State-of-the-art stellar evolution codes compute stellar structures by assuming spherical symmetry. This assumption is a physically reasonable approximation for non-rotation single stars that are not subject to strong magnetic fields. Under the assumption of spherical symmetry, the structure and evolution of stars can be described using only two coordinates: one spatial coordinate (cf. Section 2.3) and time ($t$). Stellar evolution codes hence produce one-dimensional (1D) stellar structure models and must approximate the effect of features and physical phenomena, such as rotation, that are intrinsically multi-dimensional and break spherical symmetry.

When computing the evolution of stars, stellar evolution codes are concerned with changes in the equilibrium structure that arise from composition changes, i.e. from nuclear burning and mixing processes. The time-steps used in the time integration of stellar models are chosen accordingly. When dealing with phenomena, such as turbulence, that take place on much shorter timescales, stellar evolution codes must, therefore, resort to approximative treatments, such as mixing length theory (Böhm-Vitense, 1958). I will discuss mixing length theory in Section 2.3.2.

To illustrate this point, let's take a closer look at the timescales involved. For most of their lifetime, stars convert hydrogen (H) into helium (He):

$$4\,^1\mathrm{H} \rightarrow {}^4\mathrm{He} + 2\mathrm{e}^+ + 2\nu_\mathrm{e}, \tag{2.1}$$

releasing 26.73 MeV per nuclear reaction. Here, $\mathrm{e}^+$ and $\nu_\mathrm{e}$ denote a positron and an electron neutrino, respectively. The associated timescale for the burning of hydrogen is the so-called nuclear timescale:

$$t_\mathrm{nuc} \approx 10^{10} \left(\frac{M}{\mathrm{M}_\odot}\right) \left(\frac{L}{\mathrm{L}\odot}\right)^{-1} \text{years}, \tag{2.2}$$

where $M$ and $L$ denote the total mass and the luminosity of the star, respectively. Luminosity denotes the emitted energy per unit time. $\mathrm{M}_\odot$ and $\mathrm{L}_\odot$ are the mass and luminosity of the present-day Sun. The stellar evolution can be reliably monitored by choosing an evolutionary time-step that is roughly a factor of 1000 times smaller than $t_\mathrm{nuc}$ — these evolutionary time-steps are divided into 10-20 smaller nuclear time-steps to accurately capture the chemical evolution (cf. Weiss and Schlattl, 2008). In the case of stars like the

Sun, this is still of the order of millions of years. In comparison, dynamical changes, such as flares or convective motion, take place on a much shorter timescale:

$$t_{\mathrm{dyn}} \approx 30 \left(\frac{R}{\mathrm{R}_\odot}\right)^{2/3} \left(\frac{M}{\mathrm{M}_\odot}\right)^{-1/2} \mathrm{min}. \tag{2.3}$$

Here, $R$ denotes the photospheric radius, i.e. the distance between the centre and the surface of the star. $\mathrm{R}_\odot$ corresponds to the radius of the present-day Sun. Thus, the structure of stars and their evolution involve phenomena that take place on very different timescales.

## 2.3 The Stellar Structure Equations

Stellar structures and their evolution can be described by a set of differential equations, the so-called stellar structure equations. Based on the simplifying assumptions discussed above, these equations can be written in terms of one spatial coordinate and time. Intuitively, one may choose to write the stellar structure equation, using the distance ($r$) from the stellar centre as the spatial coordinate. Assigning fluid properties to a fixed point in space at any given time is referred to as giving a Eulerian description of the fluid. For stars, this turns out to be inconvenient. Instead, stellar evolution codes commonly follow individual mass elements and thus resort to a Lagrangian description. Therefore, all differential equations presented below will be written, using the mass ($m$) as the Lagrangian coordinate.

The first differential equation that governs the internal structure of stars follows from the definition of density ($\rho$):

$$\frac{\partial r}{\partial m} = \frac{1}{4\pi r^2 \rho}. \tag{2.4}$$

Here, $r$ denotes the distance from the centre, i.e. the radius, while $m$ denotes the mass, as discussed above. At any given point in the stellar interior, the density is related to the thermal pressure ($P_{\mathrm{th}}$) and the temperature ($T$) as well as the chemical composition via the equation of state (EOS) that describes the thermodynamic behavior of the gas:

$$\rho = \rho(P_{\mathrm{th}}, T, X_j), \quad j = 1, \ldots, J. \tag{2.5}$$

Here, $X_j$ is the abundance of the $j$ths species — we consider $J$ elements in total. The thermal pressure arises from two physical processes: the pressure of the photons, i.e. the radiation pressure ($P_{\mathrm{rad}}$), and the pressure that stems from the thermal motion of the gas, i.e. the gas pressure ($P_{\mathrm{gas}}$):

$$P_{\mathrm{th}} = P_{\mathrm{gas}} + P_{\mathrm{rad}}. \tag{2.6}$$

If convection takes place, an additional pressure, the so-called turbulent pressure ($P_{\mathrm{turb}}$), arises from the bulk motion of the fluid. In this case, the thermal pressure deviates from the total pressure ($P$):

$$P = P_{\mathrm{gas}} + P_{\mathrm{rad}} + P_{\mathrm{turb}}. \tag{2.7}$$

The second differential equation that governs stellar structures encompasses the notion that stars neither contract nor expand noticeably, throughout long phases of their lives. For this

to be true, forces acting outwards must counteract the gravitational collapse of stars: if gravity was the only force present, stars would collapse on a timescale given by Eq. (2.3), i.e. within minutes or hours. The force at play arises from the pressure gradient:

$$\frac{\partial P}{\partial m} = -\frac{Gm}{4\pi r^4} \Leftrightarrow \frac{\partial P}{\partial r} = -g\rho. \tag{2.8}$$

The requirement of mechanical stability given by Eq. (2.8) is known as hydrostatic equilibrium. Here, $G$ is the gravitational constant, and $g$ denotes the gravitational acceleration:

$$g = \frac{Gm}{r^2}. \tag{2.9}$$

The temperature stratification in stars is given by yet another differential equation:

$$\frac{\partial T}{\partial m} = -\frac{GmT}{4\pi r^4 P}\nabla, \tag{2.10}$$

where $\nabla$ denotes the temperature gradient:

$$\nabla \equiv \frac{\mathrm{d}\ln T}{\mathrm{d}\ln P}. \tag{2.11}$$

Inferring the temperature gradient is an intricate business, to which I will return in Sections 2.3.1 and 2.3.2.

Both the pressure and the temperature in the stellar interior reflect the kinetic energy of the gas — that is, for non-degenerate matter[2] (see e.g. Part VIII of Kippenhahn et al. 2012 for further details). Stellar structures are hence determined by their energy generation and emission, which leads to the next stellar structure equation based on the first law of thermodynamics:

$$\frac{\partial l}{\partial m} = \epsilon_\mathrm{n} - \epsilon_\nu - c_P\frac{\partial T}{\partial t} + \frac{\delta_\mathrm{P}}{\rho}\frac{\partial P}{\partial t}. \tag{2.12}$$

Here, $l$ denotes the net energy per second passing through a sphere with radius $r$. On the right hand side, $\epsilon_\mathrm{n}$ denotes the energy produced in nuclear reactions, $\epsilon_\nu$ is the energy carried away by neutrinos, the third term describes changes in the internal energy, and the last term describes the work done on the gas. In the last two terms,

$$\delta_\mathrm{P} = -\left(\frac{\partial \ln \rho}{\partial \ln T}\right)_\mathrm{P}, \tag{2.13}$$

at constant thermal pressure, while $c_P$ denotes the heat capacity at constant thermal pressure. Both[3] $\delta_\mathrm{P}$ and $c_P$ follow from the EOS, i.e. $\delta_\mathrm{P} = \delta_\mathrm{P}(P_\mathrm{th}, T, X_j)$ and $c_P = c_P(P_\mathrm{th}, T, X_j)$.

[2]Fermions, such as electrons or neutrons, obey the Pauli exclusion principle and can hence not occupy the same quantum state (e.g. Griffiths, 2005). At sufficiently high densities, such as in the cores of evolved stars, fermions must, therefore, occupy high energy states to fulfil this requirement. Matter is then said to be degenerate. For stars like the Sun, however, the gas is non-degenerate.

[3]Note that $\delta_\mathrm{P}$ is typically referred to as $\delta$ in the literature (e.g. Kippenhahn et al. 2012). The deviating notation has been chosen in order to avoid any confusion between products containing $\delta_\mathrm{P}$ and the finite differences or Lagragian perturbations used in the following chapters.

Stars are powered by nuclear reactions. Consequently, the abundance of the $j$th element will change over time, depending on the reactions that lead to the creation and destruction of this element:

$$\frac{\partial X_j}{\partial t} = \frac{m_j}{\rho}\left(\sum_i \mathcal{R}_{ij} - \sum_k \mathcal{R}_{jk}\right), \quad j = 1, \ldots, J, \tag{2.14}$$

where $\mathcal{R}_{ij}$ and $\mathcal{R}_{jk}$ give the rates, at which the nuclei of type $j$ are created and depleted. In Eq. (2.14), $m_j$ is the mass of a single nucleus of type $j$, and $X_j$ is the number of nuclei of type $j$ per unit volume. Processes, such as gravitational settling and other mixing mechanisms, add additional terms to Eq. (2.14). For instance, diffusive mixing processes leads to an additional term on the form $\frac{\partial}{\partial m}\left(D_\mathrm{c}\frac{\partial X_j}{\partial m}\right)$. Here, $D_\mathrm{c}$ denotes the diffusion coefficient, to which I will return in Section 2.3.2 and Chapter 4. The contribution of diffusion to Eq. (2.14) follows from Fick's first law of diffusion, i.e. the assumption that the concentration gradient is proportional to the concentration flux.

### 2.3.1 Convective Instability

Energy is transported in stars from its production site to the surface by radiation, conduction, and convection. For most stars, conduction plays a minor role. This is because the stellar gas of most stars is non-degenerate. The cores of evolved stars, such as white dwarfs (cf. Section 2.6.3), on the other hand, are degenerate, due to the Pauli exclusion principle and the high densities of these celestial objects. For white dwarfs, this degeneracy implies that the kinetic energy of the electrons is so high that conduction becomes an important energy transport mechanism.

If the energy is carried by radiation, $\nabla = \nabla_\mathrm{rad}$:

$$\nabla_\mathrm{rad} = \frac{3}{16\pi acG}\frac{\kappa l P}{m T^4}. \tag{2.15}$$

Here, $c$ is the speed of light and $a$ is the radiation density constant that is related to the Stefan-Boltzmann constant ($\sigma$): $a = 4\sigma/c$. Furthermore, $\kappa$ denotes the opacity, which is a function of the thermodynamic quantities and the stellar composition:

$$\kappa = \kappa(P, T, X_j), \quad j = 1, \ldots, J. \tag{2.16}$$

The opacity can, therefore, be computed by the stellar evolution code by interpolation in tabulated functions. The same holds true for any quantity that is derived from the EOS.

Note that the opacity, like the radiative flux, is actually a function of the frequency of the emitted radiation. This is typically taken into account by using the Rosseland mean opacity, which denotes the mean over all frequencies, using the temperature derivative of the Planck function for the intensity of black-body radiation ($B(\nu, T)$) as the weighting function:

$$\frac{1}{\kappa} = \frac{\pi}{acT^3}\int_0^\infty \frac{1}{\kappa_\nu}\frac{\partial B(\nu, T)}{\partial T}\mathrm{d}\nu. \tag{2.17}$$

Here, $\nu$ denotes the frequency of the radiation and should not be confused with the stellar oscillation frequencies discussed in Chapter 3: after this point, the letter $\nu$ is solely used in combination stellar oscillation frequencies. Any contribution from conduction may, conveniently, be included in the opacity and hence in $\nabla_{\rm rad}$ (cf. Kippenhahn et al., 2012).

The solar core or the envelopes of massive stars are examples of regions, where the energy is transported by radiation. In such layers, buoyancy and gravity will act as restoring forces that suppress the growth of disturbances in the equilibrium structure. In other words, these layers are stable against convection. This is the case, if the so-called Ledoux criterion is fulfilled:

$$\nabla_{\rm rad} < \nabla_{\rm ad} + \frac{\phi}{\delta_{\rm P}} \nabla_{\mu}. \tag{2.18}$$

Here, $\phi$ is the partial derivative of the density with respect to the mean molecular weight ($\mu$). The mean molecular weight denotes the mean number of atomic mass units per particle. Furthermore, in Eq. (2.18), $\nabla_{\rm ad}$ is the adiabatic temperature gradient

$$\nabla_{\rm ad} = \left( \frac{\partial \ln T}{\partial \ln P} \right)_{\rm ad}, \tag{2.19}$$

and $\nabla_{\mu}$ is the gradient of the mean molecular weight:

$$\nabla_{\mu} = \left( \frac{{\rm d} \ln \mu}{{\rm d} \ln P} \right). \tag{2.20}$$

Under the assumption that the gas is chemically homogeneous, the Ledoux criterion reduces to the Schwarzschild criterion for convective instability:

$$\nabla_{\rm rad} < \nabla_{\rm ad}. \tag{2.21}$$

Layers, for which the Ledoux criterion is not fulfilled, are convective: disturbances grow, leading to rising and sinking fluid elements that dissolve into the surrounding material. This motion of material contributes to the energy transport and leads to mixing. Since convection takes place on the dynamical timescale, such layers are chemically homogeneous. The outer layers of the Sun ($r \gtrapprox 0.71\,{\rm R}_{\odot}$) are an example of a convective region. Throughout most of the solar convective envelope, $\nabla$ lies close to $\nabla_{\rm ad}$. In short, the convective energy transport is adiabatic. This means that neither heat nor mass is transferred between the fluid elements and their surroundings until the elements dissolve into the surrounding material. During the adiabatic rising and sinking of the fluid elements, energy is only transferred as work.

However, near the surface, convection becomes too inefficient for convective elements to carry the entire luminosity of the star. Radiation contributes significantly to the heat transport, and the superadiabatic gradient ($\nabla_{\rm sub} = \nabla - \nabla_{\rm ad}$) becomes substantial. The surface layers of stars with convective envelopes are thus said to be superadiabatic. Proper treatment of superadiabatic convection is complex: it requires very small time-steps compared to the nuclear timescale to model turbulence and some aspects, such as the asymmetry between rising granules and the falling downdrafts, are intrinsically three dimensional. In order to compute $\nabla$ in superadiabatic layers, stellar evolution codes, therefore, resort to a simplified picture, which will be discussed below.

### 2.3.2 Parameterizations of Superadiabatic Convection

Stellar evolution codes use mixing length theory (MLT, Böhm-Vitense 1958) or similar parameterizations, such as full spectrum convection theories (cf. Canuto and Mazzitelli, 1991, 1992), in order to describe superadiabatic convection. Within mixing length theory convection is described based on convective elements that are considered to rise (or sink) a characteristic distance $\ell_{\rm m}$ before they dissolve into their surroundings. This characteristic distance is the so-called mixing length and is most commonly assumed to be proportional to the pressure scale height ($H_P$):

$$\ell_{\rm m} = \alpha_{\rm MLT} H_P, \quad H_P = -P\frac{{\rm d}r}{{\rm d}P}. \tag{2.22}$$

Here, $\alpha_{\rm MLT}$ denotes the so-called mixing length parameter that is typically assumed to be constant within the star and to be independent of the global stellar parameter, such as the mass, composition, and age of the star.

Now, consider a surface of a sphere with radius $r$. Based on the assumptions above, the average convective element will have moved a distance $\ell_{\rm m}/2$, when crossing the sphere. From this statement, the kinetic energy and velocity ($v_{\rm c}$) of the average convective element can be derived. For instance,

$$v_{\rm c}^2 = g\delta_{\rm P}(\nabla - \nabla_{\rm e})\frac{\ell_{\rm m}^2}{8H_P}, \tag{2.23}$$

where the subscript 'e' refers to the element, while the other parameters are evaluated for the surroundings. In this way, we end up with five coupled equations for radiative ($F_{\rm rad}$) and convective energy flux ($F_{\rm con}$) as well as $v_{\rm c}$, $\nabla_{\rm e}$, and $\nabla$ that only depend on local quantities: $P$, $T$, $\rho$, $l$, $M$, $c_P$, $\nabla_{\rm ad}$, $\nabla_{\rm rad}$, and $g$. Having obtained the convective velocity from the local parameters, it is furthermore possible to derive quantities such as the diffusion coefficient that was briefly mentioned above[4]:

$$D_{\rm c}\frac{\partial X_j}{\partial r} = \left(\frac{1}{3}v_{\rm c}\alpha_{\rm mlt}H_P\rho r^2\right) \tag{2.24}$$

in the convective region. The case, where diffusion extends beyond the convection zone, is discussed in detail in Chapter 4.

Although it is the default assumption in state-of-the-art stellar evolution codes that $\alpha_{\rm MLT}$ is independent of the global stellar parameters as well as constant throughout the stellar envelope, this assumption is undoubtedly an oversimplification. As pointed out by Schlattl et al. (1997) and Trampedach and Stein (2011), $\alpha_{\rm MLT}$ varies with depth (see also Chapter 8). Moreover, while there is yet no consensus regarding the variation of $\alpha_{\rm MLT}$ with the global stellar parameters, both theory and observations point towards the

[4]It is common practice to describe convection as a diffusive process when incorporating the time-dependent mixing of chemical elements. However, it is worth noting that this picture is un-physical: in reality, convective mixing is an advective process, i.e. it takes place through the bulk motion of the fluid.

necessity of a mixing length parameter that changes during the evolution of stars (cf. Trampedach et al., 2014b; Magic et al., 2015; Tayar et al., 2017). The use of MLT and similar parameterizations of turbulent convection hence lead to a simplistic depiction of the surface layers of stars with convective envelopes. This affects the entire predicted structure through the improper boundary conditions for the stellar structure equations. For this reason, I developed different methods to correct for the use of MLT or even surpass the need to employ MLT by substituting the outermost layers of 1D stellar models with multi-dimensional simulations of stellar envelopes. I return to this issue, in Chapters 6-10.

### 2.3.3 Entropy

The entropy stratification is directly related to other thermodynamic quantities, such as $T$ and $P$, and the composition through the EOS. It is sometimes illustrative to phrase statements in terms of this quantity — not only because the community that provides multi-dimensional RHD simulations tends to do so. Several of the following chapters, therefore, refer to this quantity, using the terminology introduced below. In addition, Chapter 9 and Appendix B draw directly on the entropy in expressions and plots.

In the adiabatic part of the convection zone, the entropy is constant. The stratification is said to have reached its adiabat. The value of the entropy in this zone is hence referred to, as the entropy of deep asymptotic adiabat. In the superadiabatic near-surface layers, the entropy decreases dramatically, as the escaping photons carry away both energy and entropy. I will refer to this change in entropy near the stellar surface as the entropy jump. When phrased in terms of entropy, the purpose of any free parameter in parameterizations of convection, such as MLT, is then to recover the correct adiabat and bridge the entropy jump between the adiabat and the outermost edge of the stellar model.

## 2.4 Solving the Stellar Structure Equations

Stellar structures and their evolution are determined by five differential equations: Eqs (2.4), (2.8), (2.10), (2.12), and (2.14). Of these five equations, only Eqs (2.12) and (2.14) include derivatives with respect to time: the former describes the energy budget and the latter describes the changes in the chemical composition as a result of mixing processes and the nuclear fusion reactions that power the star. The stellar structure equations are, therefore, solved in two steps by performing an operator splitting. In the first step, the stellar structure is computed, assuming the composition to be fixed, i.e. only four of the five equations are considered. Note that the stellar structure is only evaluated for a discrete number of mesh points. The distribution of these mesh points reflects how non-linear the thermodynamic quantities are as a function of $m$ (cf. Kippenhahn et al. 2012). In the second step, the composition is changed, assuming that the thermodynamic quantities can be kept fixed, i.e. only Eq. (2.14) is now considered — the time derivatives in Eq. (2.12) are handled in a different manner (cf. Section 2.4.1). These two steps are repeated for every time-step. In this way, the stellar evolution code alternates between computing the equilibrium structure

at a given age and evolving the structure forward in time.

Section 2.4.1 gives a more detailed summary of the sketched iterative adjustment of stellar structure models. For an in-depth discussion of the topic, I refer to Weiss and Schlattl (2008) and Kippenhahn et al. (2012). For the purpose of understanding the work related to this thesis, a deeper understanding of the matter than given below is, however, not needed. In order to solve a set of coupled differential equations, suitable boundary conditions must be provided. I deal with this issue in Sections 2.4.2 and 2.4.3.

### 2.4.1 The Henyey Scheme and Time Integration

When computing the stellar structure for a fixed composition, i.e. when considering only four of the five equations, the Henyey scheme is used (cf. Henyey et al. 1964). Within this scheme, the stratification of thermodynamic quantities is iteratively adjusted, until the stellar structure equations are solved on the discretized grid with the required accuracy. The equilibrium structure from the previous time-step can be used as an initial educated guess, i.e. a trial solution. To illustrate this, consider, say, Eq. (2.8), i.e. the requirement of hydrostatic equilibrium, at the mesh point $i$ and $i+1$. Based on the presumed structure, the left-hand side of this equation can be computed as $(P^i - P^{i+1})/(m^i - m^{i+1})$. The right-hand side of the equation can be computed from the mass and radius at the arithmetic or geometric mean of the two mesh points. The left and right-hand side are required to be the same within a certain accuracy. This will, however, not be the case, due to changes in chemical composition that took place over the previous time-step.

The stellar structure equations can be written in terms of 4 unknown variables: $r$, $P_{\mathrm{th}}$, $T$, and $l$. If these variables are evaluated in $K$ mesh points, this discretization of the structure translates the four considered structure equations into a system of $4K-2$ non-linear equations: there are 2 and 4 equations, yielding the outer and inner boundary conditions, respectively, and $4(K-2)$ equations, yielding the 4 parameters at the remaining $K-2$ mesh points.

The idea is now to assume that the deviations between the left- and right-hand side of the discretized stellar structure equations are small. If so, these deviations can be expanded, keeping only the linear terms in the Taylor series. This approach allows writing the requirement to fulfil the stellar structure equations as a set of linear inhomogeneous equations. Since the equations have been linearized, the problem can then be written in matrix form. Within this first-order scheme, i.e. through the aforementioned discretization and linearization, any mesh point is only directly dependent on its neighbours. Therefore, the involved matrix only has non-vanishing elements in blocks on its main diagonal, which greatly reduces the computational cost of inverting the matrix. The Henyey method thus rephrases the problem of solving the stellar structure equations into $K$ inversions of $4 \times 8$ matrices (cf. Henyey et al., 1964; Kippenhahn et al., 2012, for further details).

On the other hand, a first-order scheme will not yield the correct result: the left- and right-hand side of the stellar structure equations will presumably still deviate after following each of the steps above once. This obstacle is overcome by adjusting the thermodynamic quantities in consecutive iterations. In each iteration, the steps above are repeated, thereby

progressively improving the trial solution.

When changing the chemical composition, in order to evolve the stellar model in time, an explicit time integration is used. This is done employing a predictor-corrector method. Using an *explicit* time integration scheme means that the chemical profile of the next time-step is inferred from the current stellar structure. In contrast, when using an *implicit* time integration scheme, the solution draws on information from both the current structure and the structure at the next time-step. When evaluating the time derivatives in the energy equation, i.e Eq. (2.12), an implicit scheme is used (cf. Weiss and Schlattl, 2008; Kippenhahn et al., 2012).

### 2.4.2 Setting the Inner Boundary Conditions

To solve the stellar structure equations, boundary conditions at the stellar centre and surface are needed. At the stellar centre, i.e. at $m = 0$, both the produced energy and the density must be finite, from which it follows that

$$m = 0 : \quad r = 0, \quad l = 0. \tag{2.25}$$

This is translated into a series of expansions for the four variables $r$, $l$, $P$, and $T$, using the stellar structure equations. By assuming a constant density, i.e. by using a small value of $m$, $r$ can be obtained by integration of Eq. (2.4). An analogous integration of Eq. (2.12) yields $l$ for the small value of $m$. Based on $r$ and $l$, the central pressure ($P_\mathrm{c}$) and temperature ($T_\mathrm{c}$) can be deduced by employing equations (2.8) and (2.10) — note that the pressure gradient is likewise required to vanish at $m = 0$. This leads to four equations that reflect the inner boundary, i.e. equation (2.25). In this thesis, I set the inner boundary conditions using the standard procedure, i.e. the inner boundary conditions are left unaltered. Meanwhile, in Chapters 8-10, I change the *outer* boundary conditions by employing 3D simulations of stellar envelopes. I do this in order to improve the theoretical description of the outermost superadiabatic layers of stars with convective envelopes.

### 2.4.3 Setting the Outer Boundary Conditions

The outer boundary conditions of a stellar model are commonly set at the photosphere, where the Stefan-Boltzmann law holds true:

$$L = 4\pi\sigma R^2 T_\mathrm{eff}^4. \tag{2.26}$$

Here, $T_\mathrm{eff}$ denotes the effective temperature of the star and corresponds to the value of $T$ at the photosphere, while $R$ denotes the photospheric radius, i.e. $T(r = R) = T_\mathrm{eff}$.

Beyond the photosphere lies the stellar atmosphere, which implies that the pressure at the outer boundary of the model is non-zero. In order to infer the temperature and pressure at the photosphere, it is common to use a model atmosphere, such as a plane-parallel Eddington atmosphere or semi-empirical approximations (cf. Krishna Swamy, 1966;

Vernazza et al., 1981). Within the Eddington approximation the temperature stratification of the atmosphere is asumed to be given by

$$T^4(\tau) = \frac{3}{4}\frac{L}{4\pi R^2 \sigma}\left(\tau + \frac{2}{3}\right), \tag{2.27}$$

in which case $T = T_{\rm eff}$ for $\tau = 2/3$. Here, $\tau$ is the optical depth, which depends on the opacity of and density of the overlying layers:

$$\tau = \int_r^\infty \kappa\rho \mathrm{d}r, \quad \text{i.e.} \frac{\mathrm{d}r}{\mathrm{d}\tau} = -1/(\kappa\rho). \tag{2.28}$$

When the Rosseland mean opacity is employed, the atmosphere is said to be grey. The optical depth at the photosphere varies between different approxitations, i.e. it is not generally true that $T = T_{\rm eff}$ for $\tau = 2/3$. In the following chapters, I will refer to Eq. (2.27) and similiar relations between $T$ and $\tau$ as $T(\tau)$ relations.

It follows from Eq. (2.28) in combination with the equation for hydrostatic equilibrium that the pressure in the atmosphere is described by a differential equation on the form

$$\frac{\mathrm{d}P}{\mathrm{d}\tau} = \frac{Gm}{r^2\kappa}. \tag{2.29}$$

The pressure at the photosphere ($\tau = 2/3$) can thus be computed by integration by noting that $P(\tau = 0) = 0$. In GARSTEC, the integration of Eq. (2.29) is solved, using a predictor-corrector method.

Based on the equations summarized above, the inwards integration of the atmosphere provides values for $r$, $l$, $P$, and $T$ at the photosphere. Using the nomenclature by Kippenhahn et al. (2012), I refer to the corresponding values of these exterior boundary conditions as $r_{\rm F}^{\rm ex}$, $l_{\rm F}^{\rm ex}$, $P_{\rm F}^{\rm ex}$, and $T_{\rm F}^{\rm ex}$, respectively. The values for these four quantities at the photosphere are also provided by the solution of the stellar structure equations. I refer to these values from the stellar interior as $r_{\rm F}^{\rm in}$, $l_{\rm F}^{\rm in}$, $P_{\rm F}^{\rm in}$, and $T_{\rm F}^{\rm in}$, respectively. The interior structure has a mass of $m_{\rm F}$ called the fitting mass — hence leading to the subscript 'F' for the quantities listed above. Meanwhile, the atmosphere contains the mass $M - m_{\rm F}$. In the case of, say, the Sun, the mass of the atmosphere is negligible.

In order to compute a consistent equilibrium structure, the interior structure and the model atmosphere are iteratively adjusted by employing the Henyey scheme, until the exterior and interior values are matched within the desired numerical accuracy:

$$r_{\rm F}^{\rm ex} = r_{\rm F}^{\rm in}, \quad l_{\rm F}^{\rm ex} = l_{\rm F}^{\rm in}, \quad P_{\rm F}^{\rm ex} = P_{\rm F}^{\rm in}, \quad T_{\rm F}^{\rm ex} = T_{\rm F}^{\rm in}. \tag{2.30}$$

For simplicity, the outer layers can be assumed to be thermally adjusted, i.e. $l_{\rm F}^{\rm ex} = L$. The exterior solution then has two degrees of freedom: all four exterior quantities are functions of $R$ and $L$ (or, say, $R$ and $T_{\rm eff}$, cf. Eq. 2.26). Assuming that $r_{\rm F}^{\rm ex}$ is a well-behaved function of $R$ and $L$, this means that $R = R(r_{\rm F}^{\rm ex}, L)$. $P_{\rm F}^{\rm ex}$ and $T_{\rm F}^{\rm ex}$ are, therefore, known functions ($\pi$

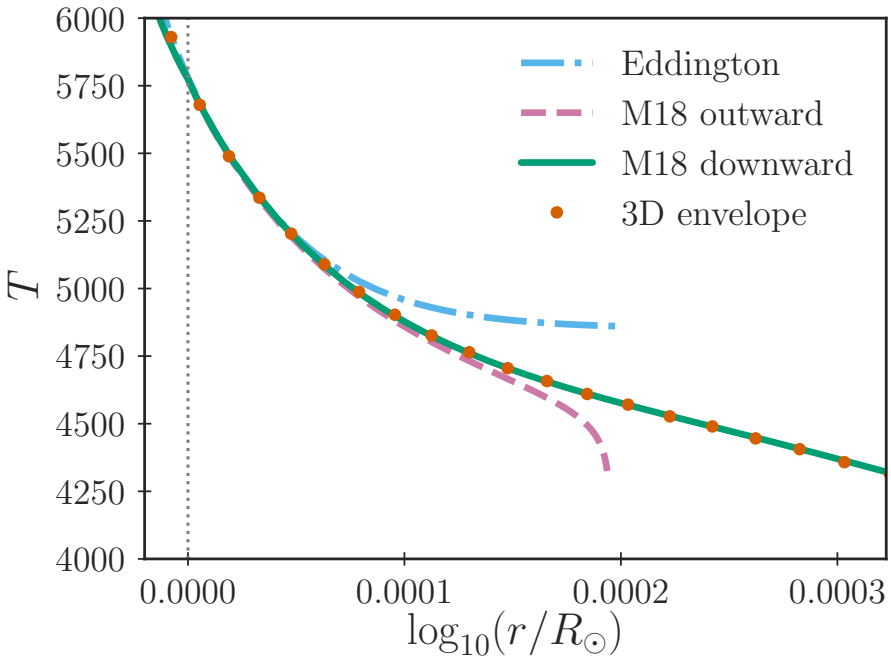


Figure 2.1: Temperature stratification of the atmosphere of the present-day Sun computed by GARSTEC. The plot shows an Eddington grey atmosphere (dashed-dotted line) as well as two atmospheres that employ the atmospheric temperature stratification by Mosumgaard et al. (2018) The atmospheres of the latter two models have been computed using the old outward integration (dashed line) and the new downward integration scheme (solid line). I refer to these atmospheres as 'M18 outward' and 'M18 downward', respectively. The implementation by Mosumgaard et al. (2018) strives to mimic the temperature stratification of the 3D radiative hydrodynamic (RHD) atmospheres by Trampedach et al. (2013) (dots). While the new downward integration achieves this, the old scheme fails to reproduce the correct structure. The dotted vertical line indicates the location of the photosphere at $R = R_\odot$.

and $\theta$) of $r_\mathrm{F}^\mathrm{ex}$ and $L$. As a consequence, the above statements can be summarized into two boundary conditions for the interior model:

$$P_\mathrm{F}^\mathrm{in} = \pi(r_\mathrm{F}^\mathrm{in}, L), \quad T_\mathrm{F}^\mathrm{in} = \theta(r_\mathrm{F}^\mathrm{in}, L). \tag{2.31}$$

In other words, at the photosphere, the pressure stratification must be continues and the continues transition in temperature must ensure that the Stefan-Boltzmann law is fulfilled.

In practice, GARSTEC computes three values for each of the functions $\pi(r_\mathrm{F}^\mathrm{ex}, L)$ and $\theta(r_\mathrm{F}^\mathrm{ex}, L)$ in each iteration, in order to approximate the derivatives that are necessary for the Henyey scheme. The computation of the outer boundary conditions hence requires several downward integrations of Eq. (2.29).

Note that GARSTEC does not store the obtained atmosphere by default. The atmosphere is commonly only needed to set the outer boundary conditions for the interior model and

can safely be discarded. However, this does not always hold true: for instance, the structure of the atmosphere does affect the seismic properties of stellar models (cf. Chapter 3). GARSTEC, therefore, allows the user to recompute and attach the discarded atmosphere to the evaluated interior structures. When doing so, the atmosphere is obtained by integration from the photosphere and outwards. In connection with a new set of atmospheres introduced by Mosumgaard et al. (2018), it became apparent that this outward integration was subject to integration errors. I solved this issue by changing the scheme that underlies the recomputation of the atmosphere: the same downward integration that is used to obtain the boundary conditions is now employed (cf. Fig. 2.1).

As regards the new atmospheres introduced by Mosumgaard et al. (2018), the implementation is based on a method that was initially suggested by Trampedach et al. (2014a). The goal of this implementation is to mimic the temperature stratification of the 3D radiative hydrodynamic (RHD) simulations of stellar atmospheres by Trampedach et al. (2013) and hence to use averaged 3D atmospheres as the outer boundary conditions for the 1D structures. Note that the method thus only recovers the atmosphere of the 3D RHD simulations and that the boundary conditions are still supplied at the photosphere. In other words, the implementation by Mosumgaard et al. (2018) involves a substitution of Eq. (2.27), i.e. the Eddington grey atmosphere, by a more realistic relation between $T$ and $\tau$. The structure below the photosphere is still computed using MLT. This being said, information from the 3D simulations also enters the computation of the convective layers below the photosphere through a modification of $\nabla_{\rm rad}$ for $\tau < 10$ and through a variation of the mixing length parameter with $T_{\rm eff}$ and $\log(g)$ — this procedure was proposed by Trampedach et al. (2014b). The use of a variable mixing length parameter is, however, insufficient to capture the complexity of the convective layers (cf. Chapter 6). Models that employ a variable mixing length parameter and the outer boundary conditions by Trampedach et al. (2014a,b) are used in Chapters 6 and 8.

As discussed above, the method presented by Trampedach et al. (2014a,b) improves the outer boundary conditions of stellar models based on 3D RHD simulations. In Chapter 8, I present a different method for setting more realistic outer boundary conditions based on such simulations. I will refer to this method as the coupling of 1D and 3D models. While the method by Trampedach et al. (2014a,b) does not recover the mean stratification of the 3D simulations below the photosphere, the presented coupling scheme is able to reliably achieve this goal. The coupling of 1D and 3D models hereby outperforms the method by Trampedach et al. (2014a,b). While the coupling scheme builds on Eq. (2.30), several of its key features differ from the standard procedure and the method by Trampedach et al. (2014a,b). In other words, the coupling scheme presented in Chapter 8 differs significantly from the mentioned implementation of 3D atmospheres by Mosumgaard et al. (2018).

## 2.5 Solar Calibration Models

The global properties of the present-day Sun, such as its mass (or rather $GM$) and age, are well constrained (e.g. Bahcall et al., 1995; Brown and Christensen-Dalsgaard, 1998; Fröhlich,

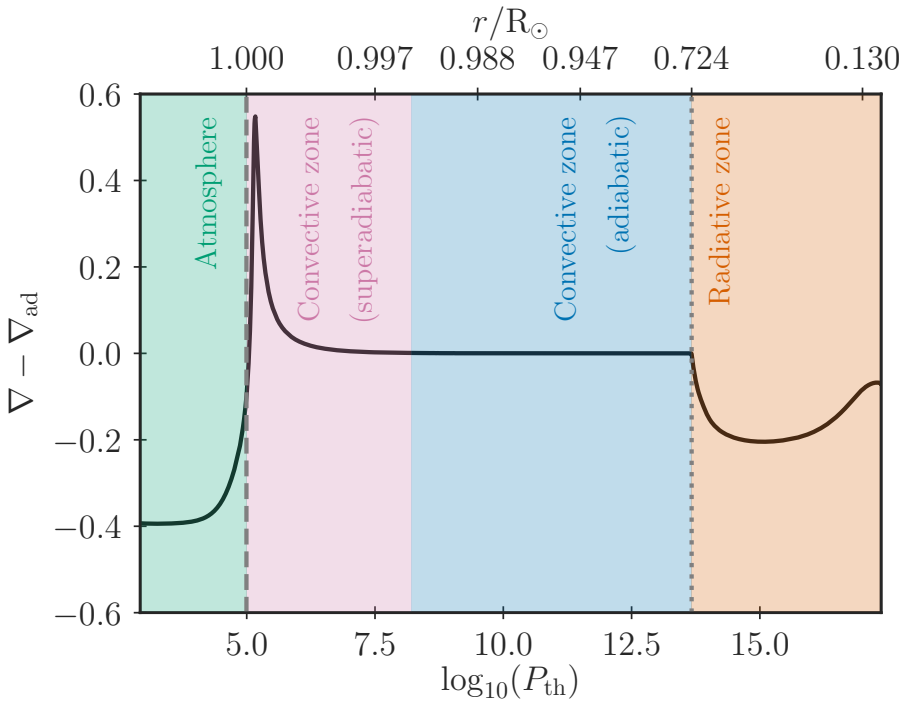


Figure 2.2: Temperature gradient of a standard solar calibration model using the composition determined by Asplund et al. (2009). The outer boundary conditions have been set using an Eddington grey atmosphere. The photosphere is marked with a dashed grey line. The dotted grey line marks the base of the convection zone. Most of the interior solar structure is radiative, i.e. the Schwarzschild criterion is fulfilled: $\nabla = \nabla_{\mathrm{rad}} < \nabla_{\mathrm{ad}}$. The Eddington grey atmosphere is, by definition, likewise radiative. Throughout most of the convective zone $\nabla \approx \nabla_{\mathrm{ad}}$. In the near-surface layers, however, convection becomes superadiabatic. Here, I have chosen to mark transition between the superadiabatic and the adiabatic regions at $\nabla - \nabla_{\mathrm{add}} = 10^{-3}$, for purely illustrative reasons.

2006). In addition, high-quality seismic data are available (cf. Chapter 3, e.g. Broomhall et al. 2009). This makes the Sun an ideal benchmark case when investigating new input physics. For this reason, my thesis includes many detailed studies of solar models.

When computing a model of the present-day Sun, GARSTEC iteratively adjusts a set of initial conditions, until a subset of the global solar properties is recovered with the desired accuracy. This procedure is referred to as a solar calibration.

The initial model that is used for the solar calibration may either be a star on the zero-age main sequence (ZAMS) or the pre-main sequence (pre-MS): stars form, when molecular clouds collapse under their own gravity. The contracting proto-stellar sphere is powered by the released gravitational potential energy. This phase of stellar evolution is called the pre-MS. When hydrogen burning sets in, the star is said to have reached the ZAMS. Section 2.6 gives a more detailed overview of both terms. GARSTEC can create

chemically homogeneous initial models on the pre-MS and ZAMS, using a Runga-Kutta integrator. For further details heron, I refer to Schlattl and Weiss (2016).

GARSTEC proposes a set of initial conditions and computes the evolution from the corresponding initial model, i.e. from the ZAMS or pre-MS, to the present solar age. GARSTEC then compares the final model with observations. If the model fits observations within the desired accuracy, the model is assumed to be a fair representation of the present-day Sun. If not, GARSTEC proposes a new set of initial conditions, constructs an initial model, computes its evolution, and compares the final model with observations. This iterative adjustment of the initial conditions is performed using a Newton solver, which implies that new combinations of initial conditions are proposed based on the previous comparisons between the final structure of the computed evolution and observations.

Usually, the solar properties that are required to be recovered are $L_\odot$, $R_\odot$, and $(Z_S/X_S)_\odot$ at the present solar age. Here, $X_S$ and $Z_S$ denote the mass fraction of hydrogen and the bulk composition of heavy elements at the solar surface, i.e. at the photosphere, respectively. All elements with a higher atomic number than helium are considered as heavy elements, i.e. as metals. The adjusted initial conditions are the initial hydrogen ($X_i$) and helium ($Y_i$) mass fractions as well as the mixing length parameter ($\alpha_{MLT}$).

By default $L_\odot$ and $R_\odot$ are set to be $3.846 \times 10^{33}$ erg/s and $6.95508 \times 10^{10}$ cm in GARSTEC, respectively. The age of the present-day Sun is typically set to be $4.57 \times 10^9$ yr. As regards, $(Z_S/X_S)_\odot$ the calibration value depends on the chosen composition. In accordance with Grevesse and Noels (1993), the default value in GARSTEC is 0.0245. However, the analysis by Grevesse and Noels (1993) was performed more than two decades ago, and more recent attempts to determine the solar composition lead to significantly lower estimates of $(Z_S/X_S)_\odot$. Indeed, in many cases presented in this thesis, I will assume $(Z_S/X_S)_\odot$ to be 0.018, in accordance with a study by Asplund et al. (2009).

The mass of the initial model for each iteration of the solar calibration is kept fixed. Note that mass loss takes place during the computed stellar evolution. In order to obtain a solar model with a mass of $1\,M_\odot = 1.9891 \times 10^{33}$ g at the present solar age, the initial mass must hence slightly exceed that of the present Sun. For the solar calibration models presented in this thesis, the initial mass is therefore set to $1.00026\,M_\odot$.

Figure 2.2 shows the structure of a solar calibration model, highlighting the different energy transport mechanisms that are at play.

## 2.6 From Cradle to Grave

Having summarized the basic concepts of stellar modelling, I briefly outline the life cycle of stars below.

### 2.6.1 Early Phases

Stars form in molecular clouds that collapse under their own gravity and fragment into smaller clumps. When the gas becomes so dense that it becomes opaque, this contraction

proceeds adiabatically. As a result, the pressure gradient nearly balances the gravitational force, i.e. the gas undergoes contraction in hydrostatic equilibrium. Furthermore, the released potential energy constitutes the sole energy source, i.e. nuclear fusion has not yet set in. This implies that the virial theorem holds true: for a non-relativistic ideal gas, the virial theorem takes the form

$$\Omega = -2U_{\mathrm{tot}}, \tag{2.32}$$

where $\Omega$ and $U_{\mathrm{tot}}$ denote the total gravitational potential energy and the total internal energy of the gas, respectively. During the gravitational collapse, only half of the released potential energy is hence converted into internal energy, heating the contracting gas. The other half is radiated away. It follows that the timescale, on which the gravitational collapse takes place, must be determined by the rate, at which the gravitational energy is emitted by the gas:

$$t_{\mathrm{KH}} = \frac{|\Omega|}{L} \approx 30 \times 10^6 \left(\frac{M}{\mathrm{M}_\odot}\right)^2 \left(\frac{R}{\mathrm{R}_\odot}\right)^{-1} \left(\frac{L}{\mathrm{L}_\odot}\right)^{-1}. \tag{2.33}$$

This is the so-called Kelvin-Helmholtz timescale ($t_{\mathrm{KH}}$). For a solar-like star, the initial hydrostatic collapse of the young stellar object takes of the order of tens of millions of years.

The evolution of stars is often illustrated using a Hertzsprung-Russell (HR) diagram that shows how the luminosity and effective temperature change with time. Note, however, that evolution tracks presented in this thesis will appear in a pendant to the HR diagram, called the Kiel diagram. The Kiel diagram shows $\log g$ as a function of $T_{\mathrm{eff}}$. Figure 2.3 shows an example of such a diagram, highlighting the different evolutionary stages discussed in this section.

Initially, the newly born star is almost fully convective and evolves at nearly constant effective temperature, while the luminosity decreases and $\log g$ increases. This corresponds to a nearly vertical track in the HR and Kiel diagrams to the left of the Hayashi track: a star on the Hayashi track is entirely convective. The fact that newly born stellar objects are fully convective means that they can be assumed to be chemically homogeneous.

The star leaves the proximity of the Hayashi track when a radiative core develops: the effective temperature of the star rises with time. In the case of the Sun, this happens roughly two million years into the collapse. When hydrogen burning is ignited, the star is said to have reached the ZAMS. This happens, when the core has reached a temperature of near $10^7$ K, which implies that the collapsing object must have a mass of at least $\sim 0.08\,\mathrm{M}_\odot$ (cf. Kippenhahn et al. 2012).

In the case of massive stars, the accretion of matter from the surroundings molecular cloud onto the newly born star hasn't ceased, when hydrogen burning sets in. While low-mass stars can be observed as they evolve along the Hayashi track, massive stars on the ZAMS are unlikely to emerge as observable objects. It is worth noting that this accretion of matter complicates the picture of the stellar infancy drawn above: the infalling matter changes the boundary conditions as it contributes to additional heating. Furthermore, magnetic fields and rotation affect the formation of stars, and stars are not born in isolation as assumed above. Rather, stars form in clusters and are subject to a variety of complex interactions.

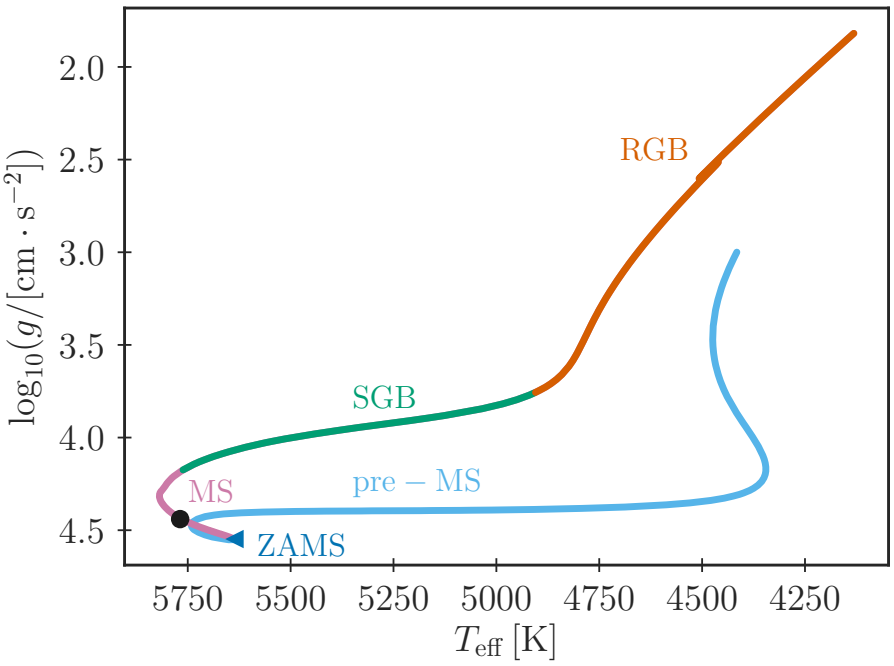


Figure 2.3: A Kiel diagram showing the theoretical evolution of the Sun from the pre-main sequence (pre-MS, cyan solid line) to the red gian branch (RGB, red solid line). Different evolutionary stages are marked with different colours. On the zero-age main sequence (ZAMS, blue triangle), hydrogen burning at the stellar centre is ignited. Nuclear fusion of hydrogen powers the star throughout the main sequence (MS, magenta solid line). The present-day Sun (black circle) is an example of a MS star. At the end of the MS, the star has reached the subgiant branch (SGB, solid green line). In this plot, the end of the MS corresponds to the point in the HR diagram, at which the hydrogen mass fraction at the centre of the star as fallen below $10^{-5}$. At the end of the SGB, the convective envelope stretches down to the core, which brings fusion products to the stellar surface and drastically changes the surface composition. This event is referred to as the first dredge-up and marks the onset of the RGB. In connection with this figure, the onset of the RGB has not been precisely determined based on any definition related to the surface composition, i.e. I merely roughly indicate the beginning of the RGB for purely illustrative purposes. Further information on the diffferent evolutionary stages are given in the text.

### 2.6.2 The Main Sequence

After the ignition of hydrogen, the star is said to have reached the main sequence (MS) and structural changes take place on the nuclear timescale given by Eq. (2.2). The fusion of hydrogen into helium requires several consecutive nuclear reactions and can take place in different ways. In the Sun and other low-mass stars, the proton-proton (*pp*) chain is the dominant chain of reactions. Here, the first reaction is the fusion of two protons into deuterium, and the second reaction leads to the creation of $^3$He. However, the subsequent creation of $^4$He involves three different branches, whose contributions are temperature dependent. In the presence of C, N, and O, these elements function as catalysts and open up for a different pathway, the so-called CNO-cycle. This is the dominant reaction network for more massive stars, as these stars have higher central temperatures: $\epsilon_{pp} \sim T^5$, while $\epsilon_{\rm CNO} \sim T^{18}$ — here, $\epsilon$ denotes the energy produced per unit mass and time.

The nuclear reactions change the chemical profile of the star — the details hereof depend on whether the core is convective or radiative (cf. Chapter 11 in Christensen-Dalsgaard 2008b). These changes affect the overall structure of the star. Indeed, due to the nuclear reactions, the luminosity of the star increases with time, which can be understood in simple terms based on the ideal gas law:

$$P_{\rm th}\mu m_{\rm u} = k_{\rm B}\rho T, \tag{2.34}$$

where $m_{\rm u}$ and $k_{\rm B}$ denote an atomic mass unit and Boltzmann's constant, respectively. When hydrogen is converted into helium, the mean molecular weight increases. Assuming Eq. (2.34) to hold true, $\rho T$ must increase, or $P$ must decrease in response to this. Indeed, the core contracts and heats up, which leads to an increase in the nuclear reaction rates and hence an increase in the stellar luminosity.

The contraction of the core is accompanied by an expansion of the outer parts of the star, i.e. the stellar radius increases during the MS. For low-mass stars, such as the Sun, this expansion is slow, which means that the increase in luminosity results in an increase in the effective temperature. Massive stars, on the other hand, expand rapidly and, therefore, get colder as they evolve along the MS.

### 2.6.3 Late Evolutionary Stages

Stars leave the MS when their central hydrogen reservoir has been exhausted. At this point in its evolution, a star is powered by the fusion of hydrogen in a shell surrounding the inert helium core. While the core within the hydrogen shell source contracts, the envelope expands. As a result, the effective temperature decreases, while the luminosity either stays constant or likewise decreases: the star moves to the right in the HR and Kiel diagrams, until it has reached the Hayashi track and has become nearly fully convective. At this point, the luminosity increases at nearly constant effective temperature, as the star continues to expand. The star has become a red giant.

In this thesis, I focus on solar-like MS stars and do not touch upon stars beyond the red giant branch (RGB). A more detailed understanding of the later stages of stellar evolution

is hence not necessary to access the content of the following chapters.

It is, nevertheless, worth mentioning that these late evolutionary stages play a crucial role for MS stars: during their lifetime, stars eject mass and hereby enrich the interstellar medium (ISM) with the products of the nuclear fusion reactions that take place in their interior. In addition, not all stars die peacefully; some are destructed in violent explosions, ending their life as supernovae. The energy released in a supernova explosion is so high that fusion processes beyond $^{56}$Ni take place, even though these consume rather than produce energy. Through various processes that produce different isotopes, the ISM is thus enriched with a wide variety of new elements. New gas and molecular clouds form from the enriched ISM, leading to the creation of new stars, whose chemical composition is determined by the lives and deaths of previous stellar populations and by galactic dynamics. When modelling different target stars, it is, therefore, vital to take variations in the chemical composition into account. In the following chapters, we quantify the chemical composition in terms of the metallicity, which denotes the surface abundance of metals ($Z_\mathrm{S}$) relative to that of hydrogen ($X_\mathrm{S}$) in units of the same ratio for the present-day Sun:

$$[\mathrm{Fe/H}] = \log_{10}\left(\frac{Z_\mathrm{S}}{X_\mathrm{S}}\right) - \log_{10}\left(\frac{\mathrm{Z_S}}{\mathrm{X_S}}\right)_\odot . \tag{2.35}$$

Since different isotopes are produced at different sites, the ratio between different metals also varies. For instance, type II supernova explosions produce a higher amount of $\alpha$ elements than type Ia supernova explosions do (Tinsley, 1979; Nomoto et al., 1997; Hillebrandt and Niemeyer, 2000; Janka et al., 2007). Here, $\alpha$ elements denote those elements, for which the nuclide of the most common isotope corresponds to an integer multiple of alpha particles (e.g. O, Ne, Na, Mg, Si, or Ti). These two types of supernova explosions are the result of two very different scenarios: type Ia supernovae occur in the wake of the accretion of mass onto a white dwarf, i.e. an inert carbon and oxygen core that constitutes the final remnant of a low-mass star, while a type II supernova explosion occurs due to the core collapse of a massive star. The onset of type Ia supernova explosions hence happens later in the evolution of the galaxy. This affects the ratio of $\alpha$ elements as a function of metallicity — there is substantial observational evidence for an enrichment of $\alpha$ elements for low metallicity stars (cf. Johnson et al., 2011, and references therein). This is what is meant by $\alpha$-enhancement in Chapters 5 and 7.

# Chapter 3

# Stellar Pulsations

The luminosity of many stars varies periodically, due to intrinsic pulsations. A prominent example of classical pulsators is a type of supergiants called Cepheid variable stars that exhibit a tight relation between the luminosity and the period of the luminosity variations (Leavitt and Pickering, 1912). As a result of this property, Cepheids are used as standard candles to measure the distances of galaxies within 20 Mpc (cf. Dodelson 2003 and Ryden 2003). Variable stars hence play a crucial role in cosmology, as they allow to establish a reliable distance ladder.

The pulsations of Cepheids are purely radial, i.e. the luminosity changes as the star contracts and expands. This implies that the stellar structure is not in hydrostatic equilibrium throughout most of the pulsation cycle, i.e. that there is an imbalance between the pressure and gravitational forces (cf. Eq. 2.8). The pulsation period of Cepheids is hence of the order of the dynamical timescale (cf. Eq. 2.3): their period ranges from 1.5 to 60 days (cf. Ryden 2003).

In each pulsation cycle, energy is dissipated, which damps the oscillations. Considering the pulsation period of Cepheids, one may hence expect the oscillations of Cepheids to die out on relatively short timescales. Nevertheless, Cepheids have been observed to reliably pulsate for centuries (Aerts et al., 2010). It stands to reason that some driving mechanism that feeds energy into the pulsations must exist. For Cepheids and other stars in the Cepheid instability strip, including RR Lyrae on the horizontal branch[1] and $\delta$ Scutis near the main sequence (MS), the stellar oscillations are driven by the so-called $\kappa$-mechanism: in the outer layers of these stars, where hydrogen and helium are partly ionized, an increase in temperature leads to an increase in opacity. A contraction of the star, therefore, traps radiation, which results in a pressure build-up that counteracts the compression of the gas and leads to a subsequent expansion. Due to the inertia of the gas, the star expands beyond its equilibrium structure. The resulting cooling leads to a decrease in opacity, which strongly reduces the pressure. This triggers a new contraction, and the described process then repeats itself. In this way, thermal energy is converted into mechanical energy: the

[1] On the horizontal branch (HB), helium burning takes place in the stellar core, while hydrogen is burned in a shell beyond the core region. Stars enter the HB when leaving the red giant branch (cf. Christensen-Dalsgaard, 2008b; Kippenhahn et al., 2012).

ionization zone has become a heat engine. The $\kappa$-mechanism is also at play in $\beta$ Cephei variables, for which the oscillations are, however, driven by partly ionized Fe-group elements (Christensen-Dalsgaard, 2003; Aerts et al., 2010).

It has been suggested that other stars pulsate due to the so-called $\epsilon$-mechanism: in this scenario, expansions and contractions affect the fusion reaction rates in such a way that the balance between the pressure and gravitational forces is disturbed and the star becomes unstable against pulsations. However, no observations support this scenario (Aerts et al., 2010).

Solar-like stars likewise pulsate, despite the fact that there is no heat-engine mechanism that sustains the oscillations. Instead, the pulsations are driven by stochastically excited sound waves in the outer convection zone: these sound waves feed acoustic energy into the global oscillations of a solar-like star. Acoustic oscillations are also known as p-modes and constitute propagating density and pressure perturbations to the equilibrium structure, for which pressure acts as the restoring force. The p-mode frequencies, at which the star resonates, are approximately given by an asymptotic relation (Christensen-Dalsgaard, 2003; Aerts et al., 2010):

$$\nu_{nl} = \Delta\nu \left( n + \frac{\ell}{2} + \tilde{a} \right) + \epsilon_{nl}. \tag{3.1}$$

Here, $v_{nl}$ denotes the frequency with radial order $n$ and degree $\ell$: the quantum number $n$ specifies the number of radial nodes, while $\ell$ denotes the number of nodes at the surface. An additional quantum number, the azimuthal order $m$, specifies whether the surface nodes are lines of longitude. This quantum number hence describes a frequency splitting that arises from deviations from spherical symmetry. In Eq. (3.1), $\Delta\nu$ is the so-called large frequency separations and denotes the average over

$$\Delta_\ell = \nu_{n+1\ell} - \nu_{n\ell}. \tag{3.2}$$

It equals 135 $\mu$Hz in the case of the present-day Sun (Christensen-Dalsgaard, 2003). Finally, $\tilde{a}$ is a constant and $\epsilon_{nl}$ is a small correction. In the case of the Sun, the mode ($\nu_{\max}$) with the largest power has a frequency of 3090 $\mu$Hz, which corresponds to a period of roughly 5 minutes (e.g. Kjeldsen et al., 2008).

In Chapter 9, I furthermore employ the small frequency separation:

$$\delta_\ell = \nu_{n\ell} - \nu_{n-1\ell+2}. \tag{3.3}$$

This is not to be confused with the frequency residuals ($\delta\nu_{n\ell}$) that are shown in many plots throughout this thesis, with other finite differences between models or between models and observations (e.g. $\delta c$), with the Lagrangian perturbations in Section 3.1.2 (e.g. $\delta P$), or with the derivative ($\delta_{\rm P}$) in Eq. (2.13).

For solar-like stars, p-mode oscillations lead to velocity amplitudes at the surface that are of the order of cm/s. The corresponding brightness variations have amplitudes of the order of a few parts per million (ppm) (Christensen-Dalsgaard, 2003). In the case of the Sun, for which it is possible to resolve the stellar surface, a large variety of modes can be

measured. For more distant stars, the luminosity variations only allow for the determination of modes with $\ell \leq 3$.

In addition to p-modes, stars also generate g-modes, for which gravity is the restoring force. The period ($\Pi_{n\ell}$) of these oscillations follow an asymptotic relation (Aerts et al., 2010):

$$\Pi_{n\ell} = \frac{2\pi^2(n+\epsilon)}{\sqrt{\ell(\ell+1)}} \left( \int \frac{N}{r} \mathrm{d}r \right)^{-1} \tag{3.4}$$

with $\epsilon$ being a small constant and $N$ being the Brunt-Väisälä or buoyancy frequency (Aerts et al., 2010):

$$N^2 = g \left( \frac{1}{\Gamma_1} \frac{\mathrm{d} \ln P}{\mathrm{d}r} - \frac{\mathrm{d} \ln \rho}{\mathrm{d}r} \right). \tag{3.5}$$

In Eq. (3.4), the integral is taken over the region, within which the g-modes are trapped. In solar-like stars, g-modes are mostly restricted to the stellar core, while p-mode oscillations probe most of the stellar interior. No direct measurement of g-mode oscillations in the Sun has, therefore, yet been successfully performed — g-mode oscillations have, however, been observed in other kinds of stars, such as $\gamma$ Dor stars. This being said, g-mode oscillations have recently been indirectly detected through p-mode frequency modulations (cf. Fossat et al. 2017). Finally, the Sun harbours surface gravity waves, so-called f-modes, at high degrees, i.e. oscillations that only propagate in the surface layers like ripples on a lake (Aerts et al., 2010).

Within the last half of a century, the study of stellar oscillations, known as asteroseismology, has become an invaluable tool to infer stellar structures and parameters: analogously to any musical instrument, the resonance frequencies of stars are determined by their interior and global properties. For comprehensive reviews on the method and its successes, I refer to Christensen-Dalsgaard (2002), Aerts et al. (2010), Christensen-Dalsgaard et al. (2010), and Chaplin and Miglio (2013).

Thus, asteroseismic analyses provide precise parameter estimates based on exhaustive comparisons between model predictions and observations (e.g. Van Eylen et al., 2012; Metcalfe et al., 2015). Such characterizations of stars also play a vital role, when unlocking the mysteries of exoplanets, since the global parameters of planets are observationally related to that of their host stars. For instance, a planet that eclipses its host star will reduce the received flux by a factor that depends on the ratio between the planetary and stellar radius. The *Kepler* and TESS space missions (Borucki et al., 2010; Ricker et al., 2015) exploit such transits to study exoplanets through the periodic changes in stellar light curves. For further details on this topic, including transits and occultations, I refer to Seager and Lissauer (2010) (see also Van Eylen et al., 2013, 2018, for case studies).

Moreover, scaling relations that translate asteroseismic properties (e.g. $\nu_{\max}$ and $\Delta\nu$) into global stellar parameters (e.g. $M$, $R$) and machine learning algorithms make it possible to characterize a large number of stars at low computational cost (cf. Kjeldsen and Bedding, 1995; Bellinger et al., 2016, 2019). These approaches allow inferring statistical properties of large samples of stars (e.g. Chaplin et al., 2011), which can be employed to extract

information about the chemical and dynamical evolution of the Milky Way galaxy (e.g. Anders et al., 2017).

In this thesis, I restrict myself to p-mode oscillations in solar-like stars. Below, I introduce the concepts and methods that are drawn upon in subsequent chapters.

## 3.1 The Pulsation Equations

This section presents the equations that underlie the computation of stellar oscillations and is primarily based on Aerts et al. (2010). For simplicity, I ignore the turbulent pressure, to begin with, since this quantity greatly complicates matters. The turbulent pressure is dealt with in Section 3.1.2.

It is assumed that the gas in stars can be treated like a continuous fluid, i.e. that the equations of hydrodynamics are applicable and that all thermodynamic quantities are continuous functions of time ($t$) and position ($\mathbf{r}$). Thus, the continuity equation that follows from the conservation of mass applies:

$$\frac{\partial \rho}{\partial t} = \mathrm{div}(\rho \mathbf{v}). \tag{3.6}$$

Here, $\mathbf{v}$ denotes the velocity and $\partial/\partial t$ is the time derivative at a fixed point, i.e. the time derivative within an Eulerian description. In contrast, $\mathrm{d}/\mathrm{d}t$ denotes the time derivative obtained when following the motion of the particles, i.e. when using Lagrangian coordinates.

Ignoring internal friction, the equation of motion that describes a volume of gas in the star is

$$\rho \frac{\partial \mathbf{v}}{\partial t} + \rho \mathbf{v} \cdot (\mathrm{div}\mathbf{v}) = -\nabla P_{\mathrm{th}} \rho \mathbf{f} \tag{3.7}$$

with $\mathbf{f}$ being the different relevant body forces per unit mass. The pressure enters, as it leads to surface forces on the volume. In the following, gravity is the only body force that is considered — thus, magnetic field body forces are neglected. The gravitational force per unit mass corresponds to the gravitational acceleration: $\mathbf{g} = -\nabla\Phi$, where $\Phi$ denotes the gravitational potential that must fulfill the Poisson equation:

$$\nabla^2 \Phi = 4\pi G \rho. \tag{3.8}$$

Furthermore, by combining the continuity equation with the first law of thermodynamics, one arrives at the energy equation of the gas:

$$\frac{\mathrm{d}q}{\mathrm{d}t} = \frac{1}{\rho(\Gamma_3 - 1)} \left( \frac{\mathrm{d}P_{\mathrm{th}}}{\mathrm{d}t} - \frac{\Gamma_1 P_{\mathrm{th}}}{\rho} \frac{\mathrm{d}\rho}{\mathrm{d}t} \right), \tag{3.9}$$

where $\mathrm{d}q/\mathrm{d}t$ denotes the rate at which heat is supplied or lost per unit mass, and where

$$\Gamma_1 = \left( \frac{\partial \ln P_{\mathrm{th}}}{\partial \ln \rho} \right)_{\mathrm{ad}}, \qquad \Gamma_3 = \left( \frac{\partial \ln P_{\mathrm{th}}}{\partial \ln \rho} \right)_{\mathrm{ad}}. \tag{3.10}$$

Assuming that there is no heating, i.e. that the gas behaves adiabatically, it follows from Eq. (3.9) that

$$\frac{\mathrm{d}P_{\mathrm{th}}}{\mathrm{d}t} - \frac{\Gamma_1 P_{\mathrm{th}}}{\rho}\frac{\mathrm{d}\rho}{\mathrm{d}t} = 0. \tag{3.11}$$

Non-adiabatic contributions are commonly ignored, when computing stellar oscillations, making Eq. (3.11) a central result. All model frequencies presented in this thesis have been computed using the Aarhus adiabatic oscillations package, ADIPLS, which solves Eq. (3.11) based on perturbation theory (cf. Christensen-Dalsgaard 2008a).

### 3.1.1 Perturbation Theory

Solar-like oscillations are small-amplitude perturbations around the hydrostatic equilibrium structure. Using a Eulerian description, the pressure can hence be written in terms of the the equilibrium pressure ($P^0_{\mathrm{th}}(\mathbf{r})$) and the a small pertubation ($P'_{\mathrm{th}}(\mathbf{r},t)$):

$$P_{\mathrm{th}}(\mathbf{r},t) = P^0_{\mathrm{th}}(\mathbf{r}) + P'_{\mathrm{th}}(\mathbf{r},t). \tag{3.12}$$

Expressions on this form for all relevant quantities is now inserted in the derived hydrodynamic equations. The equilibrium equations are subtracted, and the resulting equations are linearized. Following this approach, one ends up with a fourth-order system of ordinary differential equations that available pulsation codes, such as ADIPLS, solve by assuming spherical symmetry and adiabaticity. The angular dependence of the Eulerian perturbations to the pressure can then be written in terms of spherical harmonics ($\mathcal{Y}^m_\ell$). The evolution of the perturbations in time is $\exp(-i\omega_{n\ell}t)$, where $\omega_{n\ell}$ is the angular frequency of the considered mode, i.e. $\omega_{n\ell} = 2\pi\nu_{n\ell}$. For non-radial modes,

$$P'_{\mathrm{th}}(r,\theta,\phi,t) = \mathrm{Re}\left[p'(r)\mathcal{Y}^m_\ell(\theta,\phi)\exp(-i\omega_{n\ell}t)\right] \tag{3.13}$$

in polar coordinates: $r$, $\theta$ and $\phi$.

### 3.1.2 Dealing with Turbulent Pressure

While the turbulent pressure enters the stellar structure equations through the requirement of hydrostatic equilibrium, it is not related to thermodynamic quantities, such as e.g. $\Gamma_1 = \partial \ln P_{\mathrm{th}}/\partial \ln \rho$ or the sound speed. Thus, turbulent pressure enters some but not all the relevant quantities that dictate stellar oscillations, which necessitates a revision of the linearized oscillation equations that describe stellar pulsations.

ADIPLS treats stellar oscillations adiabatically. Consequently, the relative Lagrangian perturbation in the density ($\delta\rho/\rho$) and the relative Lagrangian perturbation in the thermal pressure ($\delta P_{\mathrm{th}}/P_{\mathrm{th}}$) are closely related (cf. Eq. 3.11, or e.g. Christensen-Dalsgaard, 2003; Aerts et al., 2010):

$$\frac{\delta\rho}{\rho} = \frac{1}{\Gamma_1}\frac{\delta P_{\mathrm{th}}}{P_{\mathrm{th}}}. \tag{3.14}$$

This expression can be rewritten in terms of the total pressure (Houdek et al., 2017):

$$\frac{\delta\rho}{\rho} = \frac{1}{\Gamma_1}\frac{P}{P_{\rm th}}\left(\frac{\delta P}{P} - \frac{\delta P_{\rm turb}}{P}\right). \tag{3.15}$$

As argued by Houdek et al. (2017), based on Houdek and Dupret (2015), the pulsational Lagrangian perturbation of the turbulent pressure ($\delta P_{\rm turb}$) mainly contributes to the driving and damping of the oscillations, i.e. to the imaginary part of the mode frequencies. Thus, $\delta P_{\rm turb}$ can safely be neglected, when computing adiabatic oscillations, i.e.

$$\frac{\delta\rho}{\rho} \approx \frac{1}{\Gamma_1^{\rm red}}\frac{\delta P}{P}, \tag{3.16}$$

where $\Gamma_1^{\rm red} = \Gamma_1 P_{\rm th}/P$. In short, turbulent pressure alters the linearized pulsation equations by a factor of $P/P_{\rm th}$, which may conveniently be taken into account by including the inverse of this factor into $\Gamma_1$. This is known as the reduced $\Gamma_1$ approximation (cf. Rosenthal et al., 1999).

In the case of ADIPLS, the above implies that one must supply $P$, $\rho$, $r$, $\Gamma_1^{\rm red}$, and $q = m/M$ at each mesh point along with the Brunt-Väisälä frequency

$$\langle N^2\rangle = \frac{1}{\Gamma_1^{\rm red}}\frac{{\rm d}\ln P}{{\rm d}\ln r} - \frac{{\rm d}\ln\rho}{{\rm d}\ln r}, \tag{3.17}$$

in order to compute stellar oscillation frequencies in a consistent manner.

While some authors include turbulent pressure, when computing stellar structures, it is commonly neglected in standard stellar models. Many authors, who include turbulent pressure in the structure calculation, nevertheless omit the necessary changes to the oscillation equations: they do not work within the reduced $\Gamma_1$ approximation but simply use the value of $\Gamma_1$ that follows from the EOS. This is known as the gas $\Gamma_1$ approximation. In order to facilitate an easy comparison with the literature, I hence use the gas $\Gamma_1$ approximation throughout most of this thesis. However, the reduced $\Gamma_1$ approximation is employed in Chapters 8 and 10.

## 3.2 Inversion Techniques

Stellar oscillations are determined by the interior structure of stars. Reversely, it is thus possible to infer the structure of a star from its oscillations: by comparing model predictions with observations, a best-fitting structure can be evaluated. The Sun is a special case[2] since it is possible to gather comprehensive data for our host star. It is hence possible to infer the actual solar sound speed and density profiles, using linear perturbation analysis.

[2]Recently, successful attempts to probe the internal structure of other stars have been made (Bellinger, 2018).

Consider a solar model that leads to the angular frequencies $\omega_{n\ell,\mathrm{mod}}$ that deviate by $\delta\omega_{n\ell}$ from observations. Assuming that $\delta\omega_{n\ell}$ is small, it can be shown that (cf. Basu et al., 1997; Rabello-Soares et al., 1999)

$$\frac{\delta\omega_{n\ell}}{\omega_{n\ell,\mathrm{mod}}} = \int_0^{R_\odot} K^{n\ell}_{c^2,\rho} \frac{\delta_r c^2}{c^2_{\mathrm{mod}}} \mathrm{d}r + \int_0^{R_\odot} K^{n\ell}_{\rho,c^2} \frac{\delta_r \rho}{\rho_{\mathrm{mod}}} \mathrm{d}r + \frac{F_{\mathrm{surf}}(\omega_{n\ell,\mathrm{mod}})}{Q_{n\ell,\mathrm{mod}}} + \epsilon_{n\ell}, \tag{3.18}$$

with $Q_{n\ell,\mathrm{mod}}$ being the mode inertia and $F_{\mathrm{surf}}(\omega_{n\ell,\mathrm{mod}})$ encoding the surface effect that is addressed in Section 3.3. Furthermore, $\epsilon_{n\ell}$ denotes the observational error and $K^{n\ell}_{c^2,\rho}$ and $K^{n\ell}_{\rho,c^2}$ are known kernels. Finally, $\delta_r\rho$ and $\delta_r c^2$ denote the difference in the density and the difference in the squared sound speed between the model and the Sun, respectively. Here, the adiabatic sound speed $c$ is given by

$$c^2 = \frac{\Gamma_1 P_{\mathrm{th}}}{\rho}. \tag{3.19}$$

At each mesh point of the modelled equilibrium structure, the solution to the inversion problem can be written as

$$\left\langle \frac{\delta_r c^2}{c^2_{\mathrm{mod}}} \right\rangle_{r=r_0} = \sum_{n\ell} \Lambda_{n\ell}(r_0) \frac{\delta\omega_{n\ell}}{\omega_{n\ell,\mathrm{mod}}}, \tag{3.20}$$

since the inversion is performed through a set of linear operations. Here, $\Lambda_{n\ell}$ denotes a set of appropriate inversion coefficients. These inversion coefficients can be established based on averaging kernels ($\mathcal{K}(r_0, r)$):

$$\mathcal{K}(r_0, r) = \sum_{n\ell} \Lambda_{n\ell}(r_0) K^{n\ell}_{c^2,\rho}. \tag{3.21}$$

Solving the inversion problem amounts to evaluating suitable averaging kernels. This is done using minimization in order to match the kernels to a target function. The narrower the target function is, the higher the resolution becomes. Different methods, including different target functions, can be found in the literature. For details on the so-called Multiplicative Optimally Localized Averages (MOLA) technique and Subtractive Optimally Localized Averaging (SOLA), I refer to Rabello-Soares et al. (1999). I employ the SOLA technique in Chapter 4.

## 3.3 The Surface Effect

The frequencies of stellar models are computed under the assumption of adiabaticity. The fact that non-adiabatic effects are thus neglected is especially crucial for the surface layers. Together with contributions from the turbulent pressure beyond those included in the reduced $\Gamma_1$ approximation (cf. Section 3.1.2), non-adiabatic effects lead to a frequency shift known as the modal surface effect (cf. Houdek et al., 2017). The modal surface effect arises

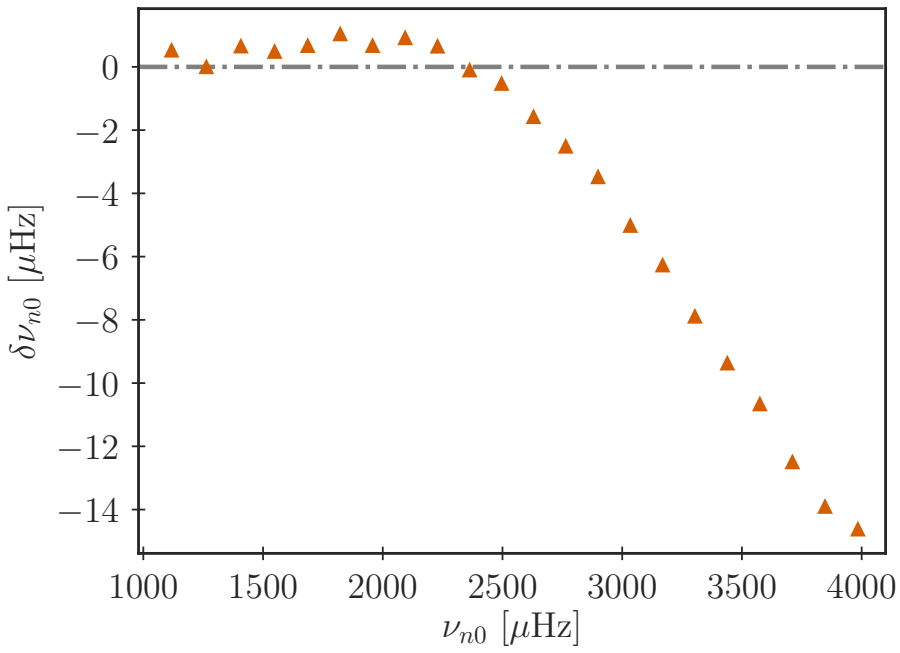


Figure 3.1: Frequency differences between BiSON observations and a standard solar model from GARSTEC. The plot only includes radial modes ($\ell = 0$) with p-mode frequencies above 1000 $\mu$Hz. The observational error bars are not included, as the markers are larger than the typical errors.

due to issues regarding the frequency computation and does hence not reflect deficiencies of the stellar structure models.

While references to the modal effect are scattered throughout this thesis in connection with data comparisons, inherent issues with the frequency computation, beyond the reduced $\Gamma_1$ approximation, are not addressed head-on. Instead, I focus on improving the structure of stellar models: the use of mixing length theory and similar approximations means that the surface layers of stars with convective envelopes are incorrectly modelled (cf. Chapter 2). This structural shortcoming leads to an additional frequency shift known as the structural surface effect. For this reason, I developed methods to overcome the aforementioned structural shortcomings by including information from 3D simulations of the superadiabatic near-surface layers into 1D stellar evolution codes. As shown in Chapters 6-10, these methods eliminate the structural contribution to the surface effect.

As a result of the modal and structural contributions to the surface effect, the adiabatic frequencies inferred from 1D standard solar models are roughly 15 $\mu$Hz too high at a frequency of 4000 $\mu$Hz. At lower frequencies the mismatch is lower, since modes with higher frequencies probe shallower regions of the star. This is illustrated for the present-day Sun in Fig. 3.1, where $\nu_{n\ell}$ denotes the mode frequency with radial order $n$ and degree $\ell$, and

$\delta\nu_{n\ell}$ denotes the frequency residual between model predictions and observations:

$$\delta\nu_{n\ell} = \nu_{n\ell}^{\rm obs} - \nu_{n\ell}^{\rm mod}, \tag{3.22}$$

where the labels 'obs' and 'mod' refer to observations and model frequencies, respectively. When comparing solar models to observations, I use observed frequencies, stemming from the Birmingham Solar Oscillation Network, BiSON (cf. Broomhall et al., 2009; Davies et al., 2014).

For simplicity, I only include radial modes ($\ell = 0$) in Fig. 3.1. I hence avoid the necessity of scaling $\delta\nu_{n\ell}$ by the ratio between the mode inertia (or modal mass) and the mode inertia of a radial mode with the same frequency (cf. Christensen-Dalsgaard, 1986). Chapters 6-10 contain several plots that are reminiscent of Fig. 3.1.

The surface effect poses an obstacle, when comparing model frequencies to observations and has haunted helio- and asteroseismology for decades (cf. Brown, 1984; Christensen-Dalsgaard et al., 1988a). With the high-quality data from the CoRoT (cf. Baglin et al. 2009) and *Kepler* (cf. Borucki et al. 2010) space missions, this has become a dire obstacle since seismic measurements have become a common tool to constrain stellar parameters (e.g. Chaplin and Miglio, 2013).

In order to mitigate the surface effect, most authors turn to empirical or theoretical surface correction relations. Such relations predict the systematic offset of each mode, allowing for a direct comparison between model frequencies and observations. Based on a fit to the present-day Sun, Kjeldsen et al. (2008) originally suggested a purely empirical correction relation. However, this approximation has been shown not to be universally applicable throughout the HR diagram (cf. Ball and Gizon 2017). This is a recurrent problem that arises in connection with such relations: they are often calibrated based on a very small set of benchmark stars.

Ball and Gizon (2014) propose a relation that builds on physical assumptions and an asymptotic analysis by Gough (1990), while Sonoi et al. (2015) derived a surface correction relation from 3D radiative hydrodynamic (RHD) simulations of convection. Neither of these relations is, however, indubious. I return to this issue in Chapter 7.

As an alternative to surface correcion relations, Roxburgh and Vorontsov (2003) suggested to circumvent the problem altogether by employing frequency ratios that are mostly insensitive to the surface layers (cf. Otí Floranes et al. 2005). These ratios are

$$r_{01}(n) = \frac{\nu_{n-1,0} - 4\nu_{n-1,1} + 6\nu_{n,0} - 4\nu_{n,1} + \nu_{n+1,0}}{8(\nu_{n,1} - \nu_{n-1,1})}, \tag{3.23}$$

$$r_{10}(n) = \frac{-\nu_{n-1,1} + 4\nu_{n,0} - 6\nu_{n,1} + 4\nu_{n+1,0} - \nu_{n+1,1}}{8(\nu_{n+1,0} - \nu_{n,0})}, \tag{3.24}$$

$$r_{02}(n) = \frac{\nu_{n,0} - \nu_{n-1,2}}{\nu_{n,1} - \nu_{n-1,1}}, \tag{3.25}$$

where $\nu_{n,\ell}$ denotes the individual oscillation frequency of radial order $n$ and degree $\ell$.

As discussed by Ball and Gizon (2017) and Nsamba et al. (2018a), the stellar parameter estimates that are obtained from asteroseismic analyses depend on how the systematic

offset of the model frequencies is accounted for. I arrive at a qualitatively similar conclusion in Chapter 7.

For instance, according to Nsamba et al. (2018a), the empirical surface correction relation by Kjeldsen et al. (2008) leads to mass estimates that are on average 3 % higher than those obtained using frequency ratios when modelling solar-like MS stars. The analysis by Ball and Gizon (2017) likewise points to significant deviations between the parameter estimates obtained based on different surface correction relations. A direct quantitative comparison between the two papers is, meanwhile, rather intricate. For instance, while both papers address the surface correction by Kjeldsen et al. (2008), they use different values for the involved power-law index (cf. Chapter 7). Furthermore, while the parameter estimates by Nsamba et al. (2018a) correspond to the means of posterior probability distributions, Ball and Gizon (2017) list the parameters of the best-fitting models in their model grid. For similar reasons, a direct comparison with the results presented for two target stars in Chapter 7 becomes equally labyrinthine.

Thus, the employed correction methods affect the results of asteroseismic analyses. This point is illustrated and further quantified in Chapter 7. Yet another way to address the surface effect is to directly correct for the underlying structural shortcomings of the models. Two different methods that are based on this notion are presented in Chapter 6-10. As shown in these chapters, both methods are able to partly or completely overcome the structural contribution to the surface effect, leaving only modal effects to be corrected for.

It is worth noting that a more realistic depiction of the outermost superadiabatic layers of stars with convection envelopes has additional advantages over alternative methods to deal with the surface effect. Not only does this approach eliminate the structural surface effect, but I show Chapters 8-10 that more realistic boundary layers also alter the stellar evolution tracks. In asteroseismic analyses, the implications of using a more realistic depiction of superadiabatic convection are hence twofold: first, this approach overcomes one of the main contributions to the surface effect. This is important since the necessity to deal with the surface effect greatly complicates the extraction of stellar parameters from stellar oscillations. Secondly, the aforementioned shift in the stellar evolution tracks may likewise affect stellar parameter estimates (cf. Chapters 8, 9, and 12). Both issues may thus potentially have severe consequences for any analysis that relies on the accurate determination of stellar parameters, including studies that deal with the chemical and dynamical evolution of the Milky Way galaxy (Miglio, 2012).

# Chapter 4

# Lithium Depletion and the Tachocline Anomaly

*The content, including most of the text, of this chapter was published in Monthly Notices of the Royal Astronomical Society by Jørgensen and Weiss (2018). I am the first author of the paper and the primary investigator of the presented research project. I wrote this chapter. My contributions include the implementation and testing of the associated modifications to* GARSTEC *as well as the subsequent data analysis. The tool for SOLA inversion and guidance for its usage was kindly provided by Jørgen Christensen-Dalsgaard, who also commented on a draft of the paper before publication. The work was performed in collaboration with Achim Weiss, who contributed with constructive and useful feedback, and who proposed the original research question.*

For most of this thesis, I investigate how multi-dimensional hydrostatic simulations of the outermost layers of low-mass stars can be used to improve 1D stellar models. Thus, I deal with the upper boundary of convective envelopes. As regards 1D stellar evolution codes, the improper treatment of convective surface layers is, however, not the only shortcoming that is related to the treatment of convection: the transition between the convection zone and the radiative interior at the lower boundary of the convective envelope[1] is likewise not well understood. In this chapter, I take a closer look at this issue. Using parameterizations of the properties of multi-dimensional simulations of convection, I seek to improve the treatment of additional mixing processes in this region. While the present chapter thus deals with a different aspect of stellar models than all the succeeding chapters, it serves to illustrate the broad applicability of multi-dimensional hydrostatic simulations in the pursuit of improving the physics in 1D stellar evolution codes.

Current standard solar models neither account properly for the photospheric lithium

[1]Note that when I refer to the convective envelope, in this chapter, I do, indeed mean the entire outer convection zone. On the other hand, in Chapters 5-10, the discussed 3D simulations of stellar envelopes only cover the uppermost layers near the stellar surface.

abundance nor reproduce the inferred solar sound speed profile. Diffusive overshooting at the base of the solar convective envelope has previously been shown to solve either of these model inadequacies (e.g. Baraffe et al., 2017; Christensen-Dalsgaard et al., 2018). In this chapter, I present an analysis of solar models with four different parameterizations of diffusive overshooting. I find that these models are able to recover the correct lithium depletion as a function of time, regardless of the parameterization, if overshooting is suppressed, during the early evolutionary stages. Furthermore, parameterizations of diffusive overshooting have been shown to improve the inferred sound speed profile. However, none of the presented models is able to simultaneously solve both model inadequacies, showing that diffusive overshooting, on its own, is deficient in accounting for observations.

## 4.1 The Role of Overshooting

Comparisons between observations and model predictions reveal several shortcomings of modern stellar structure models. Present model inadequacies include discrepancies between the predicted solar sound speed profile and the solar sound speed profile inferred from helioseismology (cf. Christensen-Dalsgaard et al., 1985, 1991), i.e. the study of solar oscillations (cf. Leighton, 1960; Ulrich, 1970). Especially near the tachocline, the sound speed difference between the Sun and current standard solar models show a striking anomaly.

Lithium depletion in stellar convective envelopes is another issue that still has to be properly accounted for: meteoritic measurements and spectroscopic measurements of the solar photosphere show that the present solar abundance of $^7$Li is roughly 100-200 times lower than the initial one (cf. Greenstein and Richardson, 1951; Asplund et al., 2009). Standard solar models do not reproduce this depletion. Moreover, surveys reveal that the Sun is not exceptional for a star of its age, mass, and metallicity: solar-like stars are generally lithium poor (e.g. Baumann et al. 2010).

The tachocline anomaly was immediately apparent from the first inversions of helioseismic data (cf. Christensen-Dalsgaard et al., 1985, 1988b). This discrepancy in the sound speed profile may partly reflect errors in the opacities (cf. Christensen-Dalsgaard et al. 2010) but can also be addressed, by including additional mixing beyond the convective boundaries of stellar models (cf. Elliott et al., 1998; Christensen-Dalsgaard et al., 1993; Richard et al., 1996). This additional mixing affects the composition and thereby alters the sound speed, potentially getting rid of the tachocline anomaly. Other seismic properties, such as the mode amplitudes, can be employed to impose further restrictions on the mixing processes (cf. Christensen-Dalsgaard et al., 2011).

Mixing below the solar convective envelope furthermore transports lithium to hotter layers, where it is depleted in thermonuclear reactions, solving the lithium depletion problem. This solution was originally suggested by Böhm (1963) and does indeed deplete lithium sufficiently to match the present solar photospheric values if the parameters involved are adequately tuned. That being said, while observations (e.g. Chaboyer 1998) indicate that this depletion mainly takes place on the main sequence (MS), solar models with overshooting deplete lithium prematurely (e.g. Ahrens et al. 1992), unless the suggested additional

mixing is somehow inhibited on the pre-main sequence (pre-MS, Schlattl and Weiss 1999). We will elaborate upon this in Section 4.3.

Consequently, as discussed by several authors, both of the issues raised above can be addressed simultaneously, by including mixing in the radiative zone (cf. Christensen-Dalsgaard et al., 1993; Richard et al., 1996; Schlattl and Weiss, 1999; Andrássy and Spruit, 2013).

Several processes have been advocated to contribute to the necessary additional mixing, including differential rotation between the radiative and the convective zones (e.g. Spiegel and Zahn 1992), internal gravity waves (e.g. Garcia Lopez and Spruit 1991), and the penetration of convective plumes into the radiative zone, so-called overshooting. Different authors offer different pictures and models for the latter; for instance, based on Spruit (1997), Andrássy and Spruit (2013) and Andrássy and Spruit (2015) argue for overshooting, assuming that convective settling beyond the convective boundary can be understood in terms of an entropy difference between the sinking material and its surroundings. After the publication of Jørgensen and Weiss (2018) that is presented in this chapter, we took a closer look at this overshooting scheme and included the necessary advection and settling processes into GARSTEC. The results of this analysis are summarized in Appendix B and are in good agreement with the conclusions drawn below.

One way of taking overshooting into account amounts to extending the adiabatic region by a fraction of a pressure scale height into the subadiabatic region beyond the base of the convection envelope. Such quasi-adiabatic penetration can be achieved, using mixing length theory (cf. Zahn 1991). However, just as it is the case for models without overshooting, this approach gives rise to an abrupt transition in the temperature gradient, which is neither favoured by helioseismic measurements nor by hydrodynamic simulations of the convective plumes. Other treatments of overshooting, on the other hand, do not suffer from this deficit (e.g. Andrássy and Spruit 2013). For a detailed discussion of this topic, we refer to Christensen-Dalsgaard et al. (2011).

Yet another method to take the structural effects of overshooting into account is to adjust the temperature gradient in the overshooting region, drawing from helioseismology and the overshooting profiles of 3D simulations (cf. Christensen-Dalsgaard et al. 2011). Finally, one may introduce additional mixing, by altering the diffusion coefficients in the overshooting layer (e.g. Baraffe et al., 2017; Christensen-Dalsgaard et al., 2018; Schlattl and Weiss, 1999). Such adjustments of the diffusion coefficient may be justified by the attempt to mimic the outcome of 2D or 3D hydrodynamic simulations (cf. Freytag et al., 1996; Pratt et al., 2016).

In this chapter, we follow the last approach mentioned above, and hence restrict ourselves to diffusive overshooting. While the diffusion coefficients are altered to accommodate for additional mixing in the radiative zone, the radiative temperature gradient is used within the overshooting layer.

We investigate four different parameterizations of the diffusion coefficients in the overshooting layer, restricting ourselves to the solar case. The aim is to evaluate, whether each of these parameterizations can solve the lithium depletion problem, and whether models that succeed simultaneously solve the tachocline anomaly. To this end, we have performed

solar calibrations for each overshooting parameterization, using GARSTEC. All solar models have a radius $R_\odot$ of $6.95508 \times 10^{10}$ cm, a total luminosity $L_\odot$ of $3.846 \times 10^{33}\,\mathrm{erg\,s^{-1}}$, and an age of $t_\odot$ of 4.57 Gyr. We employ the OPAL equation of state (EOS, Rogers and Nayfonov, 2002; Rogers et al., 1996). At low temperatures, we extend the EOS with the EOS by Hummer and Mihalas (1988). We use either the composition suggested by Grevesse and Sauval (1998) (GS98) or by Asplund et al. (2009) (AGSS09) with the corresponding OPAL opacities (cf. Ferguson et al., 2005; Iglesias and Rogers, 1996) and surface abundance $Z_\mathrm{s}$ of heavy elements relative to the surface abundance $X_\mathrm{s}$ of hydrogen. In all cases, we use the reaction rates suggested by Adelberger et al. (2011). We include the microscopic diffusion of H, $^3$He, $^4$He, $^{12}$C, $^{13}$C, $^{14}$N, $^{15}$N, $^{16}$O, $^{17}$O, $^{20}$Ne, $^{24}$Mg, and $^{28}$Si that are considered in the nuclear reaction network (cf. Weiss and Schlattl 2008). $^7$Li and $^9$Be are likewise diffused but are treated as tracer elements. Moreover, we have only implemented overshooting at the bottom of the convective envelope. We note that overshooting at the core must generally be modelled differently from envelope overshooting (e.g. Schlattl and Weiss 1999). In the case of solar calibration models, core overshooting is only relevant for the pre-main sequence (pre-MS).

## 4.2 Overshooting Approaches

A very simplistic diffusive approach is to extend the convective zone by an overshooting layer, for which the diffusion coefficient $D_\mathrm{ov}$ is assumed to be a step function:

$$D_\mathrm{ov}(r) = \begin{cases} D_0, & \text{for } r_\mathrm{cz} - l_\mathrm{ov} < r < r_\mathrm{cz}, \\ 0, & \text{otherwise.} \end{cases} \tag{4.1}$$

In the following, we use the label CON to refer to models, for which the diffusion coefficient is constant within the overshooting layer, i.e. for which the parameterization given by Eq. (4.1) is employed. The default case of no overshooting is labelled DEF.

In Eq. (4.1), $r$ denotes the distance from the stellar centre, and $r_\mathrm{cz}$ denotes the radius of the lower convective boundary, i.e. the radius below which the Schwarzschild criterion of convective instability, $\nabla_\mathrm{rad} > \nabla_\mathrm{ad}$, no longer holds true (cf. Chapter 2). $D_0$ takes the value of the diffusion coefficient half a scale height above the convective boundary, as the diffusive velocity is formally zero at the boundary. Hence, based on mixing length theory, $D_0$ is $\frac{1}{3}\ell_\mathrm{mix} v_\mathrm{MLT}$. Here, $\ell_\mathrm{mix}$ and $v_\mathrm{MLT}$ are the mixing length and the convective velocity, respectively. The units are hence $\mathrm{cm^2\,s^{-1}}$. The width $l_\mathrm{ov}$ of this overshooting layer may be chosen freely to fit observations.

Freytag et al. (1996) and Blöcker et al. (1998) have suggested a more sophisticated approach, based on two-dimensional hydrodynamical simulations. Here, we employ the implementation by Schlattl and Weiss (1999), according to which the diffusion coefficient in the overshooting region is

$$D_\mathrm{ov}(r) = D_0 \exp\left(\frac{-2(r_\mathrm{cz} - r)}{f_\mathrm{ov} H_p}\right). \tag{4.2}$$

In the following, we use the label FOV to refer to the overshooting parameterization by Freytag et al. (1996) given by Eq. (4.2).

In Eq. (4.2), $f_{\rm ov}$ is a free parameter, and $D_0$ is defined as above. Finally, $H_p$ denotes the pressure scale height at the base of the convection zone, including a geometrical restriction: if $2H_p$ exceed the extent of the convection zone ($\Delta r_{\rm cz}$), $H_p$ is adjusted by a factor of $(\Delta r_{\rm cz}/(2H_p))^2$. This geometrical limitation of overshooting is especially important when considering core overshooting but is mostly irrelevant in the present case. We refer to Higl and Weiss (2017), who have modelled detached eclipsing binaries, for a discussion of a case for which the implementation of this geometrical cut-off becomes essential. We apply this geometrical cut-off for all diffusive overshooting parameterizations presented in this chapter.

The seismic implications of the overshooting parameterization by Freytag et al. (1996) and the associated lithium depletion have previously been discussed by Schlattl and Weiss (1999). While they also address cases, where core overshooting is taken into account, we only include envelope overshooting, in order to facilitate a meaningful comparison between the different approaches. We introduce a cutoff, when $D_{\rm ov}(r)$ becomes smaller than $10^{-20}D_0$.

Generally speaking, exponentially decaying diffusive mixing is often used to improve stellar models (e.g. Miglio et al., 2007; Buldgen et al., 2017, where the scaleheight is determined by the density).

Recently, Pratt et al. (2016) and Baraffe et al. (2017) have suggested yet another overshooting parameterization, based on two-dimensional hydrodynamical simulations of compressible convection in young stellar objects (YSOs):

$$D_{\rm ov}(r) = D_0 \left\{ 1 - \exp\left[ -\exp\left( \frac{-\frac{(r_{\rm cz}-r)}{R} - \mu}{\lambda} \right) \right] \right\}. \tag{4.3}$$

We attribute the label PB to this parameterization by Pratt et al. (2016) and Baraffe et al. (2017). In accordance with Baraffe et al. (2017), we adopt $\mu = 5 \times 10^{-3}$ and $\lambda = 6 \times 10^{-3}$, based on the simulation of a $1\,M_\odot$ pre-MS star by Pratt et al. (2016). Assuming that processes, such as rotation, may restrict the overshooting of convective plumes, Baraffe et al. (2017) introduce a limiting width $d_{\rm ov}$ of the overshooting region. In order to avoid extensive lithium depletion on the pre-MS, Baraffe et al. (2017) set $d_{\rm ov}$ to $0.1\,H_{\rm p}$, when the rotation rate exceeds a certain critical value. Below this critical rotation rate, $d_{\rm ov}$ is set to $1\,H_{\rm p}$. For further details we refer to Section 4.3 and the quoted paper. While Baraffe et al. (2017) discuss the issue of depletion, they do not address the asteroseismic implications of Eq. (4.3).

Finally, Christensen-Dalsgaard and Di Mauro (2007) and Christensen-Dalsgaard et al. (2018) adopt a diffusive process that follows a power-law:

$$D_{\rm ov}(r) = D_{\rm JCD} \left( \frac{v - v_0}{v_{\rm c} - v_0} \right)^{\alpha}, \quad v = \frac{1}{\rho}. \tag{4.4}$$

We refer to this last parameterization as JCD. Here $\alpha$, $v_0$ and $D_{\rm JCD}$ are free parameters, while $v_{\rm c} = 1/\rho_{\rm c}$, where $\rho_{\rm c}$ is the density at the base of the convection zone. In order

to obtain sensible seismic results, using the solar composition recommend by AGSS09, Christensen-Dalsgaard et al. (2018) have implemented the opacity correction suggested by Christensen-Dalsgaard et al. (2010). We have not included this correction. While Christensen-Dalsgaard et al. (2018) address the helioseismic implications of their diffusive overshooting parameterization, they do not investigate the resulting lithium depletion.

In accordance with Christensen-Dalsgaard et al. (2018), we adopt $\alpha = 4.25$ and $v_0 = 0.15\,\mathrm{g}^{-1}\mathrm{cm}^3$ and introduce a cutoff at $v = v_0$. If $D_{\mathrm{ov}}(r)$ becomes smaller than $10^{-20} D_{\mathrm{ov}}(r_{\mathrm{cz}})$, we likewise introduce a cutoff. We have varied $D_{\mathrm{JCD}}$, including the value employed by Christensen-Dalsgaard et al. (2018): $D_{\mathrm{JCD}} = 150\,\mathrm{cm}^2\,\mathrm{s}^{-1}$.

## 4.3 Lithium Depletion

We have adjusted the free parameters $l_{\mathrm{ov}}$, $f_{\mathrm{ov}}$, $d_{\mathrm{ov}}$, and $D_{\mathrm{JCD}}$, in order to obtain a lithium depletion by a factor of 100-200, using the four different overshooting parameterizations described in Section 4.2.

The associated overshooting parameters can be found in the text below, together with a discussion of each case. The relative depletion of lithium until the present solar age, according to each model, is listed in Table 4.1 alongside other model properties. These include $r_{\mathrm{cz}}$ as well as the corresponding acoustic depth:

$$\tau_{\mathrm{cz}} = \int_{r_{\mathrm{cz}}}^{R_\odot} \frac{\mathrm{d}r'}{c}, \tag{4.5}$$

where $c$ denotes the sound speed. Moreover, the table includes the mixing length parameter[2] ($\alpha_{\mathrm{MLT}}$, Böhm-Vitense 1958), to illustrate the influence of the overshooting scheme on the stellar parameters. Finally, the helium mass fraction $Y_{\mathrm{s}}$ at the solar surface is listed. For all models in Table 4.1 that lead to a satisfactory depletion of lithium, $Y_{\mathrm{s}}$ is roughly within $2\sigma$ of the value recommended by Basu and Antia (2004): $0.2485 \pm 0.0035$. The model without overshooting is in slightly worse agreement with the observed value of $Y_{\mathrm{s}}$. However, this conclusion depends on the input physics, and very good agreement without overshooting can be obtained (cf. Weiss and Schlattl 2008). The variation in $Y_{\mathrm{S}}$ that results from the inclusion of overshooting reflects the requirements set by the calibration procedure: the inclusion of overshooting effectively extends the convective envelope and thereby influences the chemical profile — and thus the surface composition. At the same time, the solar calibration models are all required to reproduce the solar radius ($R_\odot$), the solar luminosity ($L_\odot$), and the solar surface abundance of heavy elements ($Z_{\mathrm{S}}/X_{\mathrm{S}}$). This is achieved by altering the mixing length parameter (see Table 4.1, last column) and the initial composition, which likewise affects $Y_{\mathrm{S}}$. Thus, the depth of the convective envelope and the surface helium abundance change, due to the regulating effect of the calibration procedure. The various overshooting schemes lead to slight variations only as a second-order effect.

[2]The value of the mixing length parameter depends on the boundary conditions used in the solar model calibration (e.g. Weiss and Schlattl 2008). We have here consistently used Eddington grey atmospheres.

Table 4.1: Properties of the models presented in Fig. 4.1, using GS98. $\mathrm{Li}_0/\mathrm{Li}_\odot$ denotes the initial model surface lithium abundance ($N(\mathrm{Li})/N(\mathrm{H})$) relative to the predicted present one. $\Delta r_{\mathrm{ov}}$ refers to the width of the overshooting layer. As regards the JCD parameterization described by Eq. (4.4), $D_{\mathrm{JCD}} = 150\,\mathrm{cm}^2\,\mathrm{s}^{-1}$ in case a, while $D_{\mathrm{JCD}}$ is two orders of magnitude higher in case b. The values for $D_{\mathrm{JCD}}$ and the remaining free parameters can be found in the text. $\alpha_{\mathrm{MLT}}$ denotes the mixing length parameter. The initial abundance of helium and heavy elements predicted by the calibration lie in the intervals $0.265 - 0.269$ and $0.0178 - 0.0187$, respectively. All models in this table take microscopic diffusion of metals into account.

| $D_{\mathrm{ov}}$ | $\mathrm{Li}_0/\mathrm{Li}_\odot$ | $\frac{\Delta r_{\mathrm{ov}}}{R_\odot}$ | $\frac{r_{\mathrm{cz}}}{R_\odot}$ | $\tau_{\mathrm{cz}}$ [s] | $Y_{\mathrm{S}}$ | $\alpha_{\mathrm{MLT}}$ |
|---|---|---|---|---|---|---|
| DEF | 3.7 | — | 0.715 | 2083 | 0.2393 | 1.80 |
| CON | $1.2 \times 10^2$ | 0.08 | 0.718 | 2074 | 0.2451 | 1.77 |
| FOV | $1.7 \times 10^2$ | 0.16 | 0.718 | 2073 | 0.2454 | 1.77 |
| PB | $1.6 \times 10^2$ | 0.08 | 0.718 | 2074 | 0.2450 | 1.77 |
| JCD, a | 4.0 | 0.36 | 0.717 | 2078 | 0.2415 | 1.79 |
| JCD, b | $1.4 \times 10^2$ | 0.36 | 0.719 | 2072 | 0.2465 | 1.77 |

When computing $D_{\mathrm{ov}}(r)$, using Eqs (4.1)-(4.3), lithium is sufficiently depleted. However, this depletion takes place on the pre-MS, as already discussed by Baraffe et al. (2017) and Schlattl and Weiss (1999). This is inconsistent with observations (e.g. of the Pleiades or the Hyades), according to which the depletion mainly takes place on the MS at a rate that depends on the angular momentum (cf. e.g. Chaboyer, 1998; Jones et al., 1997, 1999).

Ventura et al. (1998) propose that the inhibition of the lithium depletion on the pre-MS may be explained by rotationally induced magnetic fields — the authors also address the influence of changes in other input physics, such as the composition. Based on numerical studies (cf. Ziegler and Rüdiger, 2003; Brummell, 2007; Brun et al., 2017), Baraffe et al. (2017) equally argue that rotation limits the convective plumes, reducing $d_{\mathrm{ov}}$ at high angular velocities. Hence Baraffe et al. (2017) evaluate the rotation period, using Kawaler's law (cf. Kawaler, 1988; Bouvier et al., 1997; Viallet and Baraffe, 2012), and assume $d_{\mathrm{ov}}$ to be a step function of the angular velocity. This necessitates the introduction of additional parameters that are neither restricted by simulations nor by observations. That being said, for many choices of these parameters, their method effectively amounts to introducing one additional free parameter: the time $t_{\mathrm{ov}}$, before which overshooting is negligible or, at least, relatively inefficient.

Setting $t_{\mathrm{ov}}$ to the first $10^8\,\mathrm{yr}$ and changing $d_{\mathrm{ov}}$ from $0.10H_p$ to $0.99H_p$ at $t_{\mathrm{ov}}$, we obtain models that deplete lithium predominantly on the MS, when using GS98 and the PB parameterization. These parameter values are overall consistent with the results presented by Baraffe et al. (2017), who effectively use a higher value of $t_{\mathrm{ov}}$.

Applying the same arguments regarding the suppression of overshooting during the

early evolutionary stages, we have also introduced the parameter $t_{\rm ov}$, when employing the CON or FOV parameterization, i.e. Eq. (4.1) or (4.2). In accordance with Schlattl and Weiss (1999), who likewise initialized overshooting on the ZAMS, this allows us to compute models, for which the main lithium depletion takes place on the MS.

When employing the CON or FOV parameterization, we set $t_{\rm ov} = 10^8\,{\rm yr}$, $l_{\rm ov} = 1.03$, and $f_{\rm ov} = 0.083$, respectively, and neglect overshooting completely before $t_{\rm ov}$. These parameter values seem qualitatively consistent with Schlattl and Weiss (1999), according to whom a satisfactory lithium depletion can be obtained, using $f_{\rm ov} = 0.07$, when starting envelope overshooting on the ZAMS and ignoring core overshooting[3].

In the case of the JCD parameterization, i.e. Eq. (4.4), overshooting only depletes the surface lithium abundance by factor of four (cf. case a in Table 4.1), when using the parameter values suggested by Christensen-Dalsgaard et al. (2018). We therefore vary $D_{\rm JCD}$. To obtain a lithium depletion by a factor of 100-200, we need to increase $D_{\rm JCD}$ by two orders of magnitude. Figure 4.1 shows the results for[4] $D_{\rm JCD} = 1.1 \times 10^4\,{\rm cm^2\,s^{-1}}$ (cf. case b in Table 4.1). Although $D_{\rm JCD}$ is several orders of magnitudes lower than $D_0$, a high lithium depletion is achieved, as the overshooting layer is significantly deeper than for the other three parameterization schemes.

In contrast to the other overshooting parameterizations presented in this chapter, no additional parameter is needed to prevent a significant lithium depletion during the early evolutionary stages, in the case of the JCD parameterization. Here, we have set[5] $t_{\rm ov} = 0$.

For the CON, FOV, and PB parameterization, the relevant timescale for diffusion is

$$\tau_{\rm ov} \sim \frac{\Delta r_{\rm ov}^2}{\langle D_{\rm ov}(r)\rangle} = \frac{\Delta r_{\rm ov}^3}{\int D_{\rm ov}(r){\rm d}r}. \tag{4.6}$$

In the overshooting region, this timescale is of the order of decades or shorter, throughout the solar evolution up until the present solar age. In the case of the JCD parameterization, for $D_{\rm JCD} = 150\,{\rm cm^2\,s^{-1}}$, $\tau_{\rm ov} > 7.8\,{\rm Gyr}$ during the entire evolution, quickly exceeding the age of the universe by $1-2$ orders of magnitude. This clarifies, why the parameter values suggested by Christensen-Dalsgaard et al. (2018) do not lead to a sizeable lithium depletion. When increasing $D_{\rm JCD}$ by two orders of magnitude, $\tau_{\rm ov} > 1.3\,{\rm Myr}$ during the entire evolution, reaching billions of years and exceeding the age of the universe during most of the evolution.

[3]We note that Schlattl and Weiss (1999) use $Z_{\rm s}/X_{\rm s} = 0.0245$, as recommended by Grevesse and Noels (1993). Adopting the same surface metallicity, we find that lower values of $l_{\rm ov}$, $f_{\rm ov}$, $d_{\rm ov}$, and $D_{\rm JCD}$ are needed to reach the same lithium depletion than in the case of $Z_{\rm s}/X_{\rm s} = 0.0230$.

[4]For this choice of $D_{\rm JCD}$, $\rho_{\rm c}$ in Eq. (4.4) is $0.1756\,{\rm g\,cm^{-3}}$ at the age of the present Sun. When using $D_{\rm JCD} = 150\,{\rm cm^2\,s^{-1}}$, $\rho_{\rm c} = 0.1789\,{\rm g\,cm^{-3}}$ for the solar calibration model. For comparison, $\rho_{\rm c} = 0.1902\,{\rm g\,cm^{-3}}$ for the modified Model S (see Christensen-Dalsgaard et al. 1996), used by Christensen-Dalsgaard et al. (2018). We have rerun the calculations keeping $\rho_{\rm c}$ fixed, using the value from Christensen-Dalsgaard et al. (2018). While this affects the choice of $D_{\rm JCD}$, we reach the same qualitative conclusions as drawn in the present chapter.

[5]Christensen-Dalsgaard et al. (2018) start their simulation on the ZAMS. For the sake of consistency, one may hence choose a finite $t_{\rm ov}$. We have therefore repeated the computations for the JCD parameterization, setting $t_{\rm ov} = 10^7\,{\rm yr}$ and $10^8\,{\rm yr}$. The corresponding change in the depletion factor of the surface lithium abundance is $\lesssim 10\,\%$.

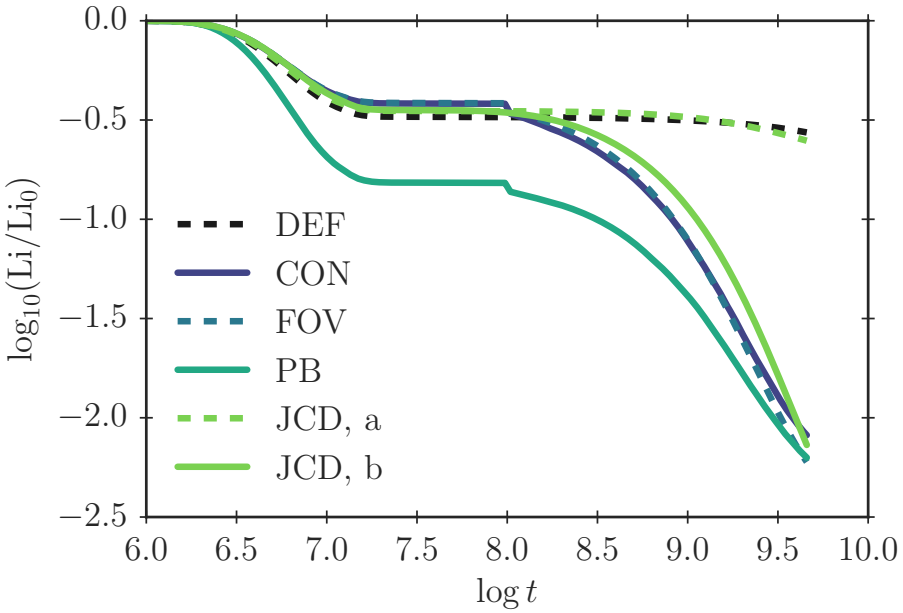


Figure 4.1: Relative change in $N(\mathrm{Li})/N(\mathrm{H})$ at the solar surface surface as a function of time ($t$) for solar models, using GS98 and four different overshooting parameterizations, as well as a standard solar model, for which overshooting is neglected. $\mathrm{Li}_0$ denotes the initial surface lithium abundance: $A(\mathrm{Li}_0) = 3.3$. According to Grevesse and Sauval (1998), the present-day photospheric lithium depletion is 2.2 dex lower than the initial (meteoritic) value.

This rationalizes, why the parameter $t_{\mathrm{ov}}$ is obsolete for this prescription. The longer timescale associated with the JCD parameterization reflects the low value of $D_{\mathrm{JCD}}$ relative to $D_0$, the decrease of the diffusion coefficient with depth and the high penetration depth. As already noted above, the longer timescale is balanced by the higher temperatures reached by the overshooting material, due to the deeper penetration depth.

Figure 4.1 summarizes the evolution of the surface lithium abundance for all models described above. Here, we compare the initial number density $N(\mathrm{Li})$ of lithium relative to the number density $N(\mathrm{H})$ of hydrogen with the final one, since the abundance $A(\mathrm{Li})$, to which the literature refers, is $\log_{10}[N(\mathrm{Li})/N(\mathrm{H})] + 12$.

It is worth noting that we found the lithium depletion to be rather sensitive to the input physics, the overshooting parameters and the other model parameters, by computing several additional solar calibration models. This includes the opacities, the element diffusion, and the bulk composition. We attribute this sensitivity to the extreme temperature dependence of the lithium burning rate.

To illustrate this sensitivity to the input physics, we have repeated the calculations for AGSS09. We set $Z_{\mathrm{s}}/X_{\mathrm{s}} = 0.0179$. The results are summarized in Table 4.2. Here, we likewise use $t_{\mathrm{ov}} = 10^8$ yr but adjust the remaining overshooting parameters, in order to obtain the required lithium depletion: we set $l_{\mathrm{ov}} = 1.26$, $f_{\mathrm{ov}} = 0.103$ and $D_{\mathrm{JCD}} = 2.5 \times 10^4\,\mathrm{cm^2\,s^{-1}}$.

Table 4.2: Same as Table 4.1 but for AGSS09. $A(\mathrm{Li}_0) = 3.2$. The initial abundances of helium and heavy elements predicted by the calibration lie in the intervals $0.259 - 0.265$ and $0.0140 - 0.0148$, respectively. All models in this table take microscopic diffusion of metals into account.

| $D_{\mathrm{ov}}$ | $\mathrm{Li}_0/\mathrm{Li}_\odot$ | $\frac{\Delta r_{\mathrm{ov}}}{R_\odot}$ | $\frac{r_{\mathrm{cz}}}{R_\odot}$ | $\tau_{\mathrm{cz}}$ [s] | $Y_{\mathrm{S}}$ | $\alpha_{\mathrm{MLT}}$ |
|---|---|---|---|---|---|---|
| DEF | 2.5 | — | 0.725 | 2051 | 0.2338 | 1.79 |
| CON | $1.3 \times 10^2$ | 0.10 | 0.728 | 2040 | 0.2407 | 1.76 |
| FOV | $1.5 \times 10^2$ | 0.19 | 0.728 | 2040 | 0.2410 | 1.75 |
| PB | $1.3 \times 10^2$ | 0.10 | 0.728 | 2040 | 0.2406 | 1.76 |
| JCD, a | 2.6 | 0.37 | 0.726 | 2048 | 0.2361 | 1.78 |
| JCD, b | $1.5 \times 10^2$ | 0.37 | 0.729 | 2038 | 0.2421 | 1.75 |

In the case of the PB parameterization, $d_{\mathrm{ov}}$ switches from $0.1H_p$ to $1.23H_p$ at $t_{\mathrm{ov}}$.

Again, the predicted helium mass fraction at the solar surface is higher, when including overshooting. Moreover, the convective envelope is too shallow, as is well known for AGSS09 (cf. Serenelli et al. 2009). This explains the deeper overshooting required in these models.

For both compositions, all models with and without overshooting predict a decrease in the surface abundance of $^9$Be by a factor of $1.1 - 1.3$. While lithium is effectively destroyed at temperatures above $2.5 \times 10^6$ K, the destruction of beryllium sets in at temperatures exceeding $3.5 \times 10^6$ K and hence requires deeper mixing. Measurements of the solar beryllium depletion are notoriously difficult, but studies seem to suggest a very small difference between the photospheric and meteoritic values (cf. Grevesse and Sauval, 1998; Asplund et al., 2009). Data are even consistent with beryllium being undepleted (Balachandran and Bell, 1998). We hence note that none of the overshooting parameterizations strongly contradict measurements of beryllium destruction.

Moreover, according to Gloeckler and Geiss (1996) and Geiss and Gloeckler (1998), the $^3$He/$^4$He ratio has not changed by more than approximately 10 % over the last 3 Gyr. Consequently, just as beryllium, $^3$He/$^4$He restricts the mixing below the base of the convection zone (cf. Vauclair 2000). For all models, we find $^3$He/$^4$He to increase by $3 - 4$ %, throughout the entire evolution from the pre-MS up to the present solar age.

## 4.4 Helioseismic Properties

The propagation of solar oscillations is determined by the adiabatic sound speed $c$ (cf. Chapter 3). The solar sound speed profile can be inferred from observed oscillation frequencies by means of the SOLA inversion technique (cf. Pijpers and Thompson, 1992; Christensen-Dalsgaard and Thompson, 1995), as described in Chapter 3. The results from inversion rely on the computation of adiabatic model frequencies, for which we have

employed ADIPLS. Figure 4.2 shows the corresponding difference in the squared sound speed between the models ($c_{\rm mod}$) and the Sun ($c_{\rm sun}$):

$$\frac{\delta c^2}{c^2} = \frac{c_{\rm sun}^2 - c_{\rm mod}^2}{c_{\rm sun}^2}. \tag{4.7}$$

For every solar calibration model, for which we present the inferred sound speed difference in this chapter, we have re-evaluated the sound speed profile of the Sun, based on the frequency differences between the associated model frequencies and observations (cf. Basu and Antia 1997), using the SOLA inversion technique. For this purpose, J. Christensen-Dalsgaard has kindly provided the necessary tools and kernels.

In stead of inferring $\delta c^2/c^2$ by inversion, many authors compare to a previously inferred solar sound speed profile based on a reference model[6]. To check our inversion results, we have compared the sound speed profile of each of our solar calibration models with the solar sound speed profile inferred by Basu and Antia (2008). From these comparisons, we draw the exact same conclusions as elaborated upon below.

As can be seen from the Fig. 4.2, the model without overshooting shows a characteristic anomaly near the base of the convective envelope: This is the tachocline anomaly.

While overshooting slightly modifies the tachocline anomaly, the implementation of overshooting alone leads to a higher discrepancy in the sound speed at lower depths (cf. Fig. 4.2), in accordance with the work published by other authors (e.g. Christensen-Dalsgaard et al., 2011, 2018; Schlattl and Weiss, 1999). We find that this feature does not appear, if the microscopic diffusion of metals (i.e. diffusion of elements other than H and $^4$He) is ignored: including the microscopic diffusion of metals improves the sound speed of the model without overshooting, throughout the radiative region, but worsens the agreement, especially in the broader vicinity of the tachocline anomaly, in the case of models with overshooting. Figure 4.3 shows the squared sound speed difference between the helioseismic Sun and solar calibration models, for which the microscopic diffusion of metals other than lithium and beryllium has been neglected. We note that the inclusion of the trace elements, lithium and beryllium, has no influence on the sound speed profile. We have used the same values for the overshooting parameters, as in the case of the models presented in Fig. 4.2. The neglect of the microscopic diffusion of metals reduces the lithium depletion slightly. Comparing Figs 4.2 and 4.3, it is clear that the inclusion of overshooting creates a sensitivity on metal diffusion. The fact that the models in Fig. 4.3 get rid of the tachocline anomaly without introducing new anomalies in the sound speed profile is a tantalizing result. Here, we refrain ourselves from performing a detailed investigation of the treatment of diffusion, as this is beyond the scope and not the focus of the present chapter. For a discussion on this issue, we refer to Appendix B.

[6]When comparing to a pre-inferred sound speed profile of the Sun, one may include the uncertainties evaluated by Degl'Innoccenti et al. (1997) (see also Vinyoles et al. 2017). However, the fact that we repeat the inversion for each solar calibration model makes these uncertainties somewhat misleading as they are most certainly too conservative (cf. J. Christensen-Dalsgaard, private communication, based on a discussion between J. Christensen-Dalsgaard and A. Serenelli). We have hence omitted these uncertainties in the plots.

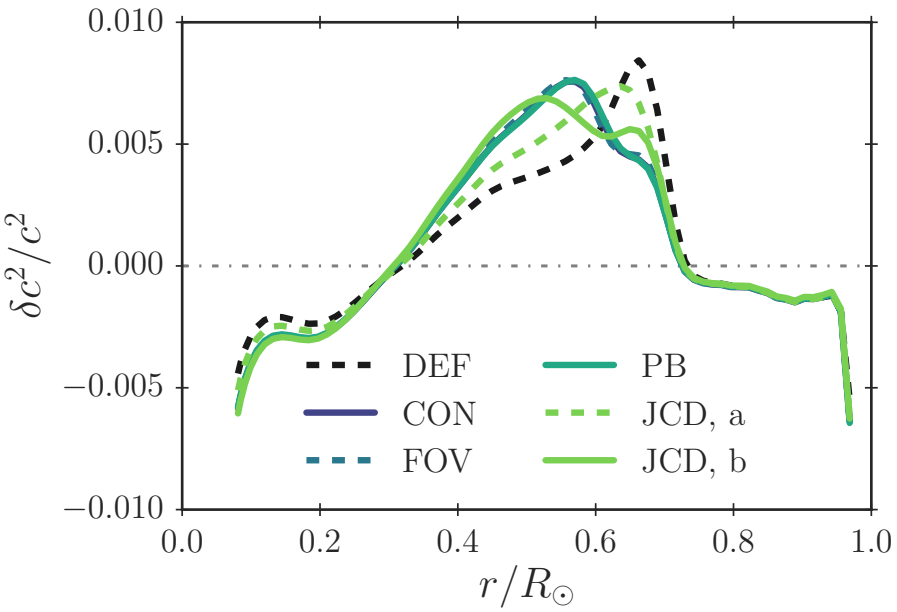


Figure 4.2: Squared sound speed difference between models with different overshooting approaches and the Sun inferred by SOLA inversion. We use GS98. The results are based on the observed 'Best-set' frequencies by Basu et al. (1997). The associated confidence intervals of $\delta c^2/c^2$ and the centres of the averaging kernels are not included for clarity. All solar calibration models in this figure take microscopic diffusion of metals into account.

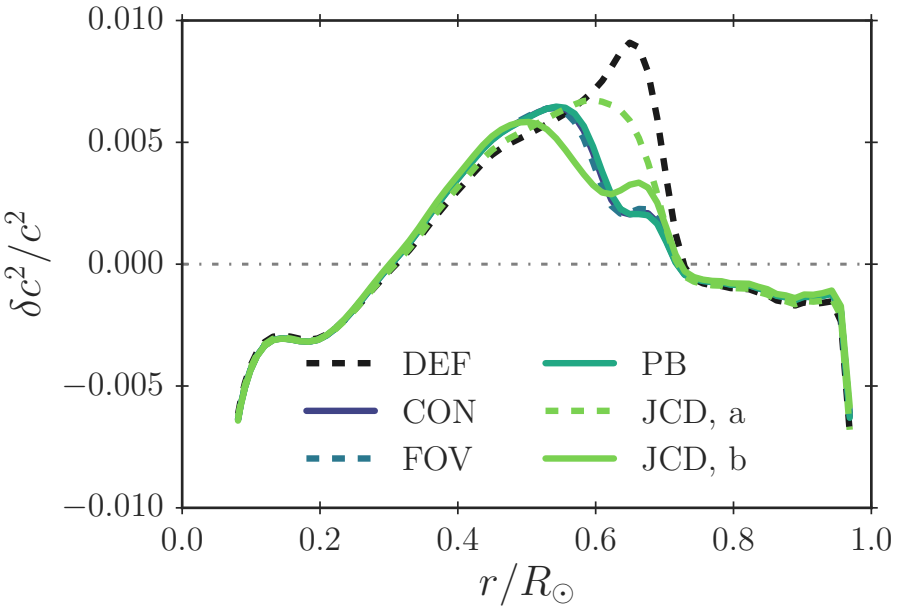


Figure 4.3: Equivalent to Fig. 4.2 but only including diffusion of H, $^4$He, $^7$Li and $^9$Be.

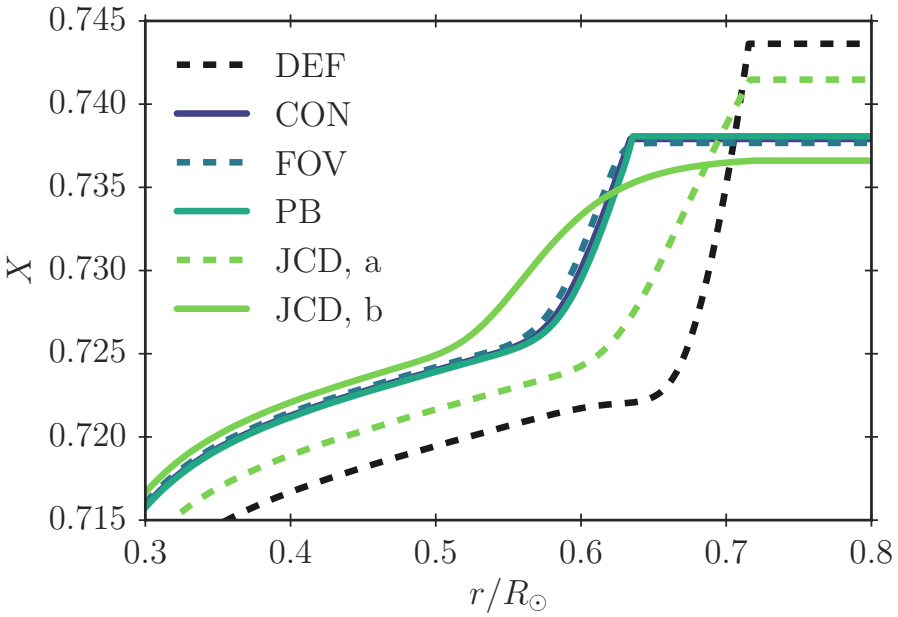


Figure 4.4: Hydrogen abundance $X$ as a function of radius for the solar calibration models presented in Table 4.1 — i.e. the models include microscopic diffusion of metals and are based on GS98.

Diffusive overshooting has been shown to lead to better agreement between the predicted sound speed and observations for lower values of the overshooting parameters involved (see, Schlattl and Weiss 1999 and Christensen-Dalsgaard et al. 2018 for the FOV and the JCD parameterization, respectively). These models do, however, not simultaneously solve the lithium problem.

Of course, dynamical processes, such as magnetic fields and rotation, may likewise alter the solar structure, partly explaining the remaining discrepancies in the obtained sound speed profile. Alternatively, corrections to the opacities may be required, as suggested by Christensen-Dalsgaard et al. (2010).

Figure 4.4 shows the hydrogen mass fraction $X$ as a function of radius for our solar calibration models that include the microscopic diffusion of metals. The strong gradient in $X$ near the base of the convective zone in the model with no overshooting gives rise to the tachocline sound speed anomaly in Fig. 4.2. Due to overshooting, $X$ increases, which results in an increase of the sound speed in this layer. As can be seen from Fig. 4.4, the JCD parameterization b leads to a dramatically different hydrogen abundance profile than the other overshooting parameterizations, while case a lies intermediate between the default and the other cases. However, just as the simplistic CON parameterization, the JCD parameterization is a mere toy model. Indeed, since Eq. (4.4) is a polynomial with three free parameters, the other suggested functional forms of $D_{\rm ov}(r)$ can be roughly mimicked by this equation.

Based on the figures discussed above, we further note that all overshooting parameteri-

zations lead to very similar chemical and thermal structures for the present-day Sun if they are to reproduce the desired lithium depletion. In this respect, the parameterization does not matter.

At the base of the solar convective envelope, there is a sharp transition in the sound speed gradient ($\nabla_{c^2}$, cf. Fig. 4.5), due to the change in the temperature gradient associated with the transition from radiative to adiabatic heat transport (cf. Christensen-Dalsgaard et al., 1991, 2011):

$$\nabla_{c^2} \equiv \frac{\mathrm{d}\ln c^2}{\mathrm{d}\ln p} \approx \nabla - \frac{\mathrm{d}\ln \mu}{\mathrm{d}\ln p}, \quad \nabla \equiv \frac{\mathrm{d}\ln T}{\mathrm{d}\ln p}. \tag{4.8}$$

Here, the second equality of the first expression holds true for an ideal gas. The abrupt transition in $\nabla_{c^2}$ is referred to as an acoustic glitch. It leads to a prominent signal in the oscillation frequencies that allows for the determination of its location and hence of the base of the convection zone. This can be done, using an asymptotic absolute method, based on the so-called Duvall relation (cf. Christensen-Dalsgaard, 2003, for an elaboration on this relation), or employing an asymptotic differential method that relies on a reference model (cf. Christensen-Dalsgaard et al., 1988b, 1989, 1991). Following the latter approach, Basu and Antia (1997) find the base of the convective zone to be at a radius of $0.713 \pm 0.001 R_\odot$. As can be seen from Fig. 4.5, the implementation of overshooting shifts the acoustic glitch outwards (cf. Fig. 4.5 and Table 4.1), leading to a slightly worse agreement between the models and Basu and Antia (1997). However, the shift is only of the order of $10^{-3}\,R_\odot$, and the acoustic glitch lies rather close to the seismically predicted base of the convective envelope for all models presented in this chapter with GS98.

Furthermore, it is worth noting from Fig. 4.5 that the transition in $\nabla_{c^2}$ is somewhat smoother for all models with overshooting than for the model with no overshooting — setting $D_{\mathrm{JCD}} = 150\,\mathrm{cm^2\,s^{-1}}$, the transition is still rather abrupt. While a lower value of $D_{\mathrm{JCD}}$ partly removes the tachocline anomaly (cf. Christensen-Dalsgaard et al. 2018), it does not necessarily improve all seismic properties of the model. However, in order to obtain quantitative helioseismic restrictions on the model, a detailed analysis of the oscillatory signal arising from the acoustic glitch is needed (see Christensen-Dalsgaard et al. 2011 and references herein), which is beyond the scope of this chapter.

For comparison, we have included the squared sound speed difference ($\delta c^2/c^2$) for solar calibration models obtained for AGSS09 in Fig 4.6 (cf. Table 4.2). The same conclusions are drawn: overshooting alone does not mend the inadequacies of the sound speed profile of the presented models. As in the case of GS98, the implementation of diffusive overshooting shifts the convective boundary outwards (cf. Table 4.2) and leads to a somewhat smoother transition in $\nabla_{c^2}$. Overall, the use of AGSS09 leads to a stronger disagreement between the model and the helioseismic Sun than the use of GS98 does. This well-known deterioration has haunted helioseismology for a decade (cf. Serenelli et al. 2009).

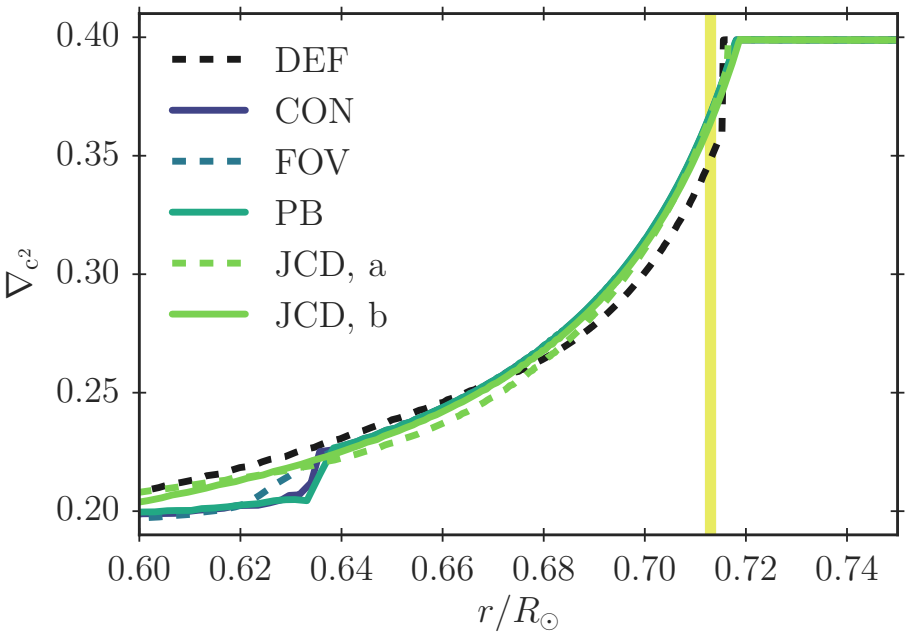


Figure 4.5: The gradient of the squared sound speed for the solar calibration models presented in Table 4.1 — i.e. the models include microscopic diffusion of metals and are based on GS98. The shaded area shows the seismically inferred confidence interval for the location of the base of the convective envelope found by Basu & Antia (1997).

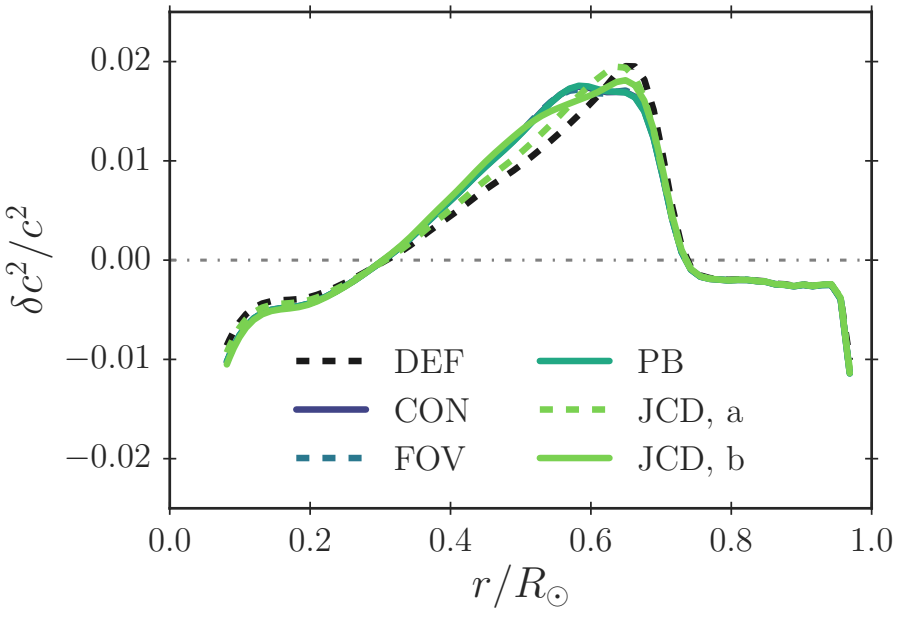


Figure 4.6: Equivalent to Fig. 4.2 but for AGSS09.

## 4.5 Summary

Diffusive overshooting has been shown to either improve the predicted sound speed profile (cf. Christensen-Dalsgaard and Di Mauro, 2007; Christensen-Dalsgaard et al., 2018) or to allow for the solution of the lithium problem (cf. Baraffe et al. 2017) when choosing suitable overshooting parameters. Discouragingly, none of the models presented in this chapter solves both problems in tandem.

For all investigated combinations of input physics, overshooting itself is not enough to obtain a perfect match between the model predictions and the inferred solar structure. In order to ensure a sufficiently high lithium depletion, each diffusive overshooting scheme introduces a new anomaly in the sound speed profile, when microscopic diffusion is taken into account. Further improvements of the input physics are needed.

Hence, the ability of a particular parameterization to solve either of the addressed problems is itself insufficient to establish, whether said parameterization leads to a physically correct description of the overshooting layer. On the other hand, combining helioseismic measurements with information about solar abundances allows for the exclusion of some scenarios and parameter choices, imposing restrictions on additional mixing processes in the radiative zone.

This being said, all four diffusive overshooting parameterizations lead to very similar sound speed profiles, when predicting a comparable evolution of the surface lithium abundance. To this extent, the parameterization is irrelevant, i.e., on their own, the suggested diagnostic tools do not lead to a clear preference. This is not to say that all models that yield the correct surface lithium abundance are indistinguishable: As shown by Schlattl and Weiss (1999), models that deplete their lithium on the pre-MS show different sound speed profiles than the models presented in this chapter.

In order for the CON, FOV, and PB parameterizations given by Eqs (4.1)-(4.3) to recover the observed trend of lithium depletion, a suppression of overshooting is required during the early stellar evolutionary stages. In accordance with Baraffe et al. (2017), we hence assume overshooting to be far less effective during the initial evolution, when using the PB parameterization. We take this into account by limiting the width of the overshooting layers, as suggested by Baraffe et al. (2017). As argued by several authors, this may be justified based on rotation (e.g. Ziegler and Rüdiger, 2003; Brummell, 2007; Brun et al., 2017). Since the underlying physical parameters describing rotation are insufficiently constrained, however, we have restricted ourselves to a more simplistic approach, when dealing with the CON and FOV parameterizations, in order to reduce the number of free parameters: we completely neglect overshooting for the first $10^8$ yr of evolution. Additional constraints on stellar rotation would render this simplification obsolete and may potentially favour one of the diffusive overshooting schemes presented here since there is also evidence for additional mixing in young clusters (cf. Baraffe et al., 2017; Bouvier et al., 2018). However, this is beyond the scope of the present thesis.

We find that the overshooting parameters involved are rather sensitive to the input physics. It is therefore not clear, to which extent the obtained parameter values from a solar calibration can be applied in the analyses of other stars without the necessity of tuning,

even if the lithium problem and the tachocline anomaly were to be solved simultaneously. Likewise, it is unclear, whether the obtained parameter values lead to an apposite description of lithium depletion at later evolutionary stages of the Sun. Simulations and observations that yield solid restrictions of and physical justifications for the employed overshooting parameters are hence much needed.

# Chapter 5

# 3D Simulations of Stellar Envelopes

*The content, including most of the text, of this chapter was published in Monthly Notices of the Royal Astronomical Society by Jørgensen et al. (2017) and Jørgensen et al. (2019). In this chapter, I solely deal with the interpolation scheme that was proposed in these two papers (see also Chapters 6 and 7 for further content from these papers). I am the first author of both papers and the primary investigator of the presented research project. I wrote this chapter. My contributions include the conception, development, and validation of the method as well as the numerical implementation of the interpolation scheme. The work was performed in collaboration with Achim Weiss, George Angelou, Víctor Silva Aguirre, J. R. Mosumgaard (JM), and Christian L. Sahlholdt. In this chapter, as well as in Chapters 6 and 7, I use a stand-alone interpolation algorithm. In Chapters 8-10, I employ an implementation of the presented interpolation scheme into* GARSTEC. *JM contributed to the implementation into* GARSTEC. *All co-authors gave valuable feedback on the papers.*

In Chapters 6-10, I introduce and apply different methods for improving the superadiabatic near-surface layers of 1D stellar structure models by using information from 3D radiative hydrodynamic (RHD) simulations of the outermost layers of stellar convective envelopes. The present chapter gives a short introduction to such 3D simulations and presents a novel and robust interpolation scheme that allows inferring the mean structure of 3D simulations across the HR diagram. The ability to interpolate in existing grids of 3D simulations is crucial when attempting to use these simulations to improve 1D stellar models of specific target stars: not only are 3D simulations computationally expensive, but the available simulations are also scarcely distributed in the relevant parameter space.

## 5.1 Terminology

The 3D simulations that are discussed in this chapter are often referred to as stellar atmosphere models in the literature. However, when dealing with stellar evolution codes, the

word 'atmosphere' is usually employed to denote the stratification above the photosphere, where a theoretical or semi-empirical $T(\tau)$ relation is commonly used to set the outer boundary conditions (cf. Chapter 2). Observers may likewise think of stellar atmospheres as stretching from the photosphere over the chromosphere to the corona. While the 3D simulations are rather shallow compared to the entire convection zone, they nevertheless cover most of the superadiabatic outermost layers and thus extend below the photosphere. In order to emphasize this and to distinguish them from the purely radiative grey atmospheres that are commonly employed in standard 1D models, we will refer to them as 3D envelopes rather than 3D atmospheres. In doing so, we adopt the nomenclature by Jørgensen et al. (2018). As mentioned above, the 3D simulations do by no means cover the entire convective envelope.

Note that some of the nomenclature changed, during the continuous development of the methods and between papers. While the nomenclature adopted in this thesis is self-consistent, the notation still reveals this development. Any such changes are hence pointed out when relevant.

## 5.2 Multi-Dimensional Stellar Envelope Simulations

We employ a grid of 3D RHD simulations of stellar envelopes by Magic et al. (2013b), to which we will refer as the Stagger grid, consisting of 206 3D simulations with different metallicities: the grid contains envelopes with $T_{\rm eff}$ between 4000 and 7000 K, $\log g$ between 1.5 and 5.0, and [Fe/H] of $-4.0$, $-3.0$, $-2.0$, $-1.0$, $-0.5$, 0.0, and 0.5. The spacing in $T_{\rm eff}$ and $\log g$ for the Stagger grid is 500 K and 0.5 dex, respectively. For [Fe/H] $\leq -1$, $\alpha$-enhancement has been taken into account (cf. Chapter 2): $[\alpha/{\rm Fe}] = 0.4$ dex (cf. Magic et al. 2013a). We excluded some Stagger-grid envelopes, since their effective temperature strongly oscillates with time, indicating that the simulations are not yet fully relaxed (R. Collet, private communication). In addition, one simulation was excluded due to its subadiabatic stratification: the temperature gradient is lower than the adiabatic gradient throughout the simulation (R. Collet, private communication). In connection with Jørgensen et al. (2017), these selection criteria led to the exclusion of 5 simulations, while we discarded 2 additional simulations, in connection with Jørgensen et al. (2019). In total, 29 Stagger-grid simulations have solar metallicity. One of these was excluded for the reasons listed above.

For comparison, we furthermore use a grid by Trampedach et al. (2013), to which we will refer as the Trampedach grid, containing 37 3D envelopes, all at solar metallicity: the grid is irregular in the $(T_{\rm eff}, \log g)$-plane.

The Stagger-grid and Trampedach-grid simulations are all *box-in-a-star* type: the simulations only a cover small representative volume of the outermost convective layers. The simulations extend from the nearly-adiabatic layers to the atmosphere, including the photosphere. According to Magic et al. (2013b), the depth of the Stagger-grid simulations thus only amounts to $0.4 - 10\,\%$ of the total stellar radius. Any sphericity effects, as well as changes in $\log g$, are, therefore, neglected: the simulations are plane-parallel, and the gravitational acceleration is kept fixed throughout the simulations.

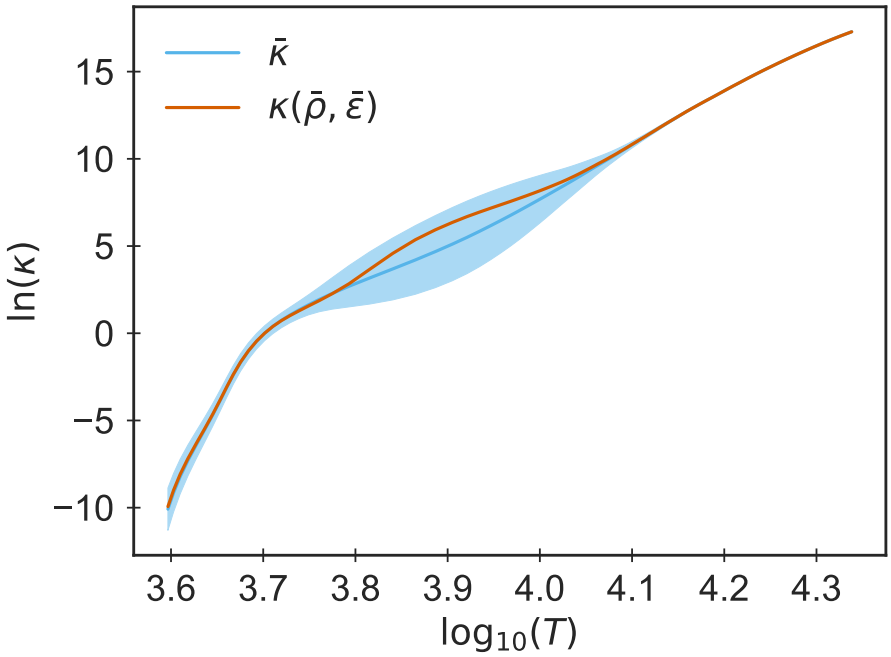


Figure 5.1: Mean opacity as well as the opacity derived from the mean quantities (the mass and energy density) as a function of temperature, for a solar 3D envelope. The average is taken over layers with the same physical depth. The shaded region shows the standard deviation. The stratification has been extracted from a trial run that I ran in collaboration with Remo Collet for the present-day Sun, using the Stagger grid code.

The Trampedach and Stagger grid were computed with successors of the Stein and Nordlund (1998) finite-difference large-eddy simulation code, using the Mihalas-Hummer-Däppen equation of state (MHD-EOS, Hummer and Mihalas 1988). The Trampedach grid is based on abundances found in Trampedach et al. (2013) and line opacities found in Kurucz (1992b) and Kurucz (1992a), while the Stagger grid employs the composition listed in Asplund et al. (2009) (AGSS09) and MARCS line opacities found in Gustafsson et al. (2008). The two grids are two distinct groups of simulations, relying on somewhat different input parameters, and differ in technical and numerical details — but are nevertheless quite similar.

As mentioned above, the 3D simulations are employed to improve 1D stellar models. Therefore, only one-dimensional spatial and temporal averages of these simulations are needed in connection with this thesis. In order to conserve hydrostatic equilibrium, the spatial average must be taken over layers of constant geometrical depth. In the rest of this thesis, these averaged structures are referred to as $\langle 3\mathrm{D} \rangle$-envelopes. For a discussion on the influence of the averaging on the evaluated stellar oscillation frequencies, we refer to Magic and Weiss (2016).

As regards the spatial average, it is worth mentioning that the resulting structure is no

longer fully consistent with the EOS: the average density is not equivalent to the density that results from the average quantities. In other words, the EOS is non-linear. The same is true for other quantities, such as the opacity that stems from the likewise non-linear opacity tables, i.e.

$$\langle \kappa(P, T, X_j) \rangle \neq \kappa(\langle P \rangle, \langle T \rangle, \langle X_j \rangle), \quad j = 1, \ldots, J, \tag{5.1}$$

where $j$ runs over all $J$ elements. This is illustrated in Fig. 5.1: in connection with my research, I have run and post-processed trial simulations using the code that underlies the Stagger grid. A snapshot from one of these trial simulations has been used for the illustration in Fig. 5.1.

## 5.3 Interpolation

Since 3D hydrodynamic simulations of convection are computationally expensive, only a small number of 3D envelopes is currently available. For most combinations of global stellar parameters, there does hence not exist a suitable $\langle$3D$\rangle$-envelope. Until recently, this has severely limited the usefulness of 3D simulations, when attempting to improve stellar models, and only a few cases had been addressed. This included the present-day Sun. In order to overcome this limitation, I developed an interpolation scheme, building upon the apparent homology of the 3D simulations. This interpolation scheme is presented below.

As shown below, my interpolation scheme is capable of accurately inferring the stratification of $\langle$3D$\rangle$-envelopes for any combination of effective temperature ($T_{\rm eff}$) and gravitational acceleration ($g$). The obtained interpolated structures were used in analyses of the Sun and stars with near-solar metallicities (cf. Chapter 6, 8, and 10). This scheme was originally published in Jørgensen et al. (2017). I subsequently extended upon this scheme in Jørgensen et al. (2019), allowing for interpolation in metallicity ([Fe/H]). Stellar models that draw upon the interpolation in metallicity are presented in Chapters 7 and 9.

### 5.3.1 Interpolation in $T_{\rm eff}$ and $\log g$

Constructing meaningful improvements of stellar models for any given model or star, based on discrete grids of 3D envelopes, often requires interpolation. As mentioned above, the grids of 3D RHD simulations cover a three-dimensional parameter space: $T_{\rm eff}$, $\log g$ and [Fe/H]. Here, we consider the case, where only an interpolation in the $(T_{\rm eff}, \log g)$-plane is needed. Section 5.3.2 deals with the interpolation in the third dimension of the parameter space.

To motivate our suggested interpolation scheme, we start out by noting that $\log \rho$ as a function of $\log P$ looks similar across the grids[1] — that is, comparing simulations from the same grid, across all parameters, as well as comparing simulations from different grids. Thus, $\log \rho$ behaves linearly at high and low pressure, while a density jump or

[1]Note that all logarithms (log as well as $\log_{10}$) are computed in base 10.

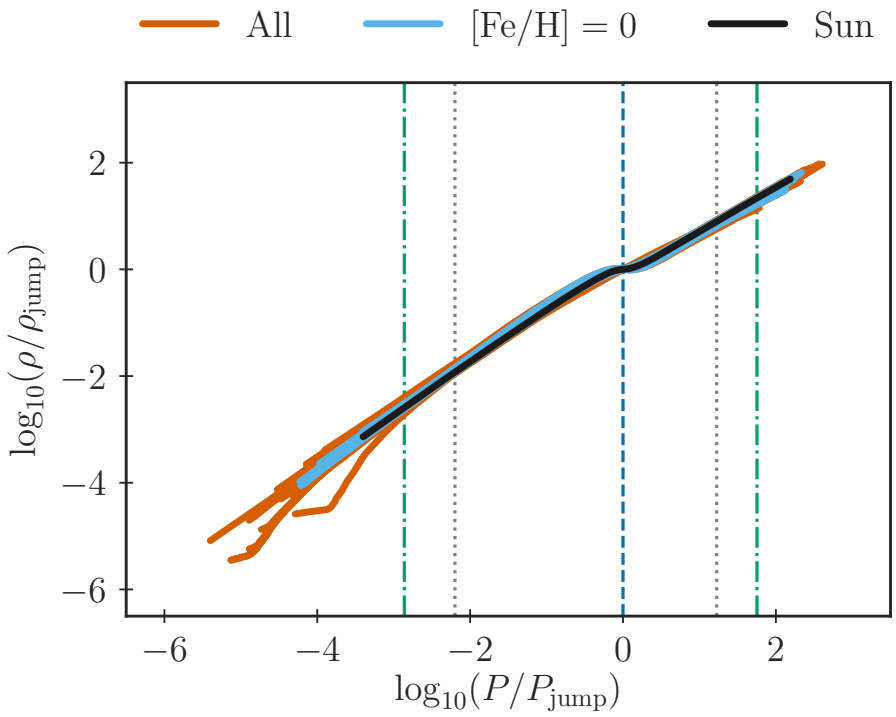


Figure 5.2: The logarithm of the density as a function of the logarithm of the pressure after shifting the stratification by the position of the density inflection (jump) for 199 simulations in the Stagger grid — i.e. for $T_{\mathrm{eff}}$ ranging from 4000 K to 7000 K, $\log g$ ranging from 1.5 to 5.0, and [Fe/H] ranging from −4 to 0.5. The stratifications of the ⟨3D⟩-envelope at solar metallicity and the solar envelope have been highlighted. The grey dotted lines, and the green dot-dashed lines show the interpolation range when including all metallicities and when including only simulations at solar metallicity, respectively. The blue dotted line highlights the position of the density inflection.

rather an inflection occurs near the stellar surface, corresponding to a local minimum in $\partial \log \rho / \partial \log P$. Moreover, the inclination and intercept of the linear regions are similar for all $\langle 3D \rangle$-envelopes. Shifting $\log \rho$ as a function of $\log P$ by the position of this density inflection thus results in nearly coinciding stratifications, as can be seen from Fig. 5.2. In short, the density stratifications of 3D simulations are rather homologous. This is relevant, because of the position of the minimum in $\partial \log \rho / \partial \log P$, i.e. of the aforementioned density inflection, behaves rather linearly as a function of both $\log T_{\rm eff}$ and $\log g$, as can be seen from the contour lines in Fig. 5.3. In other words, the position of the density inflection can reliably be computed by interpolation. It is worth noting that while $\log \rho$ as a function of $\log P$ is thus suitable for interpolation across the mapped $(\log T_{\rm eff}, \log g)$-plane, $\log P$ as a function of $\log \rho$ is not. This is due to the density inversion that can take place in the envelopes of red giants due to the strong ionization of H and He, a phenomenon found by Schwarzschild (1975). In solar-like stars, this still appears as a plateau.

Note that the nomenclature changed during the development of the method and between publications: in Jørgensen et al. (2017), we referred to the minimum in $\partial \log \rho / \partial \log P$ as a density jump. However, in order to underline that this inflection is not a discontinuity, the terminology changed. To avoid a change in notation between the papers, we kept the notation by Jørgensen et al. (2017), which means that, say, the pressure at the density inflection is called $P_{\rm jump}$.

Note that we use the total pressure as our coordinate in this chapter as well as in Chapter 6 and 7. The total pressure has three contributions: the radiative pressure, the gas pressure, and the turbulent pressure. The sum of the former two constitutes the so-called thermal pressure. When implementing our interpolation algorithm directly into GARSTEC in Chapters 8-10, on the other hand, we employ the thermal pressure as our coordinate, since only the thermal pressure enters the EOS — why this is important, becomes apparent in Chapter 8.

Not only do the density stratifications of all 3D simulations look rather similar when scaled based on the density inflection, but all relevant quantities do — although not all to the same extent. In other words, 3D simulations are, overall, very homologous.

Based on the observation that the 3D simulations thus show a large degree of homology, we start out by scaling all relevant quantities by their respective value at the density inflection[2]. We then interpolate in the scaled mean structures. As mentioned above, the interpolation of each quantity is performed using the logarithm of the scaled pressure, i.e. $\log(P/P_{\rm jump})$, as our coordinate. In this chapter as well as Chapters 6 and 7, this implies that we construct piece-wise cubic, continuously differentiable surfaces of each quantity for each desired value of the scaled pressure, triangulating the grid of 3D simulations in the $(\log T_{\rm eff}, \log g)$-plane. All tests presented in this chapter are performed using the same algorithms. Meanwhile, in Chapters 8-10, we follow a similar scheme, performing linear interpolation. This change from cubic to linear interpolation is solely based on the accessible

[2]In principle, this scaling of the 3D simulations only has to be performed once. When including the interpolation scheme directly into our stellar evolution code in Chapters 8-10, we, therefore, provide GARSTEC with previously scaled mean structures based on the stand-alone interpolation algorithm used in this chapter.

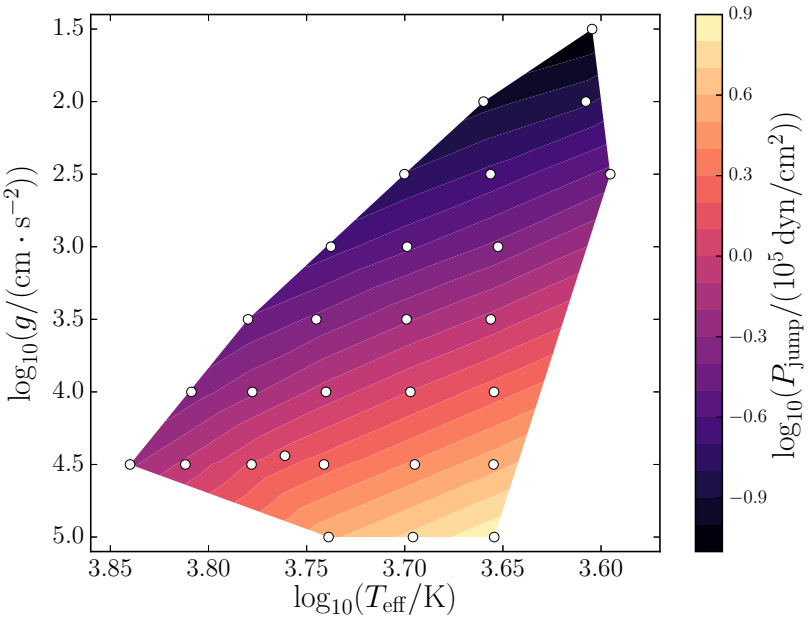


Figure 5.3: The logarithm of the pressure, $\log P_{\mathrm{Jump}}$, at the minimum of $\partial \log \rho / \partial \log P$, based on the Stagger-grid $\langle$3D$\rangle$-envelopes (white dots), at solar metallicity.

interpolation algorithms[3]. Switching to linear interpolation, however, is found to lead to lower accuracy.

The obtained stratifications are then converted into absolute physical quantities based on the corresponding values of each quantity at the density inflection, i.e. the scaling is inverted. The involved scaling factors are likewise obtained by cubic or linear interpolation in the $(\log T_{\mathrm{eff}}, \log g)$-plane. Figure 5.3 shows the logarithm of the pressure at the density inflection, for all $\langle$3D$\rangle$-envelopes in the Stagger grid, at solar metallicity. As can be seen from the figure, the logarithm of the pressure at the density inflection evolves rather linearly as a function of both $\log T_{\mathrm{eff}}$ and $\log g$. In the case of the Trampedach grid $\langle$3D$\rangle$-envelopes, the minimum in $\partial \log \rho / \partial \log P$ is a likewise well-behaved function of $\log T_{\mathrm{eff}}$ and $\log g$. The same holds true at different metallicities in the Stagger grid and for different quantities — although the scaling factors for other quantities do not, in general, behave as linearly as in the case of the density. The relevant scaling factors can hence be robustly recovered.

In Chapters 8-10, we include the interpolation scheme directly into our stellar evolution code at every time-step. In this case, only $T(P_{\mathrm{th}})$ and the turbulent pressure have to be evaluated by interpolation. The remaining quantities are evaluated from the EOS, in order to ensure continuous stratifications for all quantities in the resulting 1D models[4].

[3] In Chapters 6-7, we use a set of Python scripts, while we rely on Fortran routines in Chapters 8-10.

[4] We thus deliberately avoid to obtain all physical quantities by interpolation, as the resulting 1D models would otherwise suffer from discontinuities. We elaborate upon this in Chapter 8.

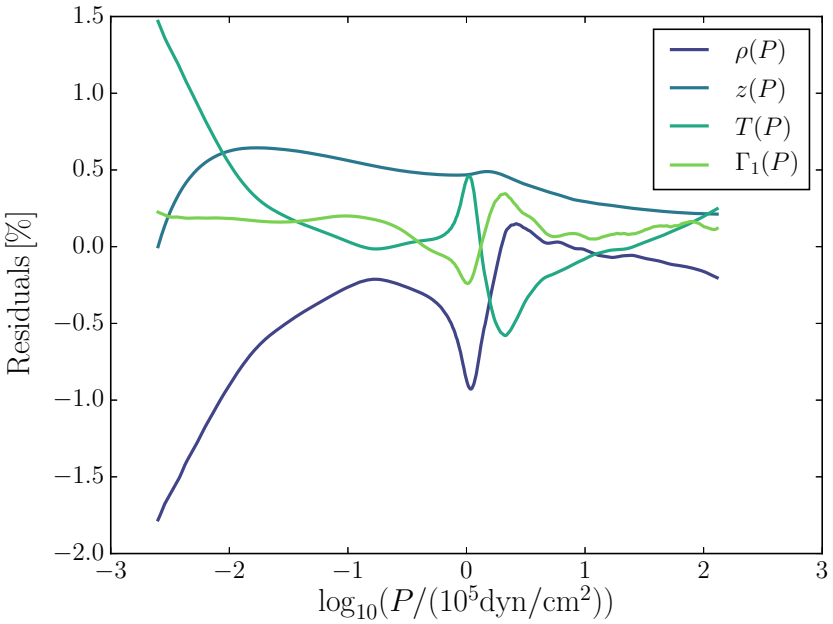


Figure 5.4: Comparison between an interpolated solar ⟨3D⟩-envelope based on the Stagger grid, and the correct structure that was excluded from the grid prior to the interpolation. $T_{\mathrm{eff}} = 5769\,\mathrm{K}$ and $\log g = 4.44$. The figure shows the relative residuals for four quantities: the density ($\rho$), the adiabatic exponent ($\Gamma_1$), the temperature ($T$), and the depth ($z$) below the outermost point of the interpolated ⟨3D⟩-envelope as a function of the total pressure ($P$).

Chapters 6 and 7, on the other hand, deal with a method, in which 3D simulations are only used to correct for the structural inadequacies of the final 1D structure models in the post-processing of the output from stellar evolution codes. We refer to this approach as patching. In this case, we perform an interpolation of $\log \rho$, $\log T$, and $\Gamma_1$, using the total pressure as our coordinate.

Having obtained $\rho(P)$ using interpolation or from the EOS, the physical depth scale can now easily be established based on the requirement of hydrostatic equilibrium (cf. Eq. 2.8). Within stellar structures, we can directly compute a radius (cf. Chapter 8). However, in this chapter, we attempt to compute interpolated ⟨3D⟩-envelopes without considering a specific interior structure. The depth $z$ below a given point can then be established by assuming constant gravitational acceleration. In Chapters 6 and 7, i.e. when patching, we employ these interpolated ⟨3D⟩-envelopes and subsequently correct for this assumption. Having obtained a length scale, the mass follows directly from $\rho$ by integration.

When patching, the derivatives needed for frequency calculations are determined based on the established stratifications using Akima spline interpolation (cf. Akima 1970). While cubic splines may show ripples in the neighbourhood of discontinuities, this piece-wise cubic,

and continuously differentiable sub-spline interpolation method yields a smooth transition, even when encountering abrupt changes in the derivatives. This feature is important near the base of the 3D simulation when constructing patched models: as described in Chapters 6 and 7, patching results in discontinuities at the base of the appended ⟨3D⟩-envelope.

To evaluate how accurately our interpolation scheme reproduces the correct structure across the $(\log T_{\rm eff}, \log g)$-plane, we have excluded simulations from the envelope grids and subsequently reconstructed these simulations. In other words, we performed a cross-validation test. An example is given in Fig. 5.4, where we show the relative residuals between the solar simulation in the Stagger grid and the corresponding interpolated ⟨3D⟩-envelope. As can be seen from the figure, all interpolated quantities are reproduced within 2 % of the expected values, at all pressures, ranging over five orders of magnitude. For the pressure range shown in Fig. 5.4, all ⟨3D⟩-envelopes in the envelope grid provide values for the pressure: in other words, the shallowest ⟨3D⟩-envelope sets the highest pressure, at which interpolation is possible[5].

The errors introduced at the base of the ⟨3D⟩-envelope in $\rho(P)$ by interpolation lie below 10 %, for all but one simulation at high temperature, but are generally of the order of a few per cent (cf. Fig. 5.5). Envelopes at the boundary of the grid were not reconstructed in this cross-validation exercise. The computed residuals constitute an upper bound for the expected error.

Magic (2016) presents another interpolation scheme, based on the generic form of the normalized entropy stratification. Comparing our results qualitatively with the published test cases (cf. Fig. 6 in Magic 2016), we conclude that our simple interpolation scheme is able to reconstruct the correct stratifications with similar or even higher accuracy, throughout the $(T_{\rm eff}, \log g)$-plane.

Having established that our interpolation scheme yields reasonably accurate results in the case of the regular Stagger grid, we now take a closer look at the irregular Trampedach grid. Here we find the accuracy to be strongly affected by the sampling rate. In regions with a high sampling rate, we are able to reconstruct the stratifications within 1 %, and acceptable accuracy is obtained for most main-sequence (MS) stars. In regions with a low sampling rate, however, the errors may reach 20 % — the highest error is again reached for MS stars at high temperatures. Figure 5.6 shows the corresponding error in $\rho(P)$ across the $(T_{\rm eff}, \log g)$-plane and should be compared to Fig. 5.5.

As regards the solar ⟨3D⟩-envelope in the Trampedach grid, we are able to reproduce $\rho(P)$ only within 5 %. Although the sampling of the Trampedach grid is higher in the vicinity of the solar 3D envelope than in the corresponding region of the Stagger grid, our cross-validation exercise thus shows that interpolation in the Trampedach grid strongly underestimates $\rho(P)$ for the Sun compared to the reconstruction of the Stagger-grid solar ⟨3D⟩-envelope. We explore the implications of this in Section 6.2.2.

[5]Note that the lowermost layers of each 3D simulation must be excluded since they are un-physical and still reflect the boundary conditions: the superadiabatic index increases with increasing depth, which is not the expected behaviour. This holds true for the Stagger as well as the Trampedach grid. This was noted after the publication of Jørgensen et al. (2017) and is hence not taken into account in the figures stemming from that paper, leading to a slightly broader interpolation range.

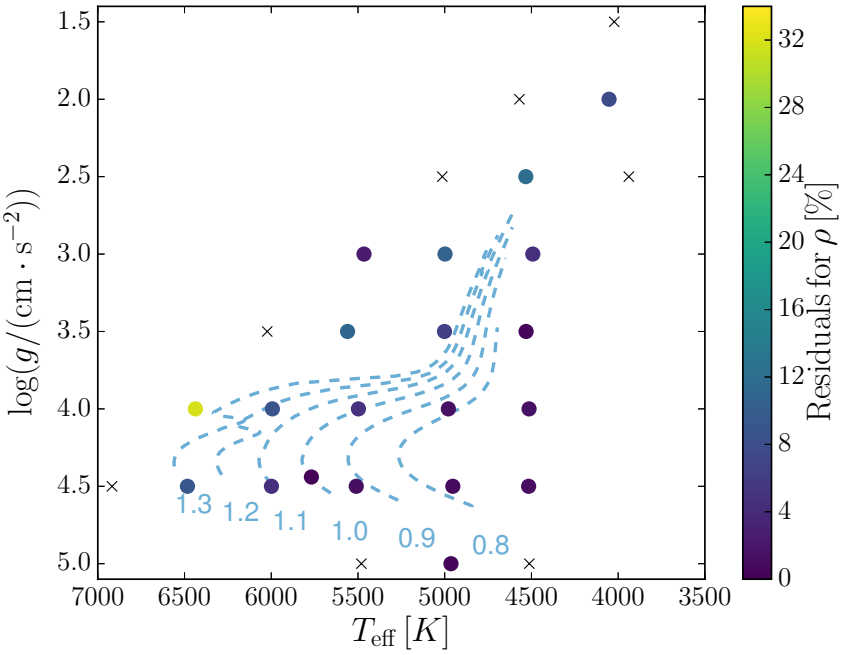


Figure 5.5: Kiel diagram, i.e. $\log g$ as function of $T_{\rm eff}$, showing residuals in per cent of $\rho(P)$ close to the base of the $\langle$3D$\rangle$-envelope between interpolated $\langle$3D$\rangle$-envelopes and the corresponding $\langle$3D$\rangle$-envelopes in the Stagger grid at solar metallicity. Here, close to the base of the 3D simulations, the pressure is $10^{1.9}$ times higher than at the density inflection. Simulations at the boundary of the grid, for which no residuals could be computed, are marked with crosses. Simulations, for which residuals could be computed, are marked with coloured dots. The dashed lines show the evolutionary paths of stars, whose masses are given on the plot in units of the solar mass.

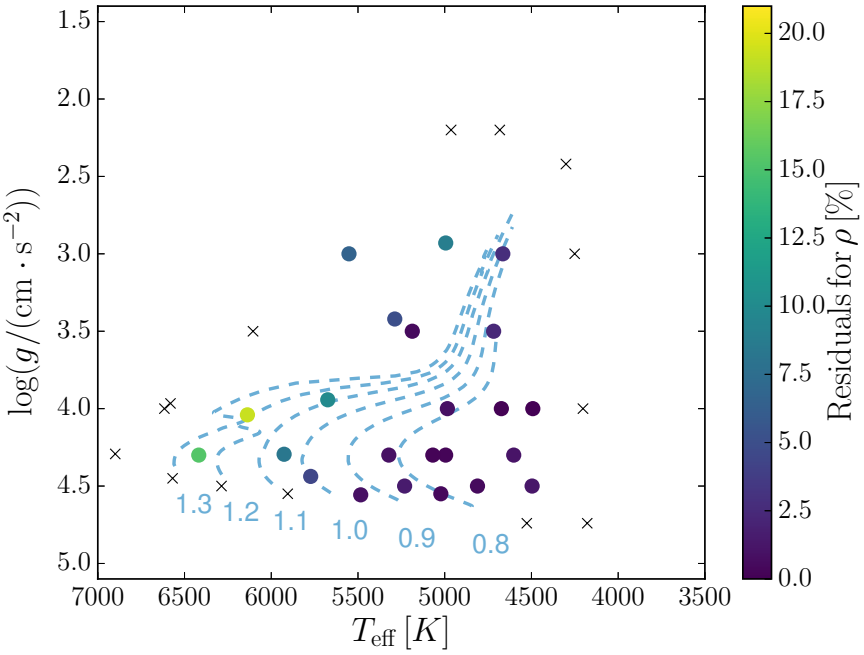


Figure 5.6: Kiel diagram corresponding to Fig. 5.5 but for the Trampedach grid.

We note that the stratifications of some quantities in the ⟨3D⟩-envelopes in the Trampedach grid show ripples. In order to remove such ripples, we smooth the interpolated ⟨3D⟩-envelopes before patching, when dealing with the Trampedach grid, although we found that these ripples have a negligible effect on the model frequencies.

### 5.3.2 Interpolation in [Fe/H]

Having established the presented scheme for interpolation in the $(T_{\rm eff}, \log g)$-plane, it is straightforward to interpolate in metallicity as well. Since the Trampedach grid only includes simulations with solar metallicity, any interpolation in the composition may only draw upon the Stagger grid.

The Stagger grid contains simulations with seven different metallicities: $-4.0$, $-3.0$, $-2.0$, $-1.0$, $-0.5$, 0.0 and 0.5. If 3D simulations with the desired metallicity exist, we interpolate only in the $(T_{\rm eff}, \log g)$-plane, using the scheme described in the Section 5.3.1. If, on the other hand, no ⟨3D⟩-envelopes with the desired metallicity exist, we first construct a ⟨3D⟩-envelope for each of the seven existing metallicities with the desired $T_{\rm eff}$ and $\log g$ by interpolation in the $(T_{\rm eff}, \log g)$-plane. For each of these ⟨3D⟩-envelopes, we then rescale $\log(\rho)$, $\log(T)$, $\Gamma_1$, and $\log(P)$ by the corresponding value at the density inflection near the surface. Based on these scaled logarithmic stratifications, we evaluate $\log(\rho)$, $\log(T)$ and $\Gamma_1$ at predetermined $\log(P/P_{\rm jump})$ for an ⟨3D⟩-envelope with the desired metallicity. The

interpolation in [Fe/H] is performed using Akima splines (cf. Akima 1970). Based on the scaling factors of the seven ⟨3D⟩-envelopes with the same $T_{\rm eff}$ and $\log g$, we determine the scaling factor for the desired parameter values, likewise using Akima spline interpolation. The derivative of the pressure with respect to the density is determined using a third-order polynomial spline. The scaling is then inverted, i.e. absolute values are computed based on the scaling factors and the scaled quantities.

#### 5.3.2.1 Testing the Interpolation Scheme

In order to assess the accuracy of our method, when interpolating in metallicity, we cross-validated the interpolation scheme at distinct metallicities in the Stagger grid. We reconstruct 95 Stagger-grid ⟨3D⟩-envelopes at [Fe/H]=-3.0, -2.0, -1.0, -0.5 and 0.0. We employ a leave many-out strategy for each ⟨3D⟩-envelope, withholding all ⟨3D⟩-envelopes at the target metallicity. These interpolated ⟨3D⟩-envelopes are hence determined based on six interpolated ⟨3D⟩-envelopes with the same $T_{\rm eff}$ and $\log g$ but different [Fe/H]. As our splines rely on the information on each side of the target metallicity, we are precluded from testing the metallicities at the edge of the grid, i.e. for [Fe/H]=-4.0 and 0.5.

The interpolation error at the base of the ⟨3D⟩-envelope is of particular interest, as it affects the selection of the so-called patching point in Chapters 6 and 7 and the matching point in Chapters 8-10: above the patching or matching point, we employ a ⟨3D⟩-envelope. Below the patching or matching point, the 1D model interior is established based on the stellar structure equations (cf. Chapter 2).

We determined the median, the mean, and the highest obtained interpolation error at the base for $\Gamma_1(P)$, $T(P)$, and $\rho(P)$, respectively, from our cross-validation exercise and summarize the results in Table 5.1. Alongside, we list the corresponding values for the errors obtained at any point within the ⟨3D⟩-envelopes, as the accuracy varies throughout the structure. Thus, even small displacements of the density inflection will lead to large residuals in the vicinity thereof, due to the large structural changes that take place near the density inflection. The relative interpolation errors are much smaller throughout most of the structures, including the base, than at the density inflection.

The errors at the base of the interpolated ⟨3D⟩-envelopes are illustrated in Fig. 5.7. In none of the 95 cases, do the interpolation errors in $\rho(P)$ at the base exceed 28 %. As can be seen from Fig. 5.7, the interpolation error for the density at the base of the ⟨3D⟩-envelope is much lower than the 28 % throughout most of the Kiel diagram: a Kiel diagram is a pendant to the HR diagram, showing $\log g$ as a function of $T_{\rm eff}$ (cf. Chapter 2). Indeed, in Fig. 5.7, the interpolation scheme only performs so badly in the high-$g$ low-$T_{\rm eff}$ corner of the grid: the mean and median of the errors shown in Fig. 5.7 are 3.9 % and 3.0 %, respectively.

Regarding the values stated above, we note that interpolation errors are expected to be smaller than in our cross-validation exercise, if all ⟨3D⟩-envelopes are used. The interpolation errors that enter, when using the interpolated ⟨3D⟩-envelopes in stellar models, are hence lower than those cited in Table 5.1.

The highest interpolation errors are obtained for the lowest metallicities. For a fixed [Fe/H], the interpolated values of $T(P)$ and $\rho(P)$ at the base of the ⟨3D⟩-envelope are

Table 5.1: Interpolation errors in $\rho$, $T$, and $\Gamma_1$ for each metallicity. The errors listed in the columns denoted by $\rho$, $T$, and $\Gamma_1$ refer to the highest value within the $\langle 3D \rangle$-envelopes: the first value of a given entry is the mean of the highest interpolation error within each $\langle 3D \rangle$-envelope, the second is the corresponding median, and the third is the highest value among the errors of all $\langle 3D \rangle$-envelopes. Consequently, the interpolation errors will be lower than the listed values throughout most of the interpolated structures. The subscript 'b' refers to the errors of the corresponding quantity at the base of the $\langle 3D \rangle$-envelope.

| [Fe/H] | $\rho$ [%] | $\rho_\mathrm{b}$ [%] | $T$ [%] | $T_\mathrm{b}$ [%] | $\Gamma_1$ [%] | $\Gamma_{1,\mathrm{b}}$ [%] |
|---|---|---|---|---|---|---|
| -3.0 | 6.8, 9.3, 37.0 | 2.3, 3.7, 17.4 | 7.0, 7.7, 16.7 | 0.7, 1.1, 4.2 | 5.8, 6.8, 13.1 | 0.1, 0.3, 2.2 |
| -2.0 | 10.0, 11.3, 40.1 | 6.6, 7.1, 28.3 | 6.1, 6.3, 12.1 | 1.0, 1.0, 4.7 | 3.9, 4.7, 15.4 | 0.1, 0.2, 0.8 |
| -1.0 | 11.3, 11.1, 19.7 | 3.5, 3.3, 6.4 | 9.7, 9.1, 14.0 | 1.8, 1.6, 3.0 | 4.0, 4.0, 6.0 | 0.2, 0.3, 0.8 |
| -0.5 | 8.5, 8.5, 12.1 | 3.6, 3.5, 5.8 | 7.0, 7.5, 13.0 | 1.3, 1.4, 2.0 | 2.7, 3.0, 4.7 | 0.1, 0.2, 0.5 |
| 0.0 | 4.5, 4.6, 7.6 | 0.8, 0.9, 2.2 | 5.7, 5.7, 8.5 | 0.8, 0.8, 1.4 | 2.9, 2.7, 3.7 | 0.1, 0.1, 0.3 |

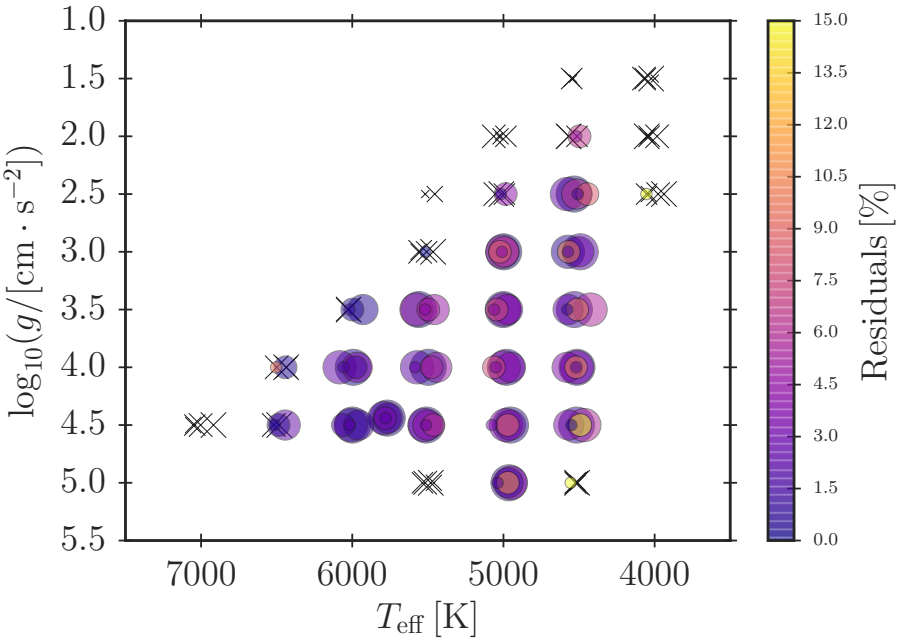


Figure 5.7: Residuals for the reconstruction of the density at the base of stellar $\langle 3D \rangle$-envelopes by interpolation in metallicity. At this mesh point, the pressure is $10^{1.23}$ times higher than at the density inflection near the surface. The larger the marker size is, the larger the metallicity is. The crosses mark the $\langle 3D \rangle$-envelopes that could not be reconstructed by interpolation, as they lie on the boundary of the Stagger grid. The colour bar shows the obtained errors in per cent. Errors higher than 15 % have all been attributed the same color.

either systematically too high or too low throughout the $(T_{\rm eff}, \log g)$-plane. Part of this inaccuracy can be attributed to our validation strategy – we withhold all $\langle$3D$\rangle$-envelopes at a given metallicity. Nevertheless, our method would benefit greatly from an increase in the Stagger grid resolution.

## 5.4 Turbulent Pressure

In Chapters 6 and 7, turbulent pressure is included through the total pressure that constitutes the interpolation coordinate. In Chapters 8 and 9, on the other hand, we use the gas or thermal pressure as our coordinate, neglecting turbulent pressure. Finally, in Chapter 10, turbulent pressure enters anew, this time as a separate quantity necessitating interpolation: in Chapter 10, the turbulent pressure is a function of the thermal pressure. Since the interpolation in the turbulent pressure as a function of the thermal pressure is thus only relevant in connection with Chapter 10, I quantify the accuracy of the interpolation scheme for this quantity separately. This is accomplished through a cross-validation exercise, similar to the ones described above.

In Chapter 10, we restrict ourselves to interpolation in the $(T_{\rm eff}, \log g)$-plane, solely considering stars at solar metallicity. I hence test the interpolation scheme at solar metallicity by withholding and reconstructing individual $\langle$3D$\rangle$-envelopes. Again, the value of the turbulent pressure at the base of the interpolated $\langle$3D$\rangle$-envelopes is of particular interest. The associated interpolation errors resulting from the cross-validation exercise are illustrated in Fig, 5.8. As can be seen from a comparison between Fig. 5.5 and Fig, 5.8, the interpolation algorithm recovers the turbulent pressure and the density at the base of the $\langle$3D$\rangle$-envelopes with similar accuracy. In both cases, the interpolation scheme performs better at high $\log g$, and the highest interpolation error is obtained for an outlier at a high temperature near the edge of the grid.

As regards the turbulent pressure at the base of the $\langle$3D$\rangle$-envelopes, I find the median, the mean, and highest interpolation errors to be 4.9 %, 6.7 %, and 21.0 %, respectively. In none of the 20 reconstructed $\langle$3D$\rangle$-envelopes does the highest interpolation error within the entire $\langle$3D$\rangle$-envelope exceed 53.0 % — the corresponding median and mean maximum errors[6] are 15.2 % and 17.0 %, respectively. The accuracy of the interpolation scheme is much higher for stars that are similar to the present-day Sun. In general, the interpolation algorithm performs best at scaled pressures that exceed that of the density inflection. Both statements are illustrated in Fig. 5.9.

Although we do not employ the interpolation of the turbulent pressure in [Fe/H] in the following chapters, I performed a cross-validation exercise along the lines of Section 5.3.2.1, in order to draw a more complete picture of the performance of the interpolation routines. Like in the case of the other quantities, I find that the highest interpolation errors are obtained for the lowest metallicities. For none of the 95 reconstructed Stagger grid simulations, does the interpolation error at the base of the $\langle$3D$\rangle$-envelope exceed 43.0 % — the associated

[6]The median and mean maximum errors are larger than the maximum of the mean and median errors, which are 11.8 % and 8.2 %, respectively (cf. Fig. 5.8).

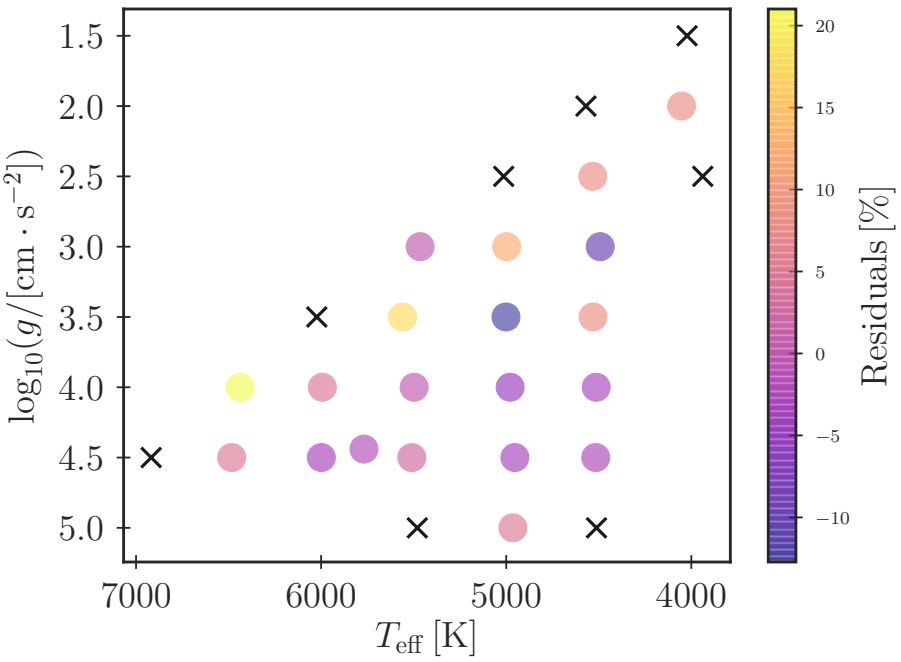


Figure 5.8: Residuals for the reconstruction of the turbulent pressure at the base of stellar ⟨3D⟩-envelopes by interpolation at solar metallicity. At the base of the ⟨3D⟩-envelopes, the pressure is $10^{1.75}$ times higher than at the density inflection near the surface. The crosses mark the ⟨3D⟩-envelopes that could not be reconstructed by interpolation, as they lie on the boundary of the Stagger grid. The colour bar shows the obtained errors in per cent.

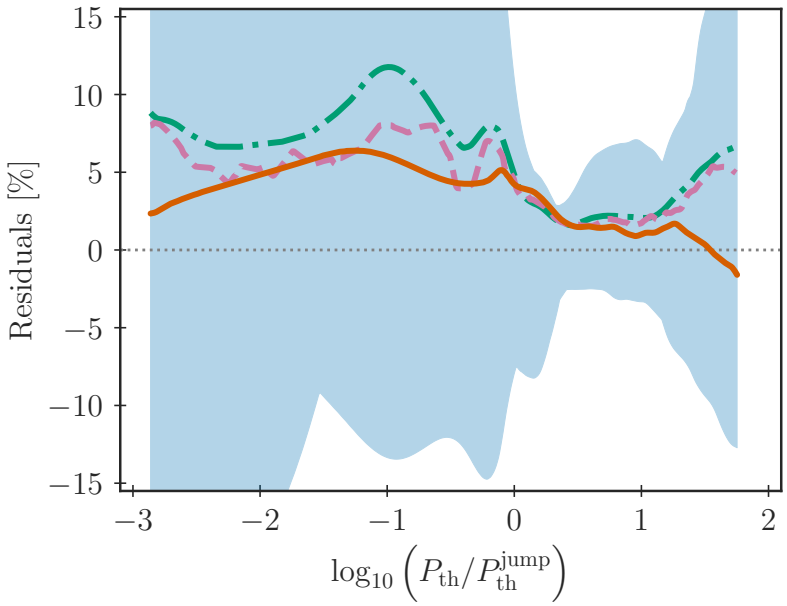


Figure 5.9: Residuals for the reconstruction of the turbulent pressure as a function of the scaled pressure for all simulations in the Stagger grid at solar metallicity. The shaded area shows the highest interpolation error for all simulations. The solid red line shows the residuals in the case of the present-day Sun, while the green dot-dashed line and the magenta dashed line show the mean and median of the absolute values of the residuals, respectively.

median and mean errors are only 4.6 % and 5.7 %, respectively. Throughout the entire ⟨3D⟩-envelope, the turbulent pressure is in all cases recovered within a factor of 2 — the associated median and mean errors are 23.4 % and 27.7 %, respectively. In short, the interpolation in [Fe/H] seems to perform worse in the case of turbulent pressure than for the other relevant physical quantities, making a refinement of the Stagger grid more crucial, when including this quantity.

I note that the performance of the interpolation scheme partly reflects the fact that I withhold ⟨3D⟩-envelopes. Better performance is hence expected when employing the entire grid. Furthermore, note that all tests in this chapter were performed using piece-wise cubic, continuously differentiable surfaces, while the interpolation in Chapters 8-10 rely on linear interpolation, which is found to affect the accuracy of the interpolation scheme.

# Chapter 6

# Post-Evolutionary Patching

*The content, including most of the text, of this chapter was published in Monthly Notices of the Royal Astronomical Society by Jørgensen et al. (2017) and Jørgensen et al. (2019) (see also Chapters 5 and 7 for further content from these papers). I am the first author of both papers and the primary investigator of the presented research project. I wrote this chapter. My contributions include the development, application and validation of the method as well as the numerical implementation of the algorithm. The work was performed in collaboration with Achim Weiss, George Angelou, Víctor Silva Aguirre, J. R. Mosumgaard (JM), and Christian L. Sahlholdt (CS). JM and CS undertook the task of performing the presented grid searches to find the best-fitting 1D models in connection with Section 6.3.3. All co-authors gave valuable feedback on the papers.*

State-of-the-art 1D stellar evolution codes do not subsume a comprehensive description of superadiabatic convection, which leads to a systematic offset in the predicted p-mode oscillation frequencies when addressing stars with convective envelopes[1] (cf. Chapters 2 and 3). Rather than subsequently correcting the model frequencies as described in Chapter 3, one may strive to correct for the underlying structural shortcomings of 1D stellar structure models. One way to achieve this amounts to substituting the outermost layers of stellar models with the mean stratifications of more sophisticated RHD simulations of stellar envelopes during the post-processing. This subsequent adjustment of the outermost layers of stellar structure models is known as *post-evolutionary patching*. The resulting hybrid models are referred to as patched models (PMs). Patching was originally proposed by Schlattl et al. (1997) and Rosenthal et al. (1999) using 1D and two-dimensional (2D) simulations of convection.

When vast grids of 3D simulations of stellar envelopes became available (e.g. Magic et al., 2013a; Trampedach et al., 2013), many authors adopted patching (cf. Piau et al., 2014; Sonoi et al., 2015; Ball et al., 2016; Magic and Weiss, 2016; Jørgensen et al., 2017; Trampedach

[1]Note that the convective envelopes of such stars extend beyond the layers covered by the 3D simulations.

et al., 2017; Jørgensen et al., 2019). Specifically, the cited authors substitute the outermost layers of 1D stellar models with 1D spatial and temporal averaged 3D structures, i.e. with $\langle 3D \rangle$-envelopes.

Patching takes place at a given evolutionary stage, i.e. after computing the stellar evolution up until a given final model. While patching is partly able to mend the structural shortcomings of stellar structure models in the post-processing, it does hence not correct for the inadequate boundary conditions that were imposed during the previous stellar evolution. This inevitably affects the evolutionary tracks. We address this issue in Chapter 8 by presenting a method that remedies this shortcoming.

In the present chapter, I mainly present the work published in Jørgensen et al. (2017), where we focus on stars with solar metallicity. When constructing such PMs, it hence is only necessary to compute interpolated $\langle 3D \rangle$-envelopes by interpolation in $T_{\rm eff}$ and $\log(g)$, which, among other things, allows for a comparison between the Trampedach and the Stagger grid and reduces the number of dimensions of the relevant parameter space (cf. Section 5.3.1). Models that rely on interpolation in metallicity are presented in Chapter 7, where I discuss parameterizations of the frequency shift that results from patching.

The main purpose of this chapter is to establish how to construct PMs in a physically consistent manner. Having discussed the criteria and restrictions for obtaining physically meaningful PMs, I am able to utilise PMs to draw conclusions on different target stars. Asteroseismic analyses based on PMs are presented in this chapter as well as in Chapter 7. These analyses exemplify how PMs can be used as a valuable diagnostic tool. Furthermore, by clarifying the advantages and drawbacks of the proposed patching procedure, the findings in the present chapter point towards aspects of the patching scheme that would benefit from further improvements. This led to the development of the procedure discussed in Chapter 8. At the same time, patching provides invaluable benchmark models. It is, for instance, possible to create physically meaningful PMs of the present-day Sun. More complex methods that aim to include 3D simulations into 1D models may hence be expected to recover, say, the model frequencies of patched solar models. As shown in Chapter 8, this is indeed the case.

The present-day Sun is observationally well-constrained, which makes it an ideal benchmark case. In order to evaluate the applicability and versatility of the presented patching procedure, I have, therefore, performed a detailed analysis of our host star. I discuss the results of this analysis in Section 6.2. The appended $\langle 3D \rangle$-envelopes draw on the interpolation scheme that is explained in the previous chapter. To investigate how interpolation errors affect the predicted stellar oscillations, Section 6.2 hence includes additional tests of the interpolation scheme. Having dealt with the Sun, I turn to an analysis of four solar-like main-sequence (MS) stars in the *Kepler* field, listing my findings in Section 6.3. Section 6.1 gives an overview of my patching method. Section 6.5 gives a summary of the present chapter.

## 6.1 Constructing Patched Models

We construct patched stellar models (PMs) by replacing the outermost stratification of 1D stellar structure models with the mean stratification of 3D stellar envelopes. In the following, we refer to the original 1D models as un-patched models (UPMs). In accordance with other authors, we perform the replacement at a given evolutionary stage. Since the previous evolution up to this point is, therefore, computed without replacing the outermost layers, we refer to our procedure as post-evolutionary patching. After all, the idea is to patch up for the errors made throughout the computed evolution when determining the properties of the final model.

### 6.1.1 The Patching Procedure

When constructing a PM, we discard all mesh points in the UPM above a certain interior patching point (i.p.). Likewise, we discard all mesh points below the so-called atmospheric patching point (a.p.) in the appended $\langle 3\mathrm{D}\rangle$-envelopes. The atmospheric patching point is typically placed within the nearly-adiabatic region below the photosphere. This apparent misnomer, refering to the lowermost point of the $\langle 3\mathrm{D}\rangle$-*envelope* as the *atmospheric* patching point, illustrates the developement of the nomenclature: in Jørgensen et al. (2017), we referred to the mean 3D structures as $\langle 3\mathrm{D}\rangle$-atmospheres.

Having discarded the mentioned mesh points, we then replace the stellar structure of the UPM beyond the interior patching point with the remaining mesh points from the $\langle 3\mathrm{D}\rangle$-envelopes. Figure 6.1 illustrates the corresponding changes in the stellar structure as well as the terminology that is introduced in this section.

There are different viable approaches one may take when selecting the patching points. One may pre-select the atmospheric patching point, at, say, a given pressure or depth. The patch is then performed, at a distance $r(\beta_{\mathrm{a.p.}})$ from the stellar centre of the UPM, at which a given patching quantity, $\beta$, takes the same value in the UPM as at the atmospheric patching point. Since a mesh point that matches the value of the patching quantity at the atmospheric patching point may not exist in the UPM, this approach requires interpolation in the UPM. As discussed below, suitable choices for the patching quantity, $\beta$, include the temperature ($T$), the total pressure ($P$), the density ($\rho$), and the first adiabatic index ($\Gamma_1$). We note that choosing any of these quantities as the patching quantity is seemingly equally physically motivated. This leaves us with a choice to make. In this chapter, we investigate the ramifications of this freedom to choose the patching quantity.

However, there are further choices to be made: one may follow different approaches that are seemingly equally valid to the one described above. Instead of pre-selecting the atmospheric patching point, one may pre-select the interior patching point. One may also define patching criteria based on two or more patching quantities. Involving more than one patching quantities, one may select the set of interior and atmospheric patching points that overall gives the best match between the $\langle 3\mathrm{D}\rangle$-envelope and the interior model for these patching quantities. For instance, one may perform the patch at that point in the $(P, \rho)$-plane, at which the density as a function of pressure predicted by the $\langle 3\mathrm{D}\rangle$-envelope

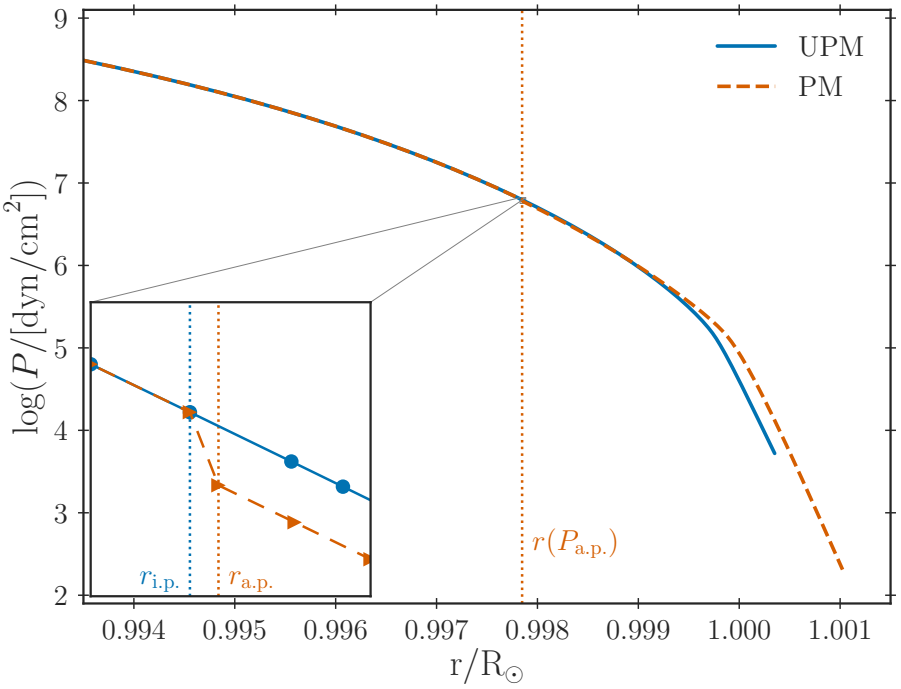


Figure 6.1: Pressure stratification of an un-patched model (UPM, solid blue line) and a patched model (PM, dashed red line) of the present-day Sun based on a GARSTEC solar calibration model and the solar Stagger-grid simulation. The temperature is used as the patching quantity ($\beta$), entering the selection of the patching points and the associated radii. As a result, the pressure stratification of the PM shows discontinuities (cf. Section 6.2.1). The zoom-in includes the interior patching point (i.p.), i.e. the outermost mesh point of the interior model, and the atmospheric patching point (a.p.) as well as the corresponding radii ($r_{\mathrm{i.p.}}$ and $r_{\mathrm{a.p.}}$). These radii are highlighted using dotted lines. In the zoom-in, the individual mesh points of the UPM and PM are indicated with circles and triangles, respectively. The patch was performed 1.5 Mm below an optical depth of 1 — that is, the patched $\langle$3D$\rangle$-envelope is roughly 1 Mm shallower than the maximal depth of the underlying 3D simulation.

lies closest to that predicted by the UPM.

When involving several patching quantities, the values of the patching quantities at the atmospheric patching point are most probably not all matched by the UPM at the same distance from the stellar centre. In other words, each patching quantity assigns a different distance from the stellar centre to the atmospheric patching point. This means that any given patching criterion will inevitably lead to discontinuities in some quantities while ensuring a continuous stratification in the patching quantity. It also implies that one has to define a suitably weighted mean of these distances when using a combination of different quantities to establish the patch. For instance, in some cases, we construct the PMs by finding the best match between the stratifications of the 1D model and that of the $\langle 3\mathrm{D}\rangle$-envelope in the $(P, \rho)$-plane. For these models, we weight $r(\rho_{\mathrm{a.p.}})$ and $r(P_{\mathrm{a.p.}})$ by the respective discrepancies of these quantities between the interior and the atmospheric patching point.

In this chapter, we follow several of the approaches described above, in order to evaluate the influence of different patching criteria. Furthermore, some approaches facilitate an easy comparison with other authors, including Ball et al. (2016). None of the listed patching methods explicitly ensures the conservation of hydrostatic equilibrium, at the patching points. We therefore also construct models, for which we determine the distance, $r_{a.p.}$, of the atmospheric patching point from the stellar centre of the UPM, in such a way as to ensure hydrostatic equilibrium to first order:

$$r_{a.p.} = r_{i.p.} - \frac{2[P_{\mathrm{a.p.}} - P_{\mathrm{i.p.}}]r_{\mathrm{i.p.}}^2}{Gm(r_{\mathrm{i.p.}})[\rho_{\mathrm{a.p.}} + \rho_{\mathrm{i.p.}}].} \tag{6.1}$$

Here, the index i.p. refers to the interior patching point, i.e. the outermost mesh point in the UPM, for which the distance to the centre is smaller than $r(\beta_{\mathrm{a.p.}})$.

We finally note that 3D RHD simulations are computed in the plane-parallel approximation, assuming constant gravitational acceleration. The same holds true for the interpolated $\langle 3\mathrm{D}\rangle$-envelopes that are employed when patching 1D and 3D simulations (cf. Chapter 5). We hence adjust $\log g$ at each mesh point in the appended $\langle 3\mathrm{D}\rangle$-envelopes based on the enclosed mass and radius of each of these mesh points in the PMs. We hereby correct for sphericity when constructing PMs. This is done iteratively: for a given PM, we compute the difference between the assumed constant gravitational acceleration of the $\langle 3\mathrm{D}\rangle$-envelope and the actual gravitational acceleration at the associated distance from the stellar centre of the PM, starting at the lowermost mesh point. We then use this difference in gravitational acceleration to correct the distance ($\mathrm{d}z$) between the considered mesh point and its nearest neighbour in the patched $\langle 3\mathrm{D}\rangle$-envelope. This correction is based on the requirement that the structure of the PM is in hydrostatic equilibrium. For the shallow $\langle 3\mathrm{D}\rangle$-envelopes of solar-like MS stars, we find this correction to have little influence.

### 6.1.2 Choosing the $\langle 3\mathrm{D}\rangle$-Envelope

One may make several seemingly equally valid choices when deciding on *which* $\langle 3\mathrm{D}\rangle$-envelope to patch to any given UPM. For instance, one could choose to patch an $\langle 3\mathrm{D}\rangle$-envelope that

has the same global parameters ($T_{\rm eff}$, $\log g$ and [Fe/H]) as the UPM in question. Based on the conclusions drawn in this chapter, we, indeed, select $\langle$3D$\rangle$-envelopes in this manner in Chapter 7. In the present chapter, on the other hand, we try a handful of different selection schemes, in order to compare them.

In Section 6.2, we present patched solar models. Throughout most of that section, we simply use existing 3D RHD simulations that attempt to model the present-day Sun. Although $T_{\rm eff}$ and $\log g$ of these simulations may slightly deviate from the global parameters of the UPMs, this choice has several advantages. First, we are able to conduct a straightforward comparison with other authors, who have followed the same approach. Secondly, we are able to construct patched models without having to interpolate in the 3D simulations. By employing the interpolated solar $\langle$3D$\rangle$-envelopes from the cross-validation exercises in Chapter 5, we are, at the same time, able to test the ramifications of interpolation errors for the seismic results.

In Section 6.3, on the other hand, we construct PMs using $\langle$3D$\rangle$-envelopes, whose global parameters match those of the underlying UPMs. However, as pointed out by Magic et al. (2013b), the temperature stratification of $\langle$3D$\rangle$-envelopes may severely deviate from their 1D counterparts. It thus stands to reason that the naive patch between an interior model and a $\langle$3D$\rangle$-envelope with the *same* $T_{\rm eff}$ may not yield a good fit in $T(r)$ when using other quantities to determine the patch and vice versa. We, therefore, also follow an alternative approach in Section 6.3: we compute a large sample of interpolated $\langle$3D$\rangle$-envelopes, requiring $T_{\rm eff}$ and $\log g$ to lie within three standard deviations of the observational mean. The observational constraints are only included to limit the investigated region of the parameter space. We then select that interpolated $\langle$3D$\rangle$-envelope that minimizes the sum of squared relative differences in $T$, $\rho$, and $\Gamma_1$ near the base of the interpolated $\langle$3D$\rangle$-envelope. For each interpolated $\langle$3D$\rangle$-envelope, the sum of squared differences is furthermore weighted by $(1 + (100 \cdot \Delta \log g)^2)$, where $\Delta \log g$ is the difference in $\log g$ at the surface. Although the expression for this weight is chosen ad hoc, the choice to include a weight that depends on $\log g$ is motivated by Occam's razor: by imposing this restriction on $\log g$, we prefer $\langle$3D$\rangle$-envelopes, whose gravitational acceleration match the value of the UPM, since any mismatch has to be subsequently corrected for, in order to obtain physically meaningful PMs. The interpolation takes place at a total pressure that is $10^{1.9}$ times higher than the pressure at the density inflection. This value lies close to the highest scaled total pressure that is common for all 3D simulations in the grids so that no extrapolation is required. In other words, the chosen total pressure lies close to the deepest possible patching point. We test this selection procedure in Sections 6.2.3 based on the present-day Sun.

## 6.2 The Solar Case

Having summarized the main aspects of our patching procedure, we proceed to an investigation of how the seismic predictions are affected by the implementation of our procedure. We base our investigation on the present-day Sun, as very detailed observational constraints exist for our host star.

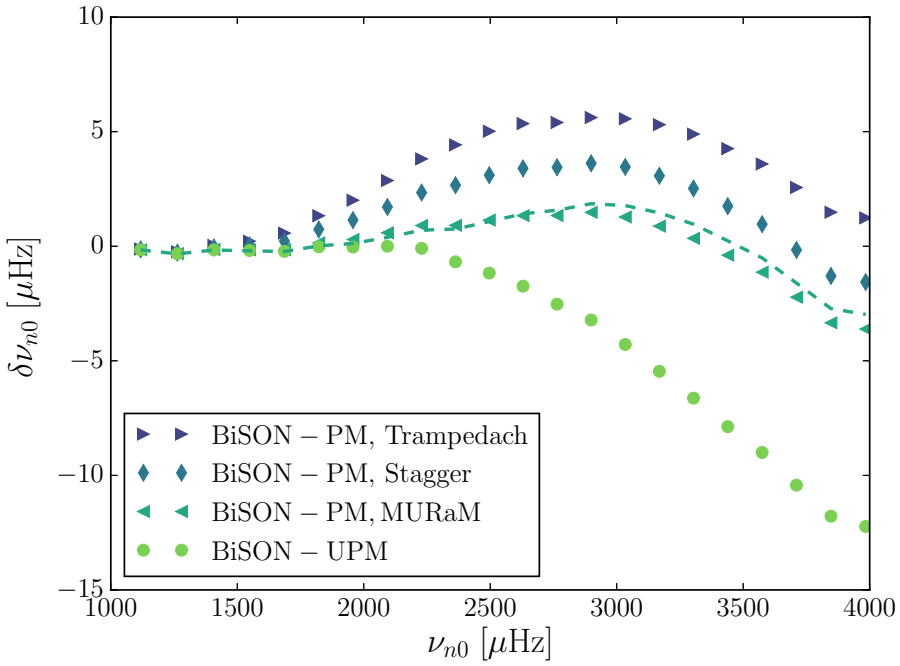


Figure 6.2: Frequency differences between BiSON observations and the un-patched Model S (UPM) as well as three patched models (PMs), for $\ell = 0$. The solar Stagger-grid $\langle 3D \rangle$-envelope, the solar Trampedach-grid $\langle 3D \rangle$-envelope and the MURaM simulation were used, respectively. For all models, a weighted combination of $P$ and $\rho$ served as the patching quantity. The patching points are chosen within the nearly-adiabatic region, at the depth, where the closest match in the $(P, \rho)$-plane between the interior and $\langle 3D \rangle$-envelope is found. The dashed line shows the results presented by Ball et al. (2016) for comparison. All frequencies are computed within the gas $\Gamma_1$ approximation.

### 6.2.1 Patched Solar Models

To facilitate an easy comparison with other authors, we have patched to Model S, a standard solar model presented by Christensen-Dalsgaard et al. (1996). For these PMs, we have computed frequency differences, $\delta\nu_{n\ell}$, between the model frequencies and BiSON observations of radial modes ($\ell = 0$). In accordance with Ball et al. (2016), we assume that the relative Lagrangian perturbations of the turbulent and thermal pressure are equal, i.e. we work within the gas $\Gamma_1$ approximation (cf. Chapter 3).

For a direct comparison with Ball et al. (2016), we have employed the same MURaM (cf. Vögler et al. 2005) radiative MHD simulation for the solar $\langle 3D \rangle$-envelope from Beeck et al. (2013) averaged over surfaces of constant geometric depth and time.

In accordance with Ball et al. (2016), we use a combination of $P$ and $\rho$ as patching quantities. Our approach, therefore, differs from that by Ball et al. (2016) only in minor details. Figure 6.2 shows the frequency difference between BiSON data and the model

frequencies of the PM. The resulting oscillation frequencies are in good agreement with the results published by Ball et al. (2016), and we were thus able to reduce the frequency difference between model frequencies and observations from roughly 12 $\mu$Hz to 4 $\mu$Hz within the gas $\Gamma_1$ approximation. As also stressed in the cited paper, this is overall consistent with the findings of other authors, including Piau et al. (2014), who present patched solar models, in which they adopt the average profile of the temperature gradient, $P$, $\rho$, $\Gamma_1$, and the Brunt-Väisälä frequency from hydrodynamic and magneto-hydrodynamic 3D simulations. Piau et al. (2014) have decreased the radius of their UPM, in order to correct for the fact that the PM is slightly larger than the UPM since $\langle$3D$\rangle$-envelopes are larger than their 1D counterparts. Like Ball et al. (2016) and Magic and Weiss (2016), we do not take this effect into account, as we fix the interior structure by Model S, meaning that the radii of our patched solar models are roughly 100 km larger than the constraints on the radius of Model S.

We have also constructed PMs based on Model S and the solar $\langle$3D$\rangle$-envelopes in the Stagger and Trampedach grids. The resulting model frequencies are lower by 2 $\mu$Hz and 5 $\mu$Hz, respectively, at high frequencies, compared to the MURaM solar patched model (cf. Fig. 6.2). We note that these frequency deviations are comparable to the discrepancy between model predictions and observations — that is, within the gas $\Gamma_1$ approximation. As was to be expected, the seismic results are very sensitive to the exact input physics of the $\langle$3D$\rangle$-envelope.

The same holds true for the interior model. Figure 6.3 summarizes the results obtained for two different GARSTEC models. Both models use the OPAL-EOS (cf. Rogers et al. 1996) and the MHD-EOS in the low-temperature regime, the OPAL opacities (cf. Iglesias and Rogers 1996), the low-temperature opacities by Ferguson et al. (2005), and the composition determined by AGSS09 but differ in their treatment of convection: one uses mixing length theory (cf. Chapter 2, Böhm-Vitense 1958), while the other employs the convection theory by Canuto and Mazzitelli (1991, 1992) with a solar calibrated mixing length parameter. Although the convection theory by Canuto and Mazzitelli (1991, 1992) leads to model frequencies (UPM, CM in Fig 6.3) that are in better agreement with observations than mixing length theory does (UPM, MLT in Fig 6.3), patching the solar Stagger-grid $\langle$3D$\rangle$-envelope to either of the two GARSTEC models yields almost identical results. This means that the patch is performed at a depth, below which the two UPMs are nearly indistinguishable. This holds true because all solar calibration models are required to recover the same global parameters and hence reach the same deep adiabat. As discussed in Chapter 8, the outer boundary conditions generally play a vital role in stellar evolution.

As can be seen from Figs 6.2 and 6.3, none of the presented patched solar models actually reproduces the observed BiSON frequencies, as we only take structural effects into account. Thus, modal effects have been neglected (cf. Chapter 3).

We now take a closer look at the patching procedure. We begin by discussing suitable choices for the patching quantity ($\beta$), as this choice determines both the patching points and the distance of the atmospheric patching point $r_{\mathrm{a.p.}}(\beta)$ from the stellar centre. The implications are twofold: firstly, the patching quantity determines the size of the acoustic cavity. Secondly, the stratification of the chosen quantity is smooth by construction, while

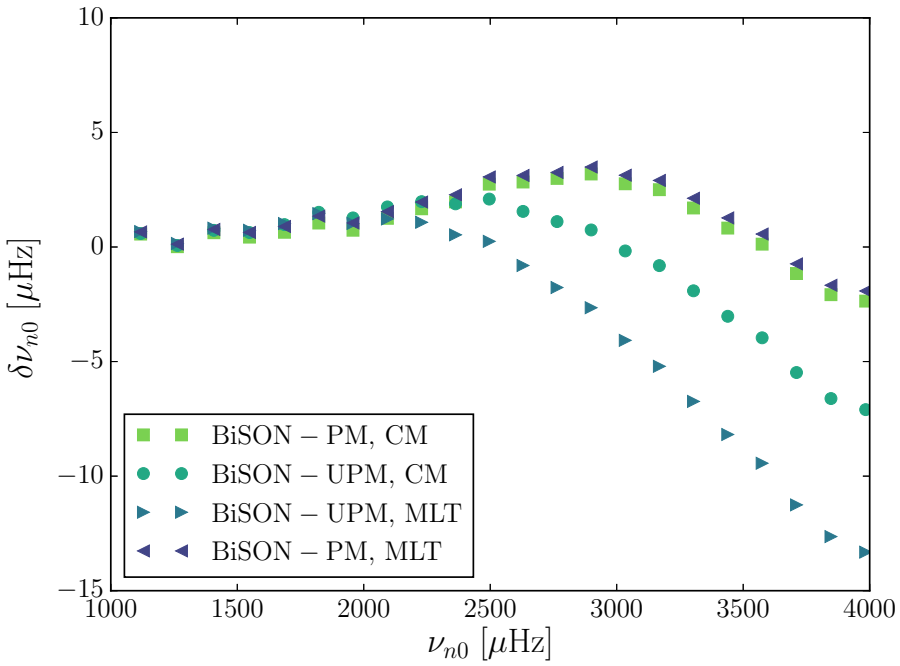


Figure 6.3: Frequency differences between BiSON observations and patched models (PM), for $\ell = 0$, based on the solar Stagger-grid simulation and GARSTEC models with difference convective treatments: mixing length theory (MLT) and the convection theory by Canuto & Mazzitelli (CM). The models are patched 2.7 Mm below the surface, i.e. below a Rosseland optical depth of 1, using a combination of $P$ and $\rho$ as the patching quantity. All frequencies are computed within the gas $\Gamma_1$ approximation.

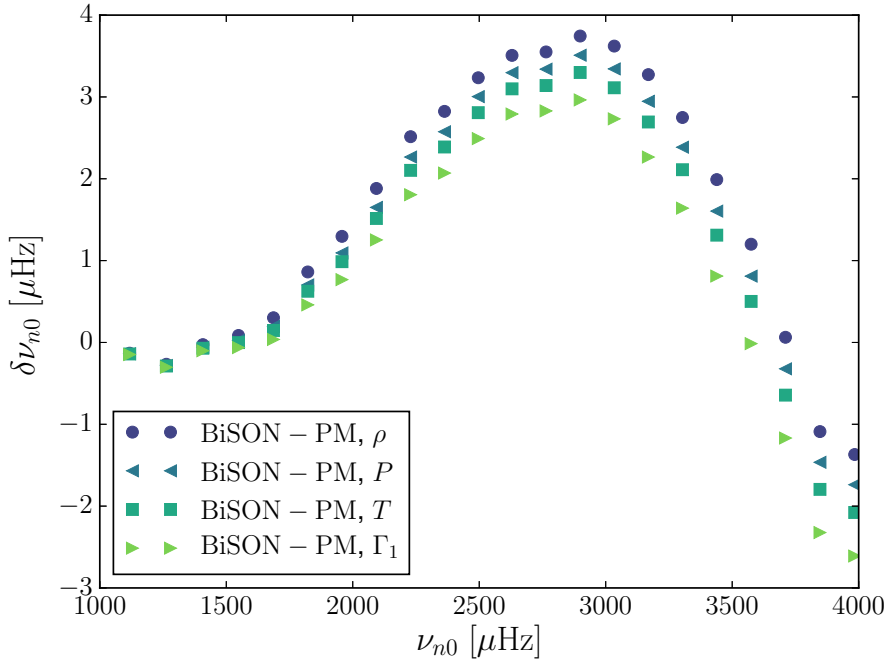


Figure 6.4: Frequency differences between BiSON observations and patched models (PM) for $\ell = 0$ based on Model S and the solar Stagger-grid $\langle$3D$\rangle$-envelope, using different quantities ($P$, $\rho$, $T$, and $\Gamma_1$) for the selection of the interior patching point and $r_{\mathrm{a.p.}}(\beta)$. All models are patched 2.7 Mm below the surface. All frequencies are computed within the gas $\Gamma_1$ approximation.

discontinuities may occur for the remaining quantities. The question thus arises as to which degree the seismic results are affected by the choice of the patching quantity. Since the frequency computation relies on $P(r)$, $\rho(r)$, and $\Gamma_1(r)$, each of these quantities constitutes a suitable choice for the patching quantity. These quantities are all related to $T(r)$ through the EOS, making the temperature yet another reasonable alternative.

As can be seen from Fig. 6.4, PMs that are based on different patching quantities yield the same oscillation frequencies within $1 - 2\,\mu$Hz, in the case of the solar Stagger-grid $\langle$3D$\rangle$-envelope. In the case of the mentioned MURaM simulation and the solar Trampedach-grid $\langle$3D$\rangle$-envelope, we find the choice of patching quantities to affect the model frequencies by up to $3\,\mu$Hz, which is of the same order as the frequency differences presented in Fig. 6.2 and small compared to the surface effect itself. When dealing with *Kepler* stars in Section 6.3, we will thus present PMs based on different patching quantities.

As mentioned in Section 6.1.1, we have also constructed PMs, determining $r_{\mathrm{a.p.}}(\beta)$, in such a way as to ensure hydrostatic equilibrium to first order, using Eq. (6.1). This procedure results in model frequencies that are consistent with the frequencies obtained when using $P$ as the patching quantity.

We have varied the patching depth, using different patching quantities: $T$, $P$, $\rho$, or $\Gamma_1$ as well as combinations thereof. For these patching quantities, we find the model frequencies to be relatively insensitive to the patching depth if the patching points are situated sufficiently deep within the nearly-adiabatic region, independently of the used solar $\langle 3D \rangle$-envelope.

Piau et al. (2014) have used the optical depth to construct PM. Using this patching quantity in our approach leads to prominent discontinuities in the stratifications of other quantities and yields model frequencies that are rather sensitive to the patching depth. These discontinuities become more prominent with patching depth, which most probably reflects the accumulation of discrepancies that stem from the integration over the opacity, due to discrepancies in the assumed chemical composition: in Model S, $Z_S/X_S$ is 0.0245 at the solar surface, while $Z_S/X_S$ is only 0.018 for the Stagger-grid simulations, in accordance with Asplund et al. (2009). These results reflect the inconsistent physical assumptions that enter the UPM and the $\langle 3D \rangle$-envelope.

Finally, we note that all models presented in Figs 6.2, 6.3, and 6.4 have been computed without correcting for sphericity or other discrepancies in $\log g$, in order to facilitate an easy comparison with Ball et al. (2016). In the case of the shallow solar $\langle 3D \rangle$-envelope, these corrections have little effect on the overall structure and hence on the oscillation frequencies. For some of the models presented in Section 6.2.3, on the other hand, these corrections strongly alter the frequencies, due to a sufficiently large mismatch between the gravitational acceleration of the UPM and the gravitational acceleration of the patched $\langle 3D \rangle$-envelope.

### 6.2.2 Testing the Interpolation Scheme

In Chapter 5, we have reproduced the solar $\langle 3D \rangle$-envelope, in both the Stagger grid and the Trampedach grid by interpolation in the $(T_{\rm eff}, \log g)$-plane. In order to assess whether the accuracy of our interpolation scheme is sufficiently high for the purpose of asteroseismic analyses, we have constructed PMs based on these interpolated solar $\langle 3D \rangle$-envelopes. We have then compared the seismic results of these models with the model frequencies that were obtained using the original solar $\langle 3D \rangle$-envelopes.

In the case of the Stagger grid, where the structure of the solar $\langle 3D \rangle$-envelope is reliably reproduced within 2 % or better, the interpolated solar $\langle 3D \rangle$-envelope yields the expected model frequencies within 1 $\mu$Hz, for all radial modes with frequencies between 1000 $\mu$Hz and 4000 $\mu$Hz, independently of the chosen patching quantity, when performing the patch at the base of the $\langle 3D \rangle$-envelope. The errors introduced by the interpolation scheme are thus of the order of the uncertainty associated with the averaging of the 3D simulations (cf. Ball et al., 2016; Magic and Weiss, 2016).

In the case of the Trampedach grid, however, a more complex picture emerges. As briefly mentioned in Chapter 5, the interpolation scheme strongly underestimates $\rho(P)$, which affects the selection of the patching points and the computation of $r_{\rm a.p.}(\beta)$. Thus, when patching by matching the stratifications in the $(P, \rho)$-plane, as we did in connection with Fig. 6.2, the errors in the model frequencies reach 6 $\mu$Hz — better agreement is reached when using $T$ as the patching quantity.

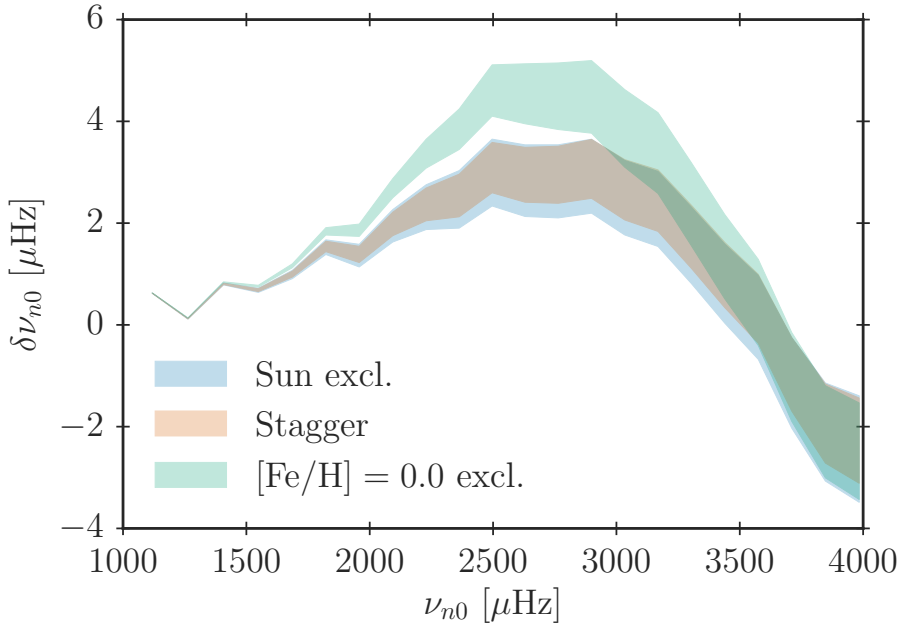


Figure 6.5: Frequency differences between BiSON observations and three patched models (PMs). For one model ('Stagger'), we have patched the original Stagger-grid ⟨3D⟩-envelope with global solar parameters. One model ('Sun excl.') is based on an interpolated ⟨3D⟩-envelope that was computed after excluding the solar ⟨3D⟩-envelope from the grid. The last solar model ('[Fe/H] = 0.0 excl.') has been constructed by patching an interpolated ⟨3D⟩-envelope that was computed after excluding all ⟨3D⟩-envelopes at solar metallicity from the grid. The width of the shaded area shows the frequency shift that is introduced when changing the patching quantity: we use $P$, $\rho$, or $T$. All frequencies are computed within the gas $\Gamma_1$ approximation.

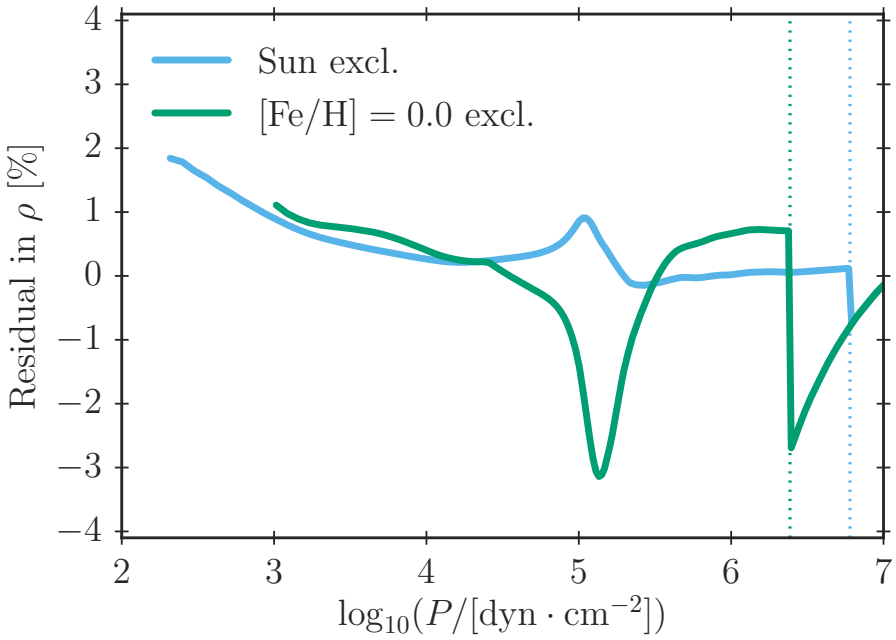


Figure 6.6: Difference between the density of patched models (PMs) and the solar ⟨3D⟩-envelope in the Stagger grid as a function of the total pressure. The vertical dotted lines indicate the location of the patching points. The colours correspond to Fig. 6.5. The density has been used as the patching quantity.

To further test the extent to which an interpolation in metallicity affects the predicted model frequencies, we compared three patched solar models with different ⟨3D⟩-envelopes in Jørgensen et al. (2019): the original Stagger-grid ⟨3D⟩-envelope and two interpolated ⟨3D⟩-envelopes from the cross-validation exercises in Chapter 5. One of the interpolated ⟨3D⟩-envelopes was obtained by interpolation in the $(T_{\rm eff}, \log g)$-plane only after excluding the solar ⟨3D⟩-envelope model in the grid as done above. The other interpolated ⟨3D⟩-envelope has been computed by interpolation in $T_{\rm eff}$, $\log g$, and [Fe/H], after excluding all models with solar metallicity. We have patched the ⟨3D⟩-envelopes to a solar calibration model, using different patching quantities, in order to show the effect of this choice — this corresponds to the test performed in connection with Fig. 6.4. The input physics of the underlying un-patched GARSTEC model is specified in Section 7.2.1. The resulting model frequency differences, relative to the observed ones, are shown in Fig. 6.5. Note that these differences reach 14 $\mu$Hz at a frequency of 4000 $\mu$Hz for the un-patched solar model.

The structural differences that give rise to the frequency differences in Fig. 6.5 are shown in Fig. 6.6. Interpolation after the exclusion of all models with solar metallicity leads to a larger displacement of the density inflection near the surface and lower accuracy in general than the interpolation in the $(T_{\rm eff}, \log g)$-plane does. Again, this calls for a refinement of the Stagger grid in [Fe/H]. Furthermore, as can be seen from the figure, the ⟨3D⟩-envelope that relies on interpolation in [Fe/H] is shallower (with a depth of 1.1 Mm)

than the ⟨3D⟩-envelope obtained from interpolation in only $T_{\rm eff}$ and $\log g$ (with a depth of 1.5 Mm). This is because the Stagger-grid ⟨3D⟩-envelope with the lowest pressure at its base relative to the pressure at the density inflection dictates the pressure at the base of the interpolated ⟨3D⟩-envelopes as described in Chapter 5. Due to this, the ⟨3D⟩-envelopes that rely on interpolation in metallicity are, in general, slightly shallower than those that solely rely on interpolation in the $(T_{\rm eff}, \log g)$-plane, depending on the metallicity. When interpolating in metallicity, the interpolated ⟨3D⟩-envelopes span roughly four orders of magnitude in pressure.

### 6.2.3 Selecting Envelope Parameters

When constructing PMs with fixed interior structures for *Kepler* stars in Section 6.3, we follow two different approaches for the selection of suitable ⟨3D⟩-envelopes: in the first approach, we patch interpolated ⟨3D⟩-envelopes that have the same $\log g$ and $T_{\rm eff}$ as the UPMs. In the second approach, we select the global parameters of the ⟨3D⟩-envelopes based on the requirement to minimize the discontinuities in several quantities near the base of the ⟨3D⟩-envelopes, as described in Section 6.1.1. Both approaches are rather simplistic and have their drawbacks: while the former approach will lead to unphysical discontinuities, minimizing these discontinuities may simply disguise inadequacies of the UPM or the ⟨3D⟩-envelopes without ensuring a physically correct representation of the stellar structure.

To test, to which extent a mismatch in $T_{\rm eff}$ and $\log g$ between the UPM and the patched ⟨3D⟩-envelope affects the seismic results, we have constructed several PMs, based on Model S and interpolated ⟨3D⟩-envelopes with different global parameters. The results are presented in Fig. 6.7. For a mismatch in $T_{\rm eff}$ of the order of 100 K, we find frequency shifts of the order of 10 $\mu$Hz. Based on the analysis presented in Section 6.2.2, this by far exceeds the error that is expected to arise from the interpolation scheme alone.

Figure 6.7 also contains a PM model with the ⟨3D⟩-envelope that minimizes the discontinuities at the base of the ⟨3D⟩-envelope, i.e. yields the best match to the UPM (cf. Section 6.1.2). In the case of the Stagger grid, the best match is found at $T_{\rm eff} = 5778$ K, i.e. for a ⟨3D⟩-envelope, for which the effective temperature lies close to the effective temperature of the UPM. In contrast, we find the effective temperature of the best-matching ⟨3D⟩-envelope to deviate significantly from the effective temperature of the UPM, in the case of the Trampedach grid. Different selection criteria for the global parameters of the patched ⟨3D⟩-envelope may hence severely affect the seismic results.

Figure 6.7 emphasizes the importance of the interpolation scheme presented in Section 5.3.1: simply selecting the nearest ⟨3D⟩-envelopes in the grid will severely distort the seismic results and is, therefore, unsuitable for correcting structural effects. Patching the nearest ⟨3D⟩-envelope in the Stagger grid, after excluding the solar ⟨3D⟩-envelope, shifts the model frequencies by up to 19 $\mu$Hz.

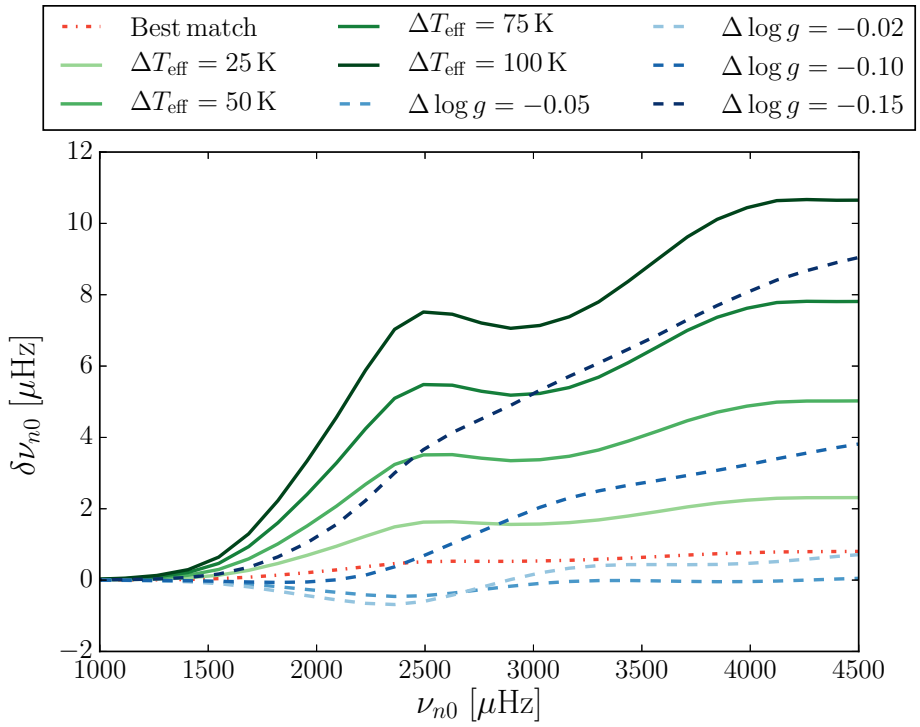


Figure 6.7: Frequency differences obtained from subtracting model frequencies of PMs, based on interpolated ⟨3D⟩-envelopes with different global parameters ($T_{\rm eff}$ and $\log g$), from model frequencies, based on the solar Stagger-grid ⟨3D⟩-envelope. All PMs are constructed, based on Model S, using a combination of $P$ and $\rho$ as the patching quantity. We have adjusted $\log g$ to fit the interior model, at the atmospheric patching point, and corrected for sphericity. When varying the effective temperature, $\log g$ has been kept fixed and vice versa. All frequencies are computed within the gas $\Gamma_1$ approximation.

## 6.3 Stars in the *Kepler* Field

We now present an asteroseismic analysis of several stars in the *Kepler* field, employing both UPMs and PMs. We only consider solar-like stars in a limited mass range, guided by the established accuracy of the interpolation scheme in different regions of the $(T_{\rm eff}, \log g)$-plane. Due to the restrictions imposed by the Trampedach grid, we selected objects that have metallicities consistent with the assumption of solar metallicity within one standard deviation of the spectroscopic values listed in Lund et al. (2017) and Silva Aguirre et al. (2015).

Keeping the composition fixed leaves us with only the mass and evolutionary stage to vary when selecting the UPM that best fits observations. In this chapter, we avoid the additional interpolation in metallicity. We also ignore the effects of atomic diffusion, thus assuming that the present surface composition is the initial one.

### 6.3.1 Selecting UPMs

To ensure a high degree of consistency between the interior model and the employed 3D simulations, we draw upon an alternative prescription for modelling superadiabatic convection in 1D models by Trampedach et al. (2014a,b). Specifically, the cited authors suggest modifications to the standard procedure for modelling superadiabatic convection using MLT: above the photosphere, the structures of the UPMs are dictated by a $T(\tau)$ relation that is derived from 3D simulations. Below the photosphere, the results from 3D simulations are taken into account via a variable $\alpha_{\rm MLT}$ and adjustments to the radiative gradient. The procedure provides more physically accurate boundary conditions at the photosphere than the Eddington grey atmosphere does and gives a better description of the transition between optically thin and optically thick regions. Furthermore, the variable $\alpha_{\rm MLT}$ gives a more realistic description of convection throughout the HR diagram than a constant mixing length parameter does. In the present section, we draw on this procedure by Trampedach et al. (2014a,b) to create UPMs. We refer to these UPMs as 3D-calibrated models.

The procedure by Trampedach et al. (2014a,b) was implemented into GARSTEC by Mosumgaard et al. (2018). We note that the implementation by Mosumgaard et al. (2018) showed that the modified outer layers shift the evolutionary tracks. However, the obtained models do not correct for the surface effect. The reason for this is that the method does not correctly mimic the structure of 3D simulations. This is due to the simplifying assumption that a single value for the mixing length parameter is sufficient to recover the correct temperature gradient throughout the $\langle 3D \rangle$-envelope. In addition, Mosumgaard et al. (2018) do not include turbulent pressure and do not include a phenomenon that is known as convective back-warming: convective temperature fluctuations and the extreme temperature sensitivity of the opacity affect the cooling of the granules and the inter-granular lanes asymmetrically. This results in warming below the photosphere and an expansion of the $\langle 3D \rangle$-envelope that is not accounted for by 1D models but found in 3D simulations. We refer to Trampedach et al. (2013, 2017) for further details.

Using GARSTEC, we have constructed a grid of 3D-calibrated UPMs, computing evolutionary tracks for models with masses between $0.70\,M_\odot$ and $1.20\,M_\odot$ in steps of $0.01\,M_\odot$. This grid covers the parameter range of the 3D simulations. Using ADIPLS, we have then computed model frequencies for all models, for which the large frequency separation, $\Delta\nu$, lies between $60\,\mu$Hz and $170\,\mu$Hz, which for a $1\,M_\odot$ star covers the evolution from the ZAMS to the onset of the red giant branch. We refer to these as 3D-calibrated models. For the purpose of consistency, these models employ the MHD-EOS at low temperatures and the same abundances as used in the hydrodynamic simulations by Trampedach et al. (2013). Where the MHD-EOS is not available, the OPAL-EOS is used. We use the same monochromatic low-temperature opacities as presented in Trampedach et al. (2014b) merged with the OP high temperature opacities (cf. Badnell et al. 2005), for the same mixture as in the Trampedach grid, and conductive opacities by Cassisi et al. (2007).

For comparison, we also include models based on a different grid that employs the OPAL-EOS, the OPAL opacities, the low-temperature opacities by Ferguson et al. (2005), the conductive opacities by Cassisi et al. (2007), and the composition by Grevesse and Sauval (1998). These models use conventional Eddington grey atmospheres. This grid includes stars with masses between $0.70\,M_\odot$ and $1.30\,M_\odot$ in steps of $0.01\,M_\odot$, for which the large frequency separation lies between $13\,\mu$Hz and $180\,\mu$Hz. The metallicity ([Fe/H]) is treated as a free parameter and varied between $-0.50$ dex and 0.50 dex in steps of 0.05 dex. We refer to these models as standard input models. The helium mass fraction is varied between 0.25 and 0.30 in steps of 0.002, and the solar calibrated mixing length parameter is set to 1.79.

We compare the obtained model frequencies with the observed frequencies extracted from *Kepler* data based on a Bayesian Markov Chain Monte Carlo 'peak-bagging' approach (cf. Davies et al., 2016; Lund et al., 2017). The best-fitting model is selected, based on the individual frequencies after applying the empirical surface correction by Ball and Gizon (2014). For comparison, we have also found the UPM that yields the best fit to the frequency ratios, $r_{01}$, $r_{10}$, and $r_{02}$, discussed in Chapter 3.

We determine the stellar parameters by choosing the model that gives the maximal likelihood based on the listed frequency ratios or the individual frequencies, using the **BA**yesian **ST**ellar **A**lgorithm, BASTA (cf. Silva Aguirre et al. 2015).

### 6.3.2 Selecting Envelopes

Table 6.1 lists the stellar parameters for the UPMs that are selected as described above to model the four *Kepler* stars. Alongside these model parameters, we list observational constraints and the global parameters for the interpolated $\langle$3D$\rangle$-envelopes that minimize the discontinuities, at the base of the $\langle$3D$\rangle$-envelope. Furthermore, Table 6.1 summarizes the values and uncertainties of the stellar mass, $T_{\rm eff}$, and $\log g$ as obtained from BASTA, i.e. key values of the mapped probability distributions. Note that the listed median does not correspond to the best-fitting model.

The observational constraints on the effective temperature and metallicities for stars in the LEGACY dwarfs sample I are derived spectroscopically and adopted from Table 1

Table 6.1: Parameters for UPMs and PMs of *Kepler* stars. The indices refer to the probability distribution (P), from which the UMPs are drawn, the UPMs that led to the best fit (U), the PMs based on the Stagger grid (S), and the PMs based on the Trampedach grid (T), respectively. The index 'con' indicates spectroscopic and asteroseismic constraints on $T_{\rm eff}$ and $\log g$ that have been adopted from either the LEGACY (1) or KAGES (2) sample, which is specified in the last column. Specific references to papers are given in the text. The uncertainties given for the UPM denote 68.3 % credibility intervals evaluated by BASTA, based on the employed grid of UPMs, fitting individual frequencies. The asterisk denotes standard input models, while the rest are 3D-calibrated models.

| KIC | $T_{\rm eff,con}$ (K) | $\log g_{\rm con}$ (cgs; dex) | $M_{\rm P}$ ($M_\odot$) | [Fe/H] (dex) | $T_{\rm eff,P}$ (K) | $\log g_{\rm P}$ (cgs; dex) | $T_{\rm eff,U}$ (K) | $\log g_{\rm U}$ (cgs; dex) | $T_{\rm eff,S}$ (K) | $T_{\rm eff,T}$ (K) | Sample |
|---|---|---|---|---|---|---|---|---|---|---|---|
| 9025370* | $5270 \pm 180$ | $4.423^{+0.004}_{-0.007}$ | $1.016^{+0.007}_{-0.007}$ | $0.06^{+0.09}_{-0.07}$ | $5758^{+71}_{-61}$ | $4.430^{+0.003}_{-0.003}$ | 5771 | 4.430 | 5773 | 5729 | 1 |
| 9025370 | $5270 \pm 180$ | $4.423^{+0.004}_{-0.007}$ | $0.988^{+0.019}_{-0.008}$ | 0 | $5905^{+38}_{-19}$ | $4.428^{+0.003}_{-0.003}$ | 5908 | 4.427 | 5761 | 5764 | 1 |
| 9955598* | $5457 \pm 77$ | $4.497^{+0.005}_{-0.007}$ | $0.900^{+0.01}_{-0.01}$ | $0.07^{+0.07}_{-0.08}$ | $5370^{+61}_{-61}$ | $4.497^{+0.002}_{-0.002}$ | 5396 | 4.497 | 5506 | 5417 | 1 |
| 9955598 | $5460 \pm 75$ | $4.495^{+0.002}_{-0.002}$ | $0.884^{+0.003}_{-0.005}$ | 0 | $5599^{+19}_{-26}$ | $4.496^{+0.002}_{-0.001}$ | 5596 | 4.496 | 5506 | 5445 | 2 |
| 11133306* | $5982 \pm 82$ | $4.314^{+0.004}_{-0.007}$ | $1.05^{+0.04}_{-0.04}$ | $0.0^{+0.1}_{-0.1}$ | $5956^{+68}_{-78}$ | $4.313^{+0.007}_{-0.007}$ | 5960 | 4.313 | 5991 | 5904 | 2 |
| 11133306 | $5982 \pm 82$ | $4.314^{+0.004}_{-0.007}$ | $1.01^{+0.03}_{-0.02}$ | 0 | $6010^{+70}_{-70}$ | $4.307^{+0.006}_{-0.008}$ | 5998 | 4.306 | 5989 | 5870 | 2 |
| 11772920* | $5180 \pm 180$ | $4.500^{+0.008}_{-0.005}$ | $0.840^{+0.01}_{-0.02}$ | $-0.11^{+0.08}_{-0.06}$ | $5345^{+70}_{-60}$ | $4.503^{+0.003}_{-0.003}$ | 5354 | 4.502 | 5506 | 5330 | 1 |
| 11772920 | $5180 \pm 180$ | $4.500^{+0.008}_{-0.005}$ | $0.854^{+0.003}_{-0.004}$ | 0 | $5476^{+28}_{-21}$ | $4.506^{+0.002}_{-0.002}$ | 5479 | 4.505 | 5506 | 5313 | 1 |

in Lund et al. (2017); in the case of KIC 9025370 and KIC 11772920, the spectroscopic values are from Pinsonneault et al. (2014). The constraints on the gravitational acceleration are derived asteroseismically and are taken from Table 3 in Silva Aguirre et al. (2017). In the case of the stars from the KAGES sample, the spectroscopic values for the effective temperatures as well as the asteroseismic constraints on $\log g$ are adopted from Table 3 in Silva Aguirre et al. (2015).

For both samples, the listed constraints on $\log g$ are obtained from modelling the individual frequencies, using BASTA. One may object to using the outcome of stellar modelling when considering models with different input physics. However, we only employ these constraints in order to restrict the region of interest, when looking for the best match in the $(T_{\rm eff}, \log g)$-plane.

As can be seen from Table 6.1, the metallicities of the best fitting standard input UPMs are in agreement with the assumption of solar metallicity, the evaluated $\log g$ are in good agreement with the findings of Silva Aguirre et al. (2015) and Silva Aguirre et al. (2017), and the masses of the standard input UPMs are in very good agreement with the masses of the 3D-calibrated UPMs — and with the findings of Silva Aguirre et al. (2017).

For all four *Kepler* stars, the effective temperatures of the standard input UPMs are lower and in better agreement with the spectroscopic constraints than their 3D-calibrated counterparts are. This, at least partly, reflects the fact that we kept the metallicity fixed, when determining the best fitting 3D-calibrated models, while the metallicity entered the analysis as a variable, in the case of the standard input models. Moreover, in contrast to the standard input models, the 3D-calibrated models have been computed neglecting atomic diffusion, due to the restrictions imposed by the Trampedach grid. According to Silva Aguirre et al. (2015), the neglect of diffusion affects the global parameters of the best-fitting UPMs.

### 6.3.3 Asteroseismic Analyses of Patched Models

For all eight UPMs listed in Table 6.1, we have constructed 6 patched models: for each envelope grid, i.e. for the Stagger grid and the Trampedach grid, we have constructed 2 PMs, employing either $T$ or a combination of $P$ and $\rho$ as patching quantities and using $\langle 3D \rangle$-envelopes, for which $T_{\rm eff}$ and $\log g$ match the parameters of the UPM. Furthermore, we have constructed one PM for each envelope grid, using a combination of $P$ and $\rho$ as the patching quantity, and selecting the $\langle 3D \rangle$-envelope, in such a way as to minimize the discontinuities between the interior model and the $\langle 3D \rangle$-envelope, near the base of the $\langle 3D \rangle$-envelope. These patching criteria have been selected based on our investigation of the solar case, from which we conclude that the choice of patching quantity and the selection of the patched $\langle 3D \rangle$-envelope have the largest effect on the seismic results.

#### 6.3.3.1 KIC 9025370

The upper and lower panel of Fig. 6.8 show a comparison between observations and model frequencies for the UPM and the associated 6 PMs of KIC 9025370. We have selected the

best-fitting UPM, based on the individual frequencies, and find that an analysis, relying on the frequency ratios, leads to similar results but depends slightly on the restrictions on $\Delta\nu$.

We note that the effective temperature of the 3D-calibrated UPM does not lie within three standard deviations of the spectroscopic value and that the effective temperature of the standard input model likewise lies above the spectroscopic value. This may suggest that the spectroscopic constraints underestimate the effective temperature in the case of KIC 9025370.

#### 6.3.3.2 KIC 9955598

Figure 6.9 summarizes the computed model frequencies for KIC 9955598 that appears in both samples. For comparison, we have selected the 3D-calibrated UPM following different approaches. Similar best-fitting UPMs are found when fitting frequency ratios and individual frequencies from either sample.

#### 6.3.3.3 KIC 11133306

Figure 6.10 summarizes the seismic results obtained for KIC 11133306. When constructing PMs for KIC 11133306 based on the Stagger grid and either UPM, minimization of the discontinuities near the base of the patched $\langle 3D \rangle$-envelope does not lead to a unique solution, within the spectroscopic and asteroseismic constraints. On the contrary, two distinct local minima are found in the investigated region of the $(T_{\rm eff}, \log g)$-plane. We chose the $\langle 3D \rangle$-envelope, whose effective temperature lies closest to the effective temperature of the UPM. This underlines the necessity of establishing a rigid scheme for the selection of the $\langle 3D \rangle$-envelope when constructing PMs based on a given UPM.

#### 6.3.3.4 KIC 11772920

Figure 6.11 summarizes the results obtained for KIC 11772920. As for the case of KIC 11133306, the suggested minimization of discontinuities does not lead to a unique solution, in the case of the Stagger grid, for either UPM. We thus find local minima at 5043 K and at 5506 K. However, when constructing PMs, based on the colder $\langle 3D \rangle$-envelope, we obtained models that are smaller than the corresponding UPM, which is inconsistent with our other patched models. Consequently, we discard this solution and set for the warmer minimum.

## 6.4 Discussion

All in all, the obtained model frequencies are in good agreement with the qualitative conclusions drawn from the solar case: patching $\langle 3D \rangle$-envelopes reduces the model frequencies, and using different 3D envelope grids, interior models, or patching quantities leads to frequency differences between these models that are of the order of a few microhertz. These

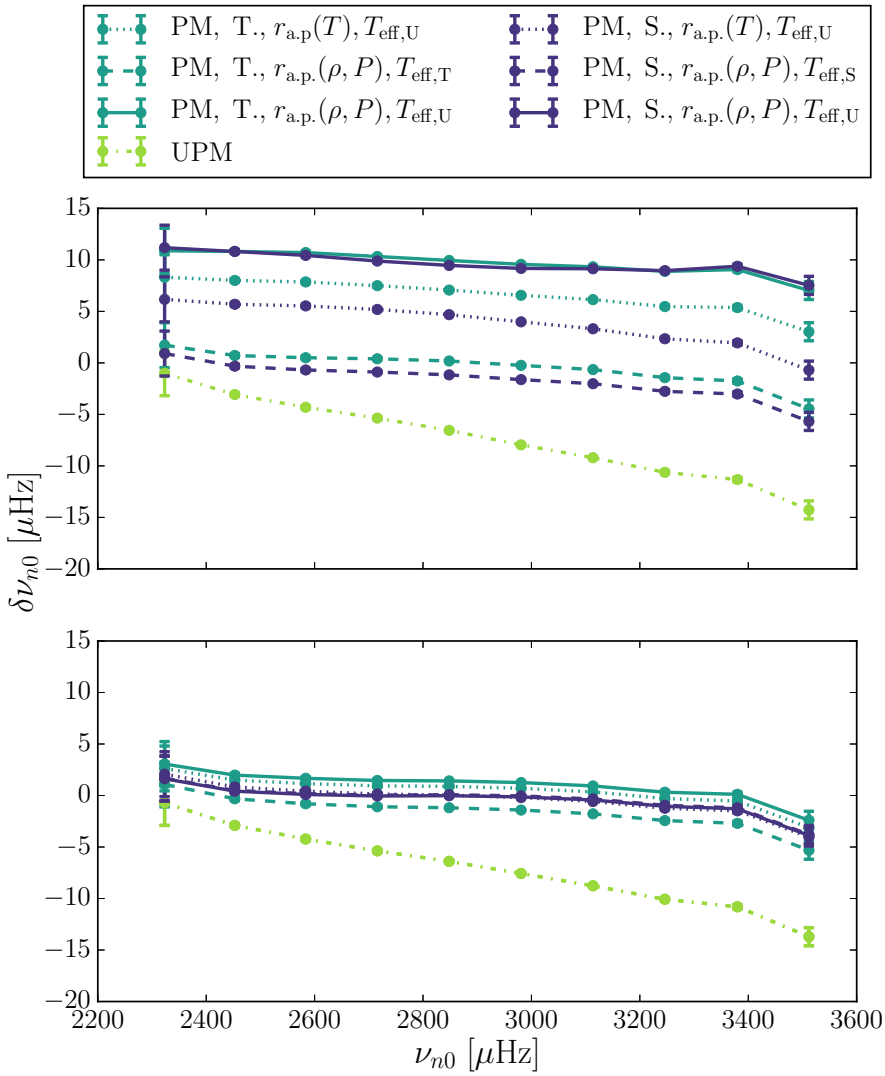


Figure 6.8: Frequency differences between observations and 2 UPM as well as 12 PMs, for KIC 9025370, based on the LEGACY frequencies. **Upper panel:** 3D-calibrated UPM. **Lower panel:** standard input UPM. The plot includes PMs, based on interpolated Trampedach-grid (T.) and Stagger-grid (S.) $\langle$3D$\rangle$-envelopes with the same $T_{\mathrm{eff}}$ ($T_{\mathrm{eff,U}}$) as the UPM, as well as PMs, based on $\langle$3D$\rangle$-envelopes with $T_{\mathrm{eff,T}}$ and $T_{\mathrm{eff,S}}$ (cf. Table 6.1). Different patching quantities are used: either $T$ or a combination of $P$ and $\rho$. In all cases, the patching points are chosen at the depth, at which the closest match in the $(P, \rho)$- or $(P, T)$-plane between the interior and the $\langle$3D$\rangle$-envelope is found. All frequencies are computed within the gas $\Gamma_1$ approximation.

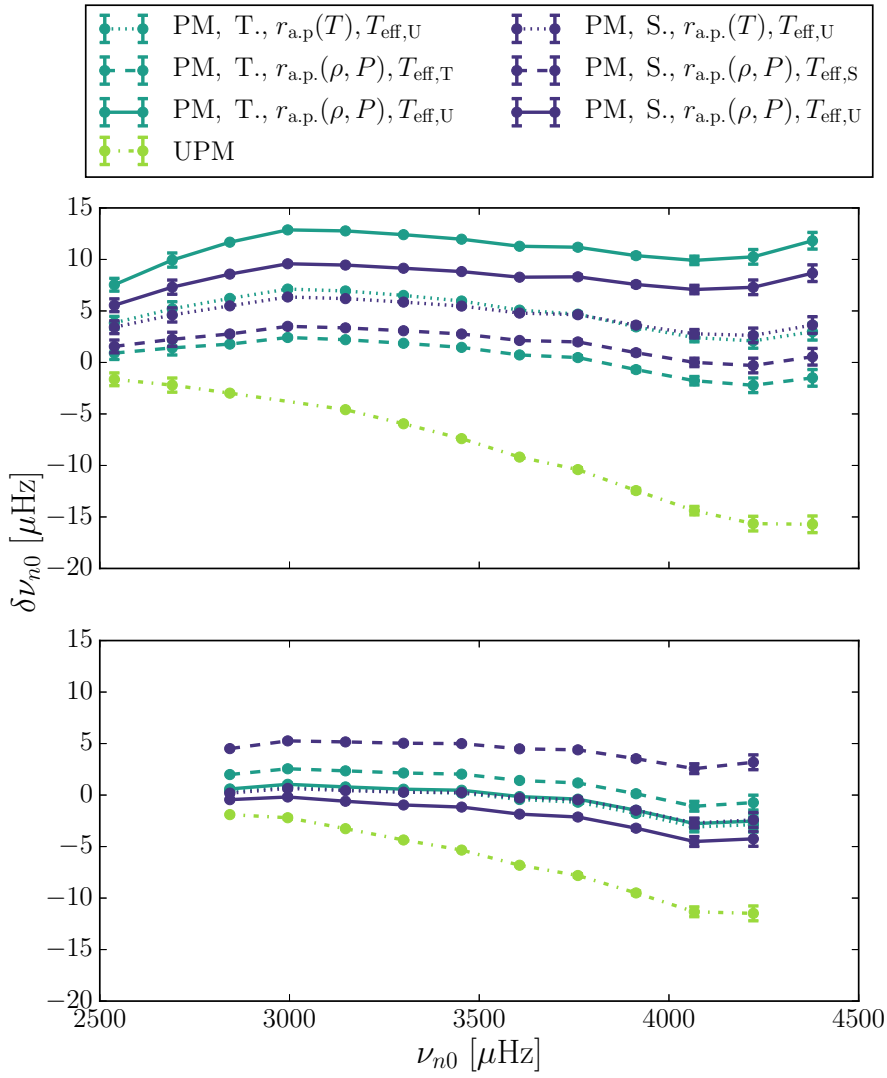


Figure 6.9: As Fig. 6.8 but for KIC 9955598. **Upper panel:** 3D-calibrated UPM, using KAGES frequencies. **Lower panel:** standard input UPM, using LEGACY frequencies. The associated effective temperatures are listed in Table 6.1.

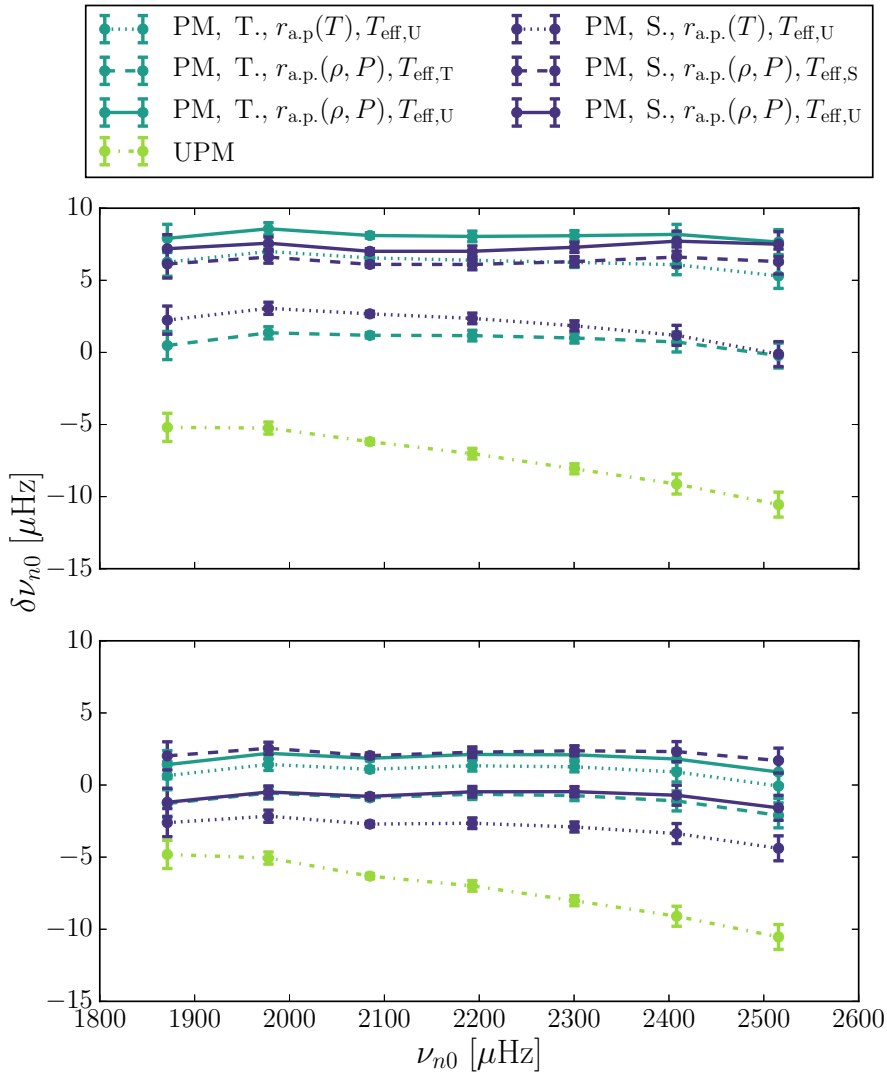


Figure 6.10: As Fig. 6.8 but for KIC 11133306, based on the KAGES sample frequencies. The associated effective temperatures are listed in Table 6.1.

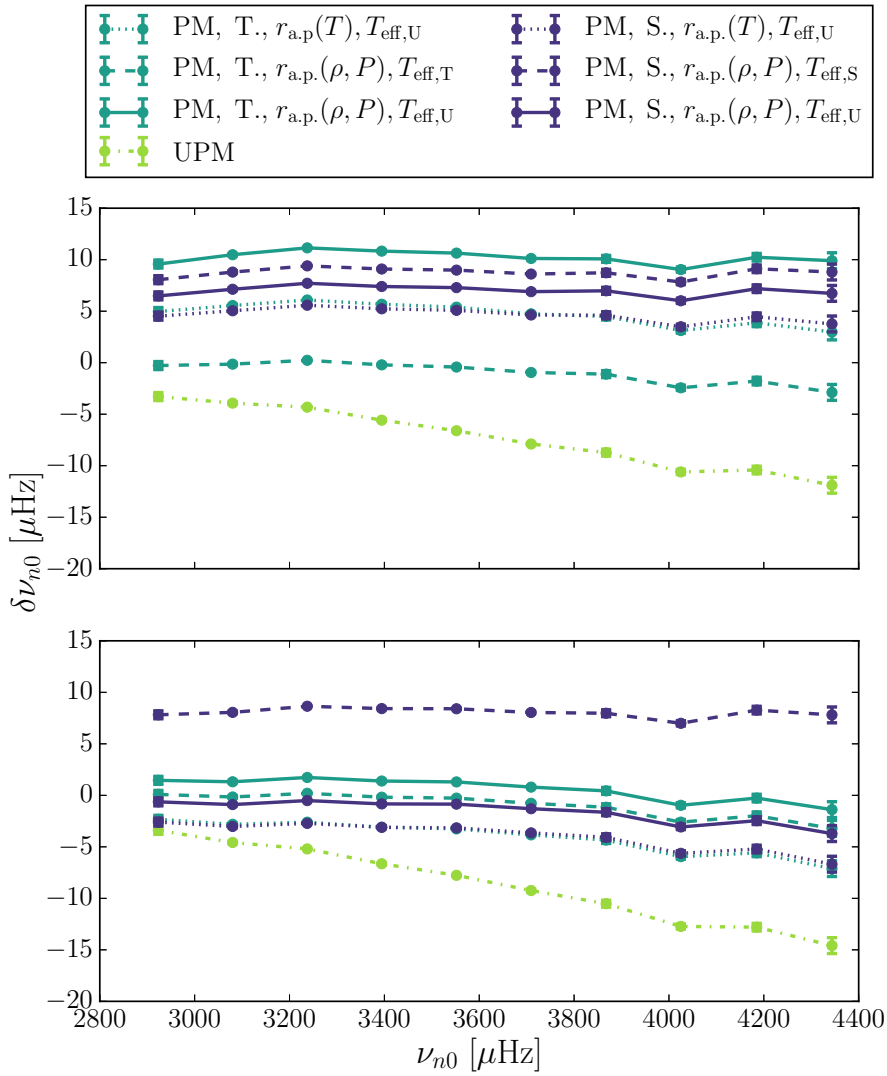


Figure 6.11: As Fig. 6.8 but for KIC 11772920, based on the LEGACY sample frequencies. The associated effective temperatures are listed in Table 6.1.

are small compared to the surface effect itself but substantial compared to the residual discrepancy between model frequencies and observations within the gas $\Gamma_1$ approximation.

While the surface effect increases with frequency for the UPMs, the discrepancies between observations and the model frequencies for all 48 PMs are not strongly frequency-dependent. Again, we emphasize that the PMs are not expected to reproduce the observations since we have not taken modal effects into account. According to Houdek et al. (2017), the neglect of modal effects is expected to lead to PMs that underestimate and hence over-correct the eigenfrequencies within the reduced $\Gamma_1$ approximation. In this connection, we note that most of the 3D-calibrated PMs do over-correct the model frequencies, while roughly half of standard input PMs do not. One may, therefore, jump to the conclusion that those PMs that already under-correct the frequencies are not expected to correctly reproduce the frequencies of the considered *Kepler* stars, once the modal effects are added. This seems to favour the 3D-calibrated models over the standard input models. However, this is not a compelling conclusion since we work within the gas $\Gamma_1$ approximation, while Houdek et al. (2017) work within the reduced $\Gamma_1$ approximation. Using the reduced $\Gamma_1$ approximation rather than the gas $\Gamma_1$ approximation is expected to further lower the model frequencies (cf. Chapters 8 and 10).

The discrepancy in effective temperature between the employed UPM and the $\langle 3D \rangle$-envelope that minimizes the discontinuities are generally found to be larger for the 3D-calibrated models (cf. Table 6.1). Just as in the solar case, such high discrepancies in the effective temperature strongly affect the evaluated surface correction. Consequently, the frequency differences between the 3D-calibrated PMs are larger than in the case of the standard input models. This may reflect discrepancies between the 3D-calibrated models and the $\langle 3D \rangle$-envelopes but may also issue from the fact that the approaches for the selection of the global parameters of the patched $\langle 3D \rangle$-envelopes are rather simplistic.

The eigenfrequencies of the 3D-calibrated models are more sensitive to the choice of the patching quantity than the standard input models are. A larger sensitivity to the choice of the patching quantity implies a larger mismatch between the patched $\langle 3D \rangle$-envelope and the structure of the UPM at the patching point, i.e. larger discontinuities. However, since the frequency shifts that are introduced by changing the patching quantity are of the order of a few microhertz, several factors may contribute to this behaviour: firstly, based on our analysis of the solar case, we conclude that the sensitivity to the choice of the patching quantity, at least partly, reflects the accuracy of the interpolation scheme. Secondly, we note that a direct comparison between the panels of Figs 6.8-6.11 is misleading since the global parameters of the 3D-calibrated models and their standard input counterparts are not the same. Indeed, for all four *Kepler* stars, the best-fitting 3D-calibrated UPM has a higher effective temperature than the associated best-fitting standard input model, and, as discussed in Section 6.1.1, the interpolation error increases with increasing effective temperature (cf. Fig. 5.6). Thirdly, a direct comparison between the panels is misleading, since the 3D-calibrated models use different equations of state, different opacity tables, and a different mixture than their standard input counterparts.

As elaborated upon in Section 6.3.1, the outermost layers of the 3D-calibrated models do not perfectly mimic the underlying 3D simulations, which contributes to the sensitivity

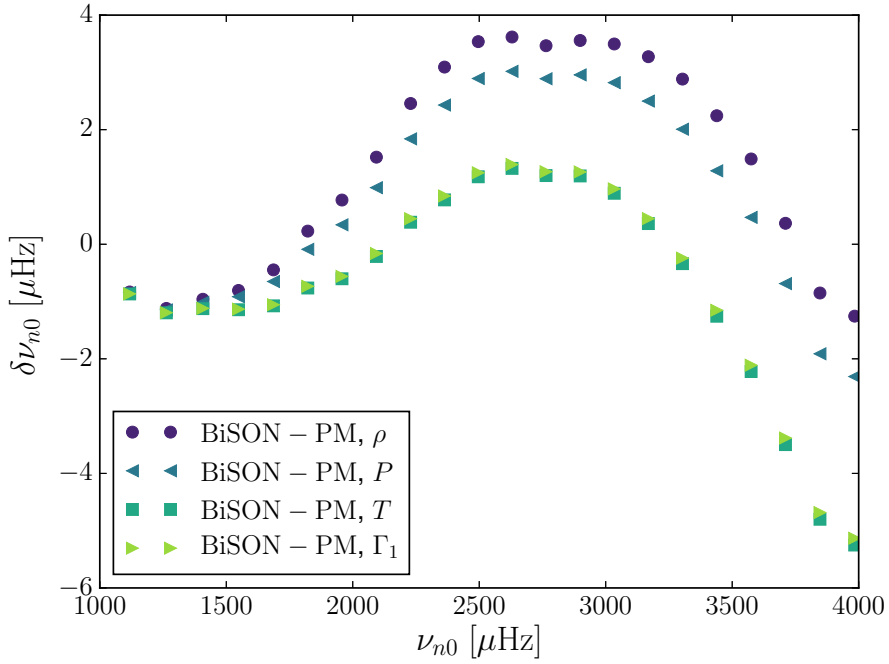


Figure 6.12: As Fig. 6.4 but for a 3D-calibrated solar model and the solar Trampedach-grid ⟨3D⟩-envelope. All models are patched 2.5 Mm below the surface. All frequencies are computed within the gas $\Gamma_1$ approximation.

to the choice of the patching quantity. In order to access, how well the implementation of the $T(\tau)$ relation and the calibrated $\alpha_{MLT}$ by Trampedach et al. (2014a,b) reproduces the structure of the Trampedach-grid ⟨3D⟩-envelopes, we present PMs, based on a 3D-calibrated solar UPM, in Fig. 6.12. The 3D-calibrated solar UPM has the same effective temperature as the solar Trampedach-grid ⟨3D⟩-envelope. Consequently, no interpolation has been performed. As can be seen from the figure, we find the choice of the patching quantity to affect the eigenfrequencies by up to 4 $\mu$Hz, i.e. by roughly the same amount, as we found for Model S when patching the same solar ⟨3D⟩-envelope (3 $\mu$Hz, cf. Section 6.2.1). This frequency difference reflects the structural change that arises from a shift in the distance of the patching point from the solar centre: $r_{\mathrm{a.p.}}(T)$ is roughly 40 km less than $r_{\mathrm{a.p.}}(P)$, as the temperature of the ⟨3D⟩-envelope is roughly 1 % higher at its base than the temperature of the UPM at the same pressure. In accordance with our study of Model S, we hence find the eigenfrequencies to be very sensitive to changes in the structure of the PM.

For comparison, we have performed yet another solar calibration with the same abundances, equation of state, opacity tables, and effective temperature as were employed for the solar model in Fig. 6.12 but with a grey Eddington atmosphere and a constant mixing length parameter along the evolution track. We find this solar model to show the same sensitivity to the patching criteria as the model in Fig. 6.12 does. Changing the boundary

conditions and the mixing length parameter merely increases the model frequencies by less than $1\,\mu$Hz for all patching quantities.

To facilitate an easy comparison between Fig. 6.12 and Figs 6.2-6.4, we have not corrected for sphericity or adjusted $\log g$ to fit the interior model, at the atmospheric patching point. Applying such corrections increases the model frequencies of the presented solar model by up to $1\,\mu$Hz.

## 6.5 Summary

Above, we present an analysis of patched stellar models (PMs), investigating several new aspects, in order to establish the necessary tools for improving theoretical predictions and for a more realistic treatment of pulsation properties in the near-surface layers of stars.

When constructing PMs, we employ the interpolation scheme presented in Chapter 5. In the present chapter, we investigate, how a mismatch between the effective temperature and gravitational acceleration of the un-patched model (UPM) and the patched mean 3D envelope ($\langle$3D$\rangle$-envelope) affects the seismic results. The fact that we consistently find even small mismatches to have a non-negligible effect on the model is rather crucial. Thus, above, we present PMs that either have the same effective temperature as the UPM or are selected in such a way as to minimize the discontinuities in several quantities, near the base of the $\langle$3D$\rangle$-envelope. Although both approaches are rather simplistic, they illustrate the importance of establishing a rigid matchmaking scheme, as the two approaches lead to different model frequencies, in several cases.

We also investigate how different patching criteria affect the seismic results, based on patched solar models. These criteria include the depth, at which the patch is performed, and the quantities, based on which the patching points are selected, and based on which the distance between the stellar centre and the lowermost point in the patched $\langle$3D$\rangle$-envelope is established. While the model frequencies are mostly unaffected by the patching depth, if the patch is performed sufficiently deep within the nearly-adiabatic region, the choice of patching quantity may shift the model frequencies by a few microhertz. These shifts are small compared to the surface effect itself but comparable to the residual discrepancy between model frequencies and observations within the gas $\Gamma_1$ approximation. Furthermore, the model frequencies are likewise sensitive to the input physics, and hence to the employed $\langle$3D$\rangle$-envelope grid.

As regards our patched solar models, the resulting model frequencies are in very good agreement with an analysis presented by Ball et al. (2016). Moreover, our results are consistent with the observed solar oscillation frequencies, considering that modal effects have not been taken into account.

Regarding the sensitivity of the model frequencies on the employed patching quantities and on the input physics, our analysis of *Kepler* stars leads to the same qualitative conclusions as in the solar case. Just as for the Sun, patching a mean $\langle$3D$\rangle$-envelope lowers the model frequencies. The remaining frequency differences between model frequencies and observations are less frequency dependent than in the case of the UPM.

Based on the presented results, we are hence able to identify several steps in the post-evolutionary patching procedure, for which different seemingly equally valid choices moderately or severely affect the outcome of asteroseismic analyses. These ambiguities in the eigenfrequencies should thus be taken into account when using post-evolutionary patching to correct for surface effects — say, in order to calibrate surface corrections relations (cf. Chapter 7). Furthermore, the sensitivity of the eigenfrequencies to the patching criteria limits the improvement that can be achieved from patching 1D stellar models.

In short, there is no unique set of patching criteria that can be claimed to be the correct choice: all the presented patching strategies are equally physically motivated. However, different patching criteria lead to different results. This is a smoking gun, pointing towards the irreconcilable physical assumptions that enter 1D and 3D simulations, exposing the inadequacies of state-of-the-art 1D stellar models. Patched models thus suffer from discontinuities that affect the seismic model predictions. Any meaningful patching strategy must attempt to minimize these discontinuities. In the next chapter, we exploit this finding turning the argument on its head: we apply several different patching strategies for each UPM and discard any PM, for which the patching criteria play a vital role for the model predictions. Following this strategy, we circumvent the prevailing discontinuities that haunt post-evolutionary patching, making the strategy in Chapter 7 a more consistent approach than following a single set of patching criteria.

As regards the UPMs, we note that the selection thereof largely depends on the employed likelihood: selecting the models based on individual frequencies or frequency ratios yield different results. Even worse, when using individual frequencies, the employed surface correction relation plays a major role, altering the stellar parameter estimates. We will address this issue further in the next chapter. Taking this into account, it is hence not straightforward to dismiss 3D-calibrated models in favour of standard input models or vice versa based on the analysis presented here. However, as discussed in Chapter 8, the 3D-calibrated models yield different stellar evolution tracks than standard input models do. This is due to the fact that 3D-calibrated models impose a slightly more realistic depiction of the outer boundary layers. Since patching solely takes place during the post-processing, patching does not alter the evolution of the UPMs but must rely on the accuracy of computed evolution tracks. Any UPM, for which the outer boundary conditions yield more realistic evolution tracks, is, therefore, preferable. In this sense, 3D-calibrated models may be assumed to be the preferred choice for UPMs.

All in all, the present chapter clearly underlines the potential of post-evolutionary patching, showing how the implementation of information from 3D hydrodynamic simulations can be used to improve 1D stellar models. Based on our patching procedure, we are thus partly able to correct for surface effects, obtaining results that are in very good agreement with qualitative expectations. The patching method presented above allows correcting for these structural inadequacies for any model within the parameter space mapped by 3D simulations. This is a novel and significant improvement compared to previous papers that have yet avoided interpolation of 3D simulations in connection with the construction of patched models.

# Chapter 7

# Parameterizations of Patched Models and the Surface Effect

*The content, including most of the text, of this chapter was published in Monthly Notices of the Royal Astronomical Society by Jørgensen et al. (2019) (see also Chapters 5 and 6 for further content from this paper). I am the first author of the paper and the primary investigator of the presented research project. I wrote this chapter. My contributions include the development, validation and application of the patching procedure and the statistical framework as well as the numerical implementation of the associated algorithms. The work was performed in collaboration with Achim Weiss, George Angelou, and Víctor Silva Aguirre. All three co-authors contributed with constructive and useful feedback.*

As discussed in Chapter 3, so-called surface correction relations, i.e. empirical or theoretical parameterizations of the surface effect, offer the possibility to deal with the surface effect in asteroseismic studies. In this chapter, we shed light on the versatility and applicability of these relations based on patched stellar models (cf. Chapter 6). Furthermore, we discuss how the structural contribution to the surface effect varies throughout the HR diagram and access the role plaid by modal effects. Our analysis hence underlines the broad potential of patched models to function as a diagnostic tool.

In Section 7.2, different parameterizations of the structural surface effect are introduced and compared based on patched models. By using a maximum likelihood estimation method, the ability of these parameterizations to recover the stellar parameters of patched models are evaluated in Section 7.3.4. In Section 7.3.5, the parameterizations are used to compute stellar parameter estimates for *Kepler* star. The obtained results are compared to those determined based on surface correction relations from the literature. Section 7.4 summarizes our conclusions.

## 7.1 The Patching Procedure

In connection with the analyses presented in this Chapter, we settle for a set of patching criteria. In contrast, we vary and compare patching criteria in Chapter 6. The patching procedure used in this chapter is, therefore, briefly summarized below.

In this chapter, we pre-select the lowermost mesh point of the interpolated ⟨3D⟩-envelopes to be the atmospheric patching points. This approach ensures that the patch is performed as deep within the nearly-adiabatic region as possible. In order to lighten the nomenclature, we simply refer to the lowermost point of the patched ⟨3D⟩-envelope as the patching point.

In Chapter 6, we frequently use combinations of different physical quantities, such as combinations of $\rho$ and $P$, as the patching quantity. In this chapter, however, we follow the simpler approach and only employ individual physical quantities as patching quantity. Considering only individual physical quantities, $T$, $\rho$, and $P$ are all suitable choices for the patching quantity. In theory, $\Gamma_1$ is also a potential patching quantity. However, in some of the present cases, it varies too slowly as a function of the distance from the stellar centre at the depth at which the patch is performed. Therefore, in practice, it is not a suitable patching quantity, contrary to the solar case (cf. Chapter 6).

Specifically, our parameterizations in Sections 7.2 and 7.3 are based on PMs that employ $\rho$ as the patching quantity. In this connection, PMs that employ either $T$ or $P$ as the patching quantity are used as diagnostic tools to reveal significant discontinuities in the patched structures and thus to discard UPMs (cf. Section 7.2.1). In Section 7.3.6, we construct PMs using all three quantities, in order to evaluate and illustrate the sensitivity of the model frequencies to the chosen patching quantity.

In this chapter, we match each UPM with a ⟨3D⟩-envelope of the same effective temperature, gravity, and metallicity. We note that other authors take the opposite approach, choosing the interior model in such a way that it matches the stratification of a given ⟨3D⟩-envelope at the patching point (e.g. Ball et al. 2016). This is due to the high computational cost of constructing 3D simulations – without an interpolation algorithm, they are limited to the existing 3D simulations.

Due to the omission of turbulent pressure and convective back-warming (cf. Trampedach et al., 2013, 2017), the superadiabatic near-surface layers predicted by stellar evolution codes are less extended than their 3D counterparts, i.e. the radius of the PMs is larger[1] than the radius of the corresponding UPMs. We define the radius of the PMs, as the distance from the stellar centre to the mesh point, at which $T = T_{\rm eff}$. Matching the UPM with a ⟨3D⟩-envelope that has the same stellar parameters, we find the difference between the radius of the PMs and the radius of the UPMs to be less than 0.45% for all 315 models that fulfil our selection criteria in Section 7.2 — here, we use $\rho$ as the patching quantity. Consequently, the effective temperature of the patched ⟨3D⟩-envelope is consistent with the Stefan-Boltzmann law within a few degrees. An alternative selection of the parameters of the patched ⟨3D⟩-envelopes is discussed in Chapter 6.

[1] Of course, e.g. large discontinuities in any quantity that enters the determination of the depth from hydrostatic equilibrium may render this statement incorrect.

The gravitational acceleration of each patched ⟨3D⟩-envelope is adjusted as a function of depth, in order to correct for the fact that $\log g$ is assumed to be constant throughout the 3D simulations. As mentioned in Section 5.2, the extent of the ⟨3D⟩-envelope is small compared to the stellar radius, and, consequently, these corrections are small.

The pressure at the deepest point of the interpolated ⟨3D⟩-envelopes is a factor of $10^{1.23}$ higher than the pressure at the density inflection. This value for the pressure at the deepest point of the interpolated ⟨3D⟩-envelope is dictated by the shallowest ⟨3D⟩-envelope that enters the interpolation[2].

## 7.2 The Surface Effect

We computed a grid of un-patched stellar structure models, using GARSTEC. These models employ MLT and Eddington grey atmospheres. For each UPM we constructed PMs with the method just described. We then computed stellar oscillation frequencies for all UPMs and PMs in the grid.

As argued by Sonoi et al. (2015), we can use the frequency difference between the UPMs and the associated PMs to derive relations for the surface correction. We note, however, that the resulting relations cannot be used in the same manner as empirical surface correction relations (e.g. Kjeldsen et al., 2008; Ball and Gizon, 2014) as we only parameterize the structural contribution, i.e. the resulting adiabatic model frequencies do not mirror observations.

As can be seen from the solar case illustrated in Fig. 6.5, the oscillation frequencies of the PMs are expected to deviate from the true stellar frequencies. The deviation is only of the order of a few microhertz — which is why Sonoi et al. (2015) use the adiabatic oscillation frequencies of PMs to approximate the surface effect. However, we note that this statement only holds true, since we use $\Gamma_1$ in the frequency calculations, omitting the corrections introduced to $\Gamma_1$ by the turbulent pressure: turbulent pressure alters the linearized expression that relates the relative thermal pressure perturbation and the density perturbation (cf. Chapter 3 or Rosenthal et al., 1999; Houdek et al., 2017). This amounts to reducing $\Gamma_1$ by the ratio of the thermal pressure to the total pressure, which leads to an additional shift in the predicted model frequencies (cf. Houdek et al., 2017; Jørgensen et al., 2018). Here, we ignore this correction. In accordance with e.g. Sonoi et al. (2015), Ball et al. (2016), Magic and Weiss (2016), and Jørgensen et al. (2017), we thus employ the gas $\Gamma_1$ approximation (cf. Chapter 3).

[2]We discard the lowermost mesh points of the Stagger-grid ⟨3D⟩-envelopes since we deem these mesh points un-physical: the superadiabatic temperature gradient increases with increasing depth. This un-physical behaviour can be explained by the closeness to the lower boundary of the simulations.

### 7.2.1 The Stellar Model Grid

We computed evolutionary tracks of un-patched stellar models with masses between $0.65\,M_\odot$ and $1.50\,M_\odot$ in steps of $\Delta M = 0.05\,M_\odot$ from the pre-main sequence[3] (pre-MS) to the red giant branch (RGB) to a $\log g$ of 3.0 or smaller. We use ten different initial compositions: these include the initial composition obtained from the underlying solar calibration as well as initial compositions that correspond to a metallicity, i.e. [Fe/H], of between -0.3 and 0.5 in steps of 0.1. We restrict ourselves to this metallicity range, as it mostly covers the parameter space that is of interest in connection with *Kepler* targets in the LEGACY and KAGES samples.

For the sake of consistency between the UPMs and the patched Stagger-grid $\langle$3D$\rangle$-envelopes, we use AGSS09. We employ the corresponding OPAL opacities (cf. Ferguson et al., 2005; Iglesias and Rogers, 1996) and use the OPAL EOS (cf. Rogers et al. 1996), extending the EOS with the EOS by Hummer and Mihalas (1988) at low temperatures. Furthermore, we use the reaction rates suggested by Adelberger et al. (2011) and the mixing length theory for convection.

The solar calibration yields a mixing length parameter ($\alpha_{\rm MLT}$) of 1.79. We use this value throughout the grid of stellar models. This is a simplifying assumption: it has been established by independent means that $\alpha_{\rm MLT}$ is not constant with regard to any of the grid parameters (cf. Trampedach et al., 2014b; Magic et al., 2015; Tayar et al., 2017). However, these studies are partly contradictory, i.e. no consensus has been reached on how to vary the mixing length parameter correctly. This being said, it appears that $\alpha_{\rm MLT}$ varies only moderately in the region of the parameter space that is of interest in our analysis (cf. Figs 4 and 5 in Trampedach et al. 2014b and Fig. 9 in Tayar et al. 2017). Thus, for our purposes, a constant mixing length parameter is a reasonable approximation. Also, although the assumption of a calibrated mixing length parameter is a simplifying approximation, it is commonly used. Adopting this assumption hence allows a point of comparison between modellers. Furthermore, the main objective of this chapter is to demonstrate the usefulness and applicability of the interpolation scheme. This is made all that more tractable by reducing the number of dimensions in our modelling.

In connection with our choice of $\alpha_{\rm MLT}$, it is worth mentioning that the structures of PMs show discontinuities at the patching point (cf. Chapter 6). This can be seen from the jumps in the residuals in Fig. 6.6: the density is used as the patching quantity, so while $\rho(r)$ is by construction a smooth function at the patching point, $P(r)$ is not. We also illustrate this in connection with our analysis of *Kepler* stars in Section 7.3.5. These discontinuities result in a sensitivity of the oscillation frequencies to the patching quantity (cf. Fig. 6.5) and reflect inconsistencies between 1D stellar models and $\langle$3D$\rangle$-envelopes — the neglect of turbulent

[3]By which we mean the hydrostatic contraction before the zero-age main sequence (ZAMS, cf. Chapter 2). Initial pre-MS models are constructed by integration of the stellar structure equations under the assumption of a constant mass-luminosity relation in the stellar interior, in order to obtain the necessary energy generation term. This assumption is consistent with a homologous contraction and is dropped as soon as the evolution proceeds. Pre-MS models typically start at luminosities between $10\,L_\odot$ and $100\,L_\odot$ and central temperatures around $10^5$ K.

pressure or convective back-warming in 1D models are examples of such inconsistencies. Since $\alpha_{\rm MLT}$ dictates the adiabat of the stellar model, these discontinuities may partly be mended by calibrating the mixing length parameter anew for each patched model (cf. Ball et al. 2016). However, ensuring smooth stratifications does not guarantee a physically meaningful structure but may rather mask the mentioned inconsistencies. Also, with our method, we aim to correct the outermost layers of stellar models with the desired interior structure rather than to adjust the interior structure to fit the ⟨3D⟩-envelope. Instead of artificially ensuring a smooth transition at the patching point, we, therefore, introduce a set of selection criteria to discard structure models that we do not deem physically reasonable. These criteria are discussed towards the end of this subsection.

The initial mass fraction of helium ($Y_{\rm i,\odot}$) and heavy elements ($Z_{\rm i,\odot}$) obtained from the mentioned solar calibration is 0.2653 and 0.0149, respectively. The corresponding model of the present Sun was used in Chapter 6 together with Model S by Christensen-Dalsgaard et al. (1996), when testing the effect of interpolation on the frequency computation (cf. Fig. 6.5). All models in this chapter include diffusion of heavy elements, and the metallicity of the patched ⟨3D⟩-envelope was chosen in such as a way as to match the metallicity of the final model.

For bulk compositions different from the Sun, we compute the initial helium mass fraction ($Y_{\rm i}$), using the following linear relation:

$$Y_{\rm i} = Y_{\rm BBN} + \frac{Y_{\rm i,\odot} - Y_{\rm BBN}}{Z_{\rm i,\odot}} Z_{\rm i}, \tag{7.1}$$

employing the solar calibration values. $Z_{\rm i}$ denotes the initial abundance of metals, and $Y_{\rm BBN}$ refers to the helium abundance resulting from the Big Bang nucleosynthesis (BBN, Cyburt et al. 2016). We have set $Y_{\rm BBN} = 0.245$ (cf. Cassisi et al. 2003). In contrast, the mass fraction of helium relative to hydrogen is kept fixed in the Stagger-grid simulations. Specifically,

$$A({\rm He}) = \log_{10}\left(\frac{n_{\rm He}}{n_{\rm H}}\right) + 12, \tag{7.2}$$

is kept constant. Here, $n_{\rm H}$ and $n_{\rm He}$ denote the number density of hydrogen and helium, respectively. The relative abundances of the metals correspond to AGSS09 but are scaled to the abundance of Fe (R. Collet, private communications). As a consequence, the helium abundance in the Stagger-grid simulations decreases with increasing metallicity, which puts the composition of the 3D simulations somewhat at odds with considerations regarding galactic chemical evolution.

Thus, while our initial helium mass fraction (cf. Eq. 7.1) is reasonable from an evolutionary perspective, it constitutes an inconsistency between the 1D models and 3D envelopes. As we aim towards modelling *Kepler* stars in Section 7.3.5, we prefer to include all relevant input physics in order to obtain realistic stellar evolution models rather than artificially mimicking the composition of the 3D simulations. The purpose of this chapter is merely to illustrate the applicability and usefulness of our interpolation scheme. While a different set of choices may likewise constitute an interesting test case, we hence restrict ourselves to cases that are relevant for the analysis of *Kepler* stars, ensuring a clean narrative.

From the evolutionary tracks, we selected 657 un-patched structure models. Due to the constraints set by theoretical evolution tracks the models are irregularly distributed in the parameter space spanned by $T_{\rm eff}$, $\log g$, and [Fe/H]. However, for each initial metallicity, we selected models that were roughly evenly distributed in the $(T_{\rm eff}, \log g)$-plane. The separations in $T_{\rm eff}$ and in $\log g$ between the models are roughly $100 - 150\,\mathrm{K}$ and $0.25\,\mathrm{dex}$, respectively.

All GARSTEC models include microscopic diffusion of H, He, Li, C, N, O, Ne, Mg, Si and Fe. Hence, the surface composition changes during the predicted evolution of a star. We note that the incorporation of the microscopic diffusion of metals may lead to an artificially high depletion of metals, especially for low-metallicity models with masses higher than the mass of the Sun. However, in this chapter, we only include models, for which $[\mathrm{Fe/H}] \geq -0.5$, hereby excluding any model, for which the abundance of heavy elements was vastly depleted.

For each of the 657 UPMs, we constructed PMs, using the density as the patching quantity. As discussed in Chapter 6, the frequencies are relatively insensitive to the patching depth, if the patch is performed sufficiently deep within the nearly-adiabatic region. In order to ensure that the patched $\langle 3\mathrm{D}\rangle$-envelope is indeed deep enough, we impose the additional criterion that the patching point must be placed deeper than the minimum in $\Gamma_1$ near the surface. This criterion leads to the omission of 25 models in the high-$g$, low-$T_{\rm eff}$ corner of the Kiel diagram — that is, main-sequence (MS) stars with $\log g = 4.5$ and $T_{\rm eff} < 5300\,\mathrm{K}$. These excluded models have masses between $0.65\,\mathrm{M}_\odot$ and $0.75\,\mathrm{M}_\odot$.

We excluded 47 additional models, for which the radius of the UPM exceeds the radius of the associated PM, since $\langle 3\mathrm{D}\rangle$-envelopes are more extended than their 1D counterparts: if the radius of the PM is smaller than the radius of the UPM, this must be associated with a large discontinuity in either $P$ or $\rho$. For all these PMs, $4.0 < \log g < 4.3$.

As shown in Chapter 6, the radius, at which the patching point is placed, is sensitive to the choice of the patching quantity. Hence, the patching quantity affects the model frequencies, as shown in Fig. 6.5. Since we investigate the structural surface effect and thus rely on the model frequencies, this ambiguity that is caused by the freedom to select any physically meaningful patching quantity is undesirable. To take this into account, we constructed two additional PMs for each of the 585 UPMs that have so far successfully passed our selection criteria, using $P$ and $T$ as the patching quantity, respectively. We then excluded 270 models, for which the choice between $P$, $T$, and $\rho$ as the patching quantity affects the model frequencies by more than $2 \times 10^{-3}\nu_{\rm max}$ unless the deviation fell below $1.0\,\mu\mathrm{Hz}$. For the Sun, $2 \times 10^{-3}\nu_{\rm max}$ would roughly correspond to twice the highest obtained deviation. The models that are hereby discarded are scattered across the Kiel diagram.

All in all, our selection criteria completely deplete certain regions of the Kiel diagram: all models with $T_{\rm eff} \gtrapprox 6000\,\mathrm{K}$ were discarded as were most cold MS stars with $\log g \approx 4.3$. Meanwhile, no PM with $\log g < 3.15$ was affected by any of our selection criteria.

It is worth to take a closer look at the models that fail to pass the last selection criterion: for some of these models, the substitution of the outermost layers by $\langle 3\mathrm{D}\rangle$-envelopes did not alter the frequencies significantly, which may suggest that the patched $\langle 3\mathrm{D}\rangle$-envelopes are too shallow in these cases. Our analysis thus calls for deeper 3D simulations — ideally,

new simulations should extend into the adiabatic layers. Furthermore, all 47 models with $R_{\rm PM} < R_{\rm UPM}$ would have fallen into this category if not previously excluded.

Alternatively, one may require a patching point deeper within the nearly-adiabatic region by excluding all models, for which $|\nabla - \nabla_{\rm ad}|$ exceeds a certain value. Also, one may exclude all models, for which the choice between $P$, $T$, and $\rho$ as the patching quantity affects the radius of the patching point by more than a certain fraction of the patching depth. In the case of the Sun, this choice, regarding the patching quantity, affects the radius of the patching point by $21-27\,$km, corresponding to roughly $2-3\,\%$ of the patching depth. However, each additional selection criterion introduces a selection bias: some regions of the Kiel diagram are more harshly depleted than others. As illustrated in Section 7.2.3, such biases will leave their mark on the parameterization of the structural surface effect. We, therefore, avoid introducing further selection criteria. In the end, 315 models passed our selection criteria. Due to microscopic diffusion, the surface metallicity of these models ranges from -0.49 and 0.45.

We emphasize that the criterion that excludes the largest number of models (270) is the requirement that the seismic results are reasonably insensitive to the choice of the patching quantity, i.e. to our patching criteria. While excluding more than half of the models in the grid may hence seem rather extravagant, it ensures the robustness of the resulting functional fits, circumventing systematics stemming from a prevailing weakness of post-evolutionary patching: discontinuities in the patched structure are, in general, unavoidable; they are a smoking gun, revealing inconsistencies between the depictions of convection in 1D models and the more realistic depiction in 3D simulations.

### 7.2.2 Parameterizations

In this chapter, we present parameterizations of the structural contribution to the surface effect. We derive these parameterizations based on the frequency difference,

$$\delta\nu = \nu_{\rm PM} - \nu_{\rm UPM}, \tag{7.3}$$

between the model frequencies of the UPM ($\nu_{\rm UPM}$) and the model frequencies of the associated PM ($\nu_{\rm PM}$). As we do not consider modal effects, there is no reason to believe that PMs encapsulate the full surface term. In fact, we see this in the solar case in Fig. 6.5, where the patched models do not perfectly reproduce the observed frequencies. In other words, the difference between model frequencies and observations is not zero at all frequencies for PMs. We investigate how well our parameterizations recovers stellar parameters of PMs and real stars in Section 7.3 in comparison with other surface correction relations.

We use the same general functional forms for the parameterizations of the structural surface effect as Sonoi et al. (2015). This includes a power-law fit to the frequency correction:

$$\frac{\delta\nu}{\nu_{\rm max}} = a \left( \frac{\nu_{\rm PM}}{\nu_{\rm max}} \right)^b . \tag{7.4}$$

We alternatively try a Lorentzian fit of the form

$$\frac{\delta\nu}{\nu_{\max}} = \alpha\left(1 - \frac{1}{1-(\nu_{\mathrm{PM}}/\nu_{\max})^{\beta}}\right). \tag{7.5}$$

In the above relations, $\nu_{\max}$ denotes the frequency of maximum power. We adopt (cf. Brown et al. 1991)

$$\nu_{\max} = \frac{g}{g_{\odot}}\left(\frac{T_{\mathrm{eff}}}{T_{\mathrm{eff}\odot}}\right)^{-1/2}\nu_{\max\odot}, \tag{7.6}$$

where $g$ and $T_{\mathrm{eff}}$ denote the gravitational acceleration and the effective temperature of the UPM, respectively. In this chapter, we set $\nu_{\max\odot} = 3090\,\mu\mathrm{Hz}$, $T_{\mathrm{eff}\odot} = 5779.57\,\mathrm{K}$, and $g_{\odot} = 4.438$ — that is $R_{\odot} = 6.95508\times10^{8}\,\mathrm{cm}$, $M_{\odot} = 1.9891\times10^{33}\,\mathrm{g}$. Finally, $a$, $b$, $\alpha$, and $\beta$ are fitting parameters.

Equation (7.4) only yields a reasonable description of the frequency difference at frequencies that are lower than or close to $\nu_{\max}$ (cf. Sonoi et al. 2015). While all frequencies are included, when determining the fitting parameters in connection with Eq. (7.5), we, therefore, only include frequencies that are lower than $1.05\nu_{\max}$ when using Eq. (7.4). We do so in accordance with Sonoi et al. (2015). Sonoi et al. (2015) note that a power law is not suitable at high frequencies but provide no further physical justification for this ad hoc upper boundary. However, we note that the fitting range plays a vital role for the obtained value of the fitting coefficients, as stated by both Kjeldsen et al. (2008) and Sonoi et al. (2015). For this reason, we stick to the same values as employed by Sonoi et al. (2015) to facilitate a straightforward comparison.

In either case, we perform the fit, using only radial modes ($\ell = 0$), in accordance with Kjeldsen et al. (2008) and Sonoi et al. (2015). We use all radial orders in the relevant frequency range.

Both Eq. (7.4) and Eq. (7.5) have two fitting parameters. These are assumed to be functions of the global stellar parameters. For all four fitting parameters we adopt power law dependencies that include four free parameters, e.g.:

$$a = A\left(\frac{T_{\mathrm{eff}}}{T_{\mathrm{eff}\odot}}\right)^{B}\left(\frac{g}{g_{\odot}}\right)^{C}\left(\frac{Z_{\mathrm{S}}/X_{\mathrm{S}}}{Z_{\odot,\mathrm{S}}/X_{\odot,\mathrm{S}}}\right)^{D}. \tag{7.7}$$

Again, all values are taken from the respective UPM. Equation (7.7) only deviates from the assumed functional dependence adopted by Sonoi et al. (2015) by the dependence on $Z_{\mathrm{S}}/X_{\mathrm{S}}$, i.e. on [Fe/H], since we consider models with non-solar metallicities.

We note that Kjeldsen et al. (2008) suggest a power-law correction, i.e. a relation on the form of Eq. (7.4), using a different definition of the coefficients, $a$ and $b$. We will state this definition of $a$ and $b$ in Section 7.3, where we include a comparison to Kjeldsen et al. (2008). In this section, however, all coefficients in Eq. (7.4) and Eq. (7.5) ($a$, $b$, $\alpha$, and $\beta$) are defined equivalently to $a$ in Eq. (7.7).

It follows from the above that a fit of $\delta\nu$ to either Eq. (7.4) or Eq. (7.5) in a parameter space spanned by $T_{\mathrm{eff}}$, $\log g$, [Fe/H], and $\nu/\nu_{\max}$ includes eight free parameters. In this

Table 7.1: Fitting parameters based on a global fit to all 315 PMs that fulfilled our selection criteria stated in Section 7.2.1. Each fitting parameter ($a$, $b$, $\alpha$, and $\beta$) in Eq. (7.4) and Eq. (7.5) is itself composed of four fitting parameters ($A$, $B$, $C$, and $D$) as given by Eq. (7.7). The uncertainties denote the square root of the diagonal of the variance-covariance matrix. We have performed the fit, using only radial modes ($\ell = 0$). The fits were established using a nonlinear least squares method.

| | A | B | C | D |
|---|---|---|---|---|
| $a$ | $(-2.259 \pm 0.050) \times 10^{-3}$ | $2.808 \pm 0.180$ | $(-7.189 \pm 0.089) \times 10^{-1}$ | $(2.513 \pm 0.127) \times 10^{-1}$ |
| $b$ | $4.517 \pm 0.175$ | $-1.290 \pm 0.308$ | $(2.020 \pm 0.151) \times 10^{-1}$ | $(-1.504 \pm 0.214) \times 10^{-1}$ |
| $\alpha$ | $(-3.949 \pm 0.035) \times 10^{-3}$ | $2.659 \pm 0.071$ | $(-6.888 \pm 0.035) \times 10^{-1}$ | $(2.633 \pm 0.052) \times 10^{-1}$ |
| $\beta$ | $5.530 \pm 0.153$ | $-1.445 \pm 0.217$ | $(2.271 \pm 0.106) \times 10^{-1}$ | $(-1.334 \pm 0.153) \times 10^{-1}$ |

chapter, we perform global fits to the entire grid presented in Section 7.2.1, constraining all eight parameters simultaneously. The advantage of performing such a global fit is that this approach allows for a robust determination of the uncertainties on the predicted frequency corrections based on the variance-covariance matrix ($\mathtt{C}$) obtained from the fit: for a fixed scaled frequency ($\nu_k/\nu_{\max}$), the associated frequency shift ($\delta\nu_k/\nu_{\max}$) is a function ($f$) of eight free parameters ($\xi_1, ..., \xi_8$) given by either Eq. (7.4) or Eq. (7.5) in combination with the equations for $a$, $b$, $\alpha$, and $\beta$ of the form of Eq. (7.7), which provides the Jacobian $\boldsymbol{J}$. The variance ($\sigma_k^2$) of $\delta\nu_k/\nu_{\max}$ is hence

$$\sigma_k^2 = \boldsymbol{J}\mathtt{C}\boldsymbol{J}^{\mathrm{T}}, \quad \boldsymbol{J} = [\partial f/\partial\xi_1, ..., \partial f/\partial\xi_8]\,. \tag{7.8}$$

The results of our global fit including all 315 PMs and their associated UPMs are summarized in Table 7.1. How well the Lorentzian fit reproduces the correct frequency shift throughout the Kiel diagram is furthermore illustrated in Fig. 7.1.

As can be seen from Fig. 7.1, the fit does not perform equally well throughout the parameter space. While the varying accuracy of an imperfect fit is not surprising, it is worth taking a closer look at this, since it suggests that the surface corrections by Kjeldsen et al. (2008) and Sonoi et al. (2015) are subject to a selection bias: after all, the relation by Kjeldsen et al. (2008) is calibrated based on the Sun only, and the relation by Sonoi et al. (2015) is based on ten PMs, for which $T_{\mathrm{eff}}$ is predominantly larger than 6000 K.

If the fit is performed based on a subsample, excluding further models from the grid, we obtain different fitting parameters. Concretely, if we exclude, say, all red giant branch (RGB) stars before evaluating the fitting parameters, we obtain a fit that performs better for MS stars and worse for RGB stars. The ramifications of this sensitivity to the subsample selection are illustrated in the next subsection, where we reconstruct the present-day Sun.

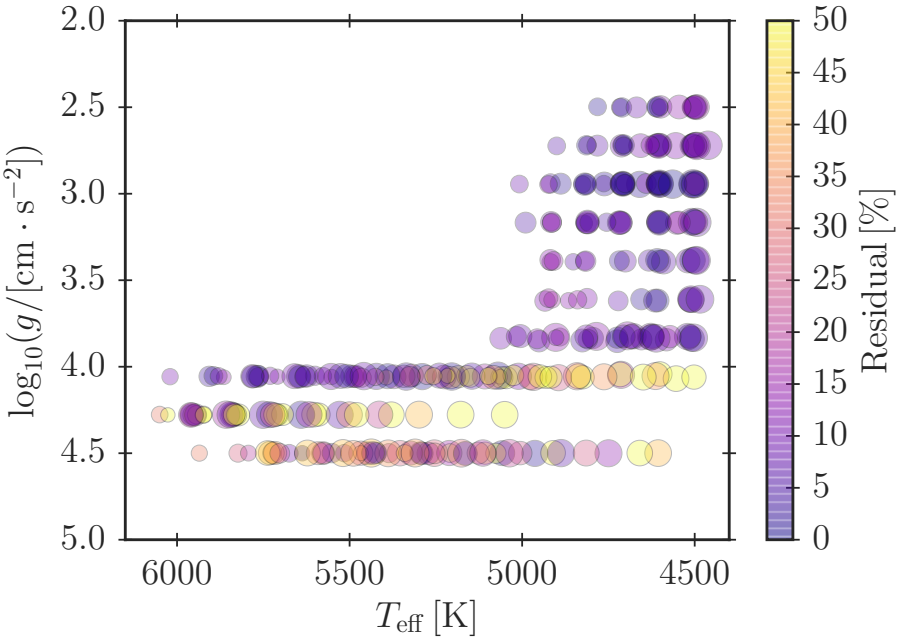


Figure 7.1: Residuals for the reconstruction of $\delta\nu$ relative to the actual value of $\delta\nu = \nu_{\mathrm{PM}} - \nu_{\mathrm{UPM}}$ for the Lorentzian fit, i.e. Eq. (7.5), summarized in Table 7.1. The residuals are computed at $1.3\nu_{\mathrm{max}}$ — for the Lorentzian fit, this lies within the covered frequency range. Residuals that exceed 50 % are indicated by the same color: the highest obtained error is 317 %. The larger the marker size is, the larger the metallicity is.

### 7.2.3 Reconstructing the Sun

As a validation for our global fit, we determine how well the parameterization mimics the frequency difference between the UPM and the associated PM for the present Sun. The solar calibration model of the present Sun, based on which we computed the evolution paths that enter the grid, is itself not in the sample of structure models used to evaluate the fitting parameters. This makes it a suitable test case.

We have used the fit summarized in Table 7.1 to predict the frequency difference, employing the solar effective temperature, metallicity and gravitational acceleration. A comparison to the actual frequency difference between the UPM and the PM is shown in Fig. 7.2. Both fits lead to residuals of $\lessapprox 2\,\mu$Hz within the relevant frequency ranges: the power-law fit is expected to work well up to $\nu_{\max}$, while the Lorentzian fit performs well up to the acoustic cut-off frequency, i.e. the highest p-mode frequency[4]. Thus, both fits perform rather well, encapsulating most of the structural surface effect — however, we note that the residuals are still much larger than the typical uncertainties of the observed frequencies.

As shown by Sonoi et al. (2015), a Lorentzian fit that is derived directly from the solar model yields smaller residuals than the global fit presented in Fig. 7.2. Based on this notion combined with Fig. 7.1, one may suspect a fit to a sample of solar-like dwarfs to perform better when inferring the solar surface effect. Indeed, when recomputing the fit based on different subsamples of the grid and subsequently examining the solar case, a more detailed picture emerges: the performance of the fit depends on the subsample. This is illustrated in Fig. 7.3 and Fig. 7.4.

Besides using all 315 models to compute fitting coefficients, we have looked at the following subsamples:

1. 45 models for which $5500\,\mathrm{K} < T_{\mathrm{eff}} < 5800\,\mathrm{K}$ and $\log g > 4.0$. There are no restrictions on [Fe/H]. We refer to this sample as *solar-like* stars.

2. 163 models for which $\log g > 4.0$. There are no restrictions on $T_{\mathrm{eff}}$ and [Fe/H]. We refer to this sample as *MS* stars.

3. 56 models for which $-0.05 < [\mathrm{Fe/H}] < 0.05$. There are no restrictions on $T_{\mathrm{eff}}$ and $\log g$.

4. 152 models for which $\log g < 4.0$. There are no restrictions on $T_{\mathrm{eff}}$ and [Fe/H]. We refer to this sample as *RGB* stars.

Given the criteria above, some models enter several subsamples.

Figures 7.3 and 7.4 include the uncertainties on the predicted frequency difference inferred from the fitting procedure, showing that the different fits are incompatible — in

[4]Accoutic waves with frequencies that exceed the so-called cut-off frequency are not trapped in the stellar interior, i.e. they are not reflected near the stellar surface and are free to propagate into the chromosphere (e.g. Fossat et al., 1992; Christensen-Dalsgaard, 2003; Jiménez et al., 2011). The acoustic cut-off frequency of the Sun is roughly $5000\,\mu$Hz.

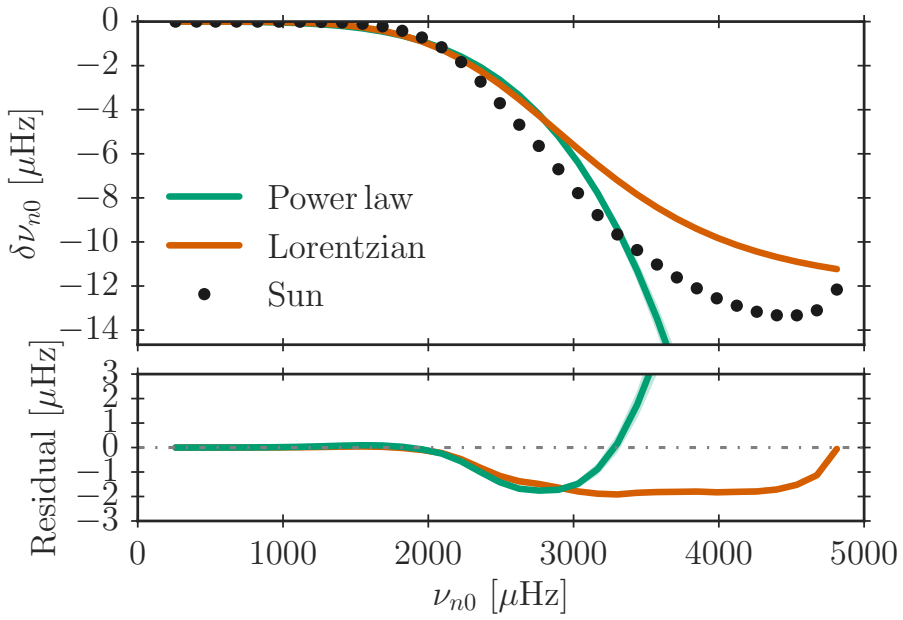


Figure 7.2: Reconstruction of the frequency difference between the solar calibration model and the associated PM, using the power-law and Lorentzian fit, i.e. Eqs (7.4) and (7.5), respectively. The fits have been evaluated based on all successful PMs in the grid (cf. Table 7.1). The actual frequency difference between the UPM and the PM are labeled "Sun" and marked with circles. The power-law fit is based on low frequencies only ($< 1.05 \times 3090\,\mu$Hz). The models, based on which the fits were derived, do not include a model of the present-day Sun, making a solar model the ideal test case.

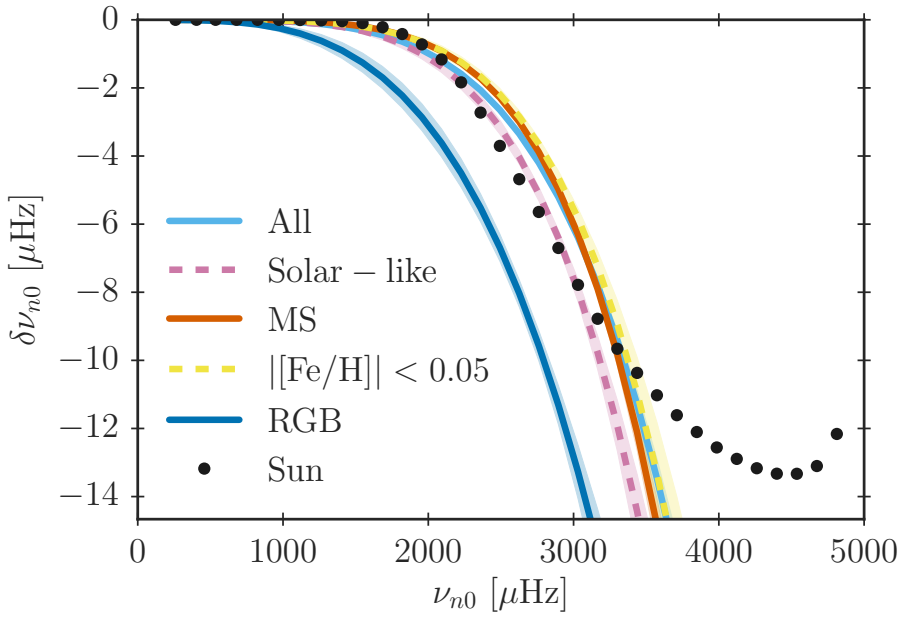


Figure 7.3: Reconstruction of the frequency difference between the solar calibration model and the associated PM, using power-law fits to different subsamples of the grid. Details are specified in the text and in the caption of Fig. 7.2.

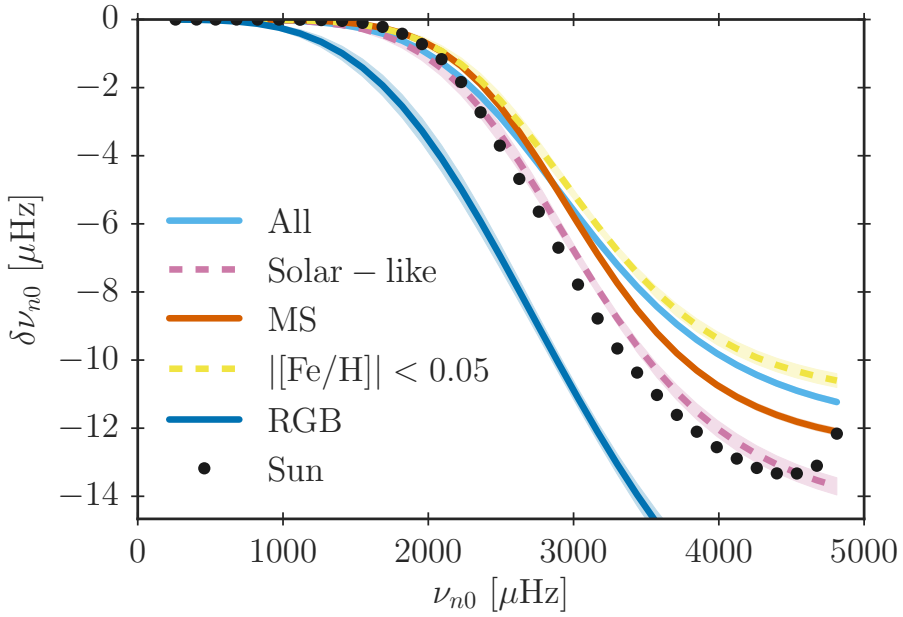


Figure 7.4: Same as Fig. 7.3 but for a Lorentzian parameterization.

some cases, the line width is broader than the inferred uncertainties. According to Figs 7.3 and 7.4, the best fit is obtained, when the models in the sample closely match the target: the residuals become significantly lower when we restrict ourselves to the 45 "solar-like" stars. The fact that different subsamples lead to different reconstructions of the solar case implies that a unique set of coefficients that applies to all evolutionary stages is not realizable with the presented parameterizations. Also, it implies that previous studies, such as the inference of a surface correction relation by Sonoi et al. (2015), is subject to a selection bias: in the mentioned case, the authors have selected ten PMs predominantly with $T_{\rm eff} > 6000\,\mathrm{K}$.

For the computation of the fitting coefficients, we have used interpolated $\langle 3\mathrm{D}\rangle$-envelopes, since additional PMs add information to the analysis due to the unique interior structure of the associated UPMs. Had we used only the original Stagger-grid simulations, we would have been limited by the small sample size. The lower number of PMs would impose restrictions on the subsample selection and affect the robustness of the inferred fitting coefficients. Furthermore, the distribution of simulations within the Stagger grid would introduce a selection bias. Interpolation gives us control over this selection bias.

## 7.3 Best-Fitting Models

As shown in Section 7.2, our Lorentzian parameterization reliably encodes the structural surface effect, if the fit is based on models, whose global parameters resemble those of the target PM. In this section, we further investigate this statement and the versatility of our Lorentzian parameterization. We do this in a hare and hound exercise, that is to say, that we attempt to recover the global parameters of PMs through a grid search using our Lorentzian parameterization.

Towards the end of this section, we take a closer look at two *Kepler* stars and evaluate the associated stellar parameters by employing our Lorentzian parameterization. This allows us to discuss the extent, to which parameterizations of the structural surface effect can be used to characterize stars, and hence allows us to investigate the limitations of such parameterizations. In other words, using this approach allows us to discuss what ramifications such parameterizations have for the stellar parameter estimates. We do so based on a comparison with surface correction relations by other authors, such as Ball and Gizon (2014). At the same time, this also allows us to shed light on the applicability and versatility of the other surface correction relations, to which we compare. This is of interest since the consulted surface correction relations are commonly used in the literature.

### 7.3.1 Maximum Likelihood Estimation

Having established a parameterization of the structural surface effect and the associated constraints on the applicability hereof (cf. Section 7.2), we can use this parameterization to evaluate stellar parameters based on a grid search, by comparing the corrected model frequencies with observations. We do this by using maximum likelihood estimation (MLE).

For this purpose, we construct a denser grid of un-patched stellar models and attribute a likelihood,

$$\mathcal{L} = \mathcal{L}_{\rm seis}\mathcal{L}_{\rm spec}, \tag{7.9}$$

to each model in the grid. The details of the grid are summarized in Section 7.3.2. In Eq. (7.9), $\mathcal{L}_{\rm seis}$ denotes the seismic contribution to the likelihood. For simplicity, we assume that the observed frequencies, as well as the model frequencies, are uncorrelated and that the observational noise is Gaussian. While we note that all three assumption are only approximately valid, we also note that at least the latter is commonly used (e.g. Silva Aguirre et al., 2015; Nsamba et al., 2018a). The seismic contribution to the likelihood is hence

$$\mathcal{L}_{\rm seis} = \prod_i^N \frac{1}{\sqrt{2\pi\sigma_i^2}} \exp\left(-\frac{(\nu_{{\rm corr},i} - \nu_{{\rm obs},i})^2}{2\sigma_i^2}\right). \tag{7.10}$$

Here, $\nu_{{\rm corr},i}$ is the $i$th corrected model frequency of the UPM, for which we determine the likelihood. There are $N$ observed frequencies. In the following, we use Eq. (7.5), i.e. our Lorentzian correction, employing fitting parameters that were determined based on an appropriate subregion of the Kiel diagram. The subregion was determined using the grid presented in Section 7.2 — that is, the models from Section 7.2 that enter the fit span the same region of the parameter space as the denser grid presented in Section 7.3.2 does. We elaborate upon this in Section 7.3.2.

In order to be consistent with the derivation of the frequency correction relation, i.e. our parameterization of the structural surface effect, we only include radial frequencies ($\ell = 0$) in our analysis (cf. Section 7.2.2). For comparison, we additionally repeat the analysis using the surface correction relations by Kjeldsen et al. (2008), Ball and Gizon (2014), and Sonoi et al. (2015).

In Eq. (7.10), each of the $N$ observed frequencies ($\nu_{{\rm obs},i}$) is compared to the corresponding corrected model frequency — the number $N$ is determined by the number of observed radial modes and will hence be fixed for a given star. We allow for the radial order of the model frequencies to deviate from observations by up to 2, since the radial orders of the observed frequencies may be incorrectly assigned. We choose the attribution of the radial order that leads to the lowest frequency deviation for the lowest frequency. Finally, in Eq. (7.10), $\sigma_i$ denotes the uncertainty of the frequency difference. We note that this is not simply the uncertainty of the observed frequency since the corrected frequencies are themselves a function of the observed frequencies. In order to take this into account, we use Eq. (7.8). As we assume the observations to be uncorrelated and the associated uncertainties to be Gaussian, Eq. (7.8) reduces to the absolute value of the derivative of $\nu_{{\rm obs},i} - \nu_{{\rm corr},i}$ with respect to $\nu_{{\rm obs},i}$ times the uncertainty on $\nu_{{\rm obs},i}$. We consistently ignore the uncertainties on the fitting parameters here, since these are not available for all surface corrections, i.e. we do so, in order to treat all corrections on equal footings.

When computing the likelihood, we also take spectroscopic constraints on the effective temperature and the metallicity into account. Again, we assume the uncertainties to be

Gaussian:

$$\mathcal{L}_{\rm spec} = \frac{1}{2\pi\sigma_T\sigma_{\rm [Fe/H]}} \exp\left(-\frac{\Delta T_{\rm eff}^2}{2\sigma_T^2} - \frac{\Delta[{\rm Fe/H}]^2}{2\sigma_{\rm [Fe/H]}^2}\right). \tag{7.11}$$

Here $\sigma_T$ and $\sigma_{\rm [Fe/H]}$ denote the standard deviation of the spectroscopically deduced effective temperature and metallicity, respectively. $\Delta T_{\rm eff}$ and $\Delta$[Fe/H] denote the difference between the observationally constrained value and the model prediction for each of the two quantities.

Out of convenience, we work with the natural logarithm of the likelihood, when performing calculations. More specifically, we work with the averaged log-likelihood:

$$\langle \ln \mathcal{L} \rangle = \frac{1}{N+2} \ln \mathcal{L}, \tag{7.12}$$

for our $N$ frequencies and two spectroscopic observables. The stellar model that maximizes the quantity in Eq. (7.12) is considered the best-fitting model in the grid.

In order to ascribe a measure for the goodness of fit, we provide $\chi^2$ of the best-fitting model:

$$\chi^2 = \frac{1}{N+2}\left(\sum_i^N \frac{(\nu_{{\rm corr},i} - \nu_{{\rm obs},i})^2}{\sigma_i^2} + \frac{\Delta T_{\rm eff}^2}{\sigma_T^2} + \frac{\Delta[{\rm Fe/H}]^2}{\sigma_{\rm [Fe/H]}^2}\right). \tag{7.13}$$

The parameter values of the best-fitting model do not on their own encode comprehensive information about the likelihood function. We hence likewise provide the weighted mean and the weighted variance of each parameter: having $K$ stellar models in the grid, the weighted mean of a parameters $\beta$ is:

$$\langle \beta \rangle = \frac{\sum_k^K \beta_k \langle \mathcal{L}_k \rangle}{\sum_k^K \langle \mathcal{L}_k \rangle}. \tag{7.14}$$

Here, $\langle \mathcal{L}_k \rangle$ is the exponential of the quantity in Eq. (7.12) for the $k$th model. Equivalently, the weighted variance is

$$\left(\sigma_\beta^{\rm mod}\right)^2 = \frac{\sum_k^K (\beta_k - \langle \beta \rangle)^2 \langle \mathcal{L}_k \rangle}{\sum_k^K \langle \mathcal{L}_k \rangle}. \tag{7.15}$$

A weighted mean that deviates from the parameter value of the best-fitting model and a large variance imply a likelihood function that deviates from a single narrow peak.

### 7.3.2 The Stellar Model Grid

While a few hundred models are sufficient for the purpose of robustly establishing the parameterizations in Section 7.2, a higher sampling of the parameter space is needed when evaluating stellar parameters based on a grid search. Using the same input physics as in Section 7.2.1, we, therefore, computed a new grid with a higher sampling rate: we computed 4,007 stellar evolution tracks with masses between $0.8\,{\rm M}_\odot$ and $1.3\,{\rm M}_\odot$ in steps of $0.01\,{\rm M}_\odot$. This includes tracks with the same composition as the underlying solar calibration as well as initial compositions on the pre-MS that correspond to a metallicity between [Fe/H] $= -0.20$

Table 7.2: Pendant to Table 7.1, containing fitting parameters based on a global fit to 73 PMs in our target region.

| | A | B | C | D |
|---|---|---|---|---|
| $\alpha$ | $(-1.644 \pm 0.029) \times 10^{-3}$ | $8.507 \pm 0.181$ | $-1.825 \pm 0.025$ | $(8.154 \pm 0.1.132) \times 10^{-1}$ |
| $\beta$ | $(1.839 \pm 0.129)^1$ | $-7.056 \pm 0.665$ | $1.616 \pm 0.094$ | $(-7.966 \pm 0.432) \times 10^{-1}$ |

and 0.55 in steps of 0.01. Due to microscopic diffusion, the metallicity decrease with age and can hence be lower than the listed initial values. We note that the high mass stars will be more efficient at draining metals from their photosphere, which implies that the sampling in metallicity depends on the other global parameters: as discussed in Section 7.2.1, the depletion may be artificially high at higher masses. For our current analysis, however, this is of no concern, since the Sun and the investigated stars all have masses below $1.2\,\mathrm{M}_\odot$.

From this set of evolution tracks, we selected a dense grid of stellar structure models. Since we have already dealt with the solar case, we investigate a different region of the Kiel diagram. Applying the same selection criteria as listed in Section 7.2.1 but demanding at least two model frequencies to be evaluated above $500\,\mu$Hz, we selected 150,719 un-patched models with effective temperatures between 5255 K and 6120 K, $\log g$ between 3.78 and 4.30 and metallicities between -0.42 and 0.47. Due to the constraints set by theoretical evolution tracks the models are irregularly distributed in the parameter space spanned by $T_{\mathrm{eff}}$,$\log g$, and [Fe/H]. Radial frequencies below $500\,\mu$Hz are ignored.

We have derived the coefficients for our Lorentzian parameterization (cf. Eq. 7.5) based on an equivalent region of the Kiel diagram: the parameterization is hence determined using 73 models from the grid presented in Section 7.2.1, for which $T_{\mathrm{eff}}$, $\log g$, and [Fe/H] lie in the intervals $[5257\,\mathrm{K}, 6050\,\mathrm{K}]$, $[4.05, 4.28]$, and $[-0.49, 0.38]$, respectively. The coefficients are summarized in Table 7.2.

### 7.3.3 Comparisons

We evaluate the best-fitting models in our grid using the MLE procedure based on a Lorentzian fit to PMs in the relevant region of the Kiel diagram as described above. For comparison, we repeat the evaluation of the best-fitting stellar parameters, employing surface correction relations by other authors. We briefly elaborate on these below.

Kjeldsen et al. (2008) suggest Eq. (7.4), i.e. a fit to a power law, as the functional form of the surface correction, setting $b = 4.90$ and

$$a = \frac{\langle \nu_{\mathrm{obs},i} \rangle - s \langle \nu_i \rangle}{N^{-1} \sum_{i=1}^{N} \left[ \nu_{\mathrm{obs},i} / \nu_{\mathrm{max}} \right]}. \tag{7.16}$$

Here, $s = 1$, $\nu_{\mathrm{obs},i}$ denotes the $i$th observed frequency, and $\nu_i$ denotes the corresponding model frequency. In the following, we refer to the surface correction relation by Kjeldsen

et al. (2008) as K08. The power-law index, $b$, in K08 is calibrated based on the present-day Sun.

Sonoi et al. (2015) suggest to use a surface correction with the functional form given by Eq. (7.5), i.e. a Lorentzian fit. The parameters $\alpha$ and $\beta$ are based on ten PMs and do not include a dependence on metallicity:

$$\log|\alpha| = -7.69\log T_{\rm eff} - 0.629\log g - 28.5, \tag{7.17}$$

and $\alpha$ is negative, while

$$\log\beta = -3.86\log T_{\rm eff} + 0.235\log g + 14.2. \tag{7.18}$$

We refer to this surface correction as S15. In principle, a comparison between the results obtained, when using our own surface correction relation, i.e. our Lorentzian parameterization, and those obtained, when using S15, allows for a discussion on the importance of the inclusion of metallicity. However, any disagreement between the results obtained from S15 and our parameterization may mainly reflect the selection bias.

Rather than computing coefficients for an assumed functional form using PMs or solar observations, Ball and Gizon (2014) present a surface correction relation that has been deduced from the variational principle by Gough (1990) based on physical considerations:

$$\frac{\delta\nu_i}{\nu_{\rm ac}} = \mathcal{I}^{-1}\left(a_{-1}\frac{\nu_{\rm ac}}{\nu} + a_3\frac{\nu^3}{\nu_{\rm ac}^3}\right). \tag{7.19}$$

Here, $\mathcal{I}$ is the mode inertia (cf. Christensen-Dalsgaard, 2008a; Aerts et al., 2010), while $\nu_{\rm ac}$ denotes the acoustic cutoff frequency:

$$\frac{\nu_{\rm ac}}{\nu_{\rm ac\odot}} = \frac{\nu_{\rm max}}{\nu_{\rm max\odot}}, \tag{7.20}$$

where we set $\nu_{\rm ac\odot} = 5000\,\mu$Hz in accordance with Ball and Gizon (2014). We will refer to this surface correction relation as B&G.

The coefficients $a_{-1}$ and $a_3$ are given by

$$\begin{pmatrix} a_{-1} \\ a_3 \end{pmatrix} = (\mathtt{X}^{\rm T}\mathtt{X})^{-1}\mathtt{X}^{\rm T}\mathbf{y}, \tag{7.21}$$

where $\mathbf{y}$ denotes the frequency difference between the observed frequencies and the model frequencies in units of the uncertainty of the observed frequencies ($\sigma_i^{\rm obs}$):

$$y_i = \frac{\nu_{{\rm obs},i} - \nu_i}{\sigma_i^{\rm obs}}. \tag{7.22}$$

The matrix $\mathtt{X}$ is a combination of model frequencies and the associated mode inertias

$$X_{i,1} = \frac{\nu_{\rm ac}^2\nu_i^{-1}}{\mathcal{I}_i\sigma_i^{\rm obs}}, \quad X_{i,2} = \frac{\nu_{\rm ac}^{-2}\nu_i^3}{\mathcal{I}_i\sigma_i^{\rm obs}}. \tag{7.23}$$

Our surface correction relation, i.e. our parameterization of the structural surface effect, was inferred from PMs without taking modal effects into account. Assuming that the asymptotic analysis that underlies B&G includes all relevant contributions, Eq. (7.19) is not subject to this inadequacy. Hence, a comparison between the results obtained when using our surface correction relation, and those obtained when using Eq. (7.19), can be used to determine how the neglect of modal effects alters the determination of model parameters. To a certain extent, this also holds true for the comparison with K08.

Since both K08 and B&G rely on the observed frequencies in order to determine the coefficients for the surface correction relations, these two surface correction relations have limited predictive power in comparison to our parameterization of the structural contribution of the surface effect or to the one by Sonoi et al. (2015). The fact that both Kjeldsen et al. (2008) and Ball and Gizon (2014) adjust the fitting coefficients according to data also implies that a comparison with our surface correction or S15 does not take place on equal footings. In order to investigate the ramifications hereof, we have repeated the evaluation of the best-fitting model based on B&G fixing the coefficients to the values obtained for our solar calibration model: $a_{-1} = 4.27 \times 10^{-12}$ and $a_3 = -6.93 \times 10^{-11}$. In this evaluation of the coefficients, we have used observed BiSON frequencies. We refer to the use of the solar values for the coefficients as "case b", while we refer to the use of Eq. (7.21) as "case a".

We note that the incorrect modelling of the surface layers results in wrong boundary conditions for solving the stellar structure equations throughout the predicted evolution. This leads to systematic errors in the associated stellar parameters, which none of the surface correction relations takes into account. We refer to Chapters 8-10 for a discussion on how the implementation of information from 3D simulations into 1D models alters the evolution tracks.

Furthermore, we recall that we restrict ourselves to radial modes ($\ell = 0$) in all cases, in order to facilitate a meaningful comparison between all surface corrections.

### 7.3.4 Hare and Hound Exercise

In order to evaluate the performance of our Lorentzian surface correction relation across the parameter space, we test how well the relation is able to recover the stellar parameters of PMs. For comparison, we have repeated the same hare and hound exercise, using K08, S15 and B&G, cases a and b.

Since the frequencies and global parameters of the PMs have no intrinsic uncertainties as such, we have attributed artificial uncertainties to mimic observational constraints. Hence, we assume the uncertainty on the effective temperature and metallicity to be 100 K and 0.1 dex, respectively. An uncertainty of 0.3 $\mu$Hz has been attributed to all frequencies. For comparison, the symmetric errors on the radial modes vary between 0.07 $\mu$Hz and 1.36 $\mu$Hz, for the two *Kepler* stars presented in Section 7.3.5. While the chosen value is hence certainly not unreasonable, we note that the use of constant uncertainties is a simplifying approximation: for instance, the uncertainty will tend to reflect the mode amplitude.

We have performed five hare and hound exercises. We have chosen models with $T_{\rm eff}$ between 5600 K and 5900 K and mostly with low metallicities. The reason for this selection

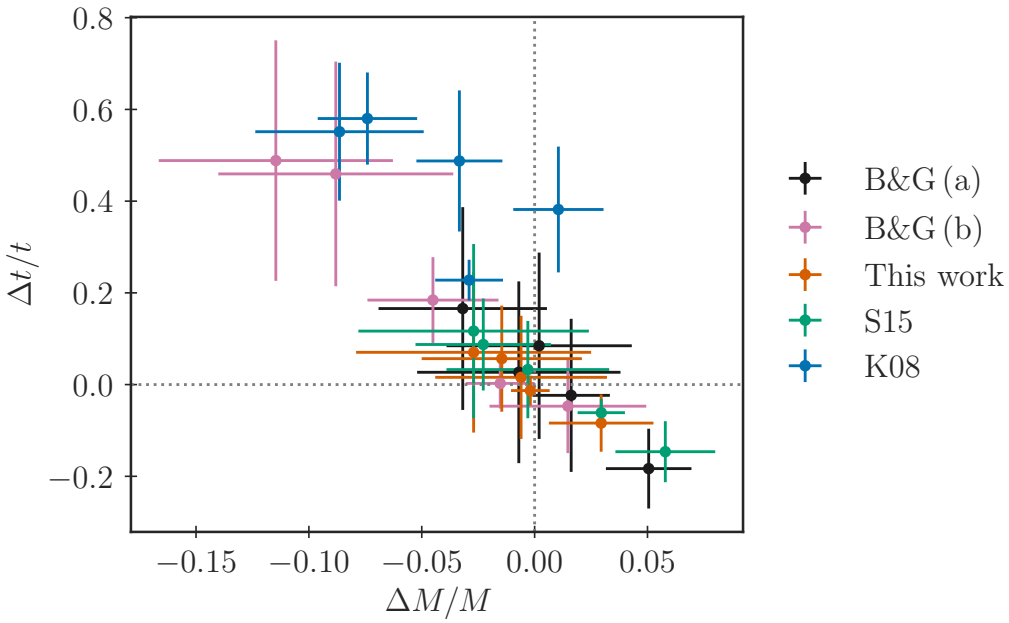


Figure 7.5: Fractional difference in age as a function of the fractional difference in mass between the 'hares' (target PMs) and 'hounds' (models from grid search) relative to the 'hares'. Positive differences imply that the parameter value of the hound exceeds the target value. The target value is marked by the intersection of the dotted lines. The plotted parameter estimates were obtained using Eq. (7.14). The uncertainties follow from Eq. (7.15.)

is the attempt to sample the likelihood for all surface corrections reliably: especially the use of K08 leads to metallicities that are systematically too high and effective temperatures that are much lower than the target value, as discussed below. In other words, we selected the target models, i.e. the 'hares', so that the best-fitting models do not lie too close to the edge of the grid. The global parameters of the five target models for the hare and hound exercises are furthermore selected so that we explore the region of the parameter space that is expected to be relevant for the *Kepler* stars that are to be addressed in Section 7.3.5. The results obtained for the hare and hound exercises from the MLE are summarized for each surface correction in Tables 7.3 and 7.4. To give a better overview of the results, some properties of the evaluated probability distributions are visualized in Figs 7.5 and 7.6.

We find our parameterization of the surface effect to recover the stellar parameters rather well, and hence we infer that the Lorentzian fit encodes detailed information about the structural contribution to the surface effect.

S15 has been calibrated on fewer models and with different input physics than our PMs, and a dependence of the coefficients on metallicity was not included. Nevertheless, it likewise performs rather well, when establishing the model parameters in the hare and hound exercise. This may reflect the fact that S15 resembles our surface correction relation in being a parameterization of the structural contribution only. Also, this underlines that a

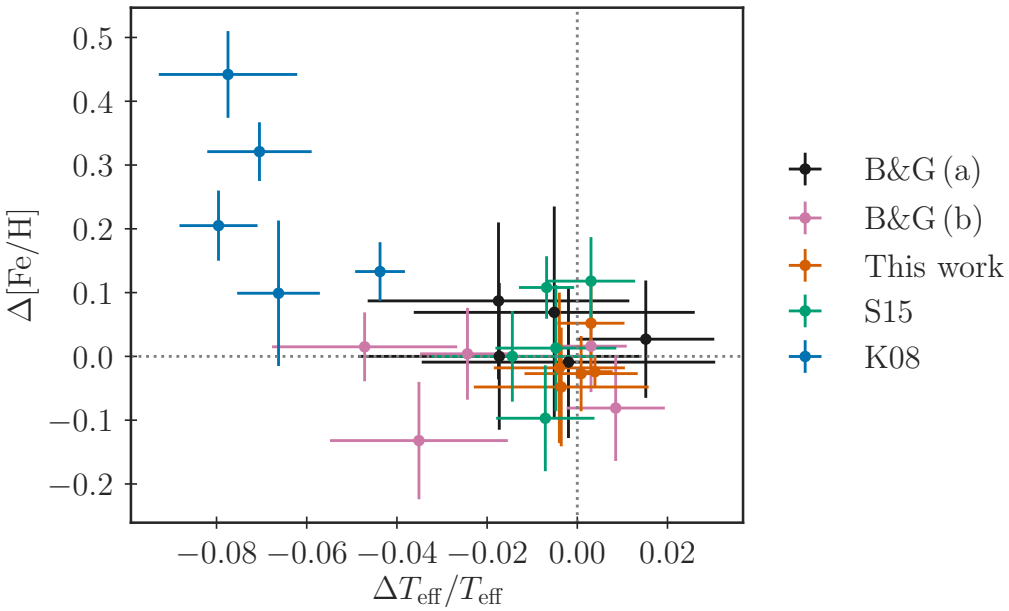


Figure 7.6: Absolute difference in metallicity as a function of the fractional difference in effective temperature between the 'hares' (target PMs) and 'hounds' (models from grid search) relative to the 'hares'. Positive differences imply that the parameter value of the hound exceeds the target value. The target value is marked by the intersection of the dotted lines. The plotted parameter estimates were obtained using Eq. (7.14). The uncertainties follow from Eq. (7.15).

Table 7.3: Global parameters from the hare and hound exercise based on PMs. Further parameters are listed in Table 7.4. The first column contains an identifier. The second through the fourth column contain the global parameters of the PMs. The fifth column lists the used surface correction relation. The sixth through the eighth column summaries the parameter values for the best-fitting model, the weighted mean and the square root of the weighted variance. The last column contains the initial metallicity of the best-fitting model. The purpose of including the latter quantity is solely to demonstrate that none of the models is at the edge of our grid of stellar models; hence we do not provide uncertainties on the initial metallicity. We compare the surface corrections by Ball & Gizon (2014) in combination with Eq. (7.21) (B&G, a), the one by Ball & Gizon (2014) with fixed coefficients (B&G, b), the one presented in this chapter, the one by Kjeldsen et al (2008) (K08), and the one by Sonoi et al. (2015) (S15).

| Hare | $T_{\rm eff}$ | $\log g$ | [Fe/H] | Surf. Corr. | $T_{\rm eff}^{\rm mod}$ | $\log g^{\rm mod}$ | $[{\rm Fe/H}]^{\rm mod}$ | $[{\rm Fe/H}]_{\rm init}^{\rm mod}$ |
|---|---|---|---|---|---|---|---|---|
| | K | dex | dex | | K | dex | dex | dex |
| A | 5624 | 4.054 | −0.028 | K08 | 5372, $5378 \pm 31$ | 4.045, $4.046 \pm 0.002$ | 0.081, $0.105 \pm 0.046$ | 0.20 |
| | | | | B&G (a) | 5596, $5613 \pm 183$ | 4.053, $4.053 \pm 0.008$ | 0.002, $-0.037 \pm 0.119$ | 0.13 |
| | | | | B&G (b) | 5463, $5487 \pm 59$ | 4.045, $4.045 \pm 0.005$ | 0.008, $-0.024 \pm 0.072$ | 0.13 |
| | | | | S15 | 5596, $5543 \pm 101$ | 4.053, $4.049 \pm 0.009$ | 0.002, $-0.028 \pm 0.071$ | 0.13 |
| | | | | This work | 5553, $5604 \pm 109$ | 4.045, $4.049 \pm 0.009$ | $-0.086$, $-0.076 \pm 0.093$ | 0.04 |
| B | 5926 | 4.185 | −0.301 | K08 | 5486, $5467 \pm 91$ | 4.181, $4.182 \pm 0.003$ | 0.096, $0.141 \pm 0.068$ | 0.25 |
| | | | | B&G (a) | 6077, $6016 \pm 90$ | 4.197, $4.196 \pm 0.004$ | $-0.334$, $-0.274 \pm 0.092$ | −0.14 |
| | | | | B&G (b) | 5917, $5944 \pm 47$ | 4.182, $4.188 \pm 0.006$ | $-0.344$, $-0.285 \pm 0.072$ | −0.16 |
| | | | | S15 | 5963, $5944 \pm 58$ | 4.194, $4.196 \pm 0.004$ | $-0.238$, $-0.183 \pm 0.069$ | −0.06 |
| | | | | This work | 5934, $5944 \pm 44$ | 4.189, $4.191 \pm 0.004$ | $-0.258$, $-0.249 \pm 0.069$ | −0.08 |
| C | 5895 | 4.053 | −0.262 | K08 | 5399, $5426 \pm 51$ | 4.035, $4.036 \pm 0.004$ | $-0.049$, $-0.057 \pm 0.055$ | 0.07 |
| | | | | B&G (a) | 5878, $5792 \pm 171$ | 4.056, $4.052 \pm 0.008$ | $-0.197$, $-0.175 \pm 0.123$ | −0.04 |
| | | | | B&G (b) | 5508, $5617 \pm 121$ | 4.027, $4.035 \pm 0.009$ | $-0.266$, $-0.247 \pm 0.054$ | −0.14 |
| | | | | S15 | 5953, $5867 \pm 79$ | 4.053, $4.053 \pm 0.006$ | $-0.349$, $-0.249 \pm 0.099$ | −0.17 |
| | | | | This work | 5819, $5900 \pm 74$ | 4.042, $4.052 \pm 0.007$ | $-0.343$, $-0.289 \pm 0.059$ | −0.19 |
| D | 5781 | 4.055 | 0.06 | K08 | 5412, $5398 \pm 53$ | 4.041, $4.037 \pm 0.006$ | 0.213, $0.159 \pm 0.114$ | 0.33 |
| | | | | B&G (a) | 5668, $5681 \pm 181$ | 4.049, $4.049 \pm 0.008$ | 0.090, $0.060 \pm 0.115$ | 0.22 |
| | | | | B&G (b) | 5667, $5578 \pm 114$ | 4.036, $4.033 \pm 0.009$ | $-0.099$, $-0.072 \pm 0.092$ | 0.03 |
| | | | | S15 | 5710, $5740 \pm 63$ | 4.051, $4.051 \pm 0.005$ | 0.076, $0.037 \pm 0.083$ | 0.21 |
| | | | | This work | 5813, $5758 \pm 84$ | 4.051, $4.053 \pm 0.006$ | $-0.042$, $0.042 \pm 0.118$ | 0.06 |
| E | 5874 | 4.219 | −0.008 | K08 | 5486, $5460 \pm 68$ | 4.213, $4.210 \pm 0.004$ | 0.322, $0.313 \pm 0.046$ | 0.47 |
| | | | | B&G (a) | 5995, $5844 \pm 183$ | 4.225, $4.222 \pm 0.004$ | $-0.075$, $0.061 \pm 0.166$ | 0.09 |
| | | | | B&G (b) | 5874, $5924 \pm 64$ | 4.219, $4.217 \pm 0.002$ | $-0.008$, $-0.089 \pm 0.083$ | 0.15 |
| | | | | S15 | 5831, $5834 \pm 36$ | 4.224, $4.224 \pm 0.001$ | 0.099, $0.100 \pm 0.049$ | 0.25 |
| | | | | This work | 5886, $5897 \pm 23$ | 4.220, $4.219 \pm 0.001$ | $-0.019$, $-0.032 \pm 0.025$ | 0.14 |

Table 7.4: Pendant to Table 7.3 with other stellar parameters. The last column contains the $\chi^2$ of the best-fitting model. The identifiers of the PMs correspond to those in Table 7.3.

| Hare | $M$ | $R$ | $t$ | Surf. Corr. | $M^{\mathrm{mod}}$ | $R^{\mathrm{mod}}$ | $t^{\mathrm{mod}}$ | $\chi^2$ |
|---|---|---|---|---|---|---|---|---|
| | $M_\odot$ | $R_\odot$ | Gyr | | $M_\odot$ | $R_\odot$ | Gyr | |
| A | 0.999 | 1.557 | 10.8 | K08 | $0.959, 0.97 \pm 0.015$ | $1.541, 1.546 \pm 0.008$ | $13.57, 13.26 \pm 0.48$ | 16.62 |
| | | | | B&G (a) | $0.999, 0.992 \pm 0.045$ | $1.557, 1.552 \pm 0.021$ | $10.88, 11.09 \pm 2.14$ | 0.4 |
| | | | | B&G (b) | $0.959, 0.954 \pm 0.029$ | $1.54, 1.537 \pm 0.015$ | $12.82, 12.79 \pm 1.01$ | 12.64 |
| | | | | S15 | $0.999, 0.972 \pm 0.051$ | $1.557, 1.543 \pm 0.026$ | $10.88, 12.06 \pm 2.05$ | 2.49 |
| | | | | This work | $0.949, 0.972 \pm 0.052$ | $1.532, 1.543 \pm 0.025$ | $12.35, 11.56 \pm 1.89$ | 1.64 |
| B | 0.950 | 1.305 | 9.77 | K08 | $0.950, 0.960 \pm 0.019$ | $1.311, 1.315 \pm 0.008$ | $13.64, 13.5 \pm 1.34$ | 11.59 |
| | | | | B&G (a) | $1.000, 0.998 \pm 0.018$ | $1.32, 1.321 \pm 0.007$ | $7.50, 7.98 \pm 0.85$ | 6.29 |
| | | | | B&G (b) | $0.930, 0.964 \pm 0.033$ | $1.295, 1.310 \pm 0.014$ | $10.35, 9.31 \pm 1.00$ | 13.32 |
| | | | | S15 | $0.990, 1.005 \pm 0.021$ | $1.319, 1.326 \pm 0.009$ | $8.53, 8.34 \pm 0.65$ | 14.21 |
| | | | | This work | $0.970, 0.978 \pm 0.022$ | $1.312, 1.315 \pm 0.01$ | $9.22, 8.95 \pm 0.61$ | 8.53 |
| C | 0.999 | 1.559 | 8.86 | K08 | $0.919, 0.925 \pm 0.022$ | $1.526, 1.529 \pm 0.012$ | $14.37, 14.0 \pm 0.89$ | 10.84 |
| | | | | B&G (a) | $1.019, 1.001 \pm 0.041$ | $1.568, 1.56 \pm 0.019$ | $8.61, 9.61 \pm 1.80$ | 0.36 |
| | | | | B&G (b) | $0.869, 0.911 \pm 0.052$ | $1.497, 1.518 \pm 0.026$ | $14.85, 12.93 \pm 2.17$ | 12.05 |
| | | | | S15 | $0.989, 0.996 \pm 0.036$ | $1.55, 1.556 \pm 0.018$ | $8.67, 9.15 \pm 0.94$ | 6.38 |
| | | | | This work | $0.939, 0.993 \pm 0.038$ | $1.530, 1.555 \pm 0.018$ | $10.55, 9.00 \pm 1.19$ | 3.41 |
| D | 1.099 | 1.63 | 7.78 | K08 | $1.029, 1.004 \pm 0.041$ | $1.604, 1.591 \pm 0.021$ | $11.36, 12.07 \pm 1.17$ | 16.47 |
| | | | | B&G (a) | $1.069, 1.064 \pm 0.041$ | $1.618, 1.614 \pm 0.018$ | $8.92, 9.07 \pm 1.72$ | 0.97 |
| | | | | B&G (b) | $1.050, 0.973 \pm 0.057$ | $1.581, 1.573 \pm 0.029$ | $10.46, 11.58 \pm 2.04$ | 18.04 |
| | | | | S15 | $1.080, 1.074 \pm 0.033$ | $1.623, 1.619 \pm 0.016$ | $8.50, 8.46 \pm 0.78$ | 5.19 |
| | | | | This work | $1.069, 1.083 \pm 0.039$ | $1.615, 1.622 \pm 0.019$ | $8.19, 8.22 \pm 0.90$ | 5.09 |
| E | 1.05 | 1.319 | 7.67 | K08 | $1.030, 1.015 \pm 0.02$ | $1.316, 1.311 \pm 0.008$ | $10.69, 11.41 \pm 1.18$ | 6.28 |
| | | | | B&G (a) | $1.070, 1.067 \pm 0.018$ | $1.323, 1.324 \pm 0.007$ | $6.51, 7.49 \pm 1.28$ | 2.18 |
| | | | | B&G (b) | $0.989, 1.034 \pm 0.016$ | $1.319, 1.312 \pm 0.007$ | $7.67, 7.69 \pm 0.42$ | 19.53 |
| | | | | S15 | $1.079, 1.081 \pm 0.011$ | $1.330, 1.331 \pm 0.005$ | $7.25, 7.20 \pm 0.23$ | 6.23 |
| | | | | This work | $1.050, 1.048 \pm 0.009$ | $1.318, 1.317 \pm 0.003$ | $7.59, 7.57 \pm 0.25$ | 2.76 |

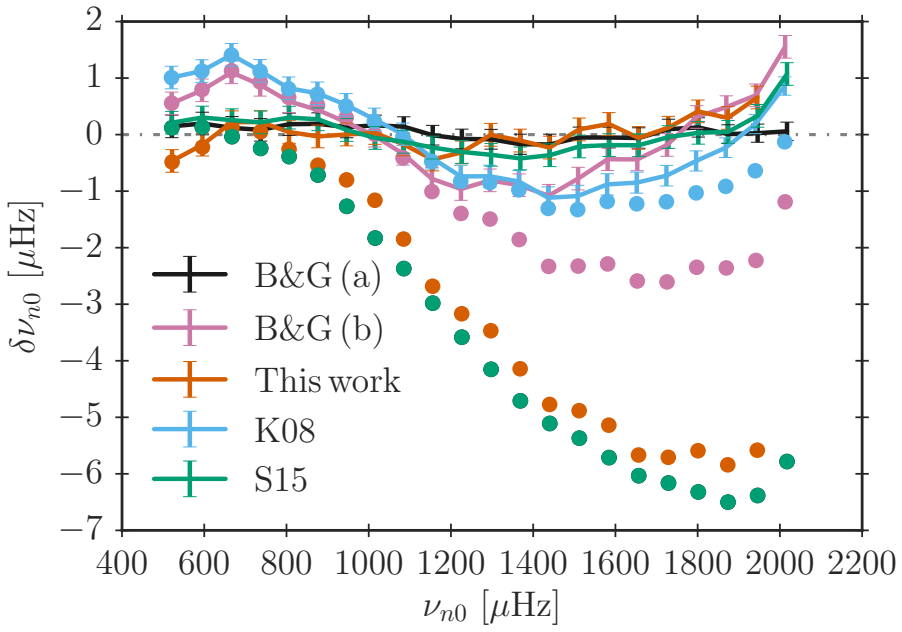


Figure 7.7: Frequency difference between the 'hare' and the 'hounds' with the identifier A in Tables 7.3 and 7.4, using different surface correction methods. The 'hare', i.e. the target model that is to be recovered, is a PM. The solid lines show the corrected frequencies. The circular markers in the same colour show the associated un-corrected frequencies of the respective best-fitting models. We note that, for this particular case, B&G (a) and S15 yield the same best-fitting UPM. A perfect match between the frequencies of the hare and hound is obtained for a given surface correction relation, if $\delta\nu_{n\ell} = 0$ for all frequencies. As can be seen from the plot, B&G (a), S15, and our surface correction relation perform quite well, while B&G (b) and K08 fail to recover the frequencies of the hare.

Lorentzian parameterization captures the structural contribution.

In contrast, K08 is less reliable. When employing this surface correction, the effective temperature of the PM is systematically underestimated by a few hundred degrees. Also, the inferred metallicity is much higher than for the original model.

Using K08 leads to the selection of a model, whose frequencies already closely match the frequencies of the PM without the necessity of a surface correction. This peculiarity also occasionally occurs, when using B&G with fixed coefficients (case b), but contrasts the selection obtained with the other surface correction relations, including B&G in combination with Eq. (7.21) (case a). It is exemplified in Fig. 7.7.

As discussed in Section 7.3.5, K08 performs better when confronted with *Kepler* data. Therefore, the issue with K08, in the hare and hound exercise, may partly reflect the neglect of modal effects, i.e. the fact that the frequency difference between the UPM and the associated PM does not fit the expected functional form: as shown in Section 7.2, the difference between a PM and the associated UPM is not well-described by a power law.

Furthermore, in the case of B&G, the inferred surface correction is lower when the coefficients are fixed to the solar values (case b) than when Eq. (7.21) is used to establish the coefficients (case a) for each model anew. It hence stands to reason that the evaluation of the coefficients based on the solar case distorts the model selection in the investigated region of the parameter space. This conclusion seems to agree with the qualitative finding of Section 7.2.3: no unique set of coefficient values is applicable throughout the Kiel diagram. This agrees with the conclusions drawn by Ball and Gizon (2017): surface corrections that employ coefficients that are calibrated to the Sun perform comparatively poorly when fitting *Kepler* observations. As can be seen from our hare and hound exercise, this may have severe consequences for the inferred parameters: for instance, the use of either K08 or case b of B&G systematically overestimates the stellar age in the hare and hound exercise. This is illustrated in Fig. 7.5. If K08 and case b of B&G likewise lead to significant systematic errors for age estimates when applied in observational studies, this will skew any analysis that relies on stellar ages — including analyses of the chemo-dynamical evolution of the Milky Way galaxy. Indeed, according to Nsamba et al. (2018a), this is the case. We take a closer look at a comparison with real data in Section 7.3.5.

Despite the neglect of the modal effects in the computation of the model frequencies of the PMs, B&G performs rather well, when using Eq. (7.21) (case a). However, in case a, B&G also leads to the broadest probability distributions, as $a_{-1}$ and $a_3$ are treated as free parameters. Thus, the higher accuracy comes at the price of lower precision.

While the different surface correction relations recover parameters such as the effective temperature and the metallicity with varying success, the gravitational acceleration is always accurately and precisely reproduced. This stems from the fact that we mainly constrain our models through the oscillation frequencies: the global oscillation properties of stars are determined by both the mass ($M$) and radius ($R$) of the star. Thus, the frequency of maximum amplitude and the large frequency separation are proportional to $g$ and $\sqrt{g}$, respectively.

### 7.3.5 *Kepler* Stars

Having established how well our Lorentzian parameterization, i.e. our surface correction relation, reproduces the stellar parameters of PMs in a grid search, we proceed to an analysis of observational data. We search for best-fitting models using our MLE approach for the *Kepler* stars KIC 10516096 and KIC 5950854. The observational constraints on the employed radial frequencies as well as on $T_{\rm eff}$ and [Fe/H] are taken from Lund et al. (2017). Both stars are in the LEGACY dwarf sample. The obtained stellar parameters from our MLE approach are summarized in Tables 7.5 and 7.6, respectively.

An analysis of MS stars with global properties that are rather similar to those of the Sun has already been presented in Chapter 6. We, therefore, selected KIC 10516096 and KIC 5950854, in order to investigate stars at a later evolutionary stage. Furthermore, spectroscopic constraints indicate that the global parameters of these two stars lie well within our computed grid of stellar models, which allows us to map the probability distributions properly.

Table 7.5: Best-fitting parameters for KIC 10516096. According to spectroscopy, $T_{\rm eff} = 5964 \pm 77$ and [Fe/H] $= -0.11 \pm 0.10$, respectively.

| Quantity | Unit | K08 | B&G (a) | B&G (b) | S15 | This work |
|---|---|---|---|---|---|---|
| $\chi^2$ | | 5.73 | 2.45 | 7.06 | 6.44 | 7.93 |
| $T_{\rm eff}$ | K | 5535, $5592 \pm 63$ | 5887, $5912 \pm 151$ | 5772, $5724 \pm 68$ | 5612, $5657 \pm 81$ | 5760, $5734 \pm 65$ |
| $\log g$ | dex | 4.169, $4.17 \pm 0.004$ | 4.178, $4.179 \pm 0.005$ | 4.175, $4.173 \pm 0.006$ | 4.173, $4.173 \pm 0.006$ | 4.175, $4.173 \pm 0.005$ |
| [Fe/H] | dex | 0.376, $0.312 \pm 0.075$ | 0.104, $0.074 \pm 0.143$ | 0.191, $0.211 \pm 0.073$ | 0.336, $0.274 \pm 0.084$ | 0.181, $0.186 \pm 0.099$ |
| $[\mathrm{Fe/H}]_{\rm init}$ | dex | 0.52 | 0.26 | 0.34 | 0.48 | 0.33 |
| $M$ | $\mathrm{M}_\odot$ | 1.080, $1.081 \pm 0.027$ | 1.120, $1.118 \pm 0.026$ | 1.110, $1.101 \pm 0.040$ | 1.100, $1.097 \pm 0.040$ | 1.100, $1.090 \pm 0.029$ |
| $R$ | $\mathrm{R}_\odot$ | 1.417, $1.417 \pm 0.011$ | 1.428, $1.425 \pm 0.01$ | 1.427, $1.424 \pm 0.016$ | 1.423, $1.421 \pm 0.015$ | 1.421, $1.417 \pm 0.012$ |
| $t$ | Gyr | 9.272, $8.979 \pm 0.957$ | 6.592, $6.507 \pm 1.038$ | 7.369, $7.852 \pm 1.248$ | 8.347, $8.244 \pm 1.247$ | 7.641, $7.995 \pm 0.751$ |

Table 7.6: Best-fitting parameters for KIC 5950854. According to spectroscopy, $T_{\rm eff} = 5853 \pm 77$ and [Fe/H] $= -0.23 \pm 0.10$, respectively.

| Quantity | Unit | K08 | B&G (a) | B&G (b) | S15 | This work |
|---|---|---|---|---|---|---|
| $\chi^2$ | | 2.08 | 0.6 | 2.33 | 3.22 | 3.4 |
| $T_{\rm eff}$ | K | 5702, $5694 \pm 170$ | 5861, $5757 \pm 175$ | 5673, $5647 \pm 148$ | 5650, $5584 \pm 129$ | 5656, $5671 \pm 145$ |
| $\log g$ | dex | 4.23, $4.235 \pm 0.013$ | 4.234, $4.218 \pm 0.034$ | 4.234, $4.234 \pm 0.012$ | 4.235, $4.232 \pm 0.010$ | 4.231, $4.234 \pm 0.011$ |
| [Fe/H] | dex | $-0.117$, $-0.037 \pm 0.161$ | $-0.211$, $-0.134 \pm 0.158$ | $-0.020$, $0.007 \pm 0.159$ | 0.000, $0.019 \pm 0.153$ | $-0.054$, $-0.033 \pm 0.151$ |
| $[{\rm Fe/H}]_{\rm init}$ | dex | 0.05 | -0.04 | 0.14 | 0.16 | 0.11 |
| $M$ | $M_\odot$ | 0.930, $0.963 \pm 0.077$ | 0.950, $0.949 \pm 0.063$ | 0.960, $0.963 \pm 0.072$ | 0.960, $0.944 \pm 0.060$ | 0.940, $0.955 \pm 0.065$ |
| $R$ | $R_\odot$ | 1.226, $1.238 \pm 0.031$ | 1.232, $1.256 \pm 0.054$ | 1.24, $1.24 \pm 0.029$ | 1.238, $1.232 \pm 0.024$ | 1.231, $1.236 \pm 0.026$ |
| $t$ | Gyr | 11.985, $11.356 \pm 3.495$ | 9.971, $11.219 \pm 3.066$ | 11.281, $11.702 \pm 3.337$ | 11.472, $12.79 \pm 2.799$ | 12.078, $11.691 \pm 3.061$ |

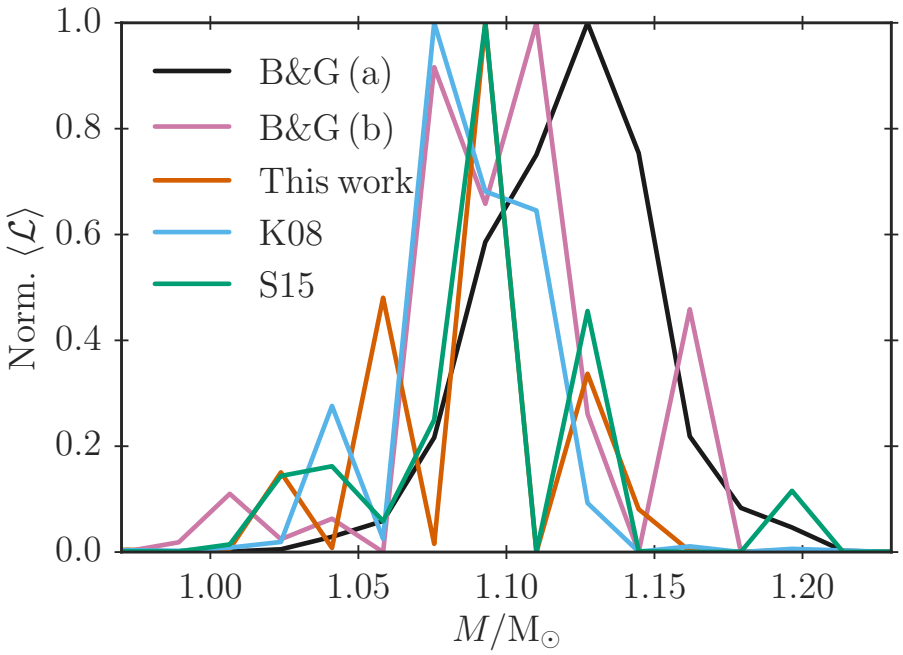


Figure 7.8: Projection of the normalized exponential of the averaged log-likelihood for the stellar mass for KIC 10516096. The normalization factor is established in such a way that the likelihood of the maximum likelihood model is 1. We use 30 bins, smoothing the likelihood function.

As can be seen from Tables 7.5 and 7.6, the use of B&G in combination with Eq. (7.21) (case a) leads to parameter estimates that are in good agreement with the spectroscopic constraints. Lesser agreement is achieved when using the other surface correction relations and case b of B&G. Thus, with the exception of B&G case a, the evaluated effective temperature is systematically too low, while the metallicity is too high in most cases — our Lorentzian fit and B&G case a perform slightly better than the remaining surface correction, recovering the metallicity within $2\sigma$ in both cases.

The stellar age estimates vary slightly between the different fits, while estimates of $\log g$ and the stellar radius are mutually consistent and precisely determined. The mass estimates also closely match. Again, this seems to reflect the fact that the global oscillation properties encode stringent constraints on $g$.

We include the projected likelihood for the mass of KIC 10516096 in Fig. 7.8. As can be seen from the figure, the use of case a of B&G leads to a much broader distribution than the remaining surface correction relations do. This is a general feature that we find for all projections — for both *Kepler* stars as well as in the hare and hound exercise. This can be explained by the fact that Eq. (7.21) adjusts the coefficients in order to optimize the fit, i.e. the fit has two additional free parameters, which ascribes artificially high likelihoods to incorrect structures.

The frequency difference between the obtained best-fitting models and observations are

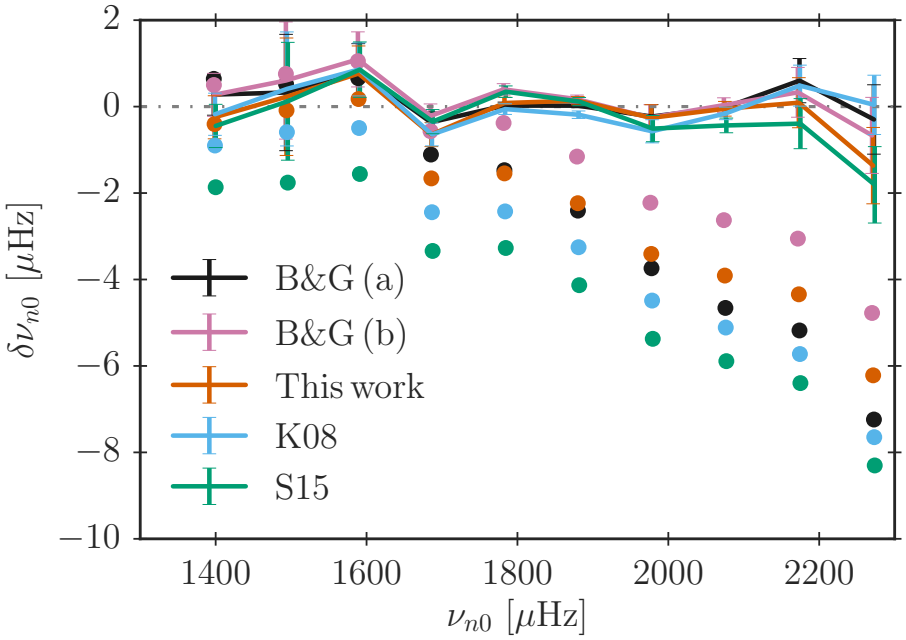


Figure 7.9: Same as Fig. 7.7 but for KIC 5950854.

shown in Figs 7.9 and 7.10. We note that the surface correction relations that rely on solar coefficients generally predict a smaller frequency correction than the remaining surface correction relations do.

At this point, we refer to Nsamba et al. (2018a) for another recently published determination of the systematics arising from different surface correction methods. Nsamba et al. (2018a) determine posterior probability distributions for the stellar mass, radius, and age using different surface correction relations by employing a Markov Chain Monte Carlo algorithm. They then compare the evaluated parameter values with those obtained, when following the same Bayesian inference technique but using the frequency ratios suggested by Roxburgh and Vorontsov (2003). Since these frequency ratios have been shown to be rather insensitive to the surface layers, the associated parameter values are a suitable reference value and are taken as a measure of the systematic errors introduced by the use of each surface correction relation. Nsamba et al. (2018a) conclude that B&G reproduces the mass, radius, and age that is inferred from frequency ratios. The same conclusion was drawn by Basu and Kinnane (2018). This suggests that B&G correctly encodes the structural as well as the modal effects. Thus, we may use parameter values that are based on case a of B&G as a benchmark for the other surface correction relations.

In order to perform a quantitative comparison between our findings and Nsamba et al. (2018a), note that each parameter estimate listed by Nsamba et al. (2018a) corresponds to the statistical mean of the associated posterior probability distribution. They must hence be compared to the results from Eqs (7.14) and (7.15) rather than the parameters of the best-fitting model. According to Nsamba et al. (2018a), K08 leads to larger intrinsic

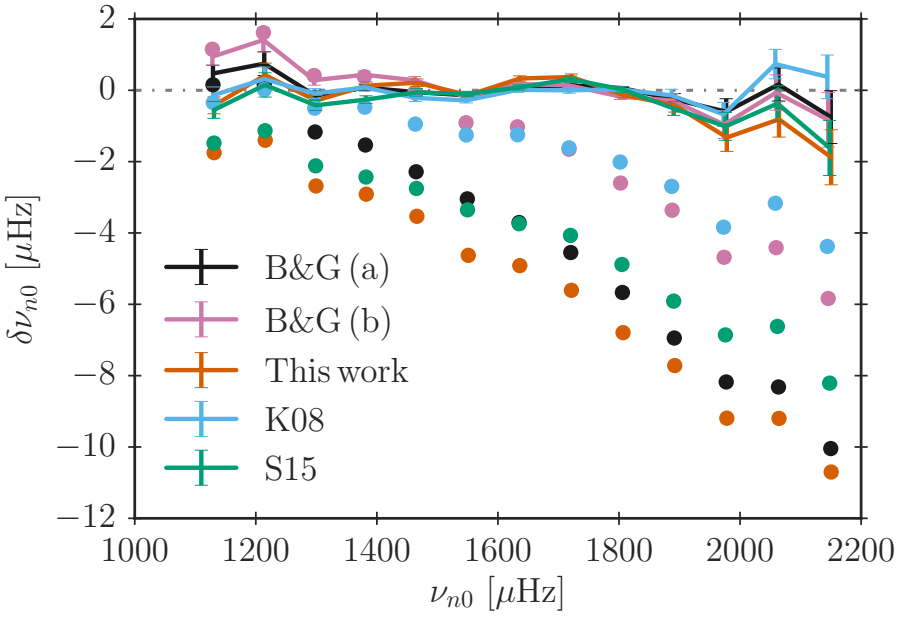


Figure 7.10: Same as Fig. 7.7 but for KIC 10516096.

systematics for the mass, radius, and age than case a of B&G does. As regards these three parameters, we cannot make an equally rigorous statement, since all surface correction relations yield consistent results within the established errorbars. This being said, we confirm that K08 does overall not perform well: we find K08 to lead to systematic errors when addressing $T_{\rm eff}$ and [Fe/H].

Furthermore, Nsamba et al. (2018a) conclude that S15 performs rather well. Again, we can neither confirm nor refute this statement for the mass, radius, and age estimates by comparing to case a of B&G. From our study, however, we conclude that the performance of S15 is rather unsatisfactory, when including $T_{\rm eff}$ and [Fe/H]. However, as regards S15, a direct comparison between our results and those obtained by Nsamba et al. (2018a) is misleading, since Nsamba et al. (2018a) defines the coefficients differently: $\beta$ is set to 4.0, while $\alpha$ is calibrated based on the observed frequencies.

### 7.3.6 Patched Models of *Kepler* Stars

Having established that case a of B&G is plausibly the most reliable surface correction relation for establishing stellar parameters, we can use the best-fitting UPMs obtained based on B&G to construct PMs, in order to model the structure of the *Kepler* targets. The associated difference between the adiabatic model frequencies of the PMs and the observations are summarized in Fig. 7.11.

In order to demonstrate the systematic errors that are introduced by our choice of the patching quantity, Fig. 7.11 includes three PMs for each *Kepler* star, using $P$, $\rho$, or $T$ as the respective patching quantity. As elaborated upon in Section 7.2, the sensitivity of the

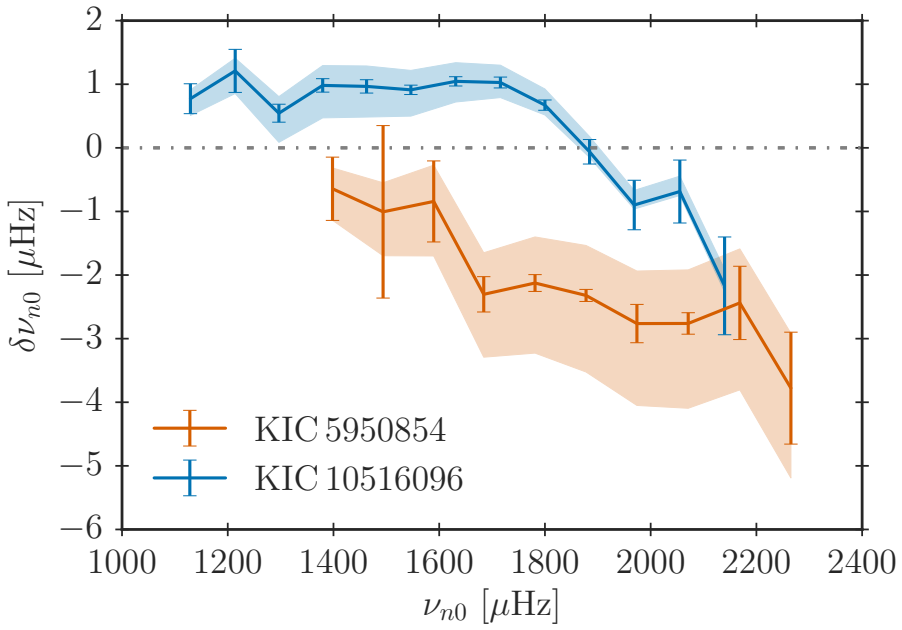


Figure 7.11: Frequency difference between observations and PMs for KIC 5950854 and KIC 10516096. The UPMs corresponds to the best-fitting models established using case a of B&G. The solid lines show the frequencies that are obtained when using $P$ as the patching quantity. The shaded area shows the frequency shift that is introduced when using $\rho$ or $T$ as the patching quantity. The error bars illustrate the error on the observed frequencies.

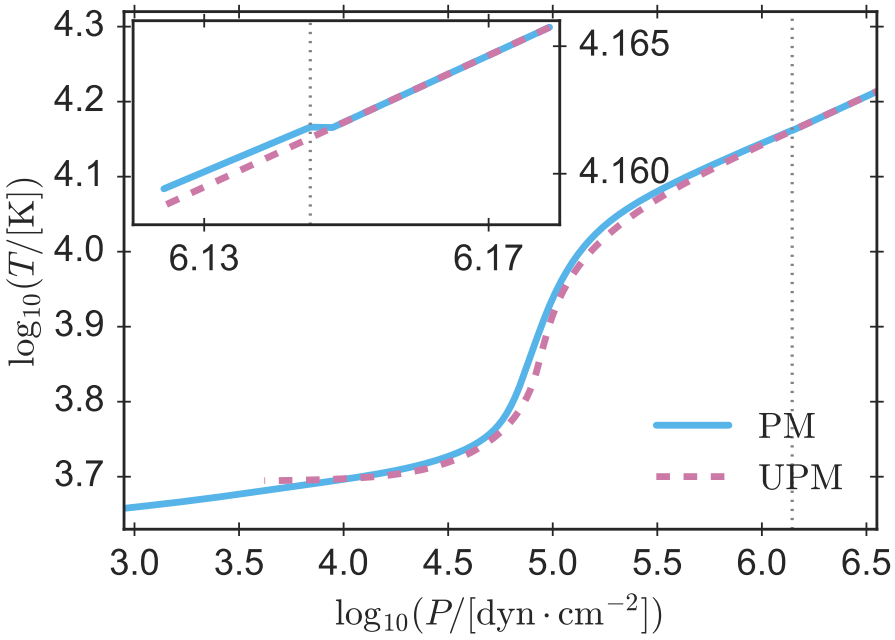


Figure 7.12: Temperature as a function of pressure for KIC 10516096. The solid cyan line and the dashed magenta line show the stratification of the PM and UPM, respectively. The dotted grey line shows the location of the innermost mesh point of the patched $\langle 3\mathrm{D}\rangle$-envelope. A zoom-in is included in the upper left corner. For the PM, $\rho$ has been used as the patching quantity. Consequently, there is a discontinuity in the temperature stratification at the patching point.

oscillation frequencies to the patching quantity stem from discontinuities in the patched structure. This is illustrated in Fig. 7.12 for KIC 10516096. In this figure, we use the density as the patching quantity, which results in a discontinuity in the temperature and pressure stratifications: while $\rho(r)$ is a smooth function by construction, neither $T(r)$ nor $P(r)$ is — consequently, $T(P)$ in Fig. 7.12 is neither. One way to quantify this discontinuity is to evaluate the change in the stellar radius that is introduced by a change in the patching quantity: using the temperature rather than the density as the patching quantity would shift the radius of the patching point by 18 km. To put this into perspective, we note that the radius of both stars is larger than that of the Sun (cf. Tables 7.5 and 7.6) and that the patch is performed roughly $2 \times 10^3$ km below the surface in either case. In comparison, this shift would be 73 km in the case of KIC 5950854. As a result, the oscillation frequencies of KIC 5950854 are more sensitive to the choice of the patching quantity than those of KIC 10516096, as shown in Fig. 7.11.

According to Houdek et al. (2017), the modal surface effect counteracts the structural surface effect, increasing the model frequencies — that is at least the case for the present-day Sun. At first glance, Fig. 7.11 seems to contradict this conclusion in the case of KIC 5950854: the obtained model frequencies of the PM are systematically higher than

the observed frequencies. However, in accordance with Ball et al. (2016), Sonoi et al. (2015), and Jørgensen et al. (2017) (i.e. Chapter 6), we use $\Gamma_1$, when calculating model frequencies, while Houdek et al. (2017) use the reduced $\Gamma_1$ approximation. Thus, the frequency differences between the model frequencies and observations in Fig. 7.11 do not only include those contributions that Houdek et al. (2017) denote as modal.

If we assume that case a of B&G accurately reproduces the stellar structure and frequencies, Fig. 7.11 rather points towards the conclusion that the structural surface effect alone does not reliably mimic the total surface effect within the gas $\Gamma_1$ approximation: the deviations are quite significant for KIC 5950854. This is an interesting notion since it illustrates why the Lorentzian correction presented in this thesis as well as the correction relation by Sonoi et al. (2015) is subject to systematic errors when estimating stellar parameters.

Whether B&G indeed accurately reproduces the underlying stellar structures is not settled. To answer this question, a detailed analysis of how the structural, as well as the modal effect, depends on the stellar parameters is needed. This is beyond the scope of this chapter.

Finally, interpolation errors may give rise to further frequency shifts: the structure of the patched $\langle 3D \rangle$-envelope may be incorrect. The sampling of existing grids of 3D envelopes may hence be too low in some regions of the parameters space. To investigate this possibility, an extension of the Stagger grid is needed.

## 7.4 Summary

In this chapter, we present patched models at non-solar metallicity[5] and show how such models can be used as a diagnostic tool to shed light on different aspects of stellar modelling.

Based on the interpolation scheme in Chapter 5, we derive parameterizations of the structural contribution of the surface effect, using the same functional forms as suggested by Sonoi et al. (2015): a power law and a Lorentzian. We find the coefficients of the parameterizations to be sensitive to the selected sample of stellar models. Hence, we conclude that no unique set of coefficients is applicable to all evolutionary stages.

From a hare and hound exercise, we conclude that our Lorentzian parameterization of the structural contribution to the surface effect performs rather well, as it is able to recover the correct stellar parameters for PMs. The surface correction relation by Sonoi et al. (2015) likewise performs reasonably well, which reflects the fact that this correction relation likewise only mimics the structural contribution to the surface effect.

[5]Manchon et al. (2018) present the first-ever published patched models at non-solar metallicity based on the CO$^5$BOLD code (cf. Ludwig et al., 2009; Freytag et al., 2012). Manchon et al. (2018) likewise derive a parameterization of the structural surface effect but do this in the parameter space spanned by the effective temperature, the surface gravity, and the Rosseland mean opacity. We have not performed a comparison with their results but note that such an analysis would be a fruitful future exercise. Their analysis builds on 29 patched models for pre-MS stars, MS stars, and subgiants with $T_{\rm eff}$ ranging from 4500 to 6800 K, $\log g$ ranging from 3.5 to 4.5 dex, and [Fe/H] $= -1.0, -0.5, 0.0, 0.5$.

When applying our Lorentzian parameterization to real data, on the other hand, it performs poorly. This was to be expected: our parameterizations only encode the structural surface effect, neglecting modal contributions (cf. Houdek et al. 2017). Specifically, using a simple maximum likelihood estimation approach, we derive stellar parameters using both our Lorentzian parameterization and the surface correction by Ball and Gizon (2014) that incorporates structural as well as modal effects. From this comparison, we conclude that the neglect of modal effects alters the parameter estimates. Consequently, without further adjustments, our results do not support the use of our parameterizations or the surface correction relation by Sonoi et al. (2015), when evaluating stellar parameters.

Finally, surface correction relations that are solely calibrated based on the present-day Sun turn out to perform as badly as our Lorentzian parametrization when addressing *Kepler* stars, while they completely fail to recover the correct model parameters in the hare and hound exercise. This is consistent with our statement above: no unique set of coefficients is applicable throughout the Kiel diagram for any of the proposed parameterizations of the surface effect. Using surface correction relations, such as the one by Kjeldsen et al. (2008), may hence severely skew stellar parameter estimates. Consequently, our results discourage the use of any semi-empirical surface correction that is calibrated to fit the Sun for stars, whose parameters deviate strongly from the solar case. Rather, surface corrections must be calibrated based on stars that closely resemble the target.

The improper characterization of stars that results from the use of inadequate surface correction relations has consequences for any adjacent field that relies on accurate stellar parameter estimates. For instance, the evaluated properties of exoplanets are observationally linked to those of the host star. Furthermore, if the use of inadequate surface correction relations leads to systematic offsets in the parameter estimates, as suggested by Nsamba et al. (2018a), adopting these surface correction relations in galactic archaeology will lead to incorrect conclusions regarding the chemical and dynamical history of the Milky Way galaxy.

# Chapter 8

# Coupling: Improving the Outer Boundary Conditions

*The content, including most of the text, of Section 8.1 was published in Monthly Notices of the Royal Astronomical Society by Jørgensen et al. (2018). I am the first author of the paper and the primary investigator of the presented research project. The figures and tables in Section 8.2 as well as Figs 8.6 and 8.7 are included in a publication with J. R. Mosumgaard (JM) as its lead author. I wrote this chapter. My contributions to both papers consist of the conception, development, and validation of the presented method and its numerical implementation. The work was performed in collaboration with Achim Weiss, Víctor Silva Aguirre, JM, and Jørgen Christensen-Dalsgaard. JM contributed to the development and implementation of the method into* GARSETC. *Furthermore, JM applied the method, computing the final models that are presented below and performing the Bayesian grid search that enters Section 8.2. We collaboratively shaped and planned both papers. All co-authors contributed with constructive and useful feedback.*

This chapter deals with a novel method for including 3D simulations into 1D stellar structure models: $\langle 3D \rangle$-envelopes are used to set the outer boundary conditions and are appended to the interior 1D structure at every time-step. To date, no other proposed scheme to improve 1D models includes the full mean stratification of 3D simulations directly into a stellar evolution code in this manner. Our method thus guarantees a unique level of consistency between the obtained hybrid models and the underlying 3D simulations.

## 8.1 A New Standard Solar Model

The patching procedure presented in Chapters 6 and 7 corrects the structure of the final model during the post-processing. In other words, patching does not account for the changes in the evolution that arises from the improper boundary conditions that result from the

use of improper outermost layers. Furthermore, the stratifications of different quantities in patched models suffer from discontinuities, which reflects inconsistencies between the physical description of the superadiabatic layers of the 1D models and the more realistic 3D simulations. In this chapter, I present a method that overcomes these issues: at every time-step, an interpolated ⟨3D⟩-envelope is appended and is used to set the boundary conditions of the interior model. I will refer to this approach as the *coupling of 1D and 3D simulations*. The resulting hybrid models are, therefore, referred to as *coupled* models. This section deals with the solar case, presenting a model of the present-day Sun using coupling. A detailed account of the effect on stellar evolution is given in Section 8.2 alongside a discussion of stars in the *Kepler* field. Further analyses that draw upon coupled models and further developments of the presented method follow in Chapters 9 and 10.

### 8.1.1 Coupling 1D Models with ⟨3D⟩-Envelopes

Coupled stellar structure models are determined, using the Henyey scheme (cf. Chapter 2). In each iteration, the solution of the stellar structure equations returns a given temperature and thermal pressure at the outermost point of the interior model. In the following, we will refer to these values of temperature and pressure as $T_{\rm m}^{\rm 1D}$ and $P_{\rm th,m}^{\rm 1D}$, respectively. The subscript 'm' indicates that the values are taken at the outer boundary of the interior model. Contrary to standard stellar models, this mesh point no longer needs to be at the photosphere but will be located in the lower layers of the superadiabatic near-surface region. We will occasionally refer to the lowermost mesh point of the appended ⟨3D⟩-envelope, which corresponds to the outermost mesh point of the interior model, as the matching point. This naming motivates the use of the letter 'm' to refer to the outermost point of the interior model.

In each iteration, we compute and append an interpolated ⟨3D⟩-envelope that by construction has the same temperature ($T_{\rm m}^{\rm 3D}$) at its base as the interior model requires. In short, $T_{\rm m}^{\rm 3D} = T_{\rm m}^{\rm 1D}$. This requirement is merely imposed in order to ensure that the temperature stratification is continuous at the transition from the interior model to the appended ⟨3D⟩-envelope.

In the solar calibration presented in Section 8.1.2, the scaled thermal pressure at the base of the appended ⟨3D⟩-envelope is consistently 16 times higher than at the density inflection near the surface throughout the computed evolution. Adopting the terminology in Chapter 5, we refer to the ratio of the pressure to the pressure at the density inflection ($P_{\rm th}/P_{\rm th}^{\rm jump}$) as the scaled pressure. A detailed discussion on which scaled pressure to use is given in Section 8.2. For the present-day Sun, this means that we set the outer boundary conditions of the interior model roughly 1 Mm below the photosphere, where the entropy is approximately constant. Thus, the outer boundary of the interior model is located in layers deep enough such that the convective stratification is nearly adiabatic. Most of the superadiabatic layers of coupled models, including the photosphere, are enclosed in the appended ⟨3D⟩-envelope. In contrast, when computing stellar models using the standard procedure described in Chapter 2, the outer boundary conditions are supplied at the photosphere. For standard stellar models, the outer superadiabatic layers are, therefore,

a part of the interior model, while this is not the case for the coupled models.

Using the interpolation scheme described in Chapter 5, we compute ⟨3D⟩-envelopes by interpolation in two global parameters: $\log g$ and $T_{\rm eff}$. In this chapter, we do not interpolate in [Fe/H] when constructing the appended ⟨3D⟩-envelopes. When computing coupled stellar models, we, generally, use the scaled thermal pressure as out coordinate. In this chapter, however, we primarily use the gas pressure. I return to this issue below. To perform the interpolation, propositions for $\log g$ and $T_{\rm eff}$ are needed. In this connection, we require the surface gravity of the ⟨3D⟩-envelope to match the surface gravity at the outer boundary of the interior model. The surface gravity of the interpolated ⟨3D⟩-envelope is hence dictated by the mass and radius of the interior model at the matching point. In other words, for any given iteration, the proposition for $\log g$ comes directly from the proposed interior structure.

For any given gravitational acceleration, a unique $T_{\rm eff}$ fulfills the requirement that $T_{\rm m}^{\rm 3D} = T_{\rm m}^{\rm 1D}$ at the required scaled pressure. Note that the resulting $T_{\rm eff}$ is merely a proposition for the current iteration: as specified below other conditions must likewise be fulfilled. Notably, $T_{\rm eff}$ must be consistent with the total energy flux of the coupled model in order to comply to its definition: the effective temperature is related to the surface energy flux ($F_{\rm tot}$) of the star by

$$F_{\rm tot} = \sigma T_{\rm eff}^4. \tag{8.1}$$

If these conditions are not fulfilled, the Henyey scheme will alter the interior structure, leading to a new $T_{\rm m}^{\rm 1D}$ and changing all other thermodynamic quanties, which results in a new proposition for $T_{\rm eff}$ and $\log g$.

Having proposed $T_{\rm eff}$ based on the required match in temperature, the scaling factor for the thermal pressure can be obtained by interpolation, as discussed in Chapter 5, where it is shown that the scaling factor varies rather linearly with the global stellar parameters. The scaled thermal pressure can hence be converted to the absolute thermal pressure ($P_{\rm th,m}^{\rm 3D}$).

From the appended ⟨3D⟩-envelope, only the turbulent pressure (cf. Section 10.1) and the temperature stratification as a function of the thermal pressure is obtained from the Stagger grid by interpolation. Other quantities, such as the density ($\rho$) or the first adiabatic index ($\Gamma_1$), are evaluated from the EOS of the 1D stellar evolution code. The individual abundances of each element in the appended ⟨3D⟩-envelope is set to be the same as at the outermost point of the interior model since the convective envelope is fully mixed. In this chapter, we neglect the turbulent pressure.

The assumed chemical composition of the appended ⟨3D⟩-envelope is hence, by construction, consistent with the composition of the interior model throughout the computed evolution. However, since we do not interpolate in metallicity, we note that the composition of the model is not necessarily fully consistent with the metallicity of the underlying Stagger-grid simulations at any given time-step. In this chapter, we restrict ourselves to interpolation in 3D simulations, for which [Fe/H] = 0.0.

The stellar model is now subject to two outer boundary conditions. Firstly, the stellar structure equations must recover the interpolated pressure at the base of the appended ⟨3D⟩-envelope, i.e. $P_{\rm th,m}^{\rm 1D} = P_{\rm th,m}^{\rm 3D}$. This ensures that the pressure stratification is continuous at the base of the appended ⟨3D⟩-envelope. Secondly, the Stefan-Boltzmann law, i.e.

Eq. (2.26), must be fulfilled. Assuming that any energy contribution from the appended ⟨3D⟩-envelope is negligible, we use the luminosity ($L_{\rm m}^{\rm 1D}$) at the outermost point of the interior model to evaluate this criterion. We use the proposed $T_{\rm eff}$ from the appended ⟨3D⟩-envelope found by interpolation.

To obtain the surface radius, we proceed as follows. The radius ($r$) of each grid point within the appended ⟨3D⟩-envelope is calculated from the requirement of hydrostatic equilibrium (cf. Eq. 2.8). Having obtained the radius of each mesh point in the model, the surface radius $R$ that enters the Stefan-Boltzmann law can be computed, and the second boundary condition can be checked: we define the surface radius as the distance from the centre, at which the temperature equals $T_{\rm eff}$ — that is, the determination of the surface radius involves interpolation in the appended ⟨3D⟩-envelope.

We note that we neglect both the turbulent pressure and the radiative pressure throughout most of this chapter. Rather than the thermal pressure, we hence use the gas pressure as our coordinate. Section 8.2.1.2, where we use the thermal pressure, is an exception. Thus, we require that $P_{\rm gas,m}^{\rm 1D} = P_{\rm gas,m}^{\rm 3D}$ rather than requiring that $P_{\rm th,m}^{\rm 1D} = P_{\rm th,m}^{\rm 3D}$ throughout most of this chapter. The reason Jørgensen et al. (2018) and its companion paper solely employ the gas pressure is the constant development of the method that took place over the last years. In Chapters 9 and 10, we include the radiative pressure using the thermal pressure for the interpolation of the ⟨3D⟩-envelopes in GARSTEC. Finally, in Chapter 10, we include the turbulent pressure. While the radiation pressure, in many cases, can be safely neglected, the consistent implementation of the turbulent pressure is key to obtaining a physically realistic picture of stellar envelopes. This is illustrated in Fig. 8.1

Note that the described procedure for constructing coupled models shows many similarities to the standard procedure discussed in Chapter 2: in both cases, the interior structure, including the stratification of all thermodynamic quantities, is iteratively adjusted, using the Henyey scheme. The stratification beyond the outer boundary of the interior model, i.e. for the Eddington atmosphere or the ⟨3D⟩-envelope, is likewise iteratively altered. Furthermore, in both cases, the Stefan-Boltzmann law and the requirement to obtain continuous transitions in all parameters at the outer boundary are used to set the outer boundary conditions. The only notable difference is that the photosphere, at which the Stefan-Boltzmann law must be fulfilled, no longer corresponds to the outer boundary of the interior model, where a continuous transition in $T$ and $P$ is imposed.

In summary, in the case of coupled models, a consistent equilibrium structure must fulfill four conditions: the surface gravity of the appended ⟨3D⟩-envelope must be consistent with the interior model, $T_{\rm m}^{\rm 3D} = T_{\rm m}^{\rm 1D}$, $P_{\rm th,m}^{\rm 1D} = P_{\rm th,m}^{\rm 3D}$ (that is, $P_{\rm gas,m}^{\rm 1D} = P_{\rm gas,m}^{\rm 3D}$, in this chapter) and the Stefan-Boltzmann law must be fulfilled. If the model does not meet all mentioned criteria, the structure is iteratively adjusted, using the Henyey scheme. Note that this implies that a new interpolated ⟨3D⟩-envelope is computed, for each iteration.

### 8.1.2 A Solar Calibration

We have performed a solar model calibration, using the Stagger grid as the boundary condition and appending a ⟨3D⟩-envelope as described above. This solar model has been

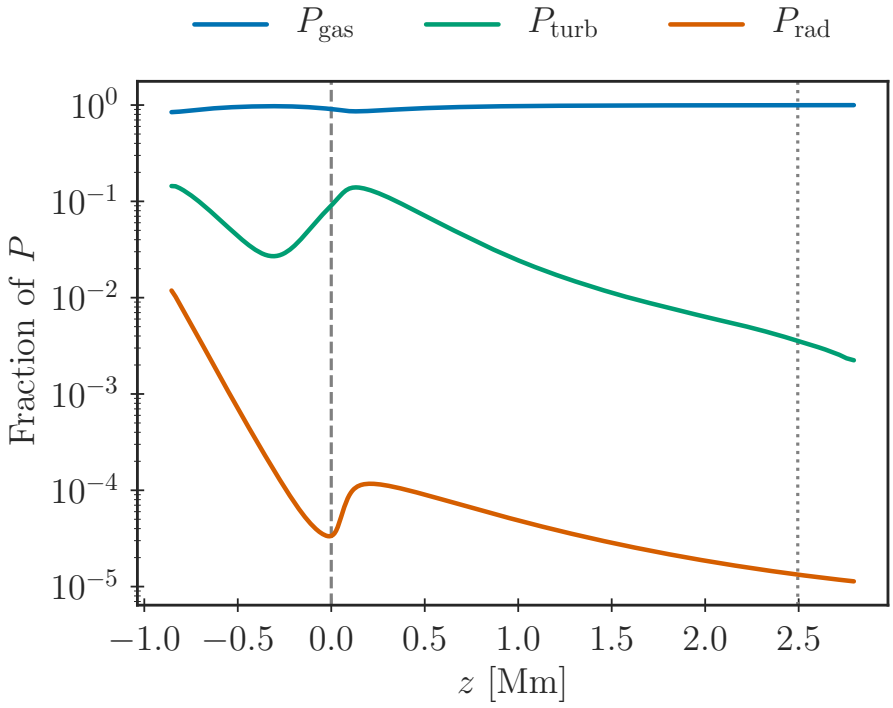


Figure 8.1: The different contributions to the total pressure in the solar Stagger-grid simulation relative to the total pressure as a function of the depth ($z$) below the photosphere. The dashed grey line indicates the location of the photosphere. The dotted grey line indicates the depth below which the stratification becomes un-physical, as the superadiabatic temperature gradient starts to increase with increasing depth. In this chapter, we use the gas pressure ($P_{\mathrm{gas}}$) as our coordinate. At least in the case of the Sun, the radiation pressure ($P_{\mathrm{rad}}$) is negligible. In Chapters 9 and 10, we use the thermal pressure, i.e. $P_{\mathrm{gas}} + P_{\mathrm{rad}}$, as our coordinate. Finally, we introduce the turbulent pressure ($P_{\mathrm{turb}}$) in Chapter 10.

obtained using the usual solar calibration procedure, i.e. a first-order Newton iteration scheme (cf. Chapter 2).

We have used the OPAL opacities (cf. Iglesias and Rogers 1996) in combination with the low-temperature opacities by Ferguson et al. (2005). We use AGSS09 and the FreeEOS by A. W. Irwin[1], which is briefly described by Cassisi et al. (2003). Our solar model includes diffusion of H, He, C, N, O, Ne, Mg, Si and Fe. As we do not interpolate in the composition of the 3D simulations, only the envelope of the final model of the present Sun has the same composition as the underlying 3D simulation.

After an initial phase on the pre-main sequence the logarithm of the scaled pressure, i.e. $\log_{10}(P^{\rm 3D}_{\rm gas,m}/P^{\rm 3D}_{\rm gas,jump})$, is fixed at 1.20 throughout the entire subsequent evolution — i.e. as noted above the scaled pressure at the matching point is 16 times higher than at the density inflection. For the associated model of the current Sun, the chosen scaled pressure corresponds to a temperature of $1.41 \times 10^4$ K and a depth of 0.94 Mm below the photosphere. The matching point should be placed as deep within the 1D model as possible since the stratification becomes more adiabatic with increasing depth. The chosen scaled pressure at the matching point is a compromise between this requisite and the limitations of the interpolation scheme imposed by the resolution of the Stagger grid and by the depths of Stagger-grid simulations.

The final calibrated solar model is required to match the current solar radius ($R_\odot$) and luminosity ($L_\odot$) as well as the desired abundance of heavy elements relative to hydrogen at the solar surface ($Z_{\rm S}/X_{\rm S} = 0.01828$) to better than a relative accuracy of $10^{-5}$. The solar values have been chosen in such a way as to recover the effective temperature of the solar Stagger-grid $\langle$3D$\rangle$-envelope: $T_{\rm eff} = 5768.5$ K.

Our implementation of $\langle$3D$\rangle$-envelopes in stellar models yields a mixing length parameter ($\alpha_{\rm MLT}$) that is roughly a factor of two higher than the value obtained when using an Eddington grey atmosphere. This reflects the fact that the mixing length parameter is calibrated to reproduce $R_\odot$: when using the Stagger grid as boundary conditions, the mixing length parameter directly affects only the extent of a superadiabatic layer that is much thinner than the corresponding layer in standard solar models, since the extent of the region beyond the matching point is dictated by the interpolated $\langle$3D$\rangle$-envelope. The change in $\alpha_{\rm MLT}$ hence reflects the fact that 3D atmospheres are more extended than their 1D counterparts, due to turbulent pressure and convective back-warming. A similar result was obtained by Schlattl et al. (1997), who pointed out that a spatially variable mixing length parameter must be introduced, when appending more realistic outer layers, in order to reproduce the temperature stratification. Physically, $\alpha_{\rm MLT}$ must provide the entropy difference between the asymptotic adiabat and the outer boundary of the interior model. In standard stellar models, the outer boundary is placed at the photosphere, and $\alpha_{\rm MLT}$ must encompass an adequate depiction of the superadiabatic surface layers that stretch over a few thousand kilometres from the photosphere to the nearly-adiabatic stellar interior. When appending $\langle$3D$\rangle$-envelopes, on the other hand, the matching point is placed within the nearly-adiabatic region below the photosphere. Consequently, $\alpha_{\rm MLT}$ merely bridges the entropy difference

[1]The code can be found on http://freeeos.sourceforge.net/

Table 8.1: Derived initial parameters as well as the helium surface abundance and the radius at the base of the convection zone for two solar calibrations, using an Eddington atmosphere and the Stagger grid as boundary conditions, respectively.

| Bound. con. | $\alpha_{\rm MLT}$ | $Y_{\rm i}$ | $Z_{\rm i}$ | $Y_{\rm S}$ | $\frac{r_{\rm cz}}{R_\odot}$ |
|---|---|---|---|---|---|
| Eddington | 1.78 | 0.2653 | 0.0152 | 0.2343 | 0.7244 |
| $\langle$3D$\rangle$-envelope | 3.30 | 0.2652 | 0.0152 | 0.2343 | 0.7243 |

within a thin layer, while the remaining entropy jump is prescribed by the $\langle$3D$\rangle$-envelope. The role plaid by $\alpha_{\rm MLT}$ thus changes substantially.

The obtained $\alpha_{\rm MLT}$ for the solar model is listed in Table 8.1 alongside other quantities that result from the solar calibration. $Y_{\rm S}$ in Table 8.1 denotes the surface helium abundance and should be compared to the seismic value obtained by Basu and Antia (2004): $0.2485 \pm 0.0035$. $r_{\rm cz}$ denotes the radius at the base of the convection zone and should be compared to the value that has been seismically inferred by Basu and Antia (1997): $0.713 \pm 0.001 R_\odot$. For both quantities, the discrepancy between the model and observations can be attributed to the use of AGSS09 (cf. Serenelli et al. 2009).

Table 8.1 also contains the corresponding values for a standard solar calibration that employs an Eddington grey atmosphere. As can be seen from Table 8.1, the coupling of 1D and 3D models does not affect $Y_{\rm S}$ or $r_{\rm cz}$ significantly. We attribute the fact that both solar calibration models lead to nearly identical radii at the base of the convection zone to their very similar boundary conditions. Furthermore, this behaviour can be explained by the fact that all models are required to recover the same global parameters, i.e. $L_\odot$, $R_\odot$, $M_\odot$ and $(\mathrm{Z_S/X_S})_\odot$, which leads to the same asymptotic entropy of the deep adiabat.

#### 8.1.2.1 The Structure of the Outermost Layers

We now compare the structure obtained by GARSTEC with that of the 3D simulation in the Stagger grid, whose global parameters correspond to the solar values. The results are shown in Figs 8.2-8.4. The figures include both GARSTEC models from Table 8.1: one uses the Stagger grid as its boundary conditions and appends the corresponding $\langle$3D$\rangle$-envelope at each time-step, while the other employs an Eddington grey atmosphere.

Figure 8.2 shows $T(P_{\rm gas})$. By construction, our new scheme reproduces this stratification correctly. From Fig. 8.3, we see that the EOS used by the 1D evolution code closely recovers $\rho(P_{\rm gas})$, although the density is systematically $1 - 2\,\%$ too low. This may partly reflect differences in the EOS used by the 1D and 3D codes. Furthermore, since $\rho$ is a non-linear function of $P_{\rm th}$ and $T$, the geometrical mean of the density in the Stagger grid is not expected to correspond to the density derived from the average of $P_{\rm th}$ and $T$ (cf. R. Collet, private communication). We note that the use of $P_{\rm gas}$ rather than $P_{\rm th}$ cannot explain the discrepancy in the density profile (cf. Chapter 10).

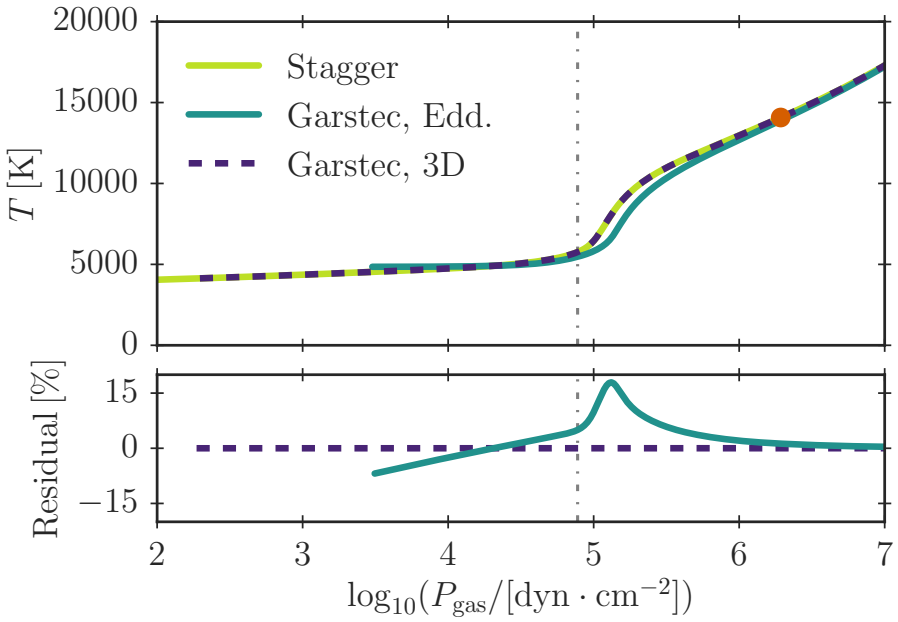


Figure 8.2: **Upper panel:** Temperature as function of gas pressure for the ⟨3D⟩ solar envelope in the Stagger grid as well as the two solar calibrations listed in Table 8.1. **Lower panel:** Residuals between the solar Stagger-grid ⟨3D⟩-envelope and each solar calibration model relative to the corresponding value in the Stagger-grid ⟨3D⟩-envelope. The vertical grey line indicates the position of the photosphere. The red dot denotes the location of the matching point.

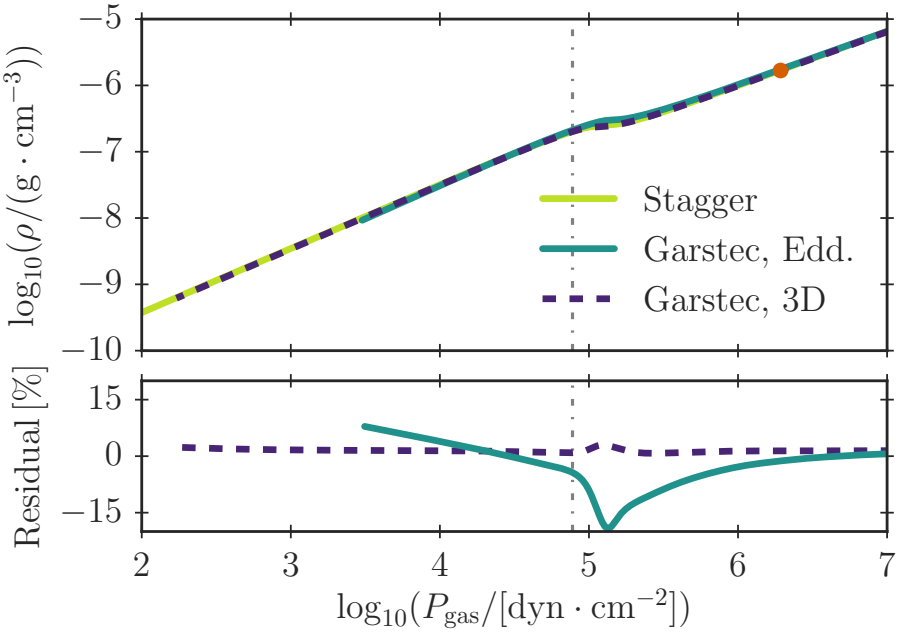


Figure 8.3: As Fig. 8.2 but for the density as a function of gas pressure. The lower panel shows the residuals in $\rho$ rather than $\log(\rho)$.

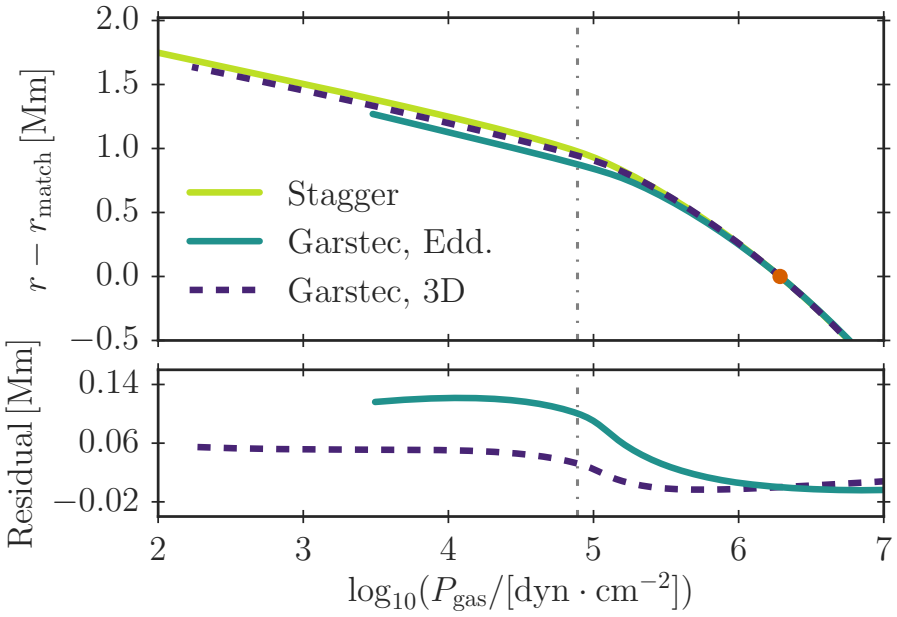


Figure 8.4: As Fig. 8.2 but for the height above the matching point as a function of gas pressure. Here we show the absolute residuals.

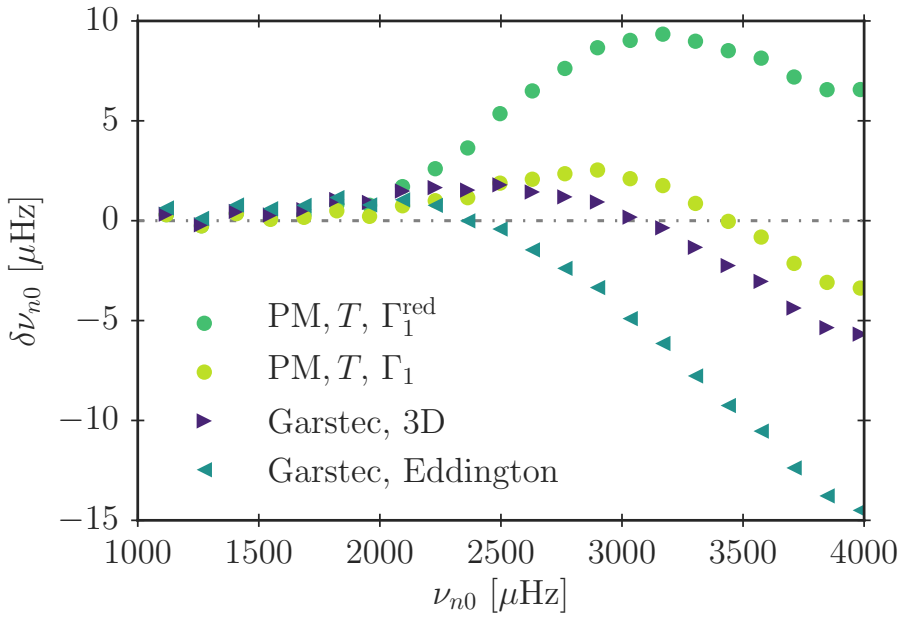


Figure 8.5: Frequency difference between BiSON observations and the solar models listed in Table 8.1. We only include radial modes ($\ell = 0$) with frequencies above 1000 $\mu$Hz.

Figure 8.4 shows that our method closely[2] reproduces the depth of the underlying 3D envelope as a function of gas pressure, despite the neglect of turbulent pressure and the discrepancy in $\rho$. Thus, our new method reproduces the expected $\langle$3D$\rangle$-structure from the Stagger grid very well, without the need for post-evolutionary patching. The Eddington grey atmosphere shows much larger residuals, as was to be expected.

#### 8.1.2.2 Oscillation Frequencies

Having obtained a structure that closely resembles the mean stratification of 3D simulations, we have computed stellar oscillation frequencies using ADIPLS. Figure 8.5 shows the frequency differences, $\delta\nu_{n\ell}$, between the predicted model frequencies and BiSON observations.

For comparison, we have also included a patched model (PM) in Fig. 8.5, i.e. a model, for which we have substituted the outermost layers *of the present-day Sun* with the entire mean structure of the solar Stagger-grid $\langle$3D$\rangle$-envelope (cf. Chapter 6). We have used $T$ to determine the radius at which to patch. The patch has been performed at a depth of 2.1 Mm below the surface, i.e. further down within the nearly-adiabatic region than the matching point. The patched model has been constructed such that it has the same interior as the final solar calibration model, whose outer layers are dictated by the Stagger grid. As opposed to the models constructed on the fly, the patched model hence includes turbulent

[2]We note that $\log g$ is assumed to be constant in the Stagger-grid $\langle$3D$\rangle$-envelope, in contrast to the 1D simulation. This slightly skews the comparison in $r$.

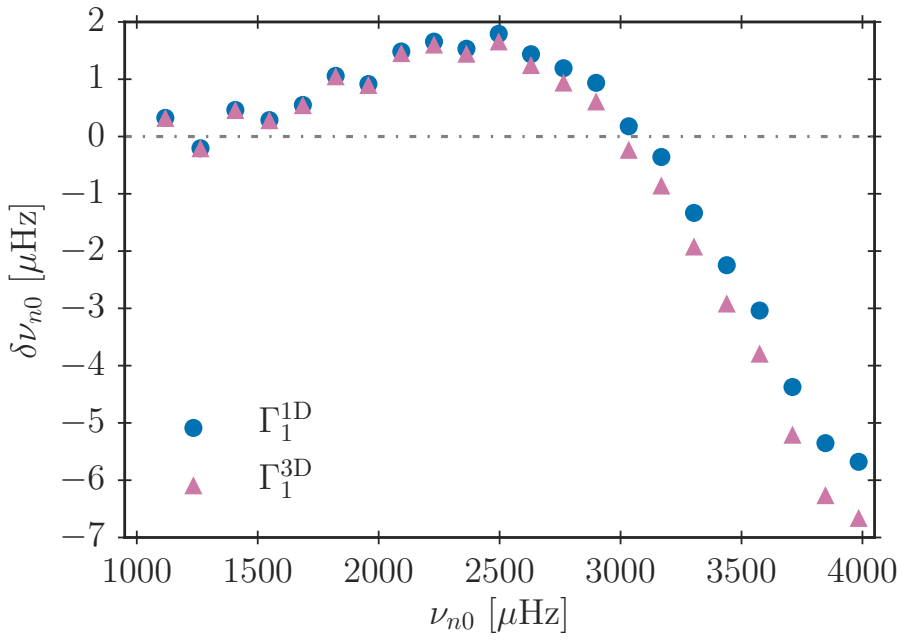


Figure 8.6: Frequency difference, $\delta\nu_{n\ell}$, between our solar calibration model and observations, using two different stratifications for the first adiabatic index: $\Gamma_1^{1D}$ denotes the value obtained from GARSTEC's EOS, while $\Gamma_1^{3D}$ comes from the stratification of the appended interpolated $\langle 3D \rangle$-envelope.

pressure in the $\langle 3D \rangle$-envelope. Turbulent pressure was neglected during the entire evolution and is not taken into account below the patched $\langle 3D \rangle$-envelope (see also Chapter 10).

As regards the patched models, we have computed frequencies, using both the reduced $\Gamma_1$ and the gas $\Gamma_1$ approximation. Computing frequencies within the gas $\Gamma_1$ approximation allows an easy comparison with our coupled models. Using the reduced $\Gamma_1$ approximation illustrates the vital role played by turbulent pressure.

As can be seen from the figure, our new method leads to model frequencies that are very similar to the frequencies obtained from patched models when using $\Gamma_1$ in the frequency calculations: at 4000 $\mu$Hz the remaining frequency difference between our solar calibration and observations is only 6 $\mu$Hz, while the frequency difference is 15 $\mu$Hz at the same frequency, when using an Eddington grey atmosphere. With our new method, we are thus able to significantly reduce the structural contribution to the surface effect.

The remaining frequency differences between the patched models and our solar calibration model that employs the Stagger grid as its boundary conditions can partly be attributed to the neglect of turbulent pressure and the discrepancies in the density stratification. Furthermore, these frequency differences will, at least to some extent, reflect the patching and matching depths. As will be discussed in Section 8.2, however, the frequencies are rather insensitive to the scaled pressure at the matching point if the matching point is placed sufficiently deep within the superadiabatic region.

As noted in 8.1.2.1, the density inferred from GARSTEC's EOS does not correspond to the interpolated mean density of 3D simulations. The same holds true for other quantities obtained from the EOS, such as $\Gamma_1$ that is essential for the inferred seismic properties. In order to quantify how the use GARSTEC's EOS affects the seismic results through the inferred value of $\Gamma_1$, we substituted the stratification of $\Gamma_1$ in our calibrated solar model ($\Gamma_1^{\mathrm{1D}}$) with that from the underlying interpolated $\langle$3D$\rangle$-envelope ($\Gamma_1^{\mathrm{3D}}$). In other words, based our new standard solar model, we constructed a patched model, where we only substituted $\Gamma_1$, leaving the remaining quantities untouched. The resulting frequency shift is illustrated in Fig. 8.6: the mismatch between $\Gamma_1^{\mathrm{1D}}$ and $\Gamma_1^{\mathrm{3D}}$ leads to a frequency shift of less than $1\,\mu$Hz for all frequencies below $4000\,\mu$Hz.

#### 8.1.2.3 The Matching Depth

The obtained value of $\alpha_{\mathrm{MLT}}$ is affected by the matching depth: in accordance with the explanation given above and the findings by Schlattl et al. (1997), $\alpha_{\mathrm{MLT}}$ increases monotonically with increasing matching depth. This is illustrated in Fig. 8.7, where we show the mixing length parameter for ten solar calibrations. For each calibration, the matching point is set at a different scaled pressure throughout the solar evolution, which results in different matching depths for the obtained model of the present-day Sun. As discussed in Section 8.2, the increase of $\alpha_{\mathrm{MLT}}$ with matching depth is shown not to shift the evolution track significantly, if the matching point is placed sufficiently deep within the superadiabatic region. Moreover, as argued in Chapter 9, the evolution tracks are rather insensitive to the exact value of $\alpha_{\mathrm{MLT}}$, even for a fixed matching depth. In Chapter 9, the match is performed deep within the superadiabatic region.

The figure also includes the frequency difference between the predicted frequency of the radial mode with $n = 28$ and the corresponding observed frequency as a function of the matching depth in the present-day Sun. As can be seen from the figure, this frequency difference becomes virtually insensitive to the matching depth, if the matching point is placed sufficiently deep within the superadiabatic region. This happens at a depth of roughly 0.6 Mm below the photosphere, which roughly coincides with the minimum of $\Gamma_1^{\mathrm{1D}}$ near the surface.

## 8.2 Stellar Evolution and Asteroseismic Applications

In this section, we investigate how the coupling of 1D and 3D models affects stellar evolution tracks. Having established that our method leads to solar models that reliably mimic the underlying 3D simulations, we furthermore apply our method to different target stars and test the robustness of the scheme throughout the $(T_{\mathrm{eff}}, \log g)$-plane in Section 8.2.2.

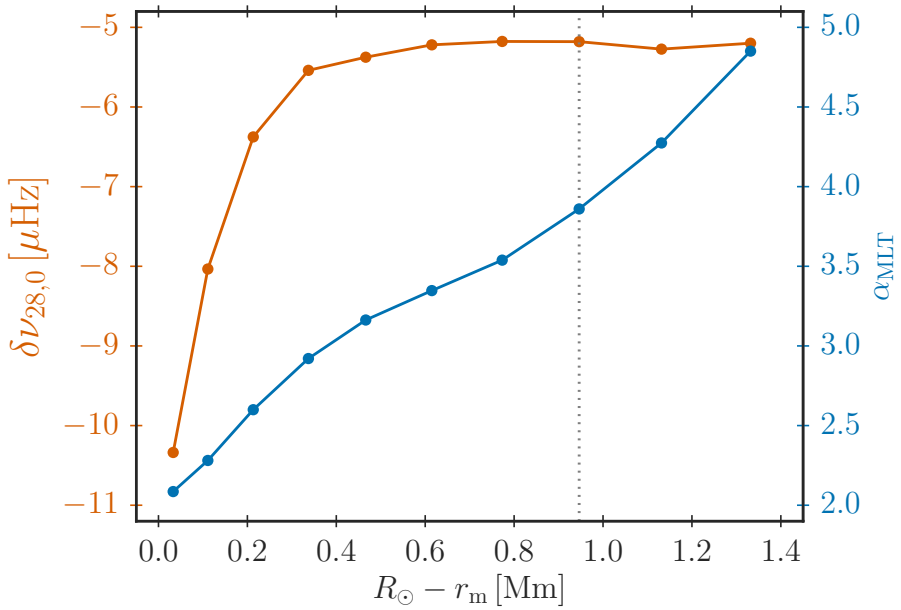


Figure 8.7: The calibrated mixing length parameter ($\alpha_{\mathrm{MLT}}$) obtained from solar calibrations and the resulting frequency difference between observations and model frequencies of radial order $n = 28$ — i.e. at roughly 4000 $\mu$Hz. Here, $r_{\mathrm{m}}$ denotes the radius, at which the matching point is placed. The dotted line shows the matching depth for the solar calibration model, for which the scaled pressure at the matching point is 16 times higher than at the density inflection. This is the same scaled pressure as for the solar calibration model, for which we present an in-depth analysis in this section. However, it is not the same model. Here, we employ a different effective temperature for the solar calibration. Thus, we use the standard value in GARSTEC rather than fixing the effective temperature to the effective temperature of the solar Stagger-grid simulation. Consequently, $\alpha_{\mathrm{MLT}}$ is also slightly higher than in Table 8.1.

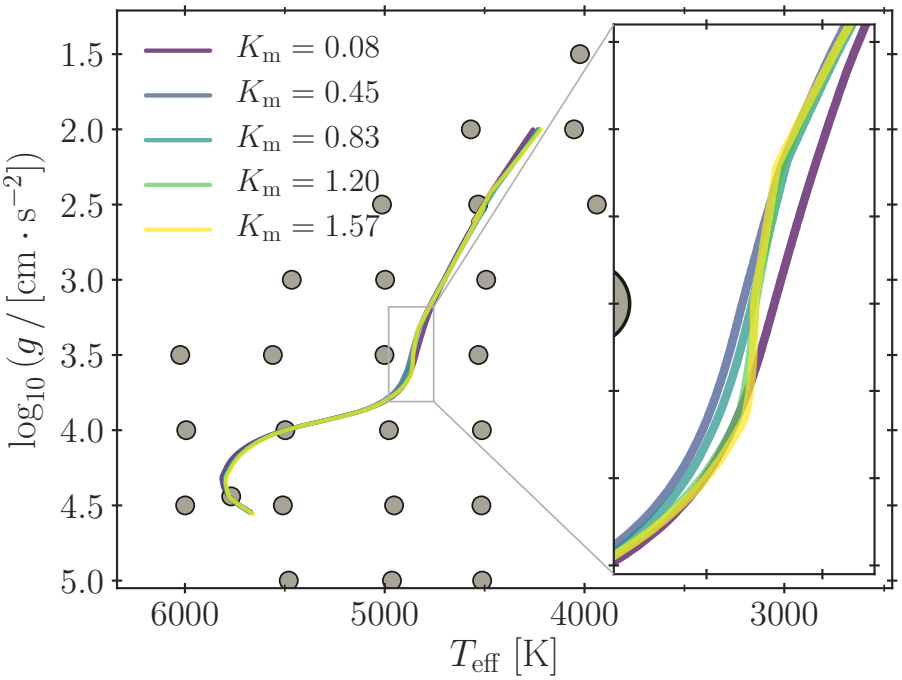


Figure 8.8: Stellar evolution tracks for five solar calibrations. $K_\mathrm{m}$ denotes the associated scaled pressures at the matching point for each simulations. For the present-day Sun, the five values of $K_\mathrm{m}$ correspond to a matching depth of 0.11 Mm, 0.34 Mm, 0.61 Mm, 0.95 Mm, and 1.33 Mm, respectively. The location of a selection of Stagger-grid simulations at solar metallicity are shown using grey dots.

## 8.2.1 Further Investigations of the Sun

### 8.2.1.1 The Matching Depth

In order to investigate how the matching depth affects the predicted stellar evolution tracks, we computed numerous solar calibration models, for which the matching point was set at different scaled pressures. The resulting evolution tracks from the ZAMS to the RGB are shown in Fig. 8.8. Here, we let $K_\mathrm{m}$ denotes the logarithm of the scaled pressure at the matching point, i.e. the ratio between the pressure at the matching point and that at the density inflection. In Section 8.1, the pressure at the matching point is 16 times higher than at the density inflection, which corresponds to $K_\mathrm{m} = 1.20$.

Changes in $K_\mathrm{m}$ are associated with dramatic changes in $\alpha_\mathrm{mlt}$. This was shown in Fig. 8.7 in Section 8.1. Despite this fact, the evolution tracks only change moderately with $K_\mathrm{m}$ compared to the changes that would occur for a standard stellar model that relies on MLT to describe the surface layers, assuming the same values of $\alpha_\mathrm{mlt}$ (cf. Chapter 9). However, with increasing matching depth, we see an increase in the number of kinks in the obtained evolution tracks. We attribute these kinks to interpolation errors. In order to test this assumption, we extended the Stagger grid by a set of additional interpolated $\langle$3D$\rangle$-envelopes:

Table 8.2: Derived initial parameters as well as the helium surface abundance and the radius at the base of the convection zone for three solar calibrations, using an Eddington grey atmosphere, the Trampedach grid or the method suggested by Trampedach et al. (2014a,b) to set the outer boundary condition.

| Model | $\alpha_{\mathrm{MLT}}$ | $Y_{\mathrm{i}}$ | $Z_{\mathrm{i}}$ | $Y_{\mathrm{S}}$ | $\frac{r_{\mathrm{cz}}}{R_\odot}$ |
|---|---|---|---|---|---|
| Eddington | 1.71 | 0.2680 | 0.0201 | 0.2388 | 0.7122 |
| RT2014 | 1.82 | 0.2680 | 0.0201 | 0.2388 | 0.7122 |
| $\langle$3D$\rangle$-envelope | 5.36 | 0.2678 | 0.0200 | 0.2387 | 0.7122 |

GARSTEC performs a linear interpolation, while the external routines that were written for patched models use cubic splines (cf. Chapter 5). The accuracy of the external routines are, therefore, higher and can to some extent be used to artificially increase the resolution of the Stagger grid — at least for such a test case. Following this procedure, we did indeed see that the kinks were affected. Note that two types of interpolations are involved: the interpolation in the $(\log T_{\mathrm{m}}^{\mathrm{1D}}, \log g)$-plane to obtain $T_{\mathrm{eff}}$ and the subsequent interpolations in the $(\log T_{\mathrm{eff}}, \log g)$-plane. Since both interpolations are intertwined and enter the boundary conditions, it is very intricate, if not impossible, to determine, which of the two types of interpolation contributes most significantly to the interpolation errors.

Generally speaking, the matching point should be placed as deep within the nearly-adiabatic region as possible, in order to extract as much information from the 3D simulations as is available. On the other hand, due to the interpolation errors, choosing the matching depth becomes a compromise: the matching point should be placed far into the nearly-adiabatic region but not so deep that interpolation errors become significant.

#### 8.2.1.2 The Trampedach Grid

Throughout this chapter, our conclusions have been drawn based on the Stagger grid. In order to assess the flexibility of our method, we have repeated some of the analysis above, using the Trampedach grid (cf. Chapter 5, Trampedach et al. 2013). For this purpose, we have performed a solar calibration with $K_{\mathrm{m}} = 0.88$, which for the present Sun corresponds to a matching depth of 0.64 Mm. While the appended $\langle$3D$\rangle$-envelope is hence somewhat shallower than in the case of the Stagger grid, the matching point is still placed within the nearly-adiabatic region. For the sake of consistency, we use the mixture by Trampedach et al. (2013) and the atmospheric opacities by Trampedach et al. (2014a) in combination with the opacities by Badnell et al. (2005).

Employing the Trampedach grid has one compelling advantage: it allows a direct comparison with a different implementation of 3D simulations into GARSTEC. As suggested by Trampedach et al. (2014a,b), one may use 3D simulations to derive a $T(\tau)$ relation as well

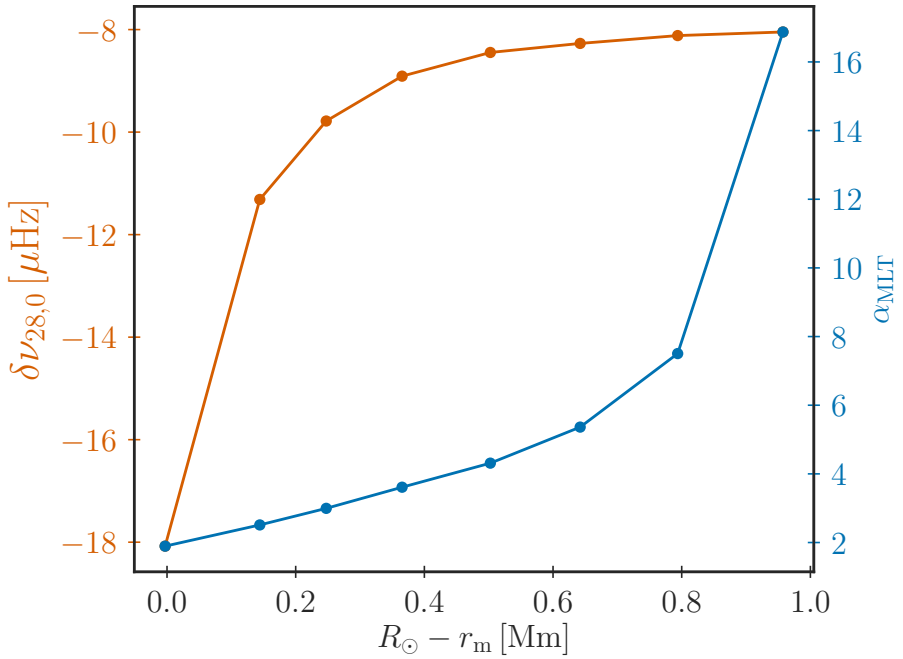


Figure 8.9: Same as Fig. 8.7 but for coupled models that use the Trampedach grid. This figure is neither included in Jørgensen et al. (2018) nor in its companion paper.

as to calibrate the mixing length parameter. The differences between this procedure and the standard method are hence three-fold: firstly, $\alpha_{\mathrm{mlt}}$ varies across the HR diagram. Secondly, a different $T(\tau)$ relation is imposed above the photosphere. Thirdly, the radiative temperature gradient is adjusted for optical depths below 10, in order to give a more realistic depiction of the photospheric transition. The scheme was introduced into GARSTEC by Mosumgaard et al. (2018) (cf. Chapter 2). We refer to the associated solar calibration model as RT2014. The specifications of this solar calibration model are summarized in Table 8.2 alongside the corresponding values for a coupled solar model that is based on the Trampedach grid and a standard solar model that uses MLT and relies on an Eddington grey atmosphere to set the outer boundary conditions. As can be seen from the Table 8.2, all three solar calibrations result in the same initial composition and lead to the same helium surface abundance and the same radius at the base of the convection zone. The most prominent difference is that the coupled model requires a much higher mixing length parameter. This is in good agreement with the qualitative conclusions drawn when performing the analysis based on the Stagger grid.

By repeating the solar calibration for different $K_\mathrm{m}$, we confirm that the mixing length parameter increases monotonically with the matching depths. Furthermore, the stellar oscillation frequencies become insensitive to the matching depth, if the matching point is placed sufficiently deep within the nearly-adiabatic layers. Both findings confirm the conclusions drawn from the Stagger grid (cf. Fig. 8.7). This is shown in Fig. 8.9.

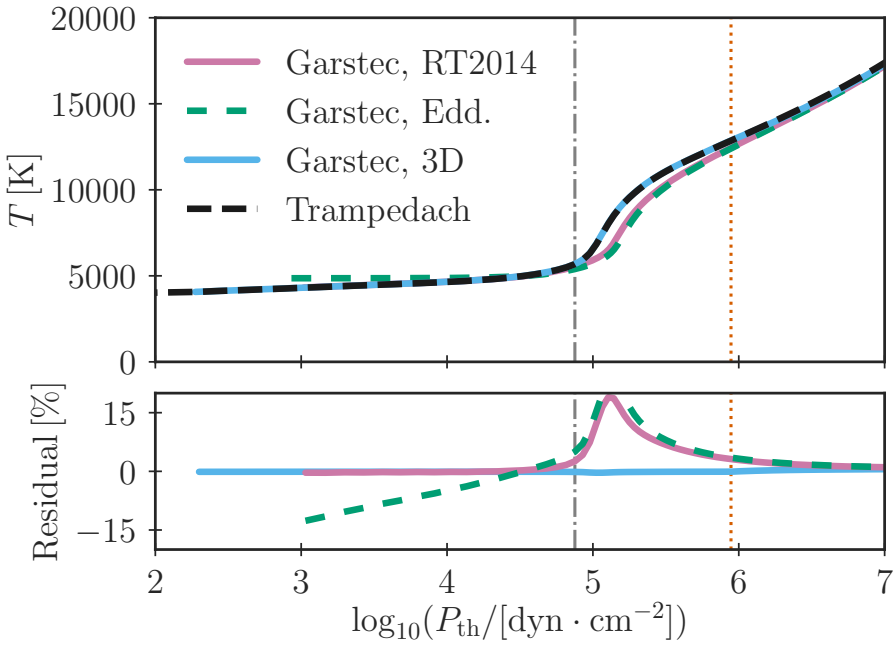


Figure 8.10: Temperature stratification of the three solar calibration models from Table 8.2. The dotted red line shows the location of the matching point of the ⟨3D⟩-envelope in the coupled model. The dash-dotted line marks the location of the photosphere. The lower panel shows the associated residuals between the solar calibration models and the solar envelope simulation in the Trampedach grid. Note that we have used the thermal pressure rather than the gas pressure when dealing with the Trampedach grid.

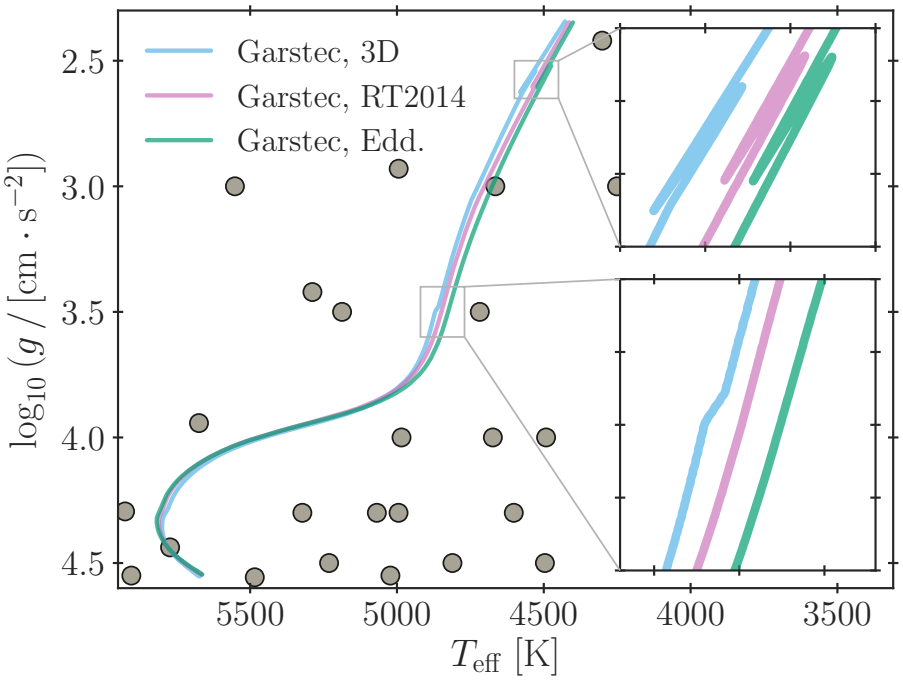


Figure 8.11: Stellar evolution tracks for the three solar calibration models presented in Table 8.2. The location of a selection of Trampedach-grid simulations is depicted, using grey dots.

The structure of the outermost layers of all three solar calibration models from Table 8.2 are shown in Fig. 8.10. As regards the coupled model, GARSTEC is able to reliably recover the correct outermost layers, despite the fact that the Trampedach grid is highly irregular. This underlines the versatility of our method. As regards, RT2014, on the other hand, the underlying method only performs better than the standard procedure above the photosphere: while $\alpha_{\mathrm{mlt}}$ is calibrated to recover certain properties of 3D simulations, a single value of the mixing length parameter is clearly insufficient to entail the complexity of turbulent convection (see also Chapter 6).

The stellar evolution tracks for all three solar calibration models are shown in Fig. 8.11. As regards these evolution tracks, both implementations of information from 3D simulations into our 1D stellar evolution code lead to similar deviations from the standard procedure: both the coupled model and RT2014 predict a lower effective temperature at the turn-off point and higher effective temperatures on the RGB.

The fact that the improved boundary conditions affect the turn-off point is crucial since turn-off stars are used to age clusters (cf. Cummings and Kalirai, 2018). Furthermore, since stellar evolution tracks converge on the RGB, the predicted shift of the RGB towards higher temperatures may potentially severely affect parameter estimates, when comparing models to data. Accurate parameter estimates for red giants play a crucial role when attempting to unravel the chemical history of our host galaxy (Miglio, 2012): estimates of stellar ages

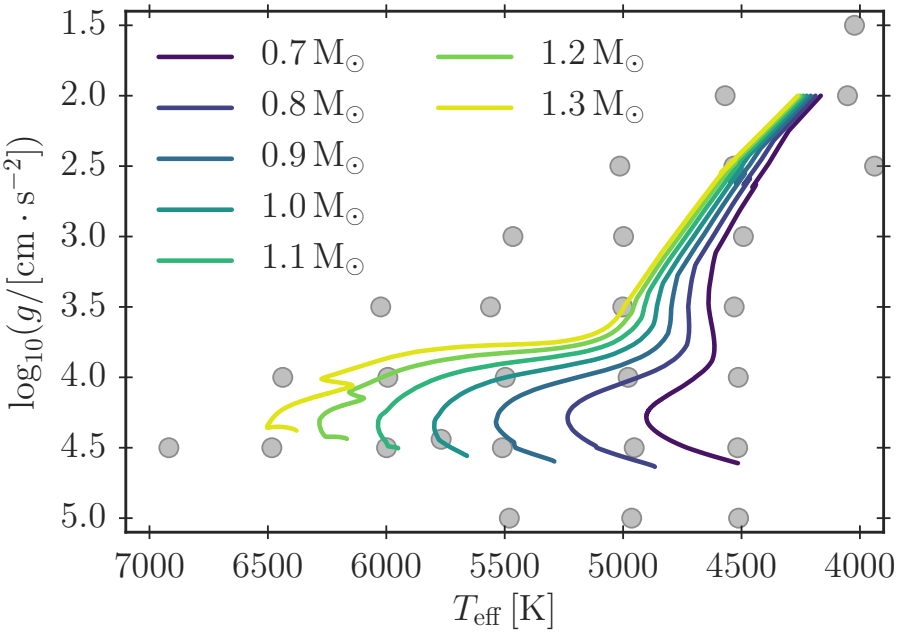


Figure 8.12: Stellar evolution tracks for a handful of coupled stellar models from the MS to the RGB.

underly the current picture of chemo-dynamical evolution of the Milky Way galaxy. The improved characterization of single stars that results from the use of more realistic boundary conditions may hence contribute to a better understanding of stellar populations, clusters, and galaxies. We plan to quantify this statement and address this topic in future projects (cf. Chapter 12). In this thesis, we have already started this endeavour by addressing main-sequence (MS) stars, as discussed in Section 8.2.2 and Chapter 9.

### 8.2.2 A Grid Search

We have computed a grid of coupled stellar models, using the Stagger grid with $K_{\rm m} = 1.20$. The grid contains models with masses between $0.7\,{\rm M}_\odot$ and $1.3\,{\rm M}_\odot$ in steps of $0.002\,{\rm M}_\odot$. Based on a solar calibration, we set $\alpha_{\rm MLT} = 3.86$, $Y_{\rm i} = 0.2659$ and $Z_{\rm i} = 0.0152$. This solar calibration differs from that presented in Section 8.1 in so far that the effective temperature is 10 K higher, i.e. we use the standard value in GARSTEC rather than the global parameters of the solar Stagger-grid simulation. In order to avoid inconsistencies between the assumed composition of the appended ⟨3D⟩-envelope and the abundances used by GARSTEC, we have not included microscopic diffusion in the coupled stellar models. All models have solar metallicity.

A representative subset of the computed evolution tracks is shown in Fig. 8.12. As in the case of the solar model, these tracks include kinks that we attribute to interpolation errors. These are especially pronounced on the RGB. The location of these kinks occur along lines that connect simulations, which seems to confirm the suspicion that the underlying cause is

connected with the triangulation that enters the interpolation scheme.

#### 8.2.2.1 The Structure of Different Evolutionary Stages

Some of the evolution tracks pass through an existing Stagger-grid simulation, which allows a direct comparison between our coupled models and the underlying $\langle 3\mathrm{D} \rangle$-envelopes. We have performed six such comparisons, requiring $\log g$ at the matching point and $T_{\mathrm{eff}}$ to match within 1 K and 0.01 dex. Several stellar models fulfil these criteria. For each 3D simulations that we compare with, we thus selected the model that minimizes the error in $\log g$ at the matching point. As a result, the mismatch in $\log g$ is $\lesssim 2 \times 10^{-3}$ dex for all performed comparisons. The solar model is an exception: it deviates by 10 K from the corresponding Stagger-grid simulations, i.e. it is not the same model as in Section 8.1. The residuals between the temperature stratifications of our stellar models and the corresponding Stagger-grid simulations are shown in the upper panel of Fig. 8.13.

As discussed when describing the method in Section 8.1.1, the temperature stratification is obtained by interpolation, i.e. any misrepresentation of the temperature profile may solely stem from interpolation errors. However, since the recovered stratifications are contained within the envelope grid, no interpolation is required, unless there is a mismatch between the global parameters of the investigated coupled models and the those of the 3D simulations that we compare with. Even without interpolation errors, such mismatches lead to temperature residuals. The residuals in the upper panel of Fig. 8.13 thus solely stem from such mismatches and the associated interpolation errors. Indeed, we find the residuals to be rather sensitive to mismatches in the global parameters. By increasing the discrepancy in $\log g$ for the most evolved model ($T_{\mathrm{eff}} = 4500$ K and $\log g = 2.5$) from $5 \times 10^{-5}$ to $2 \times 10^{-3}$ dex, we thus find the residuals in $T$ to increase from, at most, 0.06 % to more than 1 % — we note that the involved coupled models also differ in other stellar parameters, such as the mass.

For all models, we note that the residuals in $T$ show a peak close to the surface near the pressure, at which a sharp decrease in temperature occurs. In other words, this peak signifies a displacement of the stellar surface.

The associated residuals between the density stratifications of our stellar models and the corresponding Stagger-grid simulations are shown in the lower panel of Fig. 8.13. As discussed in Section 8.1.1, the density is computed from the EOS based on the pressure, the temperature, and the chemical composition. One may, therefore, expect that the residuals in the density, to a large extent, reflect the errors in the computed temperature stratifications shown in the upper panel of Fig.8.13. However, while we find that a larger mismatch in $\log g$ leads to much larger discrepancies in the temperature profile, we find that the models that show much larger residuals in $T$ do not lead to significantly larger residuals in $\rho$. In other words, while the residuals in $\rho$ partly reflect the discrepancies in the temperature profile, they are mostly determined by other factors. Thus, the discrepancies in the density largely stem from the non-linearity of the EOS (cf. Section 8.1) or deviations between the composition of the Stagger grid and the solar model — since our models do not include diffusion, the latter contribution has been minimized. Again, the most prominent feature

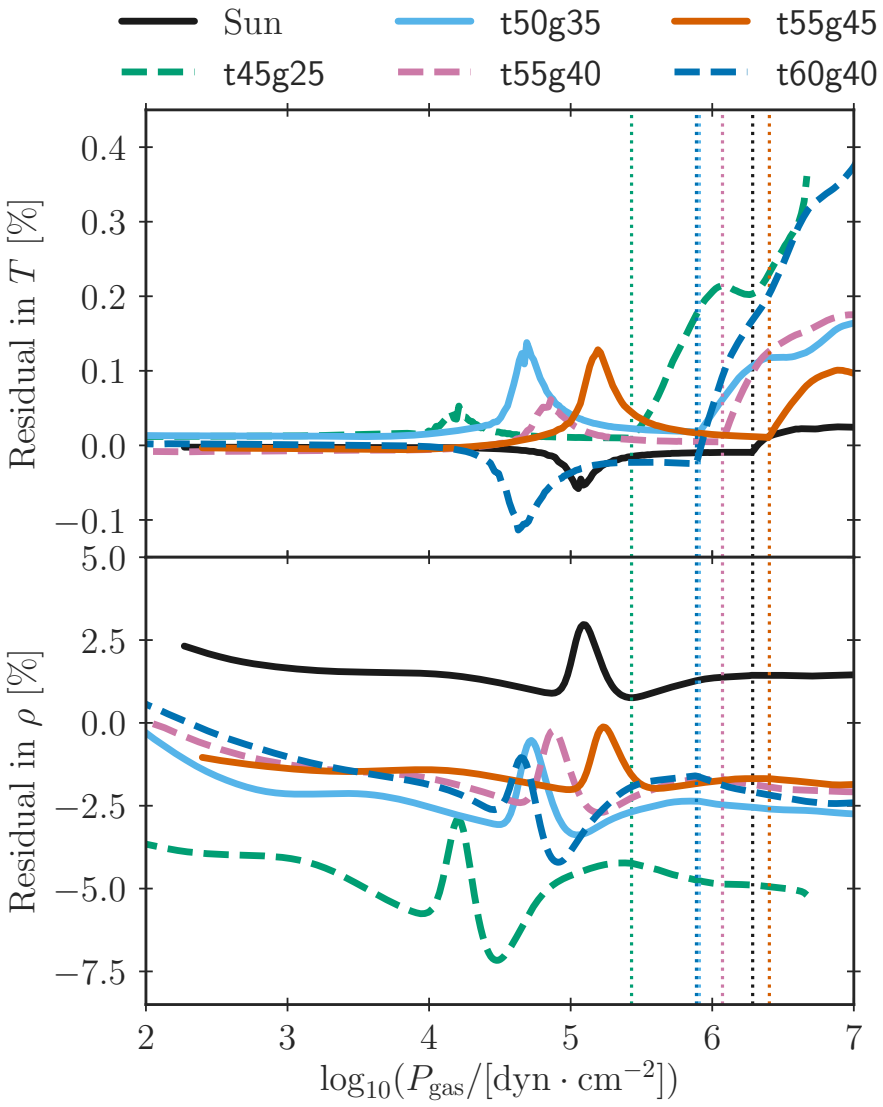


Figure 8.13: **Upper panel:** Residuals between the temperature stratification of existing Stagger-grid simulations and the computed structure of coupled models with the same $T_{\mathrm{eff}}$ and $\log g$. The naming of the models is based on these two global parameters: for instance, `t45g25` has a $T_{\mathrm{eff}}$ of 4500 K and a $\log g$ of 2.5. The dotted lines show the location of the matching point for each of the six coupled models. **Lower panel:** The equivalent plot for the residuals of the density stratification.

Table 8.3: Model parameters for *Kepler* stars using coupled and standard stellar models. The latter models draw on MLT and Eddington grey atmospheres (Edd.). We list the median of the corresponding probability distributions from BASTA as the parameter estimates. The uncertainties correspond to the 16th and 84th percentile.

| KIC | Model | $T_{\rm eff}$ [K] | $\log g$ [cgs] | Mass [$M_\odot$] | $R_{\rm phot}$ [$R_\odot$] | Age [Myr] |
|---|---|---|---|---|---|---|
| 9955598 | *Edd.* | $5572^{+13}_{-13}$ | $4.4983^{+0.0011}_{-0.0012}$ | $0.897^{+0.005}_{-0.005}$ | $0.8839^{+0.0021}_{-0.0019}$ | $6997^{+360}_{-349}$ |
| 9955598 | *Coupled* | $5584^{+10}_{-10}$ | $4.4989^{+0.0011}_{-0.0012}$ | $0.899^{+0.004}_{-0.005}$ | $0.8840^{+0.0019}_{-0.0019}$ | $6944^{+352}_{-322}$ |
| 11772920 | *Edd.* | $5423^{+15}_{-15}$ | $4.5061^{+0.0013}_{-0.0013}$ | $0.849^{+0.005}_{-0.006}$ | $0.8520^{+0.0023}_{-0.0023}$ | $9874^{+528}_{-499}$ |
| 11772920 | *Coupled* | $5449^{+16}_{-16}$ | $4.5069^{+0.0013}_{-0.0013}$ | $0.852^{+0.006}_{-0.006}$ | $0.8529^{+0.0023}_{-0.0022}$ | $9752^{+510}_{-506}$ |

of each in the density residuals arises near the surface, reflecting a misplacement of the surface of the coupled models in comparison to the 3D simulations.

### 8.2.3 Modelling *Kepler* Stars

Here, we turn to an investigation of two stars in the *Kepler* field: KIC 9955598 and KIC 11772920. We performed a grid search for both stars and established posterior probability distributions, using BASTA, a Bayesian framework developed by Silva Aguirre et al. (2015) (cf. Chapter 6). For this purpose, we computed a set of denser grids of stellar models with masses between $0.80\,M_\odot$ and $0.95\,M_\odot$ in steps of $0.001\,M_\odot$: one grid employs MLT and Eddington grey atmospheres, while the other grid is composed of coupled models. We fixed the metallicity to 0.0 and did not include microscopic diffusion. The likelihood was established using frequency ratios (cf. Chapter 6). Furthermore, the radial oscillation with the lowest observed order was required to fit within $3\,\sigma$.

#### 8.2.3.1 Best-Fitting Models

Based on our grid search, we determined the best-fitting models for both stars, using either grid. The frequencies of the best-fitting models are compared to observations in Figs 8.14 and 8.15. In accordance with the solar case, the use of coupled stellar models severely reduces the surface effect and leads to model frequencies that lie much closer to the observed frequencies than models with Eddington grey atmospheres do.

The same behaviour is found for the best-fitting models in the case of KIC 11772920. For comparison, we have furthermore computed patched models (PMs) based on the best-fitting coupled models for this *Kepler* star (cf. Chapter 6). As established above, the appended $\langle 3D \rangle$-envelopes of coupled models are not entirely identical to the underlying 3D simulations, due to interpolation errors, and since GARSTEC relies on its EOS to determine some thermodynamic quantities. By substituting the outermost layers of our models with a

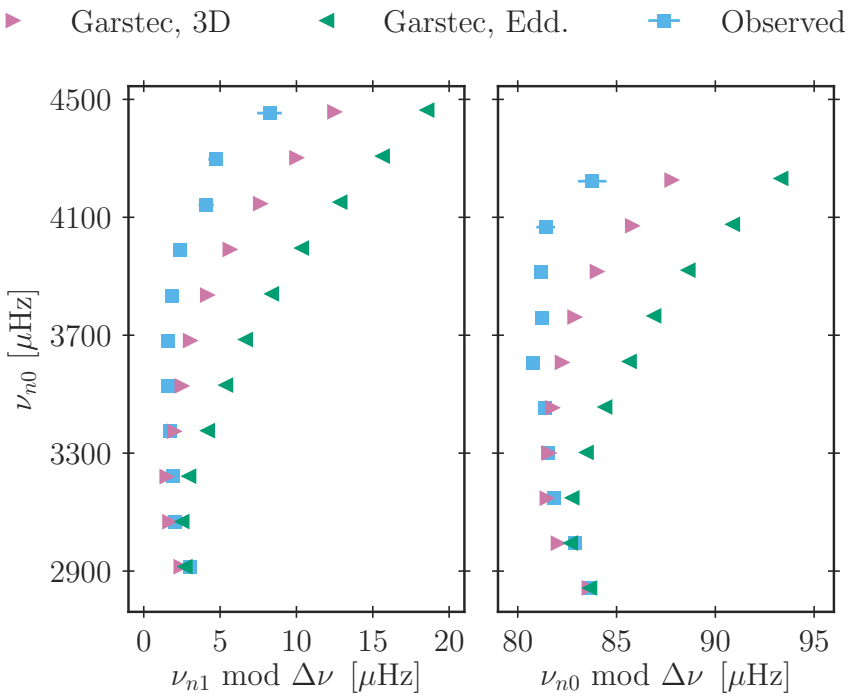


Figure 8.14: Echelle diagram for KIC 9955598 based on frequencies with $\ell = 0$ (right) and $\ell = 1$ (left). The abscissa shows the frequencies of each mode modulo the large frequency separation. All frequencies are computed within the gas $\Gamma_1$ approximation (cf. Chapter 3).

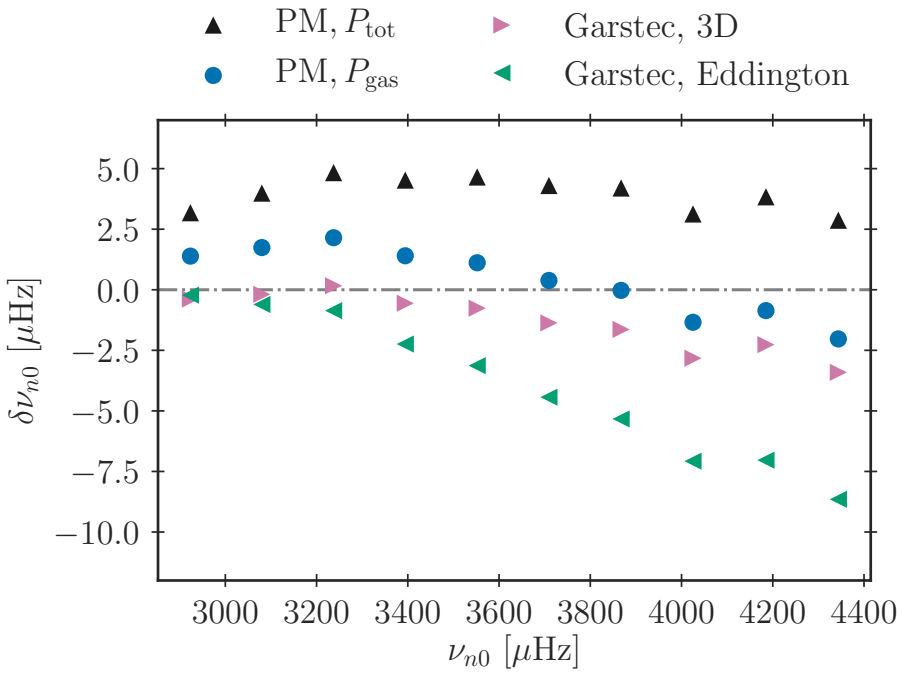


Figure 8.15: Frequency difference between the best-fitting model and observations for KIC 11772920. We only include radial modes ($\ell = 0$). For comparison, we have included two patched models (PM, cf. Chapter 6). For one of the PMs, we used the gas pressure ($P_{\mathrm{gas}}$) as the coordinate, when computing the patched $\langle$3D$\rangle$-envelope. For the other PM, we used the total pressure ($P_{\mathrm{tot}}$), hereby including turbulent pressure. All frequencies are computed within the gas $\Gamma_1$ approximation (cf. Chapter 3).

$\langle$3D$\rangle$-envelope, for which all quantities have been obtained by interpolation, we can hence illustrate the combined remaining structural inadequacies of our coupled models. We find the mismatch in the oscillation frequencies between the coupled and patched models to be smaller than $2\,\mu$Hz at all frequencies when neglecting the turbulent pressure in the PMs. This also implies that the turbulent pressure is not included in the computation of $r$. When we include the turbulent pressure, we obtain an additional frequency shift of roughly $2-5\,\mu$Hz. This illustrates the importance of including turbulent pressure. We address this issue in Chapter 10.

The global parameter estimates that result from the grid searches are listed in Table 8.3. We find that the use of coupled and standard stellar models yield parameter estimates that are mutually consistent. In other words, the stellar evolution tracks and interior structure of coupled and standard stellar models do not strongly deviate for stars on the main sequence. We will take a closer look at this issue in Chapter 9.

## 8.3 Summary

In this chapter, we have presented a novel method for including the mean pressure and temperature stratifications from 3D simulations directly in 1D stellar evolution codes, and we exploit this to adjust the structure at every time-step. This has been achieved without the need for parameterizations or post-evolutionary patching. Section 8.1 presents the first computation of stellar models, for which the structure from 3D simulations has been fully accounted for on the fly. The structure of the resulting 1D models is in very good agreement with the underlying 3D simulations, despite the neglect of turbulent pressure, and despite the fact that only a limited amount of information is taken from the 3D simulations.

We find that our new method is largely able to eliminate the structural surface effect, leading to very promising p-mode frequencies. Modal effects have not been accounted for. A direct comparison with post-evolutionary patched models shows only small frequency differences. We largely attribute the remaining differences to the neglect of turbulent pressure, which is treated in Chapter 10. Further deviations between the coupled models and the underlying 3D simulations are introduced by the non-linearity of the EOS.

In the case of the present-day Sun, our analysis confirms that post-evolutionary patching provides an adequate structural correction. A disadvantage of patching, however, is that it relies on the assumption that the evolution tracks are unaltered by the use of crude outer boundary conditions and mixing length theory. Our method, on the other hand, overcomes this deficiency by adjusting the structure of stellar models on the fly based on 3D simulations. The impact of our new method on the evolution tracks is discussed in detail in Section 8.2, where we also go beyond the present-day Sun. This includes the first asteroseismic analysis of stars in the *Kepler* field that makes use of coupled models. In accordance with our analysis of the Sun, we find that the use of coupled models strongly reduces the structural contribution to the surface effect. For the investigated main-sequence (MS) stars, the evaluated global stellar parameters are mostly unaltered by the improvement of the outer boundary conditions. We take a closer look at this issue in Chapter 9.

Our analysis also includes an investigation of how well our method reproduces the correct structures of ⟨3D⟩-envelopes throughout $(T_{\rm eff}, \log g)$-plane. We find that the evolution tracks, as well as the model frequencies, are unaffected by the depth of the matching point if the appended ⟨3D⟩-envelope extends deep enough into the nearly-adiabatic region. However, beyond a certain depth, any increase in the matching depth leads to prominent kinks in the evolution tracks — primarily on the RGB. We attribute these kinks to interpolation errors. To this end, the applicability of the scheme is mainly limited by the low resolution of the existing grids of 3D simulations.

Finally, we find that the change in the outer boundary conditions shifts the evolution track of the Sun, affecting the turn-off point and the RGB. This is crucial since turn-off stars are used to age clusters (cf. Cummings and Kalirai, 2018), and since an accurate characterization of RGB stars is important when addressing questions regarding the chemical history of our host galaxy (Miglio, 2012). The improved characterization of single stars that results from the use of more realistic boundary conditions may hence contribute to a better understanding of stellar populations, clusters, and galaxies. By investigating MS stars in this and the following chapter, we have taken the first steps in quantifying this statement.

# Chapter 9

# Inference of Stellar Parameters

*The content, including most of the text, of this chapter has been submitted for publication in Monthly Notices of the Royal Astronomical Society with the title "Bayesian inference of stellar parameters based on 1D stellar models coupled with 3D envelopes". I am the first author of the paper and the primary investigator of the presented research project. I wrote this chapter. The analysis presented below was performed using the* HEPHAESTUS *code developed by George Angelou (GA). In collaboration with him, I modified the code for my purposes and selected suitable target stars. My contributions furthermore include the subsequent data analysis. GA contributed with constructive and useful feedback and helped to shape the content and text.*

This chapter presents a characterization of Alpha Centauri A and B based on the coupling of 1D and 3D simulations (cf. Chapter 8). We explore the implications of our coupling scheme for the evaluated stellar parameters of main-sequence (MS) stars. For this purpose, we perform a differential study, in which we compare the results from coupled stellar models with standard stellar models, i.e. with models that rely on MLT and Eddington grey atmospheres (cf. Chapter 2). We do this by employing a Markov Chain Monte Carlo (MCMC) approach. Monte Carlo methods, such as MCMC, are sampling schemes that allow for a robust exploration of the parameter space and yield reliable probability distributions for model parameters. A variety of such sampling schemes has thus entered all fields of astronomy, reaching from the interpretation of *Kepler* light-curves to cosmology (e.g. Handberg and Campante, 2011; Lund et al., 2017; Jasche and Wandelt, 2013; Porqueres et al., 2019). However, due to their high computational cost, MCMC procedures are seldom used to determine stellar properties with some notable exceptions. These exceptions include the endeavour to obtain a detailed characterization of the present Sun[1] (Bahcall et al.,

[1]For some purposes, it is worth noting that alternative approaches with low computational cost can recover the correct posterior probability distributions. Thus, the posterior probability distribution of the solar neutrino flux can be derived semi-analytically, due to the linear response of the flux to changes in the stellar parameters (Jørgensen and Christensen-Dalsgaard, 2017).

2006; Vinyoles et al., 2017) and its closest neighbours, Alpha Centauri A and B (Bazot et al., 2012). This binary is also the target that we have decided to investigate in detail below. Due to its history as a benchmark for stellar physics and the high-quality data that is available for this binary (e.g. Joyce and Chaboyer, 2018), it is an ideal target for a detailed differential comparison between models with different boundary conditions.

We note that we neglect turbulent pressure in the present chapter. In contrast to Chapter 8, we include both the radiation pressure and the gas pressure, using the scaled thermal pressure as our coordinate when computing the appended ⟨3D⟩-envelopes. The neglect of turbulent pressure and the inclusion of the radiation pressure reflect the continuous development of the presented coupling method. Based on the analysis in Chapter 10, where turbulent pressure is finally included, we conclude that the neglect of turbulent pressure does not affect the stellar evolution tracks significantly — at least in the case of the Sun.

## 9.1 Bayesian Statistics

This section gives a brief overview of Bayesian statistics and MCMC algorithms with the sole intent to provide the reader with sufficient information to interpret the results in this chapter. I have adopted the notation by Gregory (2005) and Handberg and Campante (2011), to whom I refer for eloquent and more detailed introductions to the topic.

Within the framework of Bayesian statistics, probabilities encode the plausibility of a proposition given the current knowledge of the world. Bayesian statistics, therefore, deals with conditional probabilities, i.e. the probability of a hypothesis $A$ given the current state of information $B$. We write this as $p(A|B)$. The rules for conditional probabilities lead directly to the pillar of Bayesian statistics, Bayes' theorem. This theorem states that the probability of a hypothesis $A$ given the truth of the propositions $B$ and $C$ is

$$p(A|B,C) = \frac{p(A|C)p(B|A,C)}{p(B|C)}. \tag{9.1}$$

In this chapter, we compute stellar models and compare these to observational constraints on Alpha Centauri A and B. Thus, the proposition $A$, whose plausibility we attempt to access, asserts that the stellar model parameters for each target star should take the values $\boldsymbol{\Theta}$ given data ($\boldsymbol{D}$) and any prior information about the system ($\boldsymbol{I}$). In general, prior information may include physical considerations or the results of previous studies. For instance, we impose a restriction on the models, regarding the suggested age for Alpha Centauri A and B, by noting that both stars cannot be older than the Universe. In addition, we draw upon studies that constrain the mass of both stars based on radial velocity measurements. By including prior information about radial velocities, we are able to take these constraints into account, even though we do not incorporate radial velocity measurements ourselves.

For the stellar models in this study, we specifically consider four parameters:

$$\boldsymbol{\Theta} = \{M, \alpha_{\mathrm{MLT}}, X_{\mathrm{i}}, \mathrm{age}\}\,. \tag{9.2}$$

Here, $M$ denotes the stellar mass, $\alpha_{\mathrm{MLT}}$ denotes the mixing length parameter, $X_{\mathrm{i}}$ denotes the initial mass fraction of hydrogen on the zero-age main sequence (ZAMS), and the last parameter is the stellar age. Since all the considered parameters are continuous functions, we are actually dealing with probability densities. The probability density describing the degree, to which we believe in the proposition that the parameters take the values $\boldsymbol{\Theta}$ based on $\boldsymbol{D}$ and $\boldsymbol{I}$, is called the posterior probability density, $p(\boldsymbol{\Theta}|\boldsymbol{D},\boldsymbol{I})$. Using this notation, Eq. (9.2) takes the form

$$p(\boldsymbol{\Theta}|\boldsymbol{D},\boldsymbol{I}) \propto p(\boldsymbol{\Theta}|\boldsymbol{I})p(\boldsymbol{D}|\boldsymbol{\Theta},\boldsymbol{I}), \tag{9.3}$$

where we have dropped the normalization constant. In this chapter, we employ Bayes' theorem in an MCMC. Consequently, we solely deal with ratios of posterior probabilities, making any normalization obsolete.

In Eq. (9.3), $p(\boldsymbol{D}|\boldsymbol{\Theta},\boldsymbol{I})$ denotes the likelihood. The likelihood describes the probability density for obtaining the data $\boldsymbol{D}$ given the prior information $\boldsymbol{I}$ and given that the model parameters should, indeed, be $\boldsymbol{\Theta}$. Finally, $p(\boldsymbol{\Theta}|\boldsymbol{I})$ denotes the degree to which we believe in the proposition $\boldsymbol{\Theta}$ based on the prior information alone.

For any subset ($\boldsymbol{\Theta}_A$) of the model parameters, we can obtain the posterior probability distribution function (PDF) by marginalization, i.e. by integration over the remaining parameters ($\boldsymbol{\Theta}_B$):

$$p(\boldsymbol{\Theta}_A|\boldsymbol{D},\boldsymbol{I}) = \int p(\boldsymbol{\Theta}|\boldsymbol{D},\boldsymbol{I})\mathrm{d}\boldsymbol{\Theta}_B. \tag{9.4}$$

In short, the PDFs for the investigated stellar parameters can be obtained by suitable projections in the parameter space. Here, $\boldsymbol{\Theta_B}$ is referred to as nuisance parameters.

### 9.1.1 MCMC Algorithms

Stars are rather complex celestial objects, and we possess no closed-form analytic formula that straightforwardly links the stellar model parameters to observable quantities. Furthermore, the desired marginalization (cf. Eq. 9.4) requires multi-dimensional integration. In order to overcome both of these obstacles, we resort to a Monte Carlo approach: the basic idea behind MCMC algorithms is to draw samples from the parameter space, in such a way that the distribution of samples maps their posterior probability density. In this manner, marginalization reduces to the computation of discrete sums. In short, the desired PDFs can straightforwardly be obtained from the gathered samples by plotting histograms.

As mentioned above, the goal is to map the posterior probability distribution by drawing representative samples. This is achieved by performing a pseudo-random walk through the parameter space. In each step of this pseudo-random walk, the algorithm draws a new sample from a proposal distribution based on the position of the previous sample in the parameter space. The new sample is then accepted or rejected by comparison to the previous sample. Such a sequence of samples, whose probabilities solely depend on the immediately preceding sample, is called a Markov chain.

Suppose that the previous entry in our Markov chain is $\boldsymbol{\mathcal{X}}^t$. The algorithm now randomly proposes a new point $\boldsymbol{\mathcal{Y}}$ in the parameter space and computes a stellar evolution model,

using this proposed set of parameters. Specifically, we compute the evolution of a star with a certain mass, mixing length parameter and composition until a given age is reached — as any parameter, the age is drawn from a proposal distribution based on $\boldsymbol{\mathcal{X}}^t$. The structure model that is obtained at the end of this evolution is the model that we want to compare to data: based on the obtained stellar structure model and on observations, the MCMC algorithm calculates the likelihood for $\boldsymbol{\mathcal{Y}}$ and combines this with our prior information to obtain the associated posterior probability, $p(\boldsymbol{\mathcal{Y}}|\boldsymbol{D},\boldsymbol{I})$. The algorithm then compares $p(\boldsymbol{\mathcal{Y}}|\boldsymbol{D},\boldsymbol{I})$ with $p(\boldsymbol{\mathcal{X}}^t|\boldsymbol{D},\boldsymbol{I})$, and accepts $\boldsymbol{\mathcal{Y}}$ as the next entry ($\boldsymbol{\mathcal{X}}^{t+1}$) in the Markov chain with a probability that is determined by this comparison. An expression for the acceptance probability, i.e. the probability for accepting $\boldsymbol{\mathcal{Y}}$ as the next sample in the chain, is specified below. For now, it is sufficient to note that it is largely determined by the ratio of $p(\boldsymbol{\mathcal{Y}}|\boldsymbol{D},\boldsymbol{I})$ to $p(\boldsymbol{\mathcal{X}}^t|\boldsymbol{D},\boldsymbol{I})$. If $\boldsymbol{\mathcal{Y}}$ is accepted, $\boldsymbol{\mathcal{X}}^{t+1} = \boldsymbol{\mathcal{Y}}$. If $\boldsymbol{\mathcal{Y}}$ is rejected, $\boldsymbol{\mathcal{X}}^{t+1}$ is set equal to $\boldsymbol{\mathcal{X}}^t$. Having established the next entry of the Markov chain, the steps described above are repeated by randomly proposing a new position in the parameter space.

In this chapter, we employ the MCMC ensemble sampler published by Foreman-Mackey et al. (2013) — this is an implementation of the procedure suggested by Goodman and Weare (2010). Here, we include a short summary of some main aspects, referring to the cited papers for further details.

Following the approach by Goodman and Weare (2010), we evolve an ensemble of $K$ walkers in parallel — that is, we simultaneously perform $K$ coupled random walks through the parameter space. The proposed distribution for any of these walkers is determined by the position of the $K-1$ other walkers. The proposed next entry of the Markov chain for the $k$th walker at $\boldsymbol{\mathcal{X}}_k^t$ is $\boldsymbol{\mathcal{Y}}_k = \boldsymbol{\mathcal{X}}_w^t + \boldsymbol{\mathcal{Z}}$, where $\boldsymbol{\mathcal{X}}_w^t$ denotes the current position of one of the $K-1$ other walkers ($w \neq k$), which has been randomly selected. $\boldsymbol{\mathcal{Z}}$ is randomly drawn from a proposal distribution, $g(z)$, i.e. $\boldsymbol{\mathcal{Z}}$ is a realization of $z$:

$$g(z) = \begin{cases} \frac{1}{\sqrt{z}} & \text{for z} \in \left[\frac{1}{\text{a}}, \text{a}\right] \\ 0 & \text{else.} \end{cases} \tag{9.5}$$

Here, $a$ is a tuneable (scale) hyperparameter, for which a value of 2 seems to ensure wide applicability (Goodman and Weare, 2010). The acceptance probability, i.e. the probability that the proposed next entry $\boldsymbol{\mathcal{Y}}_k$ in the Markov chain is accepted, is

$$\mathcal{A} = \min\left(1, \mathcal{Z}^{N-1}\frac{p(\boldsymbol{\mathcal{Y}}_k|\boldsymbol{D},\boldsymbol{I})}{p(\boldsymbol{\mathcal{X}}_k^t|\boldsymbol{D},\boldsymbol{I})}\right). \tag{9.6}$$

Here, $N$ is the number of dimensions of the explored parameter space, i.e., in our case, $N = 4$. Having established the acceptance probability, one can then decide on rejecting or accepting $\boldsymbol{\mathcal{Y}}_k$ by drawing a random number ($\mathcal{R}$) between zero and one from a uniform distribution. If $\mathcal{A} \geq \mathcal{R}$, $\boldsymbol{\mathcal{Y}}_k$ is accepted. Otherwise, $\boldsymbol{\mathcal{Y}}_k$ is rejected.

### 9.1.2 Defining a Likelihood for Stellar Modelling

For the purpose of this chapter, we regard a stellar evolution code as a function, $f(\boldsymbol{\Theta})$, that maps $\boldsymbol{\Theta}$ to observable quantities. Specifically, we consider the mapping of $\boldsymbol{\Theta}$ to a set of

seismic and spectroscopic properties. We assume that the measurement ($D_j$) of any of the $J$ spectroscopic quantities is uncorrelated with the remaining measurements and that the noise is Gaussian. We can hence write the contribution of the spectroscopic constraints to the likelihood, $\mathcal{L} = p(\boldsymbol{D}|\boldsymbol{\Theta}, \boldsymbol{I})$, as

$$\mathcal{L}_{\mathrm{spec}} = \prod_{j=1}^{J} \frac{1}{\sqrt{2\pi\sigma_j^2}} \times \exp\left(-\frac{1}{2}\left[\frac{f(\boldsymbol{\Theta})_j - D_j}{\sigma_j}\right]^2\right). \tag{9.7}$$

Here, the sum runs over all spectroscopic quantities, and $\sigma_j$ denotes the corresponding standard deviation for the observation $D_j$. The analysis presented in this chapter only involves a single spectroscopic quantity, $T_{\mathrm{eff}}$.

We ignore the diffusion of elements and consequently assume the metallicity to be fixed, throughout the evolution. Moreover, we fix [Fe/H] in our Bayesian analysis: we vary the hydrogen abundance ($X$), the helium abundance ($Y$), and the abundance of heavy elements ($Z$) but keep the ratio of $Z$ to $X$ fixed to a predetermined value for every model in the Markov chain. Thus, all models do, by default have the same [Fe/H], which means that an implementation of [Fe/H] into the likelihood does not alter the obtained PDFs.

While there are other observational constraints, including spectroscopic measurements of $L$ or $\log g$, that we could make use of, they are not all linearly independent pieces of information about the star. Some quantities are already well constrained by the asteroseismic measurements, making further constraints redundant.

For the $Q$ asteroseismic parameters, we generalise the univariate normal distribution to higher dimensions, to take their covariances ($\mathtt{C}$) into account:

$$\mathcal{L}_{\mathrm{seis}} = (2\pi)^{-Q/2} \left|\mathtt{C}\right|^{-Q/2} \times \exp\left(-\frac{1}{2}\sum_{q=1}^{Q}\left[f(\boldsymbol{\Theta})_q - D_q\right]^T \mathtt{C}^{-1}\left[f(\boldsymbol{\Theta})_q - D_q\right]\right). \tag{9.8}$$

Here, the sum runs over all seismic quantities, and $\sigma_q$ denotes the corresponding standard deviation for the observation $D_q$.

Because the model frequencies are subject to the surface effect, a direct comparison between the individual model frequencies and observations is uninsightful if no corrections are applied. For standard stellar structure models that rely on MLT and Eddington grey atmospheres, this problem can be overcome by using surface correction relations (cf. Chapter 3 and 7). However, when appending $\langle$3D$\rangle$-envelopes, we mend the structural contribution to the surface effect, which implies that no suitable empirical surface correction relations exist. We can hence not compare standard stellar models with models that include 3D envelopes on an equal footing, by matching individual frequencies to observations. Instead, we use the frequency ratios discussed in Chapter 3. These ratios have been demonstrated to be relatively insensitive to the outermost layers.

By coupling 1D and 3D models, we improve the physical depiction of the near-surface layers significantly. Although it may thus seem as if the use of frequency ratios leads us to ignore exactly those structural features that we strive to improve, this is not the case: the

outermost layers affect the entire interior structure and shift the evolution tracks. Although the ratios primarily probe the core region, they hence also reflect the improved boundary conditions. While the surface layers do not significantly affect the ratios, the use of different surface layers will nevertheless potentially affect the stellar parameter estimates since a change in boundary conditions will affect the evolutionary tracks.

In addition, we include large and small frequency separations in our comparison with data (cf. Chapter 3). Although these two separations are impacted by the surface term, they are very valuable diagnostics: the large frequency separations, in particular, has been shown to be a far more sensitive diagnostic of stellar mass than the ratios (Angelou et al., 2017). In other words, the inclusion of the separations is a trade-off. The frequency separations help to constrain mass and age, and although they introduce some uncertainty, they display less sensitivity to the surface term than a match to individual frequencies would.

We combine $\mathcal{L}_{\rm spec}$ and $\mathcal{L}_{\rm seis}$, i.e. Eqs (9.7) and (9.8), to determine a final likelihood for the model. The reason for the two-component likelihood is that the asteroseismic quantities are highly correlated, both internally and mutually, and do not provide independent pieces of information about stellar properties (Angelou et al., 2017; Roxburgh, 2018). We, therefore, first determine the correlation matrix for every measured frequency table. We determine the correlation matrix directly from Monte Carlo realizations of the measured frequencies by perturbing each measured frequency independently with Gaussian noise according to its measurement uncertainty. We typically perform 10,000 realizations from which we calculate asteroseismic separations and ratios. From these, the correlation matrix is determined for use in Eq. (9.8).

### 9.1.3 Priors

Bayesian statistics allows us to include prior information in the posterior probability distribution. If the prior PDF of each of the $N$ parameters $\Theta_n$, to which we will refer as $p(\Theta_n|\boldsymbol{I})$, are mutually independent

$$p(\boldsymbol{\Theta}|\boldsymbol{I}) = \prod_{n=1}^{N} p(\Theta_n|\boldsymbol{I}). \tag{9.9}$$

In the present case, $\Theta_n$ is either $M$, $\alpha_{\rm MLT}$, $X_{\rm i}$, or the stellar age. For the stars investigated in this chapter, we mostly impose uniform priors:

$$p(\Theta_n|\boldsymbol{I}) = \begin{cases} \frac{1}{\Theta_n^{\rm max} - \Theta_n^{\rm min}} & \text{for } \Theta_n^{\rm max} < \Theta_n < \Theta_n^{\rm max}, \\ 0, & \text{else.} \end{cases} \tag{9.10}$$

We note that Eq. (9.10) constitutes an improper prior, as it is not normalized. We further impose a Gaussian prior on the mass of the star, as we investigate stars that are situated in a binary, i.e. for which detailed measurements of the mass are available:

$$p(\Theta_n|\boldsymbol{I}) = \frac{1}{\sqrt{2\pi\sigma_n^2}} \exp\left(\frac{-(\theta_n - \mu_n)^2}{2\sigma_n^2}\right), \tag{9.11}$$

Table 9.1: Upper and lower boundary for the uniform priors.

| | $M$ [$\mathrm{M}_\odot$] | $\alpha_{\mathrm{MLT}}$ | $X_\mathrm{i}$ | Age [Myr] |
|---|---|---|---|---|
| Upper limit | 1.30 | 2.5 (1D), 10.0 (3D) | 0.80 | 13800 |
| Lower limit | 0.65 | 1.0 | 0.60 | 50 |

where $\mu_n$ and $\sigma_n$ denote the mean and the standard deviation of the Gaussian prior, respectively.

### 9.1.4 Specification of Priors

We demand that the age of the star may not exceed the age of the Universe, setting the upper boundary on a uniform prior of the age to 13.8 Gyr (cf. Planck Collaboration et al., 2016).

As regards $\alpha_{\mathrm{mlt}}$, we use a different uniform prior when dealing with the standard stellar models than when dealing with the coupled stellar models. In either case, we set the lower boundary of the uniform prior for $\alpha_{\mathrm{mlt}}$ to 1.0. Meanwhile, the upper boundary is set to 2.5 and 10.0 for the standard and coupled stellar models, respectively. In both cases, we have chosen the width of the uniform prior based on the solar calibration models in Chapter 8. For standard models, a solar calibration yields $\alpha_{\mathrm{mlt}} = 1.78$. Allowing $\alpha_{\mathrm{mlt}}$ to deviate strongly from this may lead to multimodal distributions, due to the degeneracy between $\alpha_{\mathrm{mlt}}$ and other parameters. This is the argument for using an upper boundary that is lower than the one for the coupled stellar models. In the case of the coupled stellar models, on the other hand, the unconventionally high upper boundary for $\alpha_{\mathrm{mlt}}$ is motivated by the results shown in Chapter 8: a solar calibration that employs coupled stellar models yields a mixing length parameter of 3.30, which can be explained in terms of the entropy jump that $\alpha_{\mathrm{mlt}}$ must bridge. The mixing length parameter must hence encompass very different information in the two scenarios. We come back to this issue in Section 9.3.

Regarding the mass, we impose a uniform prior in combination with a Gaussian prior. The latter reflects radial velocity measurements (orbital analyses) of the targets. The former is motivated by the restrictions set by the Stagger grid with the upper limit chosen in order to avoid extrapolating from the simulations near the zero-age main sequence (ZAMS). Note that the metallicity of a star shifts the ZAMS. Thus, the upper limit on the mass of stars that lie within the Stagger grid decreases with metallicity. We set the lower and upper boundaries on the mass to $0.65\,\mathrm{M}_\odot$ and $1.30\,\mathrm{M}_\odot$, respectively. All boundaries of the employed uniform priors are summarized in Table 9.1.

Based on Pourbaix et al. (2002), Pourbaix and Boffin (2016) found the mass of Alpha Centauri A and B to be $1.133 \pm 0.0050\,\mathrm{M}_\odot$ and $0.972 \pm 0.0045\,\mathrm{M}_\odot$, respectively. We include this information as a prior, truncating the Gaussians, using the upper and lower limit listed in Table 9.1.

The stellar evolution code terminates when it reaches the end of the red giant branch (RGB) or leaves the parameter space covered by the Stagger grid. Very high propositions for the stellar age may, therefore, force the stellar evolution code to abort the computation, before computing a structure for the desired combination of parameters. To circumvent this problem, we attribute a posterior probability of zero to models, for which

$$\Delta\nu \approx \Delta\nu_\odot \left(\frac{M}{\mathrm{M}_\odot}\right)^{0.5} \left(\frac{T_\mathrm{eff}}{\mathrm{T}_{\mathrm{eff},\odot}}\right)^{3} \left(\frac{L}{\mathrm{L}_\odot}\right)^{-0.75} < 20\,\mu\mathrm{Hz}. \tag{9.12}$$

We assume that $\mathrm{T}_{\mathrm{eff},\odot} = 5777\,\mathrm{K}$ and that $\Delta\nu_\odot = 135\,\mu\mathrm{Hz}$.

### 9.1.5 Initial Conditions, Convergence and Burn-in

For each star, we started all walkers with initial parameters that were close to the expected maximum of the posterior probability distribution. This approach is suggested by Foreman-Mackey et al. (2013) since there is the risk that the walkers get stuck in a local maximum when sampling multi-modal probability distributions.

The initial parameters were drawn from normal distributions, for which the standard deviation corresponded to 2 % of the mean value. The mean of $X_\mathrm{i}$, $\alpha_\mathrm{mlt}$ and the age for the initial conditions of the walkers were consistently set to 0.7, 1.8 and 5.0 Gyr, respectively.

To ensure that the obtained posterior probability distributions do not reflect the initial conditions of the walkers, we allow for a burn-in phase, i.e. we discard the first models of the Markov chain. For this purpose, we have estimated the integrated autocorrelation time that describes the number of samples that is required for the walkers to forget about their initial conditions (Foreman-Mackey et al., 2013). Due to the relatively low number of samples obtained per walker, we have estimated the autocorrelation time by using a parametric description. Specifically, we use an autoregressive-moving-average (ARMA) model. ARMA models aim to describe a time series, i.e. the Markov chain, by assuming that each element of the time series depends linearly on previous entries as well as on the current and previous error terms. In other words, ARMA models are linear approximations that provide a simplified description of stochastic processes (cf. Whittle, 1951, for further details). We determined the autocorrelation time to be less than roughly 200 samples per walker. We, nevertheless, adopt a more conservative approach and set the burn-in phase to be 250 models per walker. In all cases, our exploration of the parameter space employs 16 walkers, which means that we discard 4000 samples for each run.

## 9.2 Stellar Parameter Estimates

For the determination of the stellar parameters, we do not vary [Fe/H] but keep it fixed throughout the evolution. According to Thévenin et al. (2002), [Fe/H] for Alpha Centauri A and B are $0.20 \pm 0.02$ and $0.23 \pm 0.03$, respectively. Furthermore, Nsamba et al. (2018b) estimate [Fe/H] of Alpha Centauri A to be $0.23 \pm 0.05$. These measurements are hence consistent with the hypothesis that both stars have the same composition. We, therefore,

set [Fe/H] = 0.25 for both the standard and the coupled models, based on the quoted spectroscopic constraints.

As regards the coupled stellar models, GARSTEC performs the interpolation in $T_{\rm eff}$ and $\log g$ at each time-step based on 29 interpolated $\langle$3D$\rangle$-envelopes with [Fe/H] = 0.25. These interpolated $\langle$3D$\rangle$-envelopes have been evaluated, using the interpolation in composition described in Chapter 5. This thesis hence presents the first analysis of coupled models at non-solar metallicity.

We have computed the posterior mean and use the posterior standard deviations as the associated credible intervals.

### 9.2.1 Alpha Centauri A

For the primary star in the binary, we used the observed frequencies ($\ell = 0 - 2$) by de Meulenaer et al. (2010) and spectroscopic constraints by Kervella et al. (2017): we set $T_{\rm eff} = 5795 \pm 57\,\mathrm{K}$, using three times the statistical uncertainty quoted by Kervella et al. (2017) to allow for systematic uncertainties. This effective temperature is in good agreement with that found by other authors (e.g. Thévenin et al., 2002). We set $\nu_{\rm max} = 2300 \pm 50\,\mu\mathrm{Hz}$, which can be translated into a mass of $1.11\,\mathrm{M}_\odot$, based on asteroseismic scaling relations. We use this mass estimate for the mean of the Gaussian mass distribution, from which the initial mass estimates of the walkers are drawn.

After excluding a burn-in phase, we obtained 7200 and 6848 samples for the standard and coupled models, respectively. The posterior probability distributions are summarized in Table 9.2 as well as in the corner plot shown in Fig. 9.1, showing the marginalized probability densities.

We find that the use of standard and coupled stellar models lead to parameter estimates for $M$, $X_{\rm i}$ and the stellar age that are mutually consistent. As regards $\alpha_{\rm MLT}$, the standard model yields a value of $1.78^{+0.10}_{-0.11}$, which is in good agreement with standard solar calibrations. As we ignore some input physics that enter a proper solar calibration, including metal diffusion, any deviation from the solar calibration value may reflect this neglect as well as variations in the mixing length parameter with the stellar global parameters (e.g. Tayar et al., 2017; Trampedach et al., 2014b).

The coupled models result in an estimate for $\alpha_{\rm MLT}$ of $4.30^{+2.87}_{-1.99}$. This is consistent with findings in Chapter 8: in the coupled models, MLT is only used to describe a thin nearly-adiabatic layer leading to higher values of $\alpha_{\rm MLT}$. The large error bars show that the actual value of $\alpha_{\rm MLT}$ becomes less relevant. We refer to Section 9.3 for a detailed discussion thereof.

As for the Sun, the use of $\langle$3D$\rangle$-envelopes does not significantly alter the depth of the convection zone (cf. Chapter 8): we find that the energy transport becomes radiative, i.e. that the Schwartzschild criterion for convective instability ($\nabla_{\rm rad} > \nabla_{\rm ad}$) is no longer fulfilled, for radii below $0.726\,R$ and $0.722\,R$ for the standard and coupled models, respectively. Here, $R$ denotes the photospheric radius of the star. We illustrate this in Fig. 9.2 by plotting (Christensen-Dalsgaard et al., 1991, 2011)

$$\nabla_{c^2} = \frac{\mathrm{d}\ln c^2}{\mathrm{d}\ln P_{\rm th}} \approx \nabla - \frac{\mathrm{d}\ln \mu}{\mathrm{d}\ln P_{\rm th}} \tag{9.13}$$

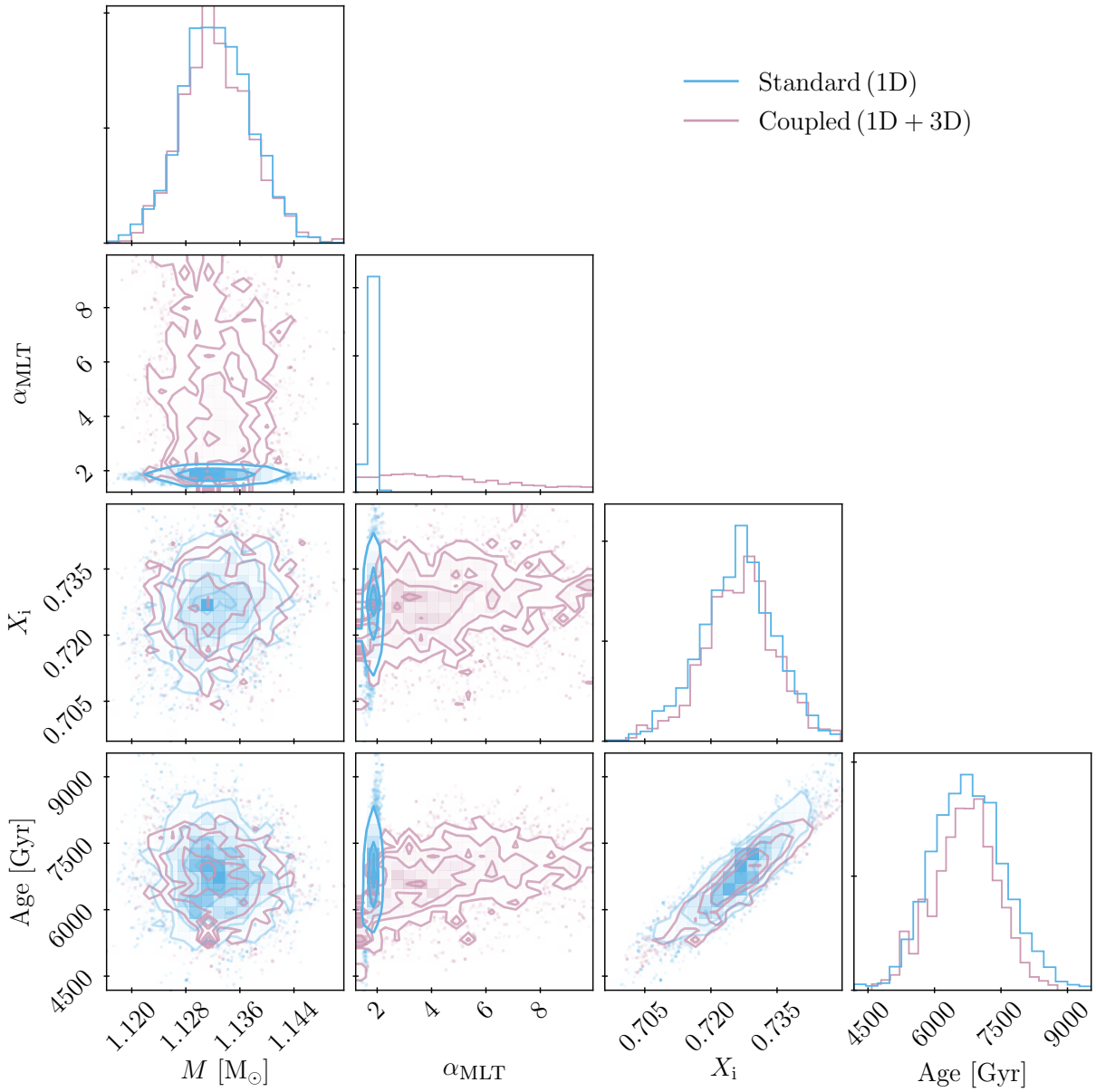


Figure 9.1: Corner plot showing different projections of the samples and of the posterior probability distributions for the stellar parameters ($M$, $\alpha_{\rm MLT}$, $X$ and age) of Alpha Centauri A. The plot is based on 7200 standard stellar models (blue) and 6848 coupled stellar models (purple).

Table 9.2: Summary of the posterior probability distributions found by using standard (1D) and coupled (3D) stellar models, respectively. We list the median of the corresponding probability distributions as the parameter estimate. The associated errors correspond to the 16th and 84th percentile.

| | $M^{1D}$ [$M_\odot$] | $M^{3D}$ [$M_\odot$] | $\alpha_{MLT}^{1D}$ | $\alpha_{MLT}^{3D}$ | $X_i^{1D}$ | $X_i^{3D}$ | Age, 1D [Gyr] | Age, 3D [Gyr] |
|---|---|---|---|---|---|---|---|---|
| $\alpha$ Cen A | $1.132^{+0.005}_{-0.005}$ | $1.132^{+0.006}_{-0.004}$ | $1.78^{+0.10}_{-0.11}$ | $4.30^{+2.87}_{-1.99}$ | $0.726^{+0.008}_{-0.008}$ | $0.727^{+0.008}_{-0.008}$ | $6.76^{+0.80}_{-0.80}$ | $6.74^{+0.69}_{-0.80}$ |
| $\alpha$ Cen B | $0.971^{+0.005}_{-0.004}$ | $0.972^{+0.004}_{-0.005}$ | $1.95^{+0.10}_{-0.10}$ | $6.41^{+2.37}_{-2.60}$ | $0.733^{+0.007}_{-0.008}$ | $0.731^{+0.008}_{-0.008}$ | $5.37^{+0.93}_{-0.91}$ | $4.86^{+0.77}_{-0.75}$ |

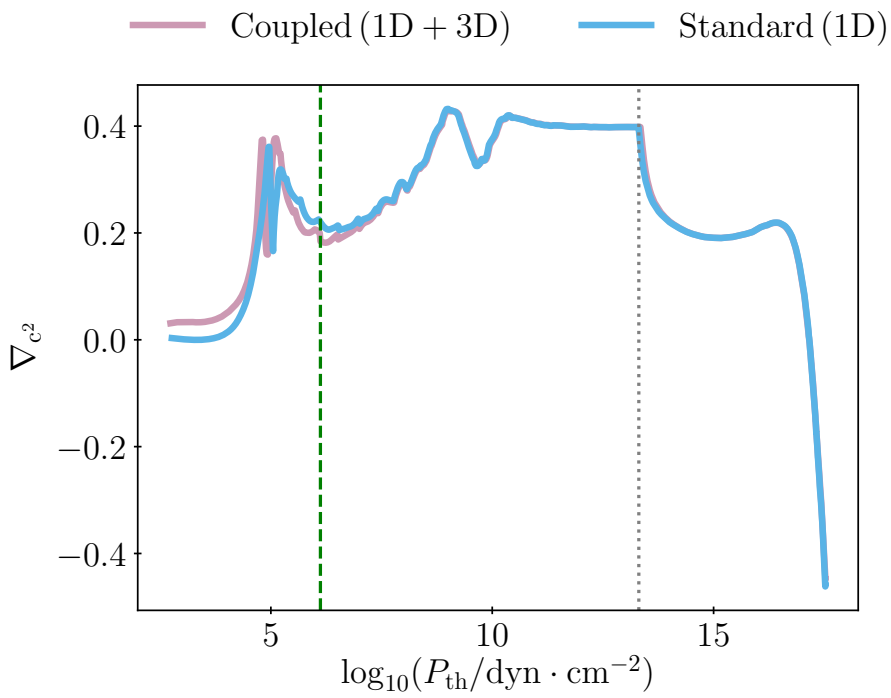


Figure 9.2: The gradient of the squared sound speed as a function of the thermal pressure for Alpha Centauri A. The figure includes the best-fitting standard (solid blue line) and coupled (solid purple line) model. The dotted grey line shows the location of the base of the convection zone. The dashed green line indicates the position of the matching point in the coupled model.

of the best-fitting standard and coupled models, i.e. the models with the highest posterior probability. Here. $\mu$ denotes the mean molecular weight.

The abrupt transition in $\nabla_{c^2}$ near $0.7\,R$ indicates the base of the convection zone. As can be seen from the figure, the interior structures of the best-fitting models are rather similar. Only the outer convective layers strongly differ. The deeper interior of the models, on the other hand, are not affected. This is, again, in very good agreement with the result found in the case of the present-day Sun.

To further illustrate this, we include the temperature as a function of pressure for both the best-fitting standard and coupled model in Fig. 9.3. As can be seen from the figure, the temperature stratifications of the two models converge in the deep interior below the matching point. Despite very different values of $\alpha_{\mathrm{MLT}}$, the two models hence reach the same deep asymptotic adiabat. We address this issue further in Section 9.3.

For the best-fitting standard stellar model, $M = 1.133\,\mathrm{M}_\odot$, $\alpha_{\mathrm{MLT}} = 1.79$, $X_{\mathrm{i}} = 0.727$ ($Y_{\mathrm{i}} = 0.249$) and the age is 6.85 Gyr. For the best-fitting coupled stellar model, $M = 1.131\,\mathrm{M}_\odot$, $\alpha_{\mathrm{MLT}} = 5.19$, $X_{\mathrm{i}} = 0.729$ ($Y_{\mathrm{i}} = 0.248$) and the age is 7.02 Gyr. Note that these parameter estimates correspond to the values that result in the highest posterior probability whereas

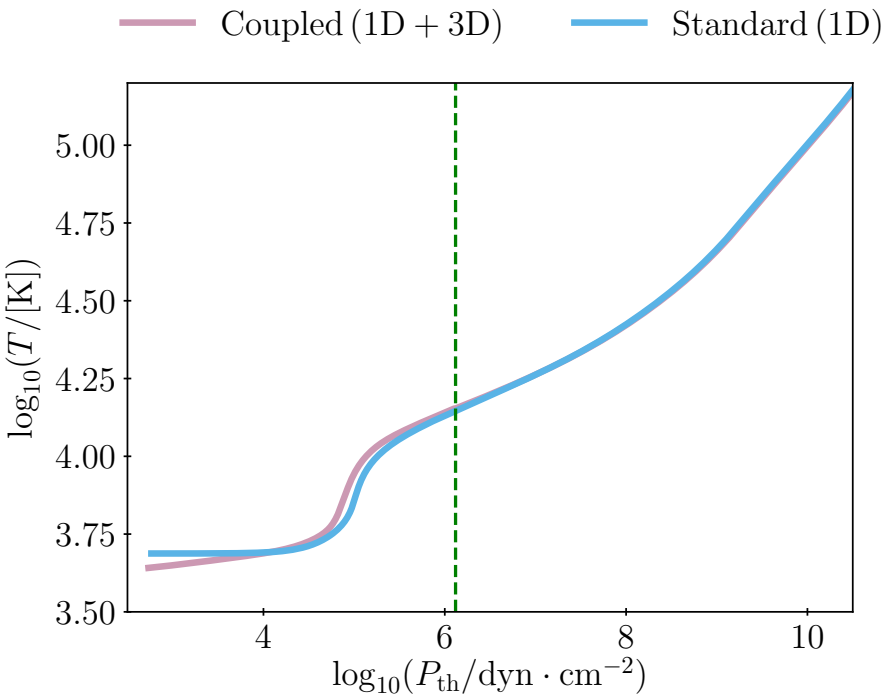


Figure 9.3: Temperature as a function of thermal pressure for the best-fitting standard and coupled model. The green dashed line shows the location of the matching point in the best-fitting coupled model.

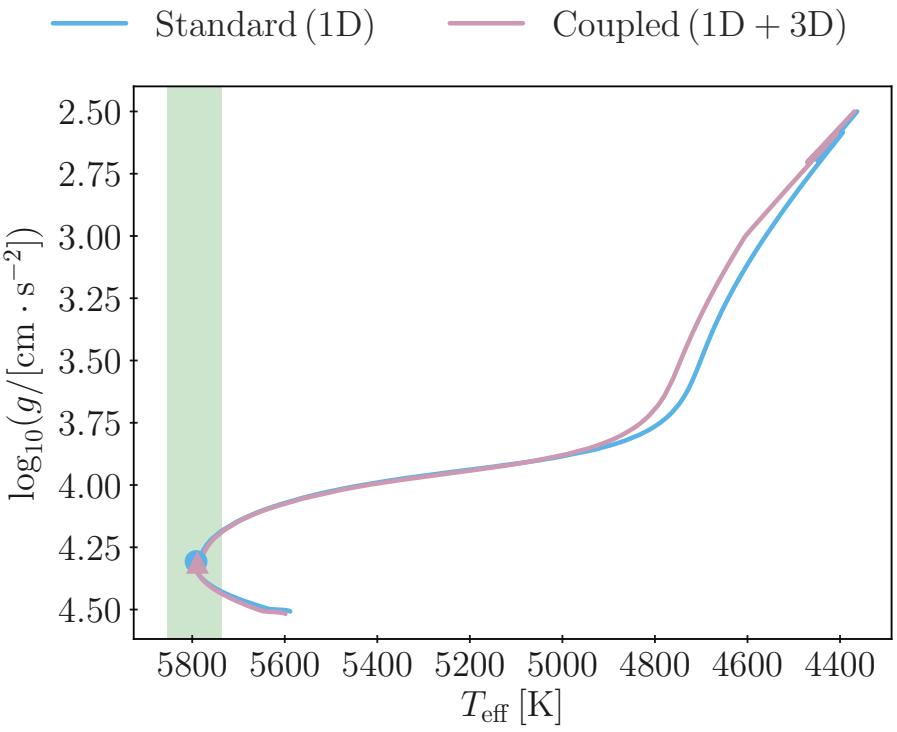


Figure 9.4: Predicted stellar evolution of Alpha Centauri A, for the best-fitting standard (blue solid line) and coupled (purple dashed line) stellar models. The shaded green area shows the 68 % credible interval for the observational constraint on the effective temperature. The global parameters of the best-fitting standard (blue circle) and coupled (purple triangle) structure models are likewise included.

the values presented in Table 9.2 denote the medians of the corresponding probability distribution functions.

All in all, for MS stars, such as the Sun or Alpha Centauri A, the use of $\langle 3\mathrm{D}\rangle$-envelopes does not seem to lead to parameter estimates that deviate significantly from those obtained using MLT with the exception of the mixing length parameter.

However, as discussed in Chapter 8, the coupling of 1D and 3D simulations affects the subsequent evolution. In the case of the Sun, coupling shifts the predicted turn-off point, i.e. the end of the MS in the HR diagram. In addition, the effective temperature on the RGB is altered. While the stellar parameter estimates of MS stars are mostly unaffected by the imposed change in the outer boundary conditions, it is to be expected that the coupling of 1D and 3D simulations has a larger effect for the parameter estimates at later evolutionary stages. For Alpha Centauri A, the changes in the evolution track are consistent with this picture on the RGB, while no shift is seen for the turn-off point. The largest discrepancy in $T_{\mathrm{eff}}$ at constant $\log(g)$ is roughly 40 K for $\log(g) > 2.5$. This is shown in Fig. 9.4.

We note that the p-mode frequencies of the best-fitting models are systematically lower than the observed frequencies. This is illustrated in Fig. 9.5. In the case of the standard

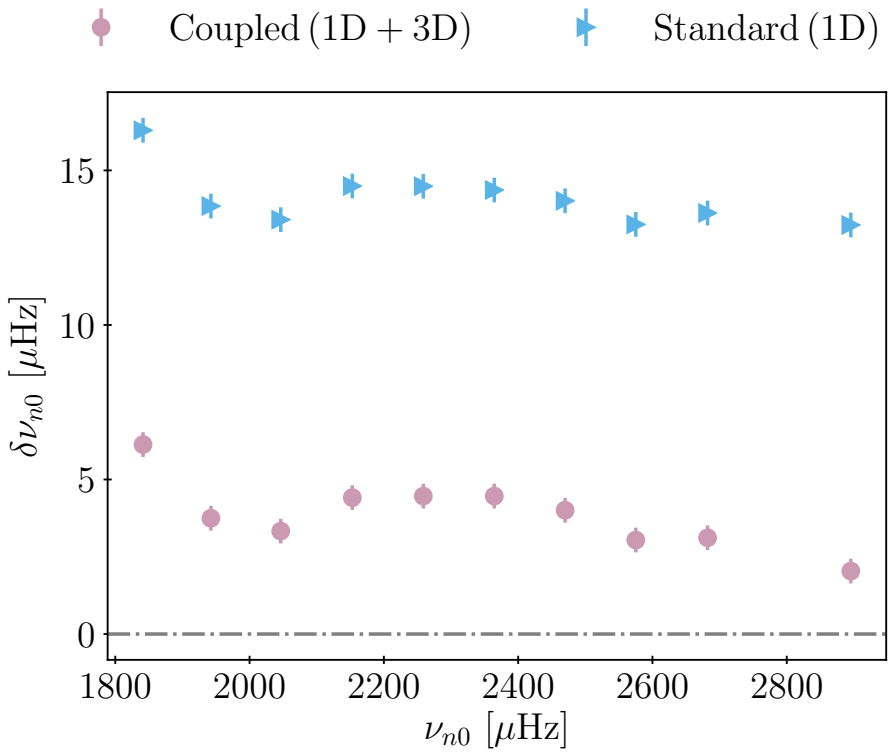


Figure 9.5: Frequency difference between observations and the best-fitting models for Alpha Centauri A. We have only included radial modes ($\ell = 0$).

models, this is slightly at odds with the expected behaviour: due to the surface effect, the model frequencies are expected to be systematically too high rather than too low. Also, for the standard stellar models, we would expect the frequency offset to increase with increasing frequency. This discrepancy reflects the fact the individual frequencies are neither directly considered by the likelihood nor by the priors. In other words, the individual frequencies are not directly required to be reproduced. Only the frequency ratios and separations must be recovered. The latter requirement does not necessitate the recovery of a frequency-dependent surface effect: as can be seen from Fig. 9.5, the systematic offset is constant as a function of frequency. In addition, the frequency ratios enter our likelihood, and it is well-known that an evaluation of model parameters based on frequency ratios lead to different results than when using individual frequencies (Silva Aguirre et al., 2013; Basu and Kinnane, 2018; Nsamba et al., 2018a). Of course, we do also not expect our best-fitting model to match observations perfectly. After all, it is just the best model in the corresponding Markov chain given the restricted input physics and our selection criteria. The inability of the model to recover the correct individual frequencies is hence a trade-off that we have found acceptable for the purposes of this exercise. Here, we merely present a differential study whereby we compare models that employ two physically different descriptions of the outer boundary layers. The likelihood was, therefore, chosen in order to facilitate a one-to-one comparison of the respective predictions.

Finally, as regards the obtained mass estimates, we note that we achieve statistical agreement with the dynamic masses from the binary orbit. However, we note that the likelihood is seemingly not sufficiently informative to put further constraints on the mass beyond those imposed by radial velocity measurements. In other words, the posterior probability distribution of the mass is dominated by the prior. This does, however, not affect the main conclusions drawn from our analysis: we mainly address the influence of the mixing length parameter when coupling 1D and 3D models.

### 9.2.2 Alpha Centauri B

For the secondary star, we used the observed frequencies ($\ell = 0 - 2$) by Kjeldsen et al. (2005) in combination with the spectroscopic constraints by Kervella et al. (2017): we hence set $T_{\rm eff} = 5231 \pm 63\,\mathrm{K}$, once again adopting $3\sigma$ uncertainties. We set the mean of the initial Gaussian mass distribution to $0.96\,\mathrm{M}_\odot$.

After excluding a burn-in phase, we obtained 7200 and 6784 samples for the standard and coupled models, respectively. The posterior probability distributions are summarized in Table 9.2 alongside those of Alpha Centauri A as well as in the corner plot shown in Fig. 9.6.

From the obtained posterior probability distributions, we draw the same qualitative conclusions as for Alpha Centauri A: the use of coupled and standard stellar models leads to consistent parameter estimates with the exception of the mixing length parameter. The posterior probability of the coupled models is found to be rather insensitive to $\alpha_{\rm MLT}$.

Furthermore, the best-fitting models for Alpha Centauri B behave in the same way as for Alpha Centauri A: the interior structure of the best-fitting coupled and standard

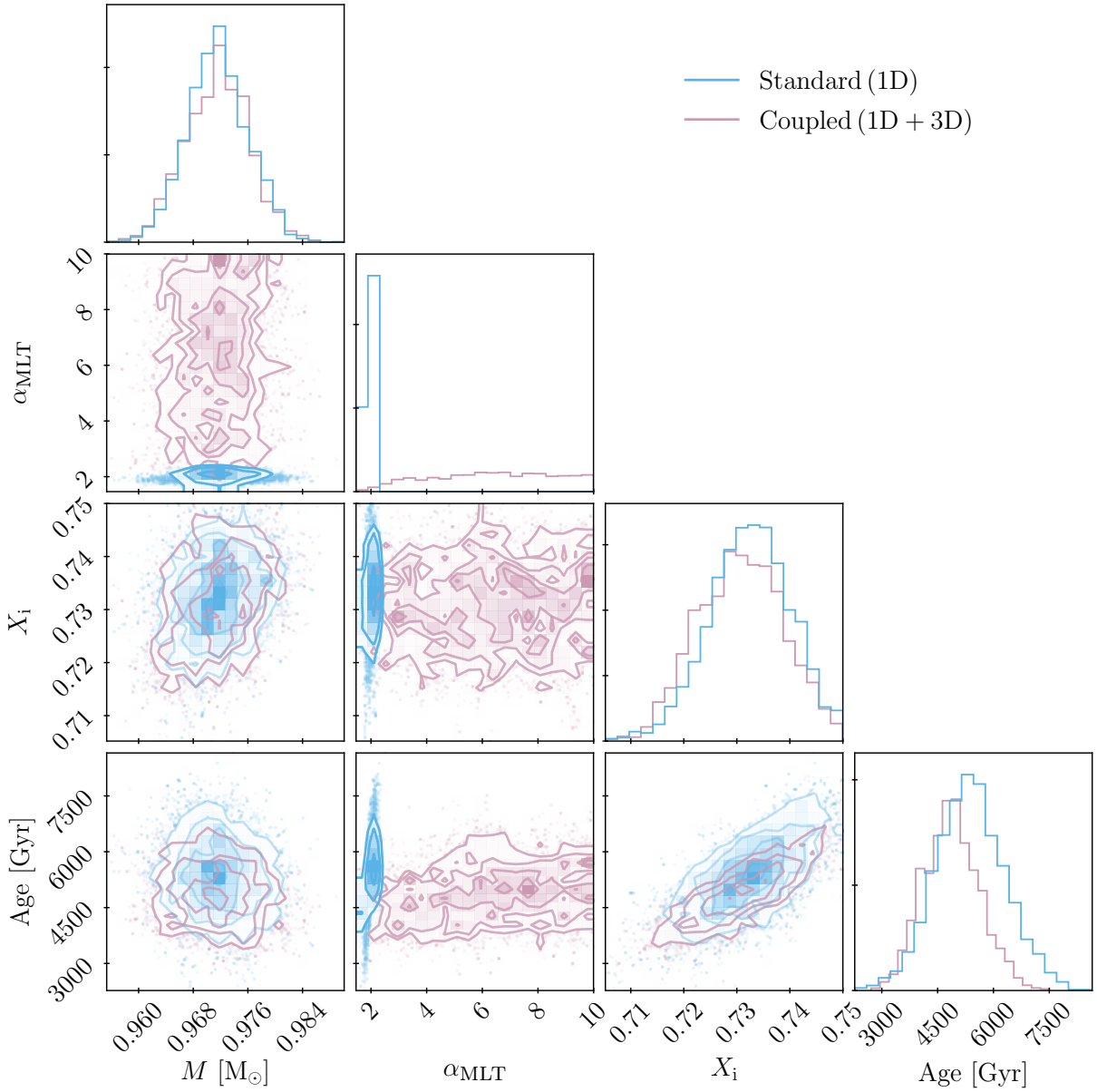


Figure 9.6: Same as Fig. 9.1 but for Alpha Centauri B. The plot is based on 7200 standard stellar models (blue) and 6784 coupled stellar models (purple).

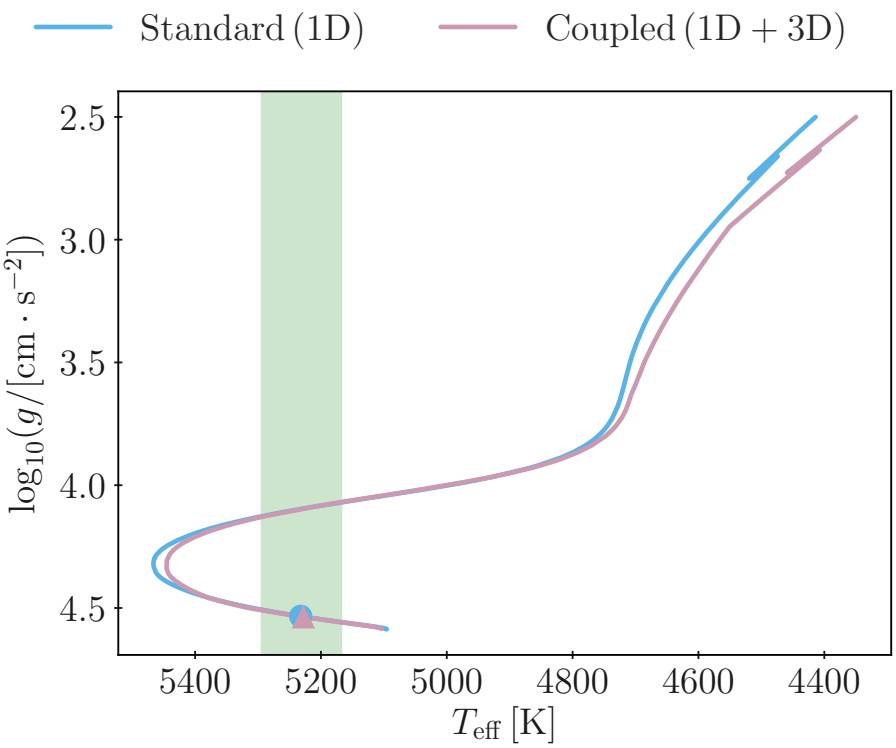


Figure 9.7: Same as Fig. 9.4 but for Alpha Centauri B.

models are rather similar; only the outer layers deviate significantly. While the best-fitting models are hence rather similar, the later evolution differs more significantly (cf. Fig. 9.7). In contrast to the case of Alpha Centauri A, and in accordance with the solar case, we see that the use of coupled models shifts the turn-off point. Finally, we note that the model frequencies of the best-fitting models are, again, systematically too low.

For the best-fitting standard stellar model, $M = 0.972\,\mathrm{M}_\odot$, $\alpha_{\mathrm{MLT}} = 1.96$, $X_\mathrm{i} = 0.731$ ($Y_\mathrm{i} = 0.245$) and the age is 5.39 Gyr. For the best-fitting coupled stellar model, $M = 0.972\,\mathrm{M}_\odot$, $\alpha_{\mathrm{MLT}} = 7.88$, $X_\mathrm{i} = 0.729$ ($Y_\mathrm{i} = 0.247$) and the age is 4.89 Gyr. The base of the convection zone is placed at $0.6855\,\mathrm{R}$ and 0.6875 for the best-fitting standard and coupled model, respectively.

We note that the ages of the primary and secondary star in the binary are comparable but not identical. This is a recurrent oddity found, when modelling stars binaries as single stars (cf. Torres et al., 2010; Higl and Weiss, 2017). It is, of course, a fundamental requirement that the ages of both companions agree within the error bars. This criterion is met.

## 9.3 Discussion

The obtained best-fitting models do robustly recover the desired properties, i.e. the frequency ratios and separations ($\Delta\nu_0$, $\delta\nu_{02}$, $r_{02}$, $r_{10}$, $r_{01}$) as well as spectroscopic constraints ($T_{\mathrm{eff}}$) within one standard deviation. However, as a trade-off, we attribute high posterior probabilities to models that do not yield the expected functional dependence of the systematic offset between the model frequencies and observations — that is, the surface effect (cf. Fig. 9.5). Matching frequency ratios rather than individual frequencies hence affects the obtained parameter estimates. This is a well-known issue (Silva Aguirre et al., 2013). For our purposes, we deem the mentioned trade-off to be acceptable: we present a differential study with the aim of comparing two different methods on equal terms. The obtained best-fitting models are meanwhile not assumed to give a perfect physical description of the interior structure of Alpha Centauri A and B. Indeed, processes, such as metal diffusion, have been neglected.

As regards the priors, we note that the Gaussian mass prior plays a crucial role, due to the degeneracy between different global stellar parameters. We have thus attempted to restrict the parameters of single stars in the *Kepler* LEGACY sample (Lund et al., 2017), using only uniform mass prior. However, we find that the resulting posterior probability distribution is multi-modal, allowing for solutions that have un-physically low or high helium contents. In other words, the likelihood and priors were not sufficiently informative when only using a uniform mass prior. This is the reason we use truncated Gaussian priors for the mass in this chapter.

We find that the use of coupled and standard stellar models lead to consistent results for the predicted interior structure as well as the global parameters, including the mass, age, and composition. This is consistent with the qualitative conclusions that were drawn in Chapter 8 when addressing the present-day Sun. We repeated the analysis presented in

Section 9.2.1 and 9.2.2 using older Gaussian mass priors by Pourbaix et al. (2002) and the spectroscopic constraints by Thévenin et al. (2002) for comparison. Doing so, we arrive at the same qualitative conclusions regarding Alpha Centauri A and B.

To this end, as regards the parameter estimates of MS stars, the use of coupled models is not crucial — nevertheless, a more physically realistic depiction of the surface layers is obtained by using coupling, which is crucial for detailed studies of stellar physics and structures. However, when using coupled stellar models, the posterior probability of the models becomes nearly insensitive to the mixing length parameter. In other words, coupled models are able to recover the correct stellar properties without suffering from the degeneracy of MLT. By eliminating this degeneracy, the coupling of 1D and 3D models becomes superior to the standard procedure, even for MS stars, yielding more robust parameter estimates.

Our method for coupling 1D and 3D models is partly motivated by the aim to ensure that the resulting coupled models are continuous at the matching point. This is a critical virtue of our method since we employ our method in asteroseismic analyses: discontinuities in the obtained structure affect the seismic properties and, therefore, greatly complicate asteroseismic analyses (cf. Chapter 6). Previously published patching procedures, therefore, likewise, take great care to achieve continuous stratifications (e.g. Trampedach et al., 2014b; Ball et al., 2016).

On the other hand, it is worth noting that the global parameters of any 3D simulation uniquely determine its asymptotic adiabat. Ludwig et al. (1999) have, therefore, suggested an alternative approach by which $\alpha_{\mathrm{MLT}}$ is calibrated in such a way as for 1D models to recover the correct asymptotic adiabat (see also Magic et al. 2015 and Spada et al. 2018 for analyses based on the same idea). However, these models do not recover the stratification of 3D simulations in the nearly-adiabatic and superadiabatic layers. Conversely, it stands to reason that neither our method nor that by Trampedach et al. (2014b) is guaranteed to yield the correct deep adiabat. While we find that the value of $\alpha_{\mathrm{MLT}}$ has little impact on the best-fitting global parameters of coupled models, one may, therefore, suspect that only certain values of $\alpha_{\mathrm{MLT}}$ make the coupled models physically fully consistent with the underlying 3D simulations.

In order to counter this argument, we have taken a closer look at a subset of standard and coupled models from our Markov chains. We have thus selected a handful of models that mainly differ from the best-fitting models by their value of $\alpha_{\mathrm{MLT}}$. $M$, $X$, $Z$, $\log g$, and $T_{\mathrm{eff}}$ match the corresponding values of the best-fitting model within $10^{-2} M_\star$, $2 \times 10^{-4}$, $10^{-4}$, $10^{-3}$ dex, and 5 K, respectively — here, $M_\star$ denotes the mass of the corresponding best-fitting model. For each of these models, we have evaluated the entropy at a thermal pressure of $10^{11}\,\mathrm{dyn\,cm^{-2}}$, i.e. deep within the adiabatically convective region. At this depth, we have reached the adiabat of the model. For simplicity, we compute the entropy ($s$) from the density and pressure by assuming that the gas behaves like an ideal gas, i.e. that the level of ionization is constant — this is a physically motivated approximation at the considered depth:

$$s = \frac{k_{\mathrm{B}}}{\mu m_{\mathrm{u}}} \ln\left(\frac{T^{5/2}}{P_{\mathrm{th}}}\right), \tag{9.14}$$

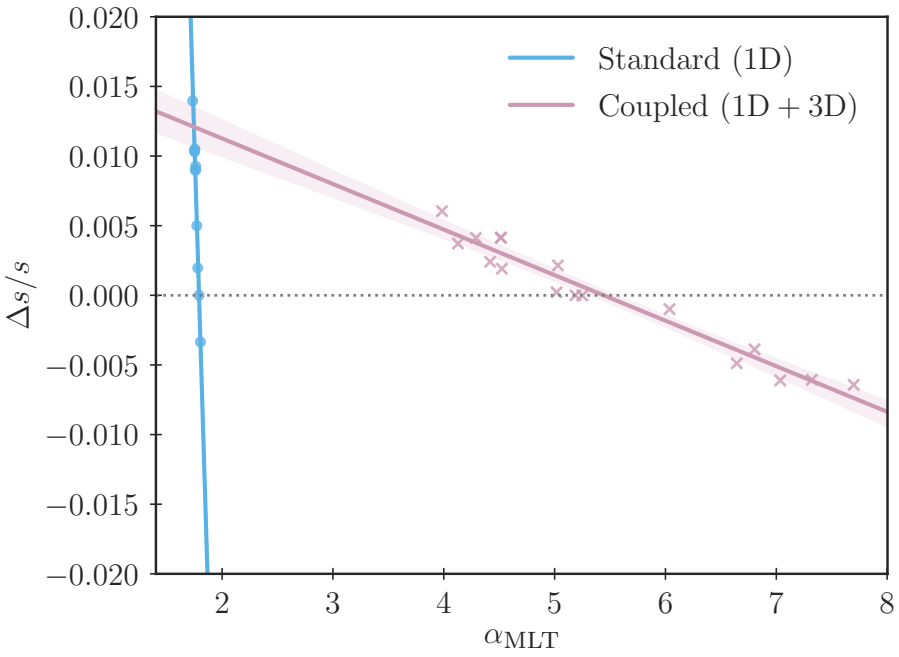


Figure 9.8: Entropy difference between a subset of models for Alpha Centauri A and the corresponding best-fitting models as a function of the mixing length parameter ($\alpha_{\rm MLT}$). The only notable difference between the models in the each subset is the value of the mixing length parameter; all other global parameters are identical within an accuracy specified in the text.

where $m_{\rm u}$ is the atomic mass unit, $k_{\rm B}$ is the Boltzmann constant, and $\mu$ is the mean molecular weight.

As expected, we find the evaluated adiabat of the standard models to be rather sensitive to the exact value of the mixing length parameter: by varying $\alpha_{\rm MLT}$ from 1.75 to 1.80, we shift the entropy of the deep adiabat by roughly 2 %. In order to achieve a comparable shift of the deep adiabat in the coupled models, $\alpha_{\rm MLT}$ must be doubled. This result is illustrated in Fig. 9.8. It emphasizes the conclusion drawn from the posterior probability distributions: coupled models are virtually insensitive to the value of the mixing length parameter. In other words, since $\alpha_{\rm MLT}$ only affects the stratification of a thin nearly-adiabatic layer, large changes in $\alpha_{\rm MLT}$ are required for these changes to have any significant effect on the asymptotic adiabat.

The fact that the interior structure is rather insensitive to $\alpha_{\rm MLT}$ is an intriguing feature of our coupled models since it implies that the evolution tracks are likewise insensitive to this parameter. That this is indeed the case is illustrated in Fig. 9.9, where we have plotted stellar evolution tracks assuming different $\alpha_{\rm MLT}$. All models take the corresponding best-fitting structure models as their starting point but use different $\alpha_{\rm MLT}$ in the subsequent evolution. For the coupled models, $\alpha_{\rm MLT}$ varies between 4.0 and 9.0, i.e. by more than a factor of 2. For the standard stellar models, $\alpha_{\rm MLT}$ varies from 1.70 to 1.95, i.e. by

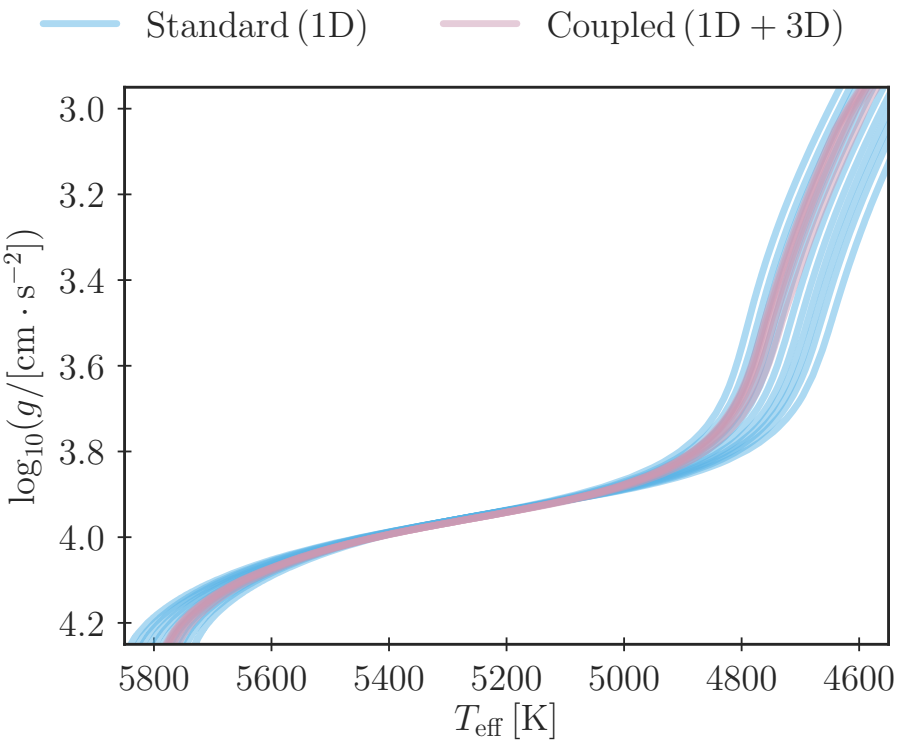


Figure 9.9: Stellar evolution tracks for the evolution of Alpha Centauri A beyond its current evolutionary state, assuming different values for $\alpha_{\mathrm{MLT}}$. For the standard stellar models, $\alpha_{\mathrm{MLT}}$ varies between 1.70 and 1.95. For the coupled stellar models, $\alpha_{\mathrm{MLT}}$ varies between 4.0 and 9.0. Note that the evolution tracks of the coupled models cover some of the evolution tracks of the standard stellar models. On the RGB, at $\log g = 3.5$, the effective temperatures of the standard stellar models deviate by roughly 140 K, while the coupled stellar models only deviate by roughly 30 K.

roughly 15 %. As can be seen from the figure, the evolution tracks of the coupled models lie closer together than those of the standard stellar models, despite the substantially larger variation in $\alpha_{\mathrm{MLT}}$. We can, therefore, draw sound conclusions about the RGB, despite the fact that we are keeping $\alpha_{\mathrm{MLT}}$ constant throughout the evolution. This is not the case for standard stellar models: as shown by Trampedach et al. (2014b) and Tayar et al. (2017), the mixing length parameter of such models has to vary across the HR diagram, in order to recover observations or the results from multi-dimensional hydrodynamic simulations. In our coupled models, on the other hand, the interior structure is dictated by the appended $\langle$3D$\rangle$-envelope rather than by $\alpha_{\mathrm{MLT}}$.

As mentioned above, the asymptotic adiabat of any given 3D simulation is uniquely determined by its global parameters. Until now, we have argued that the value of $\alpha_{\mathrm{MLT}}$ has little influence on the achieved adiabat. Whether the correct adiabat is obtained, is a different question. As shown in Chapter 8 based on a solar calibration, however, coupled

models turn out to closely recover the temperature of the underlying 3D simulation as a function of pressure *below* the matching point — this comparison can be made in the case of the Sun, since a Stagger-grid simulation at this point of the HR diagram exists. In other words, it stands to reason that the deep interiors of coupled models closely match the asymptotic adiabat that would make them consistent with the underlying 3D simulations.

Since our coupled models ensure a continuous stratification at the matching point, deeper 3D simulations would make the models converge towards a unique adiabat and render $\alpha_{\mathrm{MLT}}$ completely obsolete. Grids containing such 3D simulations are, however, currently not available.

## 9.4 Summary

Using Bayesian inference, we present a differential study of coupled and standard stellar. For this purpose, we established stellar parameters for Alpha Centauri A and B, providing the first analysis based coupled models for stars with non-solar metallicity. Owing to their proximity and binary nature, Alpha Centauri A and B are well-studied benchmarks for stellar evolution. Our analysis of these targets is consistent with previous analysis of the system also using MCMC (cf. Bazot et al., 2012).

We demonstrate that the deep adiabat and the evolution tracks of coupled models are rather insensitive to the value of the mixing length parameter. Likewise, the mixing length parameter plays no major role for the established parameter estimates. Thus, the coupling of 1D and 3D models provides a viable improvement of stellar models and a superior alternative to MLT: not only does coupling yield a more realistic depiction of superadiabatic convection, but it also reduces the importance and influence of $\alpha_{\mathrm{mlt}}$, making the models almost insensitive to this parameter. This is a compelling feature of coupled models since $\alpha_{\mathrm{mlt}}$ is degenerate with other stellar parameters, including the helium abundance and the mass of the star. Coupling, therefore, yields more robust stellar parameter estimates than the standard procedure does.

As discussed above, the change to a more realistic description of the boundary layers affects the predicted stellar evolution (see also Hoyle and Schwarzschild, 1955). While the inferred global parameters for MS stars are impacted minimally, it is not clear this is the case for later evolutionary phases. We aim to quantify this for later stages in future work but note that there are several issues that we must first overcome: the high computational cost of using an MCMC algorithm, the increased computational effort of computing stars at later evolutionary stages, and the low resolution of the Stagger grid at low $\log g$. Furthermore, by choosing Alpha Centauri A and B, we present a study of stars at near solar metallicity. Our conclusion should hence be validated, by addressing MS stars with vastly different compositions. This is beyond the scope of the present chapter.

Our analysis of Alpha Centauri A and B clearly illustrates the vital role that more realistic outer boundary layers play for our understanding of stellar evolution. Continuing this endeavour by characterizing a broad range of stars thus promises to be a fruitful exercise (cf. Chapter 12).

# Chapter 10

# Turbulent Pressure

*The content, including most of the text, of this chapter was published in Monthly Notices of the Royal Astronomical Society by Jørgensen and Weiss (2019). I am the first author of the paper and the primary investigator of the presented research project. I wrote this chapter. My contributions to the paper consist of the conception, development, application, and validation of the presented method and its numerical implementation.* GARSTEC *already included a prescription of turbulent pressure within the framework of mixing length theory and full spectrum theory. I adjusted this scheme to mimic the turbulent pressure from 3D simulations. The work was performed in collaboration with Achim Weiss, who contributed with constructive and useful feedback.*

In this chapter, I extend upon the method of coupling 1D and 3D simulations, by including turbulent pressure, i.e. the pressure that arises from the bulk motion of convective fluids. By doing so, I arrive at 1D stellar models that contain all the relevant input physics that are at play in 3D hydrodynamic simulations, which yields 1D structures that show a large degree of consistency with the underlying 3D simulations.

## 10.1 Including and Calibrating Turbulent Pressure

In convective flows, the turbulent bulk motion of the fluid contributes with an additional pressure, the so-called turbulent pressure ($P_{\rm turb}$). This pressure is related to the convective velocity ($v_{\rm c}$) of the fluid by

$$P_{\rm turb} = \beta \rho v_{\rm c}^2. \tag{10.1}$$

Here, $\beta$ denotes a scaling factor that we will address below. In MLT, $v_{\rm c}$ denotes the average velocity of a fluid element (Eq. 7.6 in Kippenhahn et al., 2012):

$$v_{\rm c}^2 = g\delta_{\rm P}(\nabla - \nabla_{\rm e})\frac{\alpha_{\rm MLT}^2 H_{\rm P}}{8}. \tag{10.2}$$

Here, $\delta_\mathrm{P} = -(\partial \ln \rho / \partial \ln T)_P$ at constant thermal pressure, and $H_\mathrm{P}$ denotes the pressure scale height. Furthermore, $\nabla$ and $\nabla_\mathrm{e}$ refer to the temperature gradient of the surroundings and of the convective element, respectively.

The stratification of the turbulent pressure from the interpolated $\langle 3\mathrm{D} \rangle$-envelope is used above the matching point. It is again obtained using the interpolation described in Chapter 5: the scaled turbulent pressure as a function of the scaled thermal pressure is evaluated by interpolation in $T_\mathrm{eff}$ and $\log g$. The associated scaling factors are likewise found by interpolation, and the scaling is then inverted, i.e. the absolute quantities are computed.

Below the matching point, we compute the turbulent pressure using Eq. (10.1), i.e. from MLT. In order to ensure a continuous transition at the matching point, we calibrate $\beta$ in Eq. (10.1) such that MLT recovers the turbulent pressure ($P^\mathrm{3D}_\mathrm{turb,m}$) at the base of the appended $\langle 3\mathrm{D} \rangle$-envelope, i.e.

$$\beta = \frac{P^\mathrm{3D}_\mathrm{turb,m}}{\rho^\mathrm{1D}_\mathrm{m} (v^\mathrm{1D}_\mathrm{c,m})^2}. \tag{10.3}$$

By following this approach, we allow $\beta$ to take a different value for each iteration and hence to evolve with time, in order to ensure a continuous stratification of $P_\mathrm{turb}$. However, as discussed in Section 10.2.4, it turns out that $\beta$ varies little over the computed evolution from the pre-main sequences (pre-MS) to the RGB.

The flowchart in Fig. 10.1 summarizes our implementation of $\langle 3\mathrm{D} \rangle$-envelopes into GARSTEC, including the calibration of the turbulent pressure.

The turbulent pressure contributes to the total pressure and must hence be accounted for when computing the radius from the requirement of hydrostatic equilibrium also in the interior model; cf. Eq. (2.8). Additionally, the turbulent pressure alters derivatives with respect to the total pressure, which enters the computation of the convective velocity, and a consistent implementation of turbulent pressure must hence iteratively take this feedback into account. Furthermore, we note that the kinetic energy of turbulent motion also adds to the total energy, contributing with $E_\mathrm{k} = v_\mathrm{c}^2/2$ per mass unit. Its change with time constitutes a further term in the energy equation solved in the interior model. We repeat that we ignore any energy contribution from the appended $\langle 3\mathrm{D} \rangle$-envelope. In order to appropriately account for the turbulent pressure in the frequency calculations, we compute model frequencies within the reduced $\Gamma_1$ approximation (cf. Chapter 3)

## 10.2 A Complete Solar Model

GARSTEC employs a first-order Newton iteration scheme, in order to evaluate the initial composition and the mixing length parameter that recover the global parameters of the Sun at the present solar age, as discussed in Chapter 2. In this chapter, we set $(\mathrm{Z_S/X_S})_\odot = 0.01792$ based on the photospheric and meteoritic abundances determined by Asplund et al. (2009) — that is, we use meteoritic values for all but the relevant isotopes of H, He, C, N, O, Ne, Si, S, Ar and Cr (cf. Serenelli et al., 2011; Jørgensen et al., 2019). The Stagger grid contains a simulation of the solar surface layers for the same composition. To facilitate an

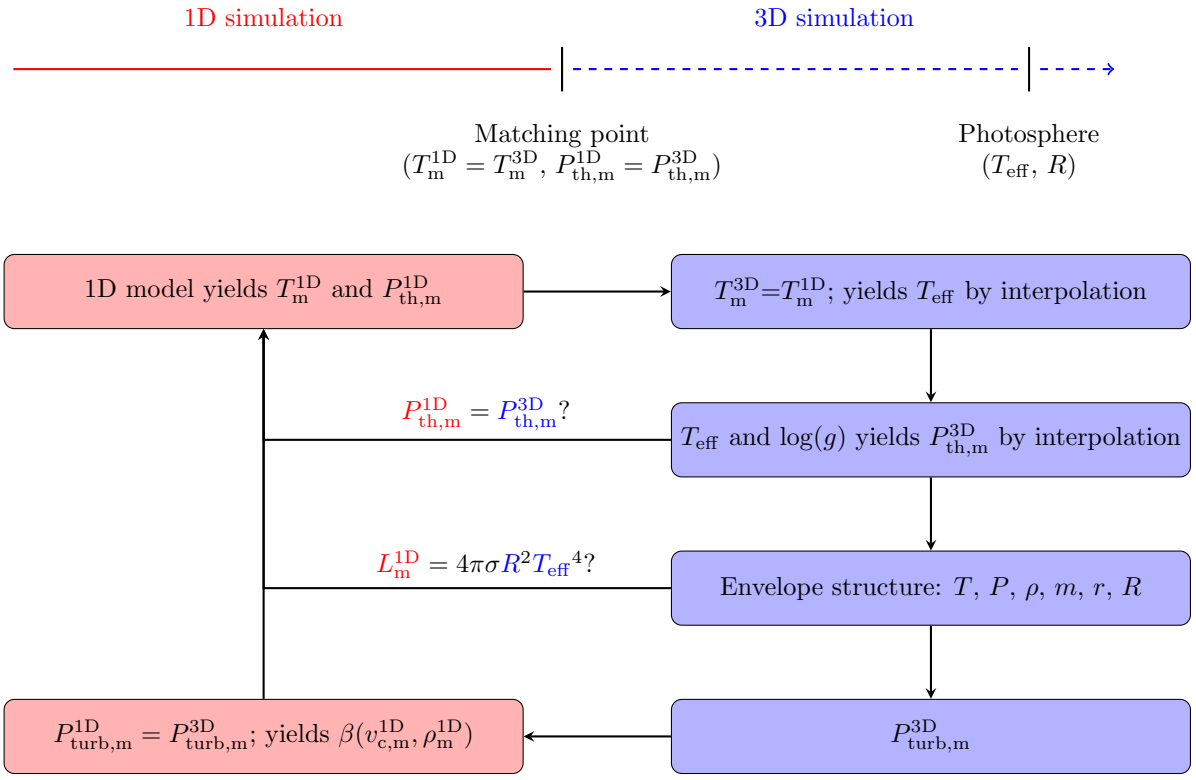


Figure 10.1: Flowchart summarizing the coupling of 1D and 3D simulations. An interpolated ⟨3D⟩-envelope is appended at each iteration and used as the outer boundary conditions to solve the stellar structure equations in the stellar interior. An equilibrium structure is found when the Stefan-Boltzmann law is fulfilled, and a continuous transition in the thermal pressure and temperature is ensured. A continuous transition in the turbulent pressure is enforced by a suitable choice of $\beta$ in Eq. (10.1).

easy comparison with this simulation, we set $T_{\mathrm{eff},\odot} = 5768.5\,\mathrm{K}$, which corresponds to the effective temperature of this simulation. Moreover, for all models of the present-day Sun presented in this chapter, $\log g$ deviates by less than 0.001 dex from the solar Stagger-grid simulation at the matching point.

Our analysis includes the following solar calibration models:

- Model A (3D + $P_{\mathrm{turb}}$) is constructed, using the method described in Chapter 8 in combination with Section 10.1. It hence appends an interpolated $\langle 3\mathrm{D}\rangle$-envelope and calibrates $\beta$ in Eq. (10.1) at each time-step.
- Model B: as model A, but the turbulent pressure has been ignored ($\beta = 0$).
- Model C (Edd. + $P_{\mathrm{turb}}$) uses an Eddington grey atmosphere as the outer boundary condition (cf. Chapter 2), and includes turbulent pressure. Interpolated $\langle 3\mathrm{D}\rangle$-envelopes are used to calibrate $\beta$ in Eq. (10.1) at every time-step: $\beta$ is chosen in such a way as to recover the turbulent pressure at the base of an $\langle 3\mathrm{D}\rangle$-envelope with the same $T_{\mathrm{eff}}$ and $\log g$ as the determined 1D model. The base of the $\langle 3\mathrm{D}\rangle$-envelope is placed at a thermal pressure that is $10^{1.2}$ times higher than the thermal pressure at the density inflection of the $\langle 3\mathrm{D}\rangle$-envelope. Note that the calibration of $\beta$ is the only role that the 3D simulations play for model C. The interpolated $\langle 3\mathrm{D}\rangle$-envelopes are not appended.
- Model D is a standard solar calibration model. It employs an Eddington grey atmosphere and does not include turbulent pressure.

In accordance with the results in Chapter 8, we find that the outer boundary conditions of models A-D do not alter the inferred abundance on the pre-MS: all four solar calibrations lead to similar initial compositions. The values obtained for $Y_{\mathrm{i}}$ and $Z_{\mathrm{i}}$ match within $10^{-4}$ and $10^{-5}$, respectively.

As discussed in Section 10.2.4, the evolution tracks of models A-D differ. Although models A-D only differ in the treatment of the outermost layers, one may expect this to affect the entire predicted structure of the present-day Sun, despite similar initial conditions. However, the differences in the stellar evolution tracks are rather small up until the current solar age. Overall, we thus find that the interior structures of models A-D are rather similar, despite the differences between the boundary conditions. Considering the similarities in the chemical evolution, this behaviour can be explained by the fact that all models are required to recover the same global parameters, i.e. $L_\odot$, $R_\odot$, $M_\odot$ and $(\mathrm{Z_S/X_S})_\odot$, which leads to the same asymptotic entropy of the deep adiabat. We will discuss the similarity of the structures of models A-D further in Section 10.2.2. At this point, one may rather turn the argument around: the fact that the interior structure, including the depth of the convection zone, is mostly unaltered by the boundary layers explains, why the initial composition is mostly insensitive to the outer boundary conditions.

The mixing length parameter ($\alpha_{\mathrm{MLT}}$), on the other hand, differs significantly between models A-D: the solar calibration yields a mixing length parameter of 1.78 when using

Table 10.1: Calibration values for the initial solar composition, the mixing length parameter and the scaling factor of the turbulent pressure. The latter is given at the age of the present Sun.

| Model | $Y_\mathrm{i}$ | $Z_\mathrm{i}$ | $\alpha_\mathrm{MLT}$ | $\beta_\odot$ |
|---|---|---|---|---|
| A (3D + $P_\mathrm{turb}$) | 0.2636 | 0.0149 | 4.8760 | 0.9977 |
| B (3D) | 0.2637 | 0.0149 | 3.6147 | — |
| C (Edd. + $P_\mathrm{turb}$) | 0.2638 | 0.0149 | 1.7362 | 1.9478 |
| D (Edd.) | 0.2638 | 0.0149 | 1.7824 | — |

standard input physics (model D). However, when coupling 1D and 3D simulations, the calibration results in a much higher mixing length parameter — that is, 4.88 and 3.61 for models A and B, respectively. This issue was discussed in detail in Chapter 8.

The substantially higher value of the mixing length parameter for models A and B illustrates the advantages of our coupling procedure over post-evolutionary patching (cf. Chapters 6 and 7), where 3D simulations are only used to substitute the outermost layers of the final model. In our coupling procedure, the interior model is required to match the physical conditions at the base of the appended $\langle$3D$\rangle$-envelope. The mixing length parameter ensures this by recovering the correct entropy difference between the deep adiabat and the matching point. For patched models, on the other hand, no such conditions are imposed, and patching an $\langle$3D$\rangle$-envelope to a SSM, such as model D, therefore leads to a structure that shows discontinuities in the stratifications of several physical quantities (cf. Chapter 6)

Taking turbulent pressure into account likewise affects $\alpha_\mathrm{MLT}$. The inclusion of turbulent pressure affects $\alpha_\mathrm{MLT}$ through a complex feedback[1], as it directly or indirectly affects different quantities. For instance, since turbulent pressure enters the hydrostatic pressure, it also affects the stellar radius, which must be accounted for by a change in $\alpha_\mathrm{MLT}$.

As regards Eq. (10.1), we find that $\beta_\odot \approx 1$ for model A, i.e. when appending interpolated $\langle$3D$\rangle$-envelopes at every time-step. Here, $\beta_\odot$ is the value of $\beta$ for our solar calibration models, i.e. at the age of the present Sun. The time evolution of $\beta$ will be addressed in Section 10.2.4. Using an Eddingon grey atmosphere and MLT, on the other hand, $\beta_\odot \approx 2$ (model C). This reflects the associated change in the calibrated mixing length parameter through the dependence of $v_\mathrm{c}$ on $\alpha_\mathrm{MLT}$ (cf. Eq. 10.2).

The initial composition, $\alpha_\mathrm{MLT}$, and $\beta_\odot$ are summarized in Table 10.1 for models A-D.

[1]As an example of the feedback on the stellar structure, we note that it is important to iteratively account for turbulent pressure when computing the convective velocity that enters the turbulent pressure. This was already mentioned in Section 10.1. If this feedback is ignored, $\alpha_\mathrm{MLT} = 1.6514$ for model C. The initial composition is unaffected.

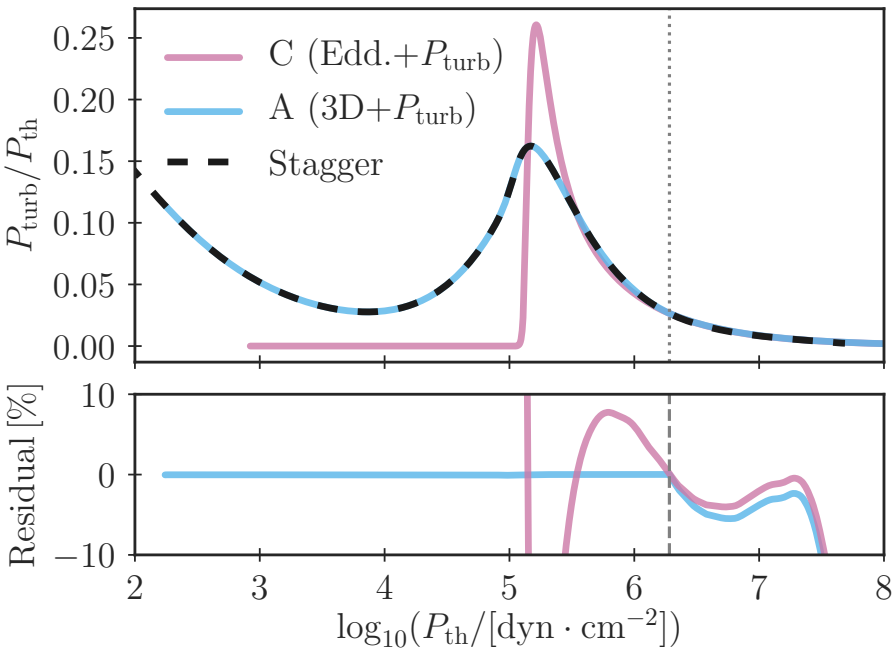


Figure 10.2: Ratio between turbulent pressure and thermal pressure in GARSTEC models of the present Sun. We include model A (3D + $P_{\rm turb}$) as well as model C (Edd. + $P_{\rm turb}$) described in Section 10.2. The dotted grey line indicates the position of the mesh point, at which the scaling factor of the turbulent pressure, i.e. $\beta$, is calibrated. In model A, this corresponds to the mesh point beyond which we append an interpolated ⟨3D⟩-envelope, i.e. it is the matching point. For comparison, we have included the original Stagger-grid simulation of the solar envelope.

### 10.2.1 The Turbulent Pressure Profile

Our interpolation scheme is able to reliably recover the stratification of the turbulent pressure in the Stagger-grid simulations. Furthermore, our coupling scheme ensures a continuous transition in turbulent pressure between the appended ⟨3D⟩-envelope and the interior model. This is illustrated in Fig. 10.2. As can be seen from the figure, the residuals between the turbulent pressure of model A relative to its thermal pressure and the corresponding quantity for the original ⟨3D⟩-envelope are negligible at any depth above the matching point. Moreover, by construction, both model A and C recover the correct turbulent pressure at the matching point.

As regards model C, we note that MLT recovers the correct stratification of the turbulent pressure at high thermal pressure when setting $\beta_\odot \approx 2$. At low thermal pressure, $v_{\rm c}$ is zero because the appended Eddington atmosphere is, by definition, radiative.

Adding turbulent pressure leads to an additional pressure-gradient force that counteracts gravity and hence affects the radius attributed to each mesh point of the model. Fig. 10.3 shows that the implementation of turbulent pressure leads to a better agreement between

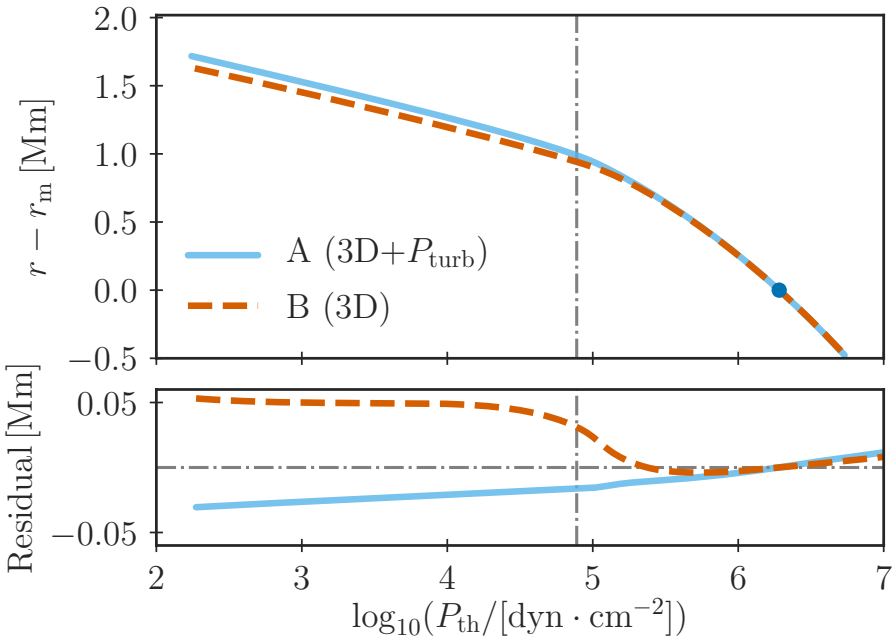


Figure 10.3: **Upper panel:** height above the base ($r_{\rm m}$) of the appended ⟨3D⟩-envelope for model A (3D + $P_{\rm turb}$) and B (3D). The location of the base of the ⟨3D⟩-envelope, i.e. the matching point, is indicated with a blue dot. The dash-dotted grey line denotes the location of the stellar surface, where the Stefan-Boltzmann law is required to be fulfilled. **Lower panel:** The associated residuals between the original solar Stagger-grid ⟨3D⟩-envelope and our solar calibration models. Positive residuals imply that the outermost layers of the GARSTEC model are less extended than the original Stagger-grid ⟨3D⟩-envelope. As discussed in Section 10.2.1, we mainly attribute the discrepancy between model A and the Stagger-grid simulation to deviations in the density stratification.

the depth scale of the underlying Stagger-grid simulation and the inferred radius of each mesh point in our GARSTEC models. For model A, the accumulated residual over the entire envelope is reduced to 30 km, i.e. 0.03 Mm. The inferred ⟨3D⟩-envelope of model A is thus larger than the original Stagger-grid ⟨3D⟩-envelope. Without turbulent pressure the residual is 50 km, i.e. 0.05 Mm, and has the opposite sign (model B).

The radius that is attributed to each mesh point follows from the requirement of hydrostatic equilibrium, i.e. Eq. (2.8). The residuals in $r$ hence reflect discrepancies in either $P$ or $\rho$. For model A, the pressure is correctly recovered, and the remaining residual in $r$ is due to the fact that the density inferred by the 1D stellar evolution code is systematically $1-3\,\%$ too low throughout the appended ⟨3D⟩-envelope. This is illustrated in Fig. 10.4. The inferred radius depends on the density through Eq. (2.8): $\mathrm{d}r \propto \rho^{-1}$. A too low density hence leads to a too large radius.

The reason for this systematic deviation of the density is many-fold: firstly, the largest deviation occurs close to the density inflection near the surface, where the temperature

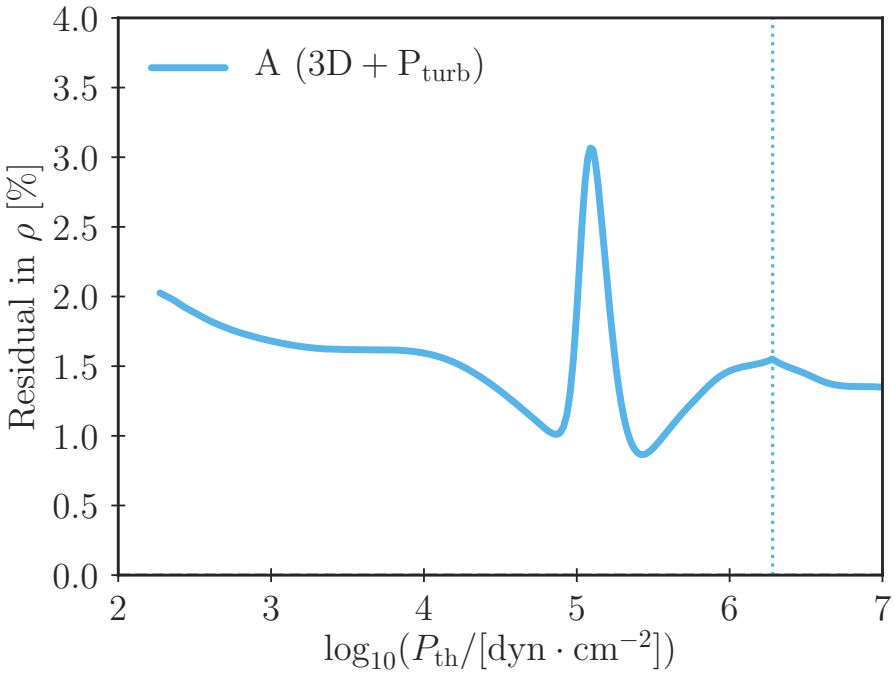


Figure 10.4: Residuals between the density stratification of the original solar Stagger-grid ⟨3D⟩-envelope and model A. Positive residuals indicate that the density of model A is too low. Different contributions to these residuals are discussed in the text.

changes rapidly. In this region, even small interpolation errors may lead to sizeable discrepancies in the temperature, which translates into errors in the density through the EOS (cf. Chapter 8). However, while the temperature residuals reach 0.05 % at the density inflection, the residuals are negligible throughout the rest of the ⟨3D⟩-envelope. Thus, only the spike close to $\log_{10}(P_{\rm th}) \approx 5$ may partly be attributed to interpolation errors. Secondly, the 1D and 3D simulation may deviate slightly in composition and hence in the mean molecular weight. However, we have attempted to reduce this contribution as far as possible by ensuring a large degree of consistency between the Stagger grid and the input physics in GARSTEC. It is also worth stressing that the convective envelope[2] is fully mixed. Thus, there are no variations in the compositions that may lead to spikes or similar features.

Thirdly, the 1D and 3D simulations do not employ the same EOS. Finally, the density is a non-linear function of the temperature, the pressure and the chemical composition. Consequently, the average density of a 3D simulation is not the same as the density derived from the mean of the underlying quantities, i.e. $\rho(\langle P\rangle, \langle T\rangle, \langle X\rangle, ...) \neq \langle\rho(P, T, X, ...)\rangle$ (cf. Collet, private communications).

In the case of model B, the density as a function of the thermal pressure is very similar to that of model A. On its own, this would result in the radius of model B being too large. However, the total pressure of model B is lower than the pressure of the solar Stagger-grid simulation, due to the neglect of turbulent pressure. All in all, this results in $r$ being too low: according to Eq. (2.8), $\mathrm{d}r \propto P$. The extent to which the neglect of the turbulent pressure affects the residuals in $r$ can be seen by comparing Fig. 10.2 with Fig. 10.3: the strong increase in the residuals around $\log_{10}(P_{\rm th}) \approx 5$ coincides with the peak in $P_{\rm turb}/P_{\rm th}$, i.e. the region where the contribution of the turbulent pressure increases by an order of magnitude.

### 10.2.2 The Sound Speed Profile

In order to assess the extent to which the evaluated solar structure is affected by the outer boundary conditions, we have computed the sound speed ($c$) of each of our four solar calibration models (models A-D):

$$c^2 = \frac{\Gamma_1 P_{\rm th}}{\rho}. \tag{10.4}$$

The sound speed is an essential quantity because it determines the propagation of acoustic oscillations in the solar interior (cf. Chapter 3). Conversely, the actual sound speed in the Sun can be reconstructed from solar oscillations by means of inversion. This is commonly done with respect to a reference model (e.g. Pijpers and Thompson, 1992; Christensen-Dalsgaard and Thompson, 1995). In this chapter, we employ the solar sound speed profile that was inferred by Basu and Antia (2008). For each solar calibration, we computed the difference between the squared sound speed of the model and the Sun:

$$\frac{\delta c^2}{c^2} = \frac{c^2_{\rm sun} - c^2_{\rm mod}}{c^2_{\rm sun}} \tag{10.5}$$

[2]Note that I refer to the entire convective envelope not only to the layers covered by the 3D simulations.

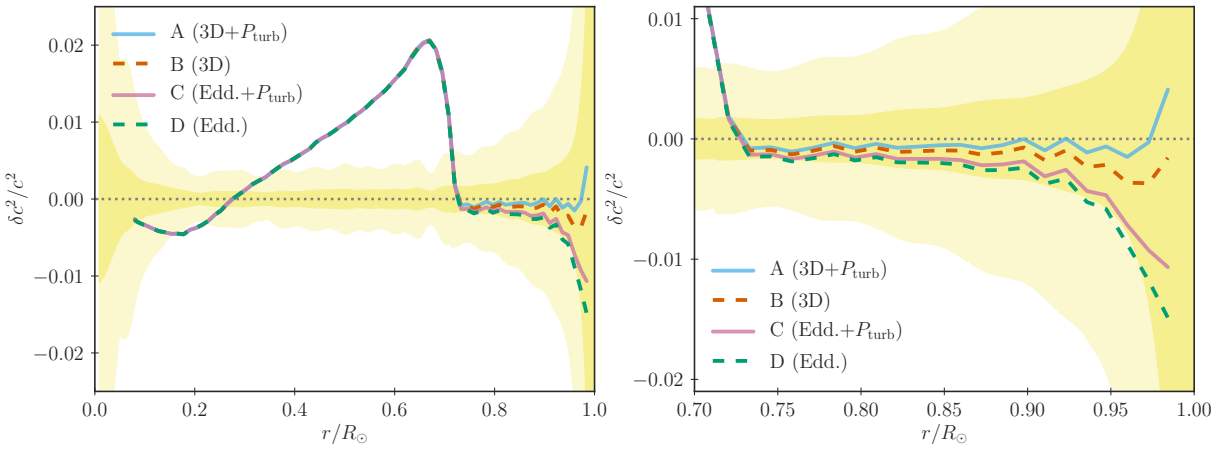


Figure 10.5: **Left-hand panel:** Squared sound speed difference between models A-D and the Sun. The shaded yellow area shows the statistical and conservative error estimates by Degl'Innocenti et al. (1997). These errors are dominated by the error that stems from the choice of reference model but also include observational errors — see text, for further details. We use the reference model by Basu & Antia (2008). The base of the ⟨3D⟩-envelope is located approximately 1 Mm below the photosphere, which roughly corresponds to $1.5 \times 10^{-3} R_\odot$. **Right-hand panel:** zoom-in in convective zone. Although the depth of the appended ⟨3D⟩-envelope is only $1.5 \times 10^{-3} R_\odot$, and although all models reach the same deep asymptotic adiabat, the different outer boundary conditions of models A-D clearly affect the stratification of the convection zone far beyond the extent of the ⟨3D⟩-envelope.

Here, $c_{\rm mod}$ and $c_{\rm sun}$ denote the sound speed of the model and the Sun, respectively. The results are shown in Fig. 10.5. For comparison, we include the uncertainties by Degl'Innoccenti et al. (1997). These uncertainties include observational errors on the measured p-mode frequencies, uncertainties of the inversion method and errors that stem from the choice of the reference model. The resulting uncertainties on the sound speed profile are mostly dominated by the latter contribution (cf. Fig. 3 in Vinyoles et al., 2017). In short, Degl'Innoccenti et al. (1997) use a small set of reference models with different input physics and vary the parameters that enter the inversion method. By adding the squared variations of the sound speed that result from this exploration of the associated parameter space, Degl'Innoccenti et al. (1997) arrive at an estimate of $\delta c/c$. They refer to this estimate as the statistical error. Noting that their exploration of the parameter space may not have been exhaustive, they furthermore give an alternative estimate of $\delta c/c$ by adding up all errors linearly. They denote this error as being conservative.

As can be seen from Fig. 10.5, we find that the inferred stratification of the outer convective layers is affected by the different boundary conditions of models A-D. Indeed, the coupling of 1D and 3D simulations leads to a better agreement between model predictions and the observationally inferred solar sound speed profile. Although the depth of the ⟨3D⟩-envelope itself is only $1.5 \times 10^{-3} R_\odot$, the different outer boundary conditions of models

A-D clearly affect the stratification of the convection zone far beyond the extent of the ⟨3D⟩-envelope. In this connection, the inclusion of turbulent pressure plays a minor role.

However, the sound speed profile of the deep interior stays unaltered. Thus, the models A-D agree on the structure of the radiative zone, which explains why the initial composition is only marginally affected by the boundary conditions (cf. Table 10.1). In particular, all four solar calibration models agree on the location of the base of the convection zone. We define the base of the convection zone ($r_{\rm cz}/R_\odot$) as usual by application of the Schwarzschild criterion for convective instability (cf. Chapter 2). For models A-D, $r_{\rm cz}/R_\odot$ is 0.7242, 0.7242, 0.7245, and 0.7245, respectively. According to Basu and Antia (1997), an inversion of solar oscillation frequencies suggests that the base of the convection zone is located at a radius of $0.713 \pm 0.001\,{\rm R}_\odot$. This is a well-known disagreement of solar models using the more recent lower present-day metallicities, in particular, those by Asplund et al. (2009). The improvements of the outer boundary conditions that results from the coupling 1D and 3D have little effect on the location of the base of the convection zone.

There is also a large anomaly in $\delta c^2/c^2$ close to the base of the convection zone (Fig. 10.5). This so-called tachocline anomaly is likewise a well-known shortcoming of state-of-the-art solar models (cf. Chapter 4 or Christensen-Dalsgaard et al., 1985, 1988b), and again the use of AGSS09 abundances is found to lead to a particularly strong disagreement with observations (Serenelli et al., 2009).

### 10.2.3 Solar Oscillations

Following the approach outlined in Section 3.1.2, we computed adiabatic model frequencies for model A. In order to assess the extent, to which our method corrects for the structural contribution to the surface effect, we compared these model frequencies to BiSON observations. The comparison is shown in Fig. 10.6.

We find that the adiabatic model frequencies of model A are systematically lower than the observed frequencies. The frequency residual is close to $12\,\mu$Hz in the vicinity of the frequency of maximum power ($\nu_{\rm max,\odot} = 3090\,\mu$Hz). Overall, the obtained frequency residuals are in very good agreement with the structural surface effect inferred by Houdek et al. (2017) and in Chapter 8 using post-evolutionary patching.

Houdek et al. (2017) have determined the modal contribution to the surface effect for the present-day Sun, using a time-dependent, non-local treatment of pulsational perturbations. Such effects include non-adiabatic energetics. According to Houdek et al. (2017), the modal surface effect counteracts the structural surface effect. Furthermore, the modal surface effect matches the frequency residuals of model A as a function of frequency (cf. Fig. 1 and 5 in Houdek et al., 2017). To illustrate this, we have included the modal surface effect from Houdek et al. (2017) in Fig. 10.6 — with the opposite sign, in order to facilitate an easy comparison with the structural surface effect. The remaining residuals between observations and the model frequencies from model A are at most $2\,\mu$Hz for frequencies below $4000\,\mu$Hz, once modal effects have been subtracted. Physical differences between our solar calibration models and those used by Houdek et al. (2017) may partly contribute to the remaining frequency residuals. However, we note that Houdek et al. (2017) obtain the

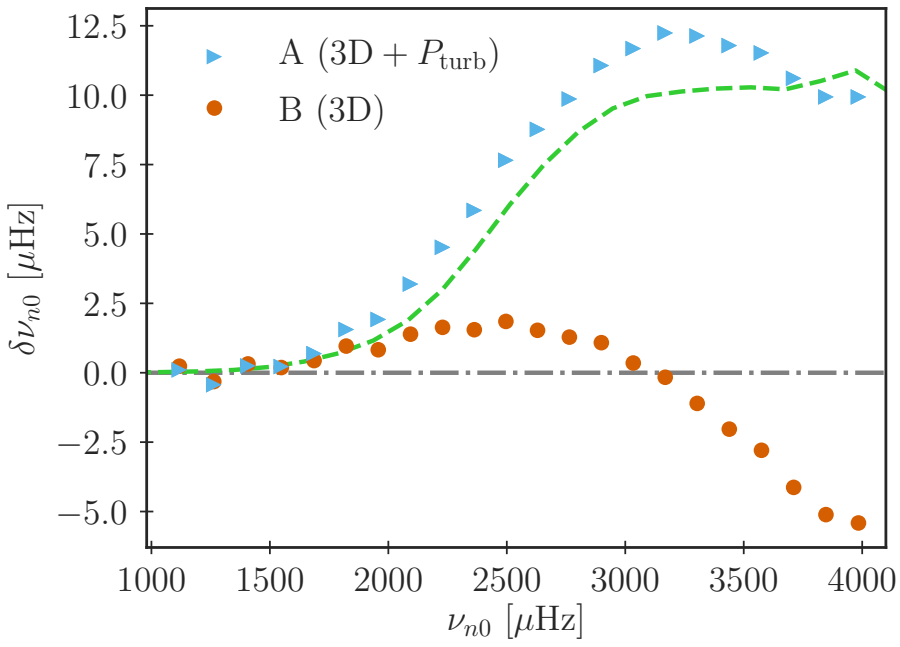


Figure 10.6: Frequency difference between BiSON observations and a model of the present Sun that appends an interpolated ⟨3D⟩-envelope and calibrates $\beta$ at each time-step (model A). Model B is included for comparison, to demonstrate the effect of including turbulent pressure. The dashed light green line shows the modal effect (with opposite sign) that was originally published in Fig. 1 in Houdek et al. (2017). The modal effect and the structural effect combine to an effective residual of at most 2 $\mu$Hz everywhere. The modal effect was kindly provided by G. Houdek. Only radial modes ($\ell = 0$) with frequencies above 1000 $\mu$Hz are included.

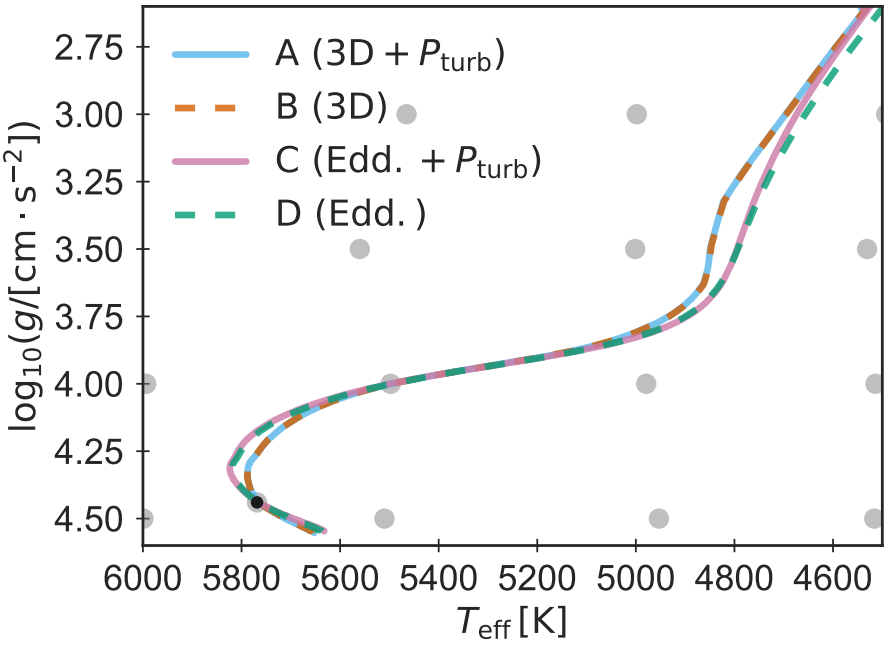


Figure 10.7: Kiel diagram showing the evolution tracks of four different solar models corresponding to models A-D, starting from the zero age main sequence (ZAMS). The grey circles show the location of a selection of Stagger-grid simulations that entered the interpolation. The black dot indicates the position of the present Sun.

same deviation of at most 2 $\mu$Hz.

From the above, we conclude that model A successfully eliminates the structural surface effect, leaving only modal effects to be corrected for. Our method hence overcomes the structural shortcomings of the surface layers that haunt current standard stellar structure models. The remaining systematic offset between model frequencies and observations is mainly due to the assumption of adiabaticity that enters the frequency computation.

### 10.2.4 Evolution of the Sun

Below, we discuss the predicted evolution of the Sun based on our four calibration models of the present Sun (models A-D). The computed evolutionary tracks are shown in Fig. 10.7.

We find that the coupling of 1D and 3D simulations leads to a lower effective temperature at the turn-off point, i.e. at the end of the MS, and to higher effective temperatures on the RGB. This is consistent with the findings of Mosumgaard et al. (2018), who use a variable $\alpha_{\mathrm{MLT}}$ and altered boundary conditions in order to encapsulate the basic properties of 3D simulations (Trampedach et al., 2014a,b): Mosumgaard et al. (2018) conclude that their implementation of information from 3D simulations lead to higher temperature on the RGB. A detailed comparison with this method is discussed in Chapter 8.

As can be seen from Fig. 10.7, the evolution of solar models with Eddington atmospheres

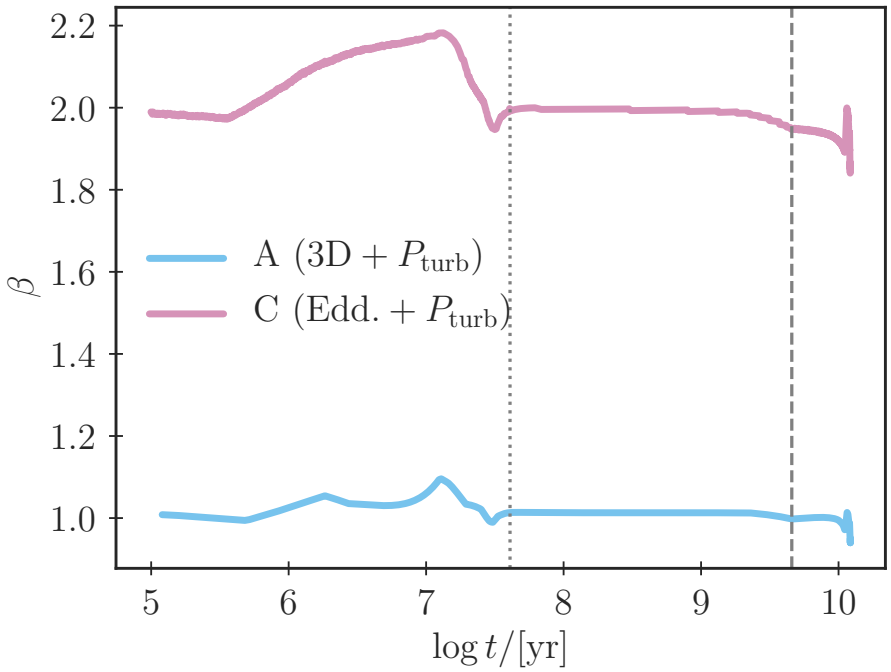


Figure 10.8: The calibrated scaling factor ($\beta$) of the turbulent pressure as function of the stellar age for model A (3D + $P_{\mathrm{turb}}$) and model C (Edd. + $P_{\mathrm{turb}}$). The dotted line indicates the age of the models on the ZAMS, while the dashed line marks the age of the current Sun. We have computed the stellar evolution up until an age of roughly 12 Gyr.

(models C and D) are not significantly altered by taking turbulent pressure into account until the RGB. When coupling 1D and 3D simulations, turbulent pressure is mostly irrelevant for the evaluated evolutionary track.

We note that models that include ⟨3D⟩-envelopes on the fly are subject to interpolation errors, due to the low number and the distribution of the simulations in the Stagger grid. This can be seen from Fig. 10.7, where kinks in the evolutionary tracks reflect the triangulation that underlies the interpolation procedure and thereby indirectly reflects the depth of the appended ⟨3D⟩-envelope. This issue is discussed in detail in Chapter 8, and we will hence not touch further upon it in this chapter. We solely note that our results call for a refinement of the Stagger grid.

From our analysis we conclude that $\beta$ in Eq. (10.1) is approximately constant from the pre-MS to the RGB — that is, at least in the solar case. This result is summarized in Fig. 10.8.

The fact that $\beta$ is constant as a function of time partly reflects the fact that we have assumed $\alpha_{\mathrm{MLT}}$ to be constant across the HR diagram, i.e. to correspond to the value obtained from the respective solar calibration. This is a simplifying approximation: asteroseismic and spectroscopic measurements and simulations point towards a variation of $\alpha_{\mathrm{MLT}}$ with $T_{\mathrm{eff}}$, $\log g$ and [Fe/H] (see for example Trampedach et al., 2014b; Magic et al., 2015; Tayar et al.,

2017). As discussed in Chapter 9, this simplifying assumption plays a minor role for coupled models but is rather important when dealing with standard stellar models. However, no consensus has yet been reached. Also, this simplifying assumption is commonly used, and so by employing a constant mixing length parameter, we facilitate a more straightforward comparison with standard stellar models.

While the use of a constant $\alpha_{\rm MLT}$ may affect the predicted evolution after the MS, we furthermore note that this assumption is irrelevant for the solar calibrations themselves: the variation in $\alpha_{\rm MLT}$ across the relevant parameter space is negligible (cf. Figs 4 and 5 in Trampedach et al. 2014b).

## 10.3 Summary

In previous chapters, we have discussed how to improve upon the modelling of stars with convective envelopes by replacing the outermost superadiabatic layers in 1D stellar evolution codes with mean 3D structures. Building upon these previous steps, we have now included turbulent pressure at every time-step of the predicted stellar evolution based on 3D RHD simulations. We have shown that our improved method reliably recovers the mean stratification of 3D hydrodynamic simulations of stellar envelopes, in the case of the present Sun. Furthermore, our method removes most of the need for describing convection by MLT in the superadiabatic regions near the surface. The appended 3D boundary layers are coupled to the nearly-adiabatic regions during the entire stellar evolution.

We have applied our method to the solar case and did complete standard solar model calibrations for different atmosphere models with and without including turbulent pressure. By comparing to helioseismic observations, we show that our method fully corrects for the structural contribution to the surface effect. Only modal effects are still left to be accounted for, but the remaining discrepancy agrees with the predicted correction if oscillations frequencies would be computed including deviations from adiabaticity (Houdek et al., 2017). The computation of oscillation frequencies, however, is not an issue of hydrostatic stellar models, but concerns pulsation codes. Furthermore, we show that our method leads to a better reconstruction of the solar sound speed profile than the standard procedure does. However, we note that this conclusion is not necessarily compelling due to the large error-bars involved.

We find that the altered boundary layers affect the predicted solar evolution: our method leads to higher effective temperatures on the RGB and shifts the turn-off point at the end of the MS. The consistent implementation of turbulent pressure, however, is found to have a negligible effect on the evolution track.

The described implications for stellar evolution tracks will have ramifications for the asteroseimically and spectroscopically inferred global parameters of low-mass stars with convective envelopes. This is relevant for the interpretation of high-quality data from the CoRoT, *Kepler*, K2, and TESS space missions as well as for the upcoming PLATO mission (e.g. Ricker et al., 2015; Miglio et al., 2017): in its search for habitable Earth-like planets, PLATO will focus on solar-like dwarfs.

Our analysis shows how essential a realistic treatment of superadiabatic convection is for the computation and applicability of stellar models. In light of this, our method constitutes a useful improvement of 1D stellar evolution codes. However, we note that our method is presently subject to interpolation errors due to the low number of existing 3D simulations. These errors may potentially alter the predicted evolution, affecting the inferred stellar parameter estimates. The necessity to remedy this issue calls for a refinement of current grids of 3D envelopes since the robustness of the interpolation depends on how densely the available 3D simulations cover the relevant regions of the parameter space. For a more detailed discussion on interpolation errors and the implications of the coupling of 1D and 3D simulations on the stellar evolution tracks, I refer to Chapters 8 and 9.

# Chapter 11

# Conclusions

This thesis explores several different methods to improve standard one-dimensional (1D) models for stellar structures and their evolution by drawing upon multi-dimensional simulations of hydrodynamic processes. In particular, two issues are addressed: firstly, 1D stellar models yield an incomplete depiction of the outermost superadiabatic layers of stars with convective envelopes. This affects the predicted evolution through improper boundary conditions as well as the predicted oscillations frequencies. The simplified depiction of the surface layers in 1D models is thus known to manifest itself as a systematic offset between model frequencies and observations. This offset is, therefore, referred to as the surface-effect. Secondly, observational constraints point towards an improper modelling of the transition between the radiative interior and the convective envelope. Both of these issues arise due to a simplified description of convection. In contrast to 1D stellar models, multi-dimensional hydrodynamic simulations have been shown to paint a more realistic picture of the physical processes that are at play. By including information from two- and three-dimensional (2D and 3D) simulations into a 1D stellar evolution code, I am thus partly able to remedy the mentioned shortcomings of 1D models.

Chapter 4 presents a self-contained analysis of the transition region between the convective envelope and the radiative interior of the Sun. Chapters 5-10, on the other hand, constitute a continuous body of work and show the gradual development of different methods to improve the description of the superadiabatic near-surface layers of stars with convective envelopes. In the following, I give a detailed summary of the main conclusions of each chapter, highlighting the central take-aways.

Chapter 4 deals with additional mixing processes at the base of the convection zone based on information extracted from hydrodynamic simulations of convection (see also Appendix B). The reasoning behind the implementation of such additional mixing processes is twofold: firstly, the depletion of lithium that is predicted by standard stellar models at the solar surface is incompatible with photospheric and meteoritic measurements of element abundances. By including additional mixing below the convective envelope, lithium is transported to regions, where it is efficiently burned. In this way, I am able to construct solar models that yield the correct photospheric lithium abundance. Moreover, by precluding these mixing processes from taking place on the pre-main sequence, the depletion of

lithium becomes qualitatively consistent with measurements of star clusters. Secondly, the commonly assumed abrupt transition between the convective envelope and the radiative interior leads to an anomaly in the inferred sound speed profile of standard solar models. Again, additional mixing may partly solve this model deficiency. However, it turns out that different degrees of mixing are needed to address each the two problems. In other words, the investigated mixing processes are, on their own, insufficient to solve both discrepancies in tandem. This conclusion is the main take-away from Chapter 4: although parameterizations of diffusive mixing beyond the convective boundary are frequently employed in 1D stellar models, these prescriptions do not seem to encompass all the relevant physics.

The core chapters of this thesis focus on the outermost superadiabatic layers of stars with convective envelopes. Two different methods for improving the depiction of these layers in 1D stellar models are discussed. Both methods draw upon more realistic 3D hydrodynamic simulations that span from the outer atmosphere to the nearly-adiabatic interior below the photosphere. Since these simulations are computationally expensive, I developed and tested a method that allows interpolating in existing grids of 3D simulations based on their apparent homology. Since the obtained structures are to be implemented in 1D stellar models, the interpolated temporal and spatial averages of the relevant quantities suffice. I refer to these averages as $\langle 3D \rangle$-envelopes. As demonstrated through several cross-validation exercises discussed in Chapter 5, the interpolation method reliably recovers the correct mean stratification of $\langle 3D \rangle$-envelopes — that is, at least for cold main-sequence stars. The subsequent chapters build on this finding, making it the primary take-away from Chapter 5.

In Chapter 6, I compute the evolution of stellar structures using standard input physics. For each computed stellar evolution track, I subsequently substitute the improper outermost layers of the final model with a suitable (interpolated) $\langle 3D \rangle$-envelope. This ad hoc correction of the surface layers is commonly referred to as patching. I implemented and validated my own patching procedure and applied my patching method to study the present-day Sun as well as various *Kepler* stars. The application to *Kepler* stars only became possible based on the interpolation scheme presented in Chapter 5. One of the main novelties of the analysis in Chapter 6 is hence the broad applicability of the presented method.

The irreconcilable physical assumptions that enter 1D and 3D simulations lead to discontinuities in the patched structures. This issue can be addressed following several different but equally physically motivated strategies. To shed light on this issue, I implemented and compared several different patching criteria, quantifying how these different criteria affect the resulting patched models and their seismic properties. By uncovering the systematic errors that are associated with the seismic predictions of patched models, Chapter 6 lays the groundwork for applying patched models in asteroseismic analyses.

Patching largely corrects for the structural inadequacies of the surface layers of 1D stellar models and hereby partly eliminates the structural contribution to the surface effect. By far the largest contribution to the remaining surface effect stems from the fact that the frequency calculations do not consistently account for the contribution of turbulent pressure and neglect non-adiabatic energetics. These systematic errors are collectively referred to as modal effects. Building upon the ability of patched models to partly overcome the surface

effect, I examine different parameterizations of the model frequencies of patched models. These parameterizations are presented in Chapter 7, where I use them to discuss properties of empirical surface correction relations. Such relations are commonly employed to deal with the surface effect. I find that my parameterizations are biased by the selection criteria that determine which models are to enter my analysis. Moreover, I show that surface correction relations that are calibrated based on the Sun alone perform worse than surface correction relations that are not calibrated in this manner. Both of these findings point towards the conclusion that there exists no unique set of coefficients that applies to all combinations of global stellar parameters. This statement is intriguing, as it rules out any empirical surface correction relations that are calibrated based on stars, whose global parameters strongly deviate from the target star. Furthermore, I show that the neglect of modal effects affects the inferred stellar parameter estimates from asteroseismic analyses, which likewise discourages the use of certain surface correction relations. Thus, Chapter 7 illustrates that patching is undeniably a strong diagnostic tool: patching is able to shed light on crucial aspects of asteroseismic analyses and on the performance of stellar structure models.

Due to the inconsistencies between the physics employed in the 1D and 3D simulations, a continuous transition between the interior and the patched $\langle 3D \rangle$-envelope can, however, not be achieved for all thermodynamic quantities without adjusting the interior structure. Furthermore, although patching partly corrects for the structural drawbacks of the final model, it does not correct for the use of improper boundary layers throughout the computed evolution. This thesis, therefore, presents a more sophisticated method that employs interpolated $\langle 3D \rangle$-envelopes to iteratively set the outer boundary conditions of 1D stellar models at every time-step. Beyond the outer boundary of the 1D model, an interpolated $\langle 3D \rangle$-envelope is appended. This $\langle 3D \rangle$-envelope extends from low optical depths to the nearly-adiabatic interior. Our treatment encompasses all relevant input physics, including a properly calibrated depiction of turbulent pressure. By coupling 1D and 3D simulations in this manner, I find that our stellar evolution code reliably mimics the underlying 3D simulations. Like patching, this coupling procedure hence largely corrects for the structural surface effect. In addition, the new boundary layers also affect the evolution tracks, leading to higher effective temperatures for red giants, and shifting the point in the Hertzsprung-Russel diagram, at which stars leave the main sequence.

In Chapters 8-10, I give a detailed account of the mentioned coupling scheme and present several analyses of the present-day Sun, since this is a vital seismic benchmark case. The method is further applied in asteroseismic analyses of solar-like stars in the *Kepler* field and to Alpha Centauri A and B. From these analyses, I conclude that the presented coupling method is, in many ways, superior to mixing length theory (MLT) and equivalent parameterizations of turbulent convection: in the case of the present-day Sun, near-perfect agreement with seismic constraints is achieved. Moreover, based on Bayesian statistics, I show that the coupling of 1D and 3D simulations lead to stellar parameter estimates that are mostly insensitive to the mixing length parameter. In this way, the presented coupling method does not suffer from the same degeneracies as models that rely on MLT do.

In summary, there are three main take-aways from Chapters 8-10: first, the obtained 1D stellar models reliably mimic 3D simulations without suffering from the same inconsistencies

as patched models do. Secondly, by including all relevant input physics from 3D simulations, the structural contribution to the surface effects is successfully eliminated. Thirdly, the improvement of the outer boundary conditions affects the stellar evolution tracks and leads to more robust stellar parameter estimates. The presented coupling procedure is, therefore, a powerful improvement of stellar models.

In this thesis, I focus on low-mass main-sequence stars. Such stars are of utmost importance for current and next-generation surveys that strive to find habitable Earth-like planets orbiting solar-like hosts. Since the coupling of 1D and 3D models primarily affects the evolution track of later phases, future detailed analyses of subgiants and red giants likewise promise to be fruitful. Such stars are of particular interest when performing an analysis of the chemo-dynamical evolution of the Milky Way galaxy. However, proper exploitation of the coupling and patching of 1D and 3D simulations requires a refinement of the existing grids of 3D simulations when addressing stars beyond the main sequence.

All in all, the results presented in this thesis underline the tremendous potential of multi-dimensional hydrodynamic simulations to significantly improve state-of-the-art 1D stellar models. Due to the apparent discrepancies between model predictions and high-quality observations, such improvements are much needed: the progress of stellar physics relies on the interplay between ever more profound and precise observational constraints and ever more accurate models, in order to interpret and understand the underlying physical phenomena. Furthermore, nearly every field of astronomy — from cosmology to exoplanet research — relies directly or indirectly on a proper comprehension of stars.

# Chapter 12

# Outlook

In the previous chapters, I mainly focus on two different methods for including 3D simulations of stellar envelopes into 1D stellar models (cf. Chapters 5-10). The first method allows for an ad hoc correction of the final model by substitution of the outermost layers in the post-processing. The second in-situ method includes 3D simulations at every time-step, yielding a more realistic depiction of stars than the standard procedures in stellar modelling do. In combination with spectroscopic, astrometric and asteroseismic measurements (cf. Section 12.4), our novel methods may provide new insights into stellar physics as well as adjacent fields, such as galactic archaeology and exoplanet research.

In this thesis, I have addressed low-mass main-sequence stars, such as the present-day Sun, Alpha Centauri A and B, and a handful of *Kepler* targets. Through these first applications of the methods, I have demonstrated the applicability and versatility of the methods. For instance, the results in Chapter 7 clearly underline how the presented methods may be used as a valuable diagnostic tool, while the results in Chapter 9 imply that the in-situ method yields more robust parameter estimates than the standard procedure does. Moreover, the work presented in this thesis lies the groundwork for a broad range of applications of my methods.

Low-mass stars are of the utmost importance when dealing with current and next-generation surveys, such as PLATO: in their quest for finding habitable Earth-like planets, these surveys focus on solar-like stars (cf. Rauer et al., 2014). It would, therefore, be fruitful to apply the method to characterize a broad range of stars, to provide the community with more accurate stellar parameter estimates. This may be achieved through a parameterization of the properties of coupled models, entering the realm of big-data science (e.g. Bellinger et al., 2016).

It would, furthermore, be interesting to extend the analysis to include subgiants and giants — in particular, more peculiar targets, such as low metallicity giants with abnormal seismic properties (e.g. KIC 4671239, Thygesen et al., 2012; Mosser et al., 2017). This is first and foremost due to accumulated structural changes that arise from the more realistic depiction of superadiabatic convection provided by 3D simulations. Thus, as shown in Chapters 8-10, the use of 3D simulations in 1D stellar evolution codes affects stellar evolution tracks, especially beyond the main sequence. It is, therefore, important to quantify

the extent to which the improved boundary conditions affect stellar parameter estimates. One reason this is crucial is the circumstance that accurate age estimates for red giants are fundamental when addressing questions that deal with the chemo-dynamical evolution of the Milky Way galaxy (e.g. Silva Aguirre et al., 2018).

## 12.1 Extending Grids of 3D Stellar Envelopes

Presently, only a limited amount of 3D simulations of stellar envelopes is available, which limits the application of the methods presented in this paper. As discussed in Chapter 5 and subsequent chapters, the low refinement of these grids leads to interpolation errors. Although high accuracy can be guaranteed for MS stars, which makes my methods broadly applicable in connection with, say, *Kepler* data, this not the case throughout the HR diagram. Interpolation errors and the systematic errors that may arise from these pose a problem for later evolutionary stages. A refinement of the existing grids of 3D simulations is, therefore, much needed.

Another problem is the composition of the 3D simulations: although the Stagger grid includes simulations with different compositions, the helium mass fraction is fixed for any given metallicity. Even worse, for the Stagger grid, an increase in metallicity is accompanied by a decrease of the helium mass fraction, which is counterintuitive from the point of view of galactic chemical evolution. A fully consistent implementation of 3D simulations into 1D stellar evolution codes, therefore, requires an extension of the Stagger grid, by including the helium abundance as another dimension in the parameter space of 3D simulations.

By further extending the dimensions of the parameter space, much can be learned, since standard stellar structure models are haunted by several shortcomings stemming from approximations in connection with MHD processes. For instance, the effect of magnetic fields on stellar structures and mixing processes as well as magnetic activity, including the underlying physical phenomena, are not well-understood (cf. Solanki et al., 2006). As in the case of convection, the implementation and parameterization of results from 3D simulations may be used to properly account for magnetic fields in the convective envelopes of 1D models. Magic and Weiss (2016) presented first attempts to address this issue, showing that the presence of magnetic fields affects helioseismic properties. It would hence be fruitful to capture and parameterize the essential features of magnetic fields from 3D simulations, by expanding the parameter space of 3D envelopes by the magnetic field strength and morphology. In combination with 1D models and asteroseismic measurements, this may lead to a better understanding of the underlying physical processes.

Generally speaking, much can be gained from further expansions of the parameter space of 3D envelopes, and many issues of 1D models may be addressed by using multi-dimensional MHD simulations of stellar envelopes and cores. As discussed in this thesis, this includes the treatment of convective boundaries. Furthermore, mass loss mechanisms, angular momentum transport in stellar interiors and the role of rotational mixing are poorly understood, and the coupling of multi-dimensional MHD simulations with 1D stellar evolution codes may help to shed light on these issues (see also Meakin and Arnett, 2007;

Rieutord, 2016; Jiang et al., 2018; Cristini et al., 2019).

## 12.2 Alternative Approaches

Rather than including the entire stratification of 3D envelopes into the stellar evolution code, one may include the parameterization of core properties. One example of such an approach is the scheme suggested by Trampedach et al. (2014a,b). Here, the mixing length parameter is calibrated to ensure that the interior model is consistent with the 3D simulations at their lowermost point. Moreover, the $T(\tau)$ relation that describes the radiative atmosphere is directly extracted from the 3D simulations, and the radiative gradient at low optical depths is adjusted to give a more realistic depiction of the photospheric transition. As discussed in Chapter 8, the resulting solar evolution track is qualitatively speaking in better agreement with the evolution predicted by coupled models than the tracks from standard solar models are. However, whether this is generally the case, i.e. whether the scheme by Trampedach et al. (2014a,b) universally yields the correct evolution, is unclear. Furthermore, as discussed in Chapters 6 and 8, a mixing length parameter that is constant as a function of depth does not recover the complexity of turbulent convection as predicted by 3D simulations. Indeed, as discussed by Trampedach and Stein (2011), a mixing length parameter that varies with depth gives a more realistic picture: based on the mass flux in 3D simulations, Trampedach and Stein (2011) determine the typical length scale, the so-called mass mixing length, over which ascending fluids turn over. The ratio between this length scale and the pressure scale height, i.e. the mass mixing length parameter, varies greatly with depth. Interestingly, as shown by Trampedach and Stein (2011), the mass mixing length parameter is a rather generic function of the pressure in units of the pressure at the stellar surface, which may facilitate a parameterization of the mass mixing length parameter as a function of the global stellar parameters. Including a mixing length parameter that varies with depth based on 3D simulations may thus be a step forward. All in all, however, the coupling of 1D and 3D simulations, as presented in Chapters 8-10, is the most physically consistent approach.

## 12.3 Non-adiabatic Effects

The methods presented in this thesis have been shown to completely eliminate the structural shortcomings of 1D models that contribute to the surface effect. However, the structural surface effect, on its own, does not explain the systematic offset between model frequencies and observations. Another contribution stems from simplifying assumptions that enter the frequency calculation: modal effects, including the contributions from non-adiabatic energetics, are commonly neglected, leading to systematic errors in the computed frequencies. This obstacle can be circumvented in asteroseismic analyses by using frequency ratios as proposed by Roxburgh (2005). However, in the case of the Sun, the problem of modal effects has recently been overcome (Houdek et al., 2017). In order to fully eliminate the

surface effect and substitute the need for empirical surface correction relations, widely applicable and user-friendly tools that compute stellar frequencies without the assumption of adiabaticity must be provided to the community.

## 12.4 A Bigger Picture

The conclusions drawn from stellar models enter nearly all fields of astrophysics. Consequently, the accuracy of stellar models is crucial for a detailed understanding of the cosmos. For instance, a proper characterization of a planet that orbits a distant star relies on a minute knowledge of its host star through Kepler's laws. The climate and the habitability of planets are likewise determined by their host stars. As a result, a proper understanding of stellar structures and their evolution is critical, when addressing many pressing questions such as: what fraction of exoplanets may potentially harbour life? Stellar physics plays an important role in the search for Earth-like planets around Sun-like hosts. The extent to which the improved depiction of the outermost superadiabatic layers affects the inferred properties of exoplanets remains to be quantified.

In addition, stellar models provide the progenitors for supernova simulations (cf. Janka et al., 2007). Since supernova explosions and stellar winds enrich the interstellar medium, stellar models are essential to get a sound grasp of the formation history of, say, molecular clouds. Furthermore, the determination of the age of star clusters naturally relies on stellar models. In short, the study of the chemo-dynamical evolution of the Milky Way galaxy builds on conclusions drawn from stellar physics (Miglio, 2012). After all, galaxies are essentially composed of stars that move in the potential well of a dark matter halo. Stellar physics thus contributes, when answering questions such as: how did the galaxy form? Especially, in combination with the high-quality astrometric and spectroscopic measurements from surveys, such as GAIA and APOGEE (cf. Gaia Collaboration et al., 2016; Eisenstein et al., 2011), asteroseismology provides invaluable insights on this topic (e.g. Silva Aguirre et al., 2018).

In this way, a diverse collection of astrophysical studies, ranging from supernova simulations to galactic archaeology, rely on the accuracy of stellar evolution calculation. As shown in this thesis, the improved depiction of the outermost superadiabatic layers affects the stellar evolution tracks. The extent to which this affects, say, the inferred chemical history of the Milky Way galaxy remains to be quantified.

Even fields of research that lie outside of astrophysics sometimes greatly benefit from stellar structure models. One prominent example is the field of particle physics, where the Sun is used as a laboratory (e.g. Raffelt, 1996). Thus, solar models have been used to put constraints on neutrino oscillations: the fusion reactions that power the Sun produce electron neutrinos. However, some of these have changed their weak flavour, when they reach the Earth's orbit since the weak eigenstates are not mass eigenstates. Based on minute knowledge of the solar neutrino flux, constraints can be put on the parameters that govern neutrino oscillations (e.g. Haxton et al. 2013). It has even been suggested that stars may help to constrain the properties of so-called dark matter (e.g. Cumberbatch et al., 2010;

Casanellas and Lopes, 2013, 2014): the movement of stars in galaxies and galaxies in clusters suggests the presence of matter that does not seem to interact via the electromagnetic force but does feel gravity (cf. Zwicky, 1937; Rubin and Ford, 1970). It is possible that dark matter also interacts via other forces, say, the weak force. If so, dark matter may lose energy as a result of scattering, when passing through stellar interiors. This would lead to an accumulation of dark matter in the centre of stars, which would contribute to the heat transport and affect the stellar structure. In this way, stellar observations may help to reveal the nature of dark matter, shedding light on a fundamental aspect of particle physics. However, in order to do so, sources of error and inadequacies in stellar models must be eliminated. In other words, the fact that standard stellar models are haunted by systematic effects, such as the surface effect, undoubtedly restricts their usefulness as laboratories for nuclear and particle physics. Moreover, having eliminated one of these systematics not only increases the versatility of stellar models, but it may also help to reveal other model deficiencies that were previously overshadowed. Through the improved characterization and depiction of stellar structures that result from the use of more realistic boundary layers, the methods presented in this thesis may hence have interesting implications for other fields of research outside of astrophysics. Again, these implications remain to be quantified.

Indeed, very few areas are not directly or indirectly affected by results derived based on stellar physics. The current understanding of stars even affects cosmological predictions. For instance, stellar age estimates of the oldest stars provide a lower limit on the Hubble constant (cf. Jimenez et al., 2019). As a final example, it is worth mentioning that knowledge about the first stars and luminous sources is crucial for our understanding of the reionization of the intergalactic medium that occurred in the early history of the Universe (e.g. Tumlinson and Shull, 2000; Barkana, 2006).

# Appendix A

# Acronyms and Nomenclature

**1D** ..... One-dimensional

**3D** ..... Three-dimensional

$\langle$**3D**$\rangle$ ..... 1D spatial and temporal average of 3D structure

**ADIPLS** ..... The Aarhus adiabatic pulsation code

**AGSS09** ..... Solar composition determined by Asplund et al. (2009)

**B&G** ..... Surface correction relation by Ball and Gizon (2014) (Chapter 7)

**BASTA** ..... The BAyesian STellar Algorithm

**BiSON** ..... The Birmingham Solar Oscillations Network

**CON** ..... Constant diffusion coefficient in the overshooting region (Chapter 4)

**CoRoT** ..... Convection, Rotation and planetary Transits (satellite)

**DEF** ..... No overshooting (Chapter 4)

**EOS** ..... Equation of state

**FOV** ..... Overshooting scheme by Freytag et al. (1996) (Chapter 4)

**GARSTEC** .. The GArching STellar Evolution Code

**GS98** ..... Solar composition determined by Grevesse and Sauval (1998)

**HR digram** .. Hertzsprung-Russell diagram

**ISM** ..... Interstellar medium

**JCD** ..... Overshooting scheme by Christensen-Dalsgaard et al. (2018) (Chapter 4)

**K08** ..... Surface correction relation by Kjeldsen et al. (2008) (Chapter 7)

**K2** ..... "Second light" mission of the *Kepler* satellite

**KIC** ..... *Kepler* Input Catalog

**M18** ..... SSM using the method by Mosumgaard et al. (2018) (Chapter 2)

**MCMC** ..... Marcov chain Monte Carlo

**MHD** ..... Magneto-hydrodynamic

**MHD-EOS** ... EOS by Däppen et al. (1988)

**MLE** ..... Maximum likelihood estimation

**MLT** ..... Mixing length theory

**MOLA** ..... Multiplicative Optimally Localized Averages

**MS** ..... Main sequence

**MURaM** ..... The MPS/University of Chicago Radiative MHD code

**PB** ..... Overshooting scheme by Pratt et al. (2016) (Chapter 4)

**PLATO** ..... PLAnetary Transits and Oscillations of stars (satellite)

**PM** ..... Patched model

**pre-MS** ..... Pre-main sequence

**RGB** ..... Red giant branch

**RHD** ..... Radiative hydrodynamic

**RT2014** ..... SSM using the method by Mosumgaard et al. (2018) (Chapter 8)

**S15** ..... Surface correction relation by Sonoi et al. (2015) (Chapter 7)

**SOLA** ..... Subtractive Optimally Localized Averaging

**SSM** ..... Standard solar model

**UPM** ..... Un-patched model

**TESS** ..... Transiting Exoplanet Survey Satellite

**ZAMS** ..... Zero-age main sequence

## A.1 Jargon

In this thesis, I draw upon different existing grids of 3D RHD simulations of the outermost superadiabatic layers of stellar convective envelopes. The grid by Magic et al. (2013a) and Trampedach et al. (2013) are referred to as the **Stagger grid** and the **Trampedach grid**, respectively. Both Magic et al. (2013a) and Trampedach et al. (2013) refer to their simulations as 3D atmospheres. However, in 1D stellar structure models, the term 'atmosphere' is often used to denote the stratification above the photosphere, above and below which the propagation of photons is treated using fundamentally different approximations. To stress that the 3D simulations extend into the nearly-adiabatic region below the photosphere, I refer to the 3D simulations as 3D envelopes, although the simulations do by no means encompass the entire convective zone. The spatial and temporal averages of the 3D simulations are referred to as **⟨3D⟩-envelopes** throughout this thesis.

Chapters 6 and 7 deal with a method for substituting the outermost layers of 1D stellar structure models with ⟨3D⟩-envelopes at a given evolutionary stage, i.e. without correcting the 1D structure based on 3D simulations during the computed evolution. This approach is named post-evolutionary **patching**. The resulting structure models are called patched models (**PMs**), while the underlying un-altered 1D structures are referred to as un-patched models (**UPMs**)

In Chapters 8-10, interpolated ⟨3D⟩-envelopes are included at every single iteration of the stellar evolution calculations: ⟨3D⟩-envelopes are employed to set the outer boundary conditions and are appended on the fly. This procedure is referred to as the **coupling of 1D and 3D models**. The resulting hybrid models are said to be **coupled**.

# Appendix B

# Advection and Convective Settling

*In addition to the investigation of overshooting published in Jørgensen and Weiss (2018), I have taken a closer look at the mixing scheme proposed by Andrássy and Spruit (2013, 2015). I performed the actual implementation of this scheme into* GARSTEC*, in collaboration with Robert Andrássy, and conducted the subsequent post-processing. All obtained results were discussed with Robert Andrássy, Henk Spruit, and Achim Weiss, who all contributed with constructive feedback and fruitful ideas.*

## B.1 Implementation

The basic idea behind the overshooting scheme by Andrássy and Spruit (2013, 2015) is that convective downflows are created with a characteristic entropy distribution by rapid cooling at the photosphere. These downflows will penetrate into the radiative zone, where each downflow settles when its entropy corresponds to that of its surroundings. Once the gas has settled, it will advect upwards anew, i.e. there will be an upwards bulk motion of the gas in an overshooting layer below the base of the convective envelope[1]. Since the downflows are far narrower than the upflow, this advection takes place on much longer time-scales than that of the convective settling of the gas. It is, therefore, sufficient to model the upflow and assume that the advected mass will immediately be replaced by gas from the convective envelope. Since the settling rate must equal the rate, at which mass is advected, and since the settling rate is determined by the entropy contrast between the downflows and the surroundings, the advection speed follows from the presumed characteristic entropy distribution of the downflows. In accordance with Andrássy and Spruit (2013, 2015), we assume this distribution function to be a power law, which yields two free parameters: the power-law distribution function is determined by one free parameter ($\beta$), setting both its exponent and its normalization factor, while the second parameter ($\dot{M}_0$) comes into play by setting the total mass settling rate.

[1]Here, I refer to the entire convection zone, which extends beyond the layers that are covered by the 3D simulations encountered in Chapters 5-10.

Andrássy and Spruit (2013, 2015) apply their overshooting scheme in the post-processing of stellar models, i.e. they assume that the imposed additional processes leave the equilibrium structure unaltered, ignoring the complex feedback between the chemical composition profile and the thermodynamic quantities. In order to take this feedback into account, we implemented the advection of all elements in the overshooting region and the convective settling of the downflows into GARSTEC — that is, we have included the relocation of elements while ignoring the heat transport of the downflows. For this purpose, we use the forward Euler method to compute the mass flow rate of the down- and upflows. Since this scheme may easily run into issues regarding numerical stability, we model the mass flow, using time-steps that are several orders of magnitude shorter than the evolutionary time-step. While more sophisticated numerical schemes at lower computational cost exist, the forward Euler method is sufficient for our purposes: we merely compute a handful of solar models as a proof of concept to evaluate the potential of the proposed overshooting scheme.

Based on Andrássy and Spruit (2013, 2015), the advective velocity is set to be

$$v_{\mathrm{ad}} = \frac{\dot{M} F(s)}{4\pi r^2 \rho}, \tag{B.1}$$

where $\dot{M}$ is the total mass flow rate, which is computed using Eqs (7)–(10) in Andrássy and Spruit (2015). The total mass flow rate incorporates one free parameter, $\dot{M}_0$. $F(s)$ denotes the cumulative distribution function that determines the fraction of the downflows that settles at the entropy $s$. It is determined using Eqs (3)–(7) in Andrássy and Spruit (2015). It incorporates one additional free parameter, $\beta$. Both $\dot{M}$ and $F(s)$ rely on the lowest assumed entropy contrast, which is estimated based on the superadiabatic gradient at the point in the convection zone, at which the pressure is $e^{-1/2}$ times lower than at the base of the convective envelope. The maximal entropy contrast, on the other hand, is extracted from the Stagger-grid simulations. In this way, the present overshooting scheme, once again, relies on multi-dimensional simulations of hydrodynamic processes.

We compute the entropy at any given depth from the temperature and pressure stratifications, under the assumption that we are dealing with an ideal gas (cf. Eq. 1 in Andrássy and Spruit 2015):

$$s = \frac{k_{\mathrm{B}}}{\mu m_{\mathrm{u}}} \ln\left(\frac{T^{5/2}}{P_{\mathrm{th}}}\right), \tag{B.2}$$

where $m_{\mathrm{u}}$ is the atomic mass unit, $k_{\mathrm{B}}$ is the Boltzmann constant, and $\mu$ is the mean molecular weight, which we estimate as (Christensen-Dalsgaard, 2008b)

$$\mu(m) \approx \frac{4}{3 + 5X(m) - Z(m)}. \tag{B.3}$$

Equation (B.2) amounts to the assumption that the level of ionization is constant, which should hold true below the base of the convective envelope. A comparison with the entropy from the FreeEOS by A. W. Irwin validates that Eq. (B.2) is, indeed, a reasonable approximation.

Close to the base of the convection zone, the advective velocity becomes very large, at which point both the downflows and upflows of the gas are assumed to happen instantaneously. In this region, we simply assume the gas to have the same composition as the convective envelope and switch to diffusive overshooting. The width of this diffusive region is roughly $2 \times 10^{-3}\,\mathrm{R}_\odot$ or lower throughout the solar evolution, i.e. small compared to the entire overshooting region: the entire overshooting region has a width that is an order of magnitude larger. By including this narrow diffusive layer, we only need to solve for the advective mass flow rate in a region, where the advective velocity is low, i.e. where we can ensure a high degree of numerical stability without using excessively short time-steps. In this way, we both address the mentioned weakness of the forward Euler method and greatly reduce the numerical costs.

Our implementation ensures that the total mass of each element is conserved during advection.

## B.2 Results and Discussion

I computed a solar calibration model that includes advection and convective settling, setting $\dot{M}_0 = 5.2 \times 10^{21}\,\mathrm{g/s}$ and $\beta = 2.0$. These values seem reasonable based on Fig. 4 in Andrássy and Spruit (2015). I use the same EOS and opacity tables as in Chapter 4 utilizing the composition determined by Grevesse and Sauval (1998). During the evolution up until the present-day Sun, the model predicts lithium and beryllium to be depleted by a factor of 150 and 1.3, respectively.

We find that the advective overshooting scheme by Andrássy and Spruit (2013, 2015) leads to the same qualitative behaviour as the diffusive overshooting schemes presented in Chapter 4: by suppressing overshooting on the pre-MS, it is possible to ensure that the lithium depletion mainly takes place on the MS as required by observations. Here, we suppress overshooting for the first $10^8$ years. The results are summarized in Fig. B.1

In addition, the tachocline anomaly in the sound speed profile disappears. However, a new hump in the sound speed profile deeper within the radiative zone emerges. This is shown in Fig. B.2. The same new feature appears in the sound speed profiles in Chapter 4. We explain this behaviour by pointing out that any additional mixing process, be it diffusion or advection, reduces the composition gradient between the convective envelope and the radiative interior. Consider the case where the initial composition on the ZAMS is unchanged compared to the case with no overshooting. In this case, the additional mixing below the base of the convection zone will mostly leave the composition of the radiative zone unaltered, since this zone contains the larger fraction of the total mass. The composition of the envelope and hence at the stellar surface, on the other hand, changes: additional mixing will lead to a lower hydrogen surface abundance ($X_\mathrm{s}$) and a higher fraction of metals ($Z_\mathrm{s}$). Since the solar calibration model is required to recover a certain value of $Z_\mathrm{s}/X_\mathrm{s}$, the initial composition must consequently be adjusted. This adjustment necessarily leads to a lower mean molecular weight in the radiative interior, which raises the sound speed in the radiative zone, leading to the new sound speed anomaly. To illustrate this, I have included

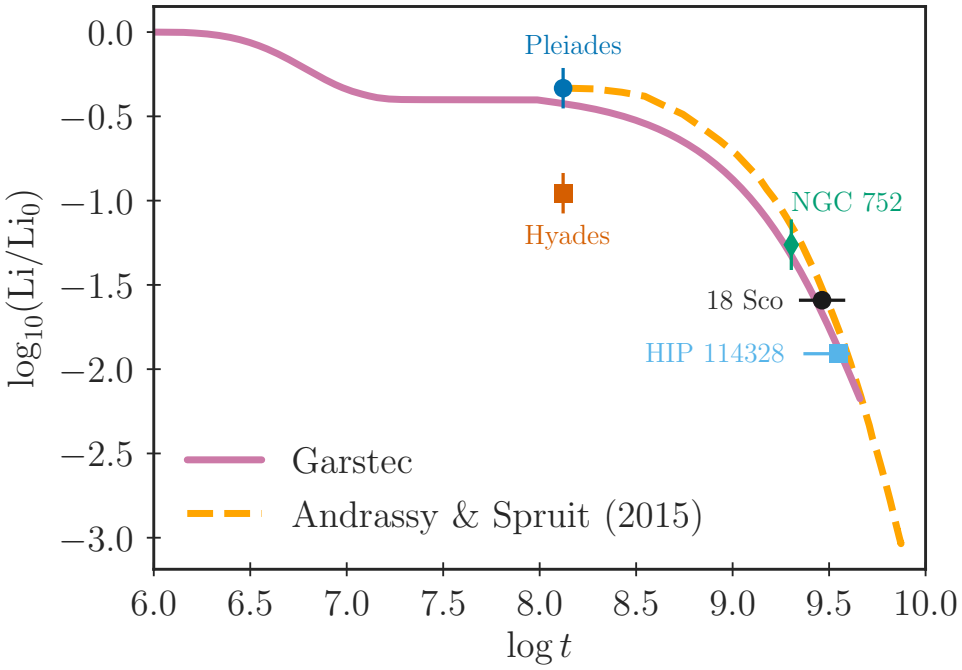


Figure B.1: Lithium depletion at the solar surface as function of time (cf. Fig. 4.1) based on a solar calibration model that includes advection and convective settling. The figure includes the predicted lithium depletion shown in Fig. 5 in Andrássy and Spruit (2015) as well as observational constraints on the lithium depletion of different stars and star clusters — these have likewise been extracted from Fig. 5 in Andrássy and Spruit (2015).

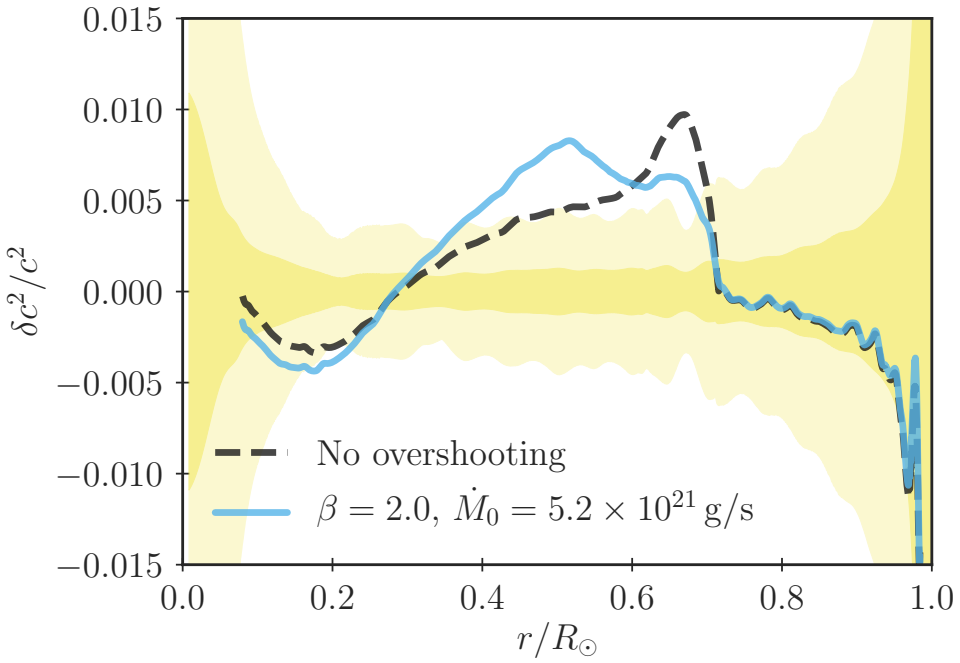


Figure B.2: The squared sound speed difference between solar calibration models with and without overshooting and the inferred sound speed profile by Basu and Antia (2008). The uncertainties are taken from Degl'Innoccenti et al. (1997).

the hydrogen mass fraction of solar calibration models with and without overshooting in Fig. B.3

To show that it is indeed the feedback between the initial conditions and the implementation of additional mixing processes that leads to the new anomaly in the sound speed profile, we computed the evolution of a 1 solar mass star that included advection up until the present solar age, using the same initial conditions as for the model without overshooting. By setting $\dot{M}_0 = 3.2 \times 10^{21}\,\mathrm{g/s}$ and $\beta = 2.0$, we achieve a lithium depletion by a factor of 126. We find that the sound speed profile of this model is in much better agreement with the inferred sound speed of the Sun than any of the models in Fig. B.2. Meanwhile, the model does not recover the correct global solar parameters: $T_{\mathrm{eff}} = 5786\,\mathrm{K}$ rather than 5777 K and $Z_{\mathrm{s}}/X_{\mathrm{s}} = 0.0244$ rather than 0.0230 at the present solar age.

Finally, Fig. B.4 shows the evolution of the total mass settling rate and the minimal entropy contrast for the solar calibration model with advection and convective settling. The evaluated behaviour of these two quantities can be compared with the results obtained by Andrássy and Spruit (2013, 2015), who imposed their overshooting scheme in the post-processing of stellar models, assuming that overshooting does not significantly affect the equilibrium structure. Although my analysis clearly illustrates that this assumption is incorrect, i.e. that advection and convective settling affect the thermodynamic quantities, the results that are shown in Fig. B.4 are both qualitatively and quantitatively similar to

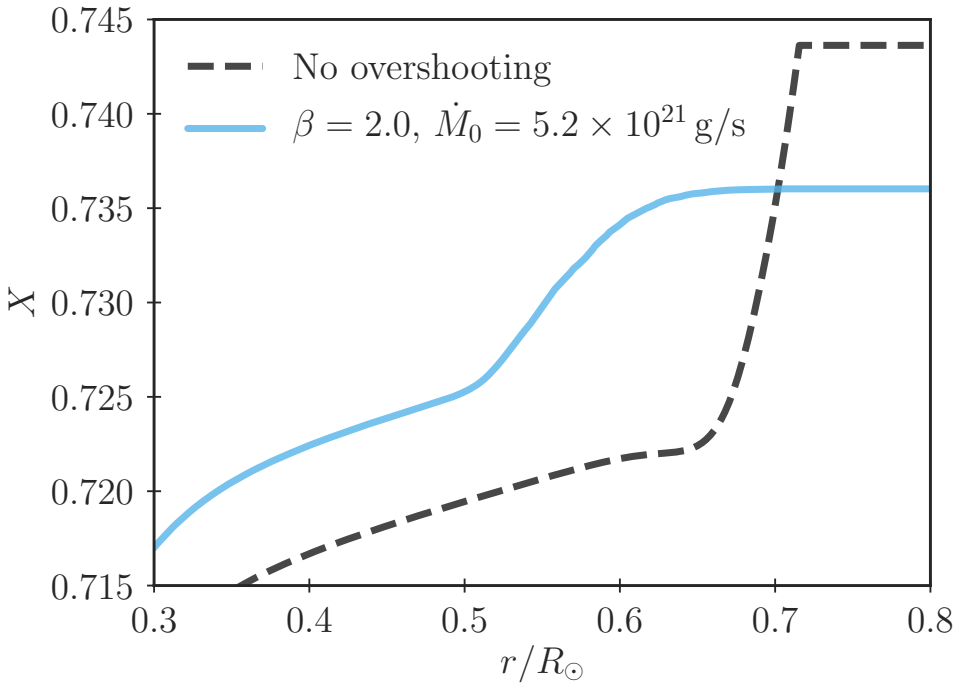


Figure B.3: Hydrogen abundance profile for the solar calibration models in Fig. B.2.

those shown for a one solar mass star in Figs 3 and 4 in Andrássy and Spruit (2015).

In accordance with the conclusions drawn in Chapter 4, we hence find that the implementation of additional mixing processes is, on its own, insufficient to solve both the lithium depletion problem and the tachocline anomaly in tandem. This points towards additional missing input physics. For instance, we ignore the heat transport that results from overshooting and only take the change of the chemical profile that results from the mixing processes into account. Indeed, including additional heat transport will affect the temperature stratification, which will show up in the sound speed profile and will affect the lithium burning rate.

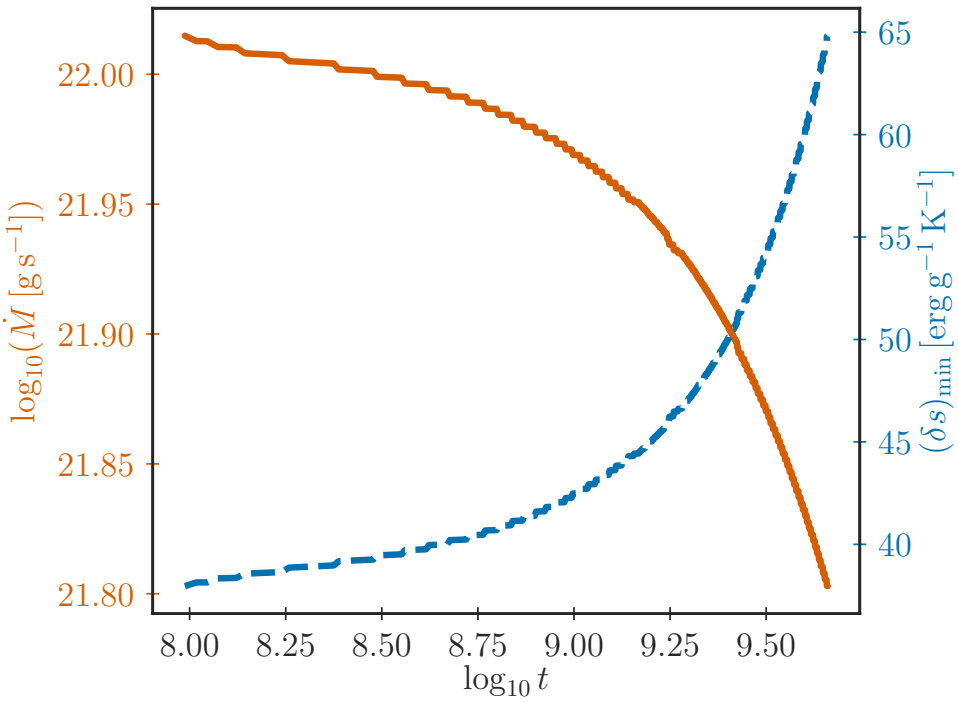


Figure B.4: Total mass settling rate (solid red line) and the minimal entropy contrast (dashed blue line) as a function of time for the solar calibration model with $\dot{M}_0 = 5.2 \times 10^{21}$ g/s and $\beta = 2.0$.

# Bibliography


Adelberger, E. G., García, A., Robertson, R. G. H., Snover, K. A., Balantekin, A. B., Heeger, K., Ramsey-Musolf, M. J., Bemmerer, D., Junghans, A., Bertulani, C. A., Chen, J.-W., Costantini, H., Prati, P., Couder, M., Uberseder, E., Wiescher, M., Cyburt, R., Davids, B., Freedman, S. J., Gai, M., Gazit, D., Gialanella, L., Imbriani, G., Greife, U., Hass, M., Haxton, W. C., Itahashi, T., Kubodera, K., Langanke, K., Leitner, D., Leitner, M., Vetter, P., Winslow, L., Marcucci, L. E., Motobayashi, T., Mukhamedzhanov, A., Tribble, R. E., Nollett, K. M., Nunes, F. M., Park, T.-S., Parker, P. D., Schiavilla, R., Simpson, E. C., Spitaleri, C., Strieder, F., Trautvetter, H.-P., Suemmerer, K., and Typel, S. (2011). Solar fusion cross sections. II. The pp chain and CNO cycles. *Reviews of Modern Physics*, 83:195–246.

Aerts, C., Christensen-Dalsgaard, J., and Kurtz, D. W. (2010). *Asteroseismology*.

Ahrens, B., Stix, M., and Thorn, M. (1992). On the depletion of lithium in the sun. *Astronomy and Astrophysics*, 264:673–678.

Akima, H. (1970). A New Method of Interpolation and Smooth Curve Fitting Based on Local Procedures. *Journal of the ACM*, 17(4):589–602.

Anders, F., Chiappini, C., Rodrigues, T. S., Miglio, A., Montalbán, J., Mosser, B., Girardi, L., Valentini, M., Noels, A., and Morel, T. (2017). Galactic archaeology with asteroseismology and spectroscopy: Red giants observed by CoRoT and APOGEE. *Astronomy and Astrophysics*, 597:A30.

Andrássy, R. and Spruit, H. C. (2013). Overshooting by convective settling. *Astronomy and Astrophysics*, 559:A122.

Andrássy, R. and Spruit, H. C. (2015). Convective settling in main sequence stars: Li and Be depletion. *Astronomy and Astrophysics*, 579:A122.

Angelou, G. C., Bellinger, E. P., Hekker, S., and Basu, S. (2017). On the Statistical Properties of the Lower Main Sequence. *The Astrophysical Journal*, 839(2):116.

Asplund, M., Grevesse, N., Sauval, A. J., and Scott, P. (2009). The Chemical Composition of the Sun. *Annual Review of Astronomy and Astrophysics*, 47(1):481–522.

Badnell, N. R., Bautista, M. A., Butler, K., Delahaye, F., Mendoza, C., Palmeri, P., Zeippen, C. J., and Seaton, M. J. (2005). Updated opacities from the Opacity Project. *Monthly Notices of the Royal Astronomical Society*, 360(2):458–464.

Baglin, A., Auvergne, M., Barge, P., Deleuil, M., Michel, E., and CoRoT Exoplanet Science Team (2009). CoRoT: Description of the Mission and Early Results. *Proceedings of the International Astronomical Union*, 253:71–81.

Bahcall, J. N., Pinsonneault, M. H., and Wasserburg, G. J. (1995). Solar models with helium and heavy-element diffusion. *Reviews of Modern Physics*, 67(4):781–808.

Bahcall, J. N., Serenelli, A. M., and Basu, S. (2006). 10,000 Standard Solar Models: A Monte Carlo Simulation. *The Astrophysical Journals*, 165:400–431.

Balachandran, S. C. and Bell, R. A. (1998). Shallow mixing in the solar photosphere inferred from revised beryllium abundances. *Nature*, 392:791–793.

Ball, W. H., Beeck, B., Cameron, R. H., and Gizon, L. (2016). MESA meets MURaM. Surface effects in main-sequence solar-like oscillators computed using three-dimensional radiation. *Astronomy and Astrophysics*, 592:A159.

Ball, W. H. and Gizon, L. (2014). A new correction of stellar oscillation frequencies for near-surface effects. *Astronomy and Astrophysics*, 568:A123.

Ball, W. H. and Gizon, L. (2017). Surface-effect corrections for oscillation frequencies of evolved stars. *Astronomy and Astrophysics*, 600:A128.

Baraffe, I., Pratt, J., Goffrey, T., Constantino, T., Folini, D., Popov, M. V., Walder, R., and Viallet, M. (2017). Lithium Depletion in Solar-like Stars: Effect of Overshooting Based on Realistic Multi-dimensional Simulations. *The Astrophysical Journal; Letters*, 845:L6.

Barkana, R. (2006). The First Stars in the Universe and Cosmic Reionization. *Science*, 313(5789):931–934.

Basu, S. and Antia, H. M. (1997). Seismic measurement of the depth of the solar convection zone. *Monthly Notices of the Royal Astronomical Society*, 287(1):189–198.

Basu, S. and Antia, H. M. (2004). Constraining Solar Abundances Using Helioseismology. *The Astrophysical Journal*, 606(1):L85–L88.

Basu, S. and Antia, H. M. (2008). Helioseismology and solar abundances. *Physics Reports*, 457:217–283.

Basu, S., Christensen-Dalsgaard, J., Chaplin, W. J., Elsworth, Y., Isaak, G. R., New, R., Schou, J., Thompson, M. J., and Tomczyk, S. (1997). Solar internal sound speed as inferred from combined BiSON and LOWL oscillation frequencies. *Monthly Notices of the Royal Astronomical Society*, 292:243.

Basu, S. and Kinnane, A. (2018). The Robustness of Asteroseismic Estimates of Global Stellar Parameters to Surface Term Corrections. *The Astrophysical Journal*, 869:8.

Baumann, P., Ramírez, I., Meléndez, J., Asplund, M., and Lind, K. (2010). Lithium depletion in solar-like stars: no planet connection. *Astronomy and Astrophysics*, 519:A87.

Bazot, M., Bourguignon, S., and Christensen-Dalsgaard, J. (2012). A Bayesian approach to the modelling of $\alpha$ Cen A. *Monthly Notices of the Royal Astronomical Society*, 427:1847–1866.

Beeck, B., Cameron, R. H., Reiners, A., and Schüssler, M. (2013). Three-dimensional simulations of near-surface convection in main-sequence stars. I. Overall structure. *Astronomy and Astrophysics*, 558:A48.

Bellinger, E. P. (2018). Inverse Problems in Asteroseismology. *arXiv e-prints*.

Bellinger, E. P., Angelou, G. C., Hekker, S., Basu, S., Ball, W. H., and Guggenberger, E. (2016). Fundamental Parameters of Main-Sequence Stars in an Instant with Machine Learning. *The Astrophysical Journal*, 830(1):31.

Bellinger, E. P., Hekker, S., Angelou, G. C., Stokholm, A., and Basu, S. (2019). Stellar ages, masses, and radii from asteroseismic modeling are robust to systematic errors in spectroscopy. *Astronomy and Astrophysics*, 622:A130.

Blöcker, T., Holweger, H., Freytag, B., Herwig, F., Ludwig, H.-G., and Steffen, M. (1998). Lithium Depletion in the Sun: A Study of Mixing Based on Hydrodynamical Simulations. *Space Science Reviews*, 85:105–112.

Böhm, K.-H. (1963). The Mixing of Matter in the Layer Below the Outer Solar Convection Zone. *The Astrophysical Journal*, 138:297.

Böhm-Vitense, E. (1958). Über die Wasserstoffkonvektionszone in Sternen verschiedener Effektivtemperaturen und Leuchtkräfte. *Zeitschrift für Astrophysik*, 46:108.

Borucki, W. J., Koch, D., Basri, G., Batalha, N., Brown, T., Caldwell, D., Caldwell, J., Christensen-Dalsgaard, J., Cochran, W. D., DeVore, E., Dunham, E. W., Dupree, A. K., Gautier, T. N., Geary, J. C., Gilliland, R., Gould, A., Howell, S. B., Jenkins, J. M., Kondo, Y., Latham, D. W., Marcy, G. W., Meibom, S., Kjeldsen, H., Lissauer, J. J., Monet, D. G., Morrison, D., Sasselov, D., Tarter, J., Boss, A., Brownlee, D., Owen, T., Buzasi, D., Charbonneau, D., Doyle, L., Fortney, J., Ford, E. B., Holman, M. J., Seager, S., Steffen, J. H., Welsh, W. F., Rowe, J., Anderson, H., Buchhave, L., Ciardi, D., Walkowicz, L., Sherry, W., Horch, E., Isaacson, H., Everett, M. E., Fischer, D., Torres, G., Johnson, J. A., Endl, M., MacQueen, P., Bryson, S. T., Dotson, J., Haas, M., Kolodziejczak, J., Van Cleve, J., Chandrasekaran, H., Twicken, J. D., Quintana, E. V., Clarke, B. D., Allen, C., Li, J., Wu, H., Tenenbaum, P., Verner, E., Bruhweiler, F., Barnes, J., and Prsa, A. (2010). Kepler Planet-Detection Mission: Introduction and First Results. *Science*, 327:977.

Bouvier, J., Barrado, D., Moraux, E., Stauffer, J., Rebull, L., Hillenbrand, L., Bayo, A., Boisse, I., Bouy, H., DiFolco, E., Lillo-Box, J., and Morales Calderón, M. (2018). The lithium-rotation connection in the 125 Myr-old Pleiades cluster. *Astronomy and Astrophysics*, 613:A63.

Bouvier, J., Forestini, M., and Allain, S. (1997). The angular momentum evolution of low-mass stars. *Astronomy and Astrophysics*, 326:1023–1043.

Broomhall, A.-M., Chaplin, W. J., Davies, G. R., Elsworth, Y., Fletcher, S. T., Hale, S. J., Miller, B., and New, R. (2009). Definitive Sun-as-a-star p-mode frequencies: 23 years of BiSON observations. *Monthly Notices of the Royal Astronomical Society: Letters*, 396(1):L100–L104.

Brown, T. M. (1984). Solar p-mode eigenfrequencies are decreased by turbulent convection. *Science*, 226:687–689.

Brown, T. M. and Christensen-Dalsgaard, J. (1998). Accurate Determination of the Solar Photospheric Radius. *The Astrophysical Journal, Letters*, 500(2):L195–L198.

Brown, T. M., Gilliland, R. L., Noyes, R. W., and Ramsey, L. W. (1991). Detection of Possible p-Mode Oscillations on Procyon. *The Astrophysical Journal*, 368:599.

Brummell, N. H. (2007). Turbulent compressible convection with rotation. In Kupka, F., Roxburgh, I., and Chan, K. L., editors, *Convection in Astrophysics*, volume 239 of *IAU Symposium*, pages 417–424.

Brun, A. S., Strugarek, A., Varela, J., Matt, S. P., Augustson, K. C., Emeriau, C., DoCao, O. L., Brown, B., and Toomre, J. (2017). On Differential Rotation and Overshooting in Solar-like Stars. *The Astrophysical Journal*, 836:192.

Buldgen, G., Salmon, S. J. A. J., Godart, M., Noels, A., Scuflaire, R., Dupret, M. A., Reese, D. R., Colgan, J., Fontes, C. J., Eggenberger, P., Hakel, P., Kilcrease, D. P., and Richard, O. (2017). Inversions of the Ledoux discriminant: a closer look at the tachocline. *Monthly Notices of the Royal Astronomical Society*, 472:L70–L74.

Canuto, V. M. and Mazzitelli, I. (1991). . *The Astrophysical Journal*, 370:295–311.

Canuto, V. M. and Mazzitelli, I. (1992). . *The Astrophysical Journal*, 389:724–730.

Casanellas, J. and Lopes, I. (2013). First Asteroseismic Limits on the Nature of Dark Matter. *Astrophysical Journal, Letters*, 765:L21.

Casanellas, J. and Lopes, I. (2014). The Sun and stars: Giving light to dark matter. *Modern Physics Letters A*, 29:1440001.

Cassisi, S., Potekhin, A. Y., Pietrinferni, A., Catelan, M., and Salaris, M. (2007). Updated Electron-Conduction Opacities: The Impact on Low-Mass Stellar Models. *The Astrophysical Journal*, 661(2):1094.

Cassisi, S., Salaris, M., and Irwin, A. W. (2003). The Initial Helium Content of Galactic Globular Cluster Stars from the R-Parameter: Comparison with the Cosmic Microwave Background Constraint. *The Astrophysical Journal*, 588:862.

Chaboyer, B. (1998). Internal rotation, mixing, and the Lithium-abundance. In Deubner, F.-L., Christensen-Dalsgaard, J., and Kurtz, D., editors, *New Eyes to See Inside the Sun and Stars*, volume 185 of *IAU Symposium*, page 25.

Chaplin, W. J., Kjeldsen, H., Christensen-Dalsgaard, J., Basu, S., Miglio, A., Appourchaux, T., Bedding, T. R., Elsworth, Y., García, R. A., and Gilliland, R. L. (2011). Ensemble Asteroseismology of Solar-Type Stars with the NASA Kepler Mission. *Science*, 332(6026):213.

Chaplin, W. J. and Miglio, A. (2013). Asteroseismology of Solar-Type and Red-Giant Stars. *Annual Review of Astronomy and Astrophysics*, 51:353–392.

Chiavassa, A., Casagrande, L., Collet, R., Magic, Z., Bigot, L., Thévenin, F., and Asplund, M. (2018). The STAGGER-grid: A grid of 3D stellar atmosphere models. V. Synthetic stellar spectra and broad-band photometry. *Astronomy and Astrophysics*, 611:A11.

Christensen-Dalsgaard, J. (1986). Theoretical aspects of helio- and asteroseismology. In Gough, D. O., editor, *NATO Advanced Science Institutes (ASI) Series C*, volume 169, pages 23–53.

Christensen-Dalsgaard, J. (2002). Helioseismology. *Reviews of Modern Physics*, 74:1073–1129.

Christensen-Dalsgaard, J. (2003). *Lecture Notes on Stellar Oscillations*. 5 edition.

Christensen-Dalsgaard, J. (2008a). ADIPLS - The Aarhus adiabatic oscillation package. *Astrophysics and Space Science*, 316(1-4):113–120.

Christensen-Dalsgaard, J. (2008b). *Lecture Notes on Stellar Structure and Evolution*. 6 edition.

Christensen-Dalsgaard, J., Däppen, W., Ajukov, S. V., Anderson, E. R., Antia, H. M., Basu, S., Baturin, V. A., Berthomieu, G., Chaboyer, B., Chitre, S. M., Cox, A. N., Demarque, P., Donatowicz, J., Dziembowski, W. A., Gabriel, M., Gough, D. O., Guenther, D. B., Guzik, J. A., Harvey, J. W., Hill, F., Houdek, G., Iglesias, C. A., Kosovichev, A. G., Leibacher, J. W., Morel, P., Proffitt, C. R., Provost, J., Reiter, J., Rhodes, Jr., E. J., Rogers, F. J., Roxburgh, I. W., Thompson, M. J., and Ulrich, R. K. (1996). The Current State of Solar Modeling. *Science*, 272:1286–1292.

Christensen-Dalsgaard, J., Däppen, W., and Lebreton, Y. (1988a). Solar oscillation frequencies and the equation of state. *Nature*, 336(6200):634–638.

Christensen-Dalsgaard, J. and Di Mauro, M. P. (2007). Diffusion and Helioseismology. In Straka, C. W., Lebreton, Y., and Monteiro, M. J. P. F. G., editors, *EAS Publications Series*, volume 26 of *EAS Publications Series*, pages 3–16.

Christensen-Dalsgaard, J., Duvall, Jr., T. L., Gough, D. O., Harvey, J. W., and Rhodes, Jr., E. J. (1985). Speed of sound in the solar interior. *Nature*, 315:378–382.

Christensen-Dalsgaard, J., Gough, D. O., and Knudstrup, E. (2018). On the hydrostatic stratification of the solar tachocline. *Monthly Notices of the Royal Astronomical Society*, 477:3845–3852.

Christensen-Dalsgaard, J., Gough, D. O., and Thompson, M. J. (1988b). Determination of the solar internal sound speed by means of a differential asymptotic inversion. In Rolfe, E. J., editor, *Seismology of the Sun and Sun-Like Stars*, volume 286 of *ESA Special Publication*.

Christensen-Dalsgaard, J., Gough, D. O., and Thompson, M. J. (1991). The depth of the solar convection zone. *The Astrophysical Journal*, 378:413–437.

Christensen-Dalsgaard, J., Kjeldsen, H., Brown, T. M., Gilliland, R. L., Arentoft, T., Frandsen, S., Quirion, P.-O., Borucki, W. J., Koch, D., and Jenkins, J. M. (2010). Asteroseismic Investigation of Known Planet Hosts in the Kepler Field. *The Astrophysical Journal; Letters*, 713:L164–L168.

Christensen-Dalsgaard, J., Monteiro, M. J. P. F. G., Rempel, M., and Thompson, M. J. (2011). A more realistic representation of overshoot at the base of the solar convective envelope as seen by helioseismology. *Monthly Notices of the Royal Astronomical Society*, 414:1158–1174.

Christensen-Dalsgaard, J., Proffitt, C. R., and Thompson, M. J. (1993). Effects of diffusion on solar models and their oscillation frequencies. *The Astrophysical Journal; Letters*, 403:L75–L78.

Christensen-Dalsgaard, J. and Thompson, M. J. (1995). SOLA Inversions for the Radial Structure of the Sun. In Ulrich, R. K., Rhodes, Jr., E. J., and Dappen, W., editors, *GONG 1994. Helio- and Astro-Seismology from the Earth and Space*, volume 76 of *Astronomical Society of the Pacific Conference Series*, page 144.

Christensen-Dalsgaard, J., Thompson, M. J., and Gough, D. O. (1989). Differential asymptotic sound-speed inversions. *Monthly Notices of the Royal Astronomical Society*, 238:481–502.

Cristini, A., Hirschi, R., Meakin, C., Arnett, D., Georgy, C., and Walkington, I. (2019). Dependence of convective boundary mixing on boundary properties and turbulence strength. *Monthly Notices of the Royal Astronomical Society*, 484(4):4645–4664.

Cumberbatch, D. T., Guzik, J. A., Silk, J., Watson, L. S., and West, S. M. (2010). Light WIMPs in the Sun: Constraints from helioseismology. *Rhysical Review D*, 82(10):103503.

Cummings, J. D. and Kalirai, J. S. (2018). Improved Main-sequence Turnoff Ages of Young Open Clusters: Multicolor UBV Techniques and the Challenges of Rotation. *Astronomical Journal*, 156(4):165.

Cyburt, R. H., Fields, B. D., Olive, K. A., and Yeh, T.-H. (2016). Big bang nucleosynthesis: Present status. *Reviews of Modern Physics*, 88(1):015004.

Däppen, W., Mihalas, D., Hummer, D. G., and Mihalas, B. W. (1988). The Equation Of State For Stellar Envelopes. III - Thermodynamic Quantities. *The Astrophysical Journal*, 332:261.

Davies, G. R., Broomhall, A.-M., Chaplin, W. J., Elsworth, Y., and Hale, S. J. (2014). Low-frequency, low-degree solar p-mode properties from 22 years of Birmingham Solar Oscillations Network data. *Monthly Notices of the Royal Astronomical Society*, 439(2):2025–2032.

Davies, G. R., Silva Aguirre, V., Bedding, T. R., Handberg, R., Lund, M. N., Chaplin, W. J., Huber, D., White, T. R., Benomar, O., Hekker, S., Basu, S., Campante, T. L., Christensen-Dalsgaard, J., Elsworth, Y., Karoff, C., Kjeldsen, H., Lundkvist, M. S., Metcalfe, T. S., and Stello, D. (2016). Oscillation frequencies for 35 Kepler solar-type planet-hosting stars using Bayesian techniques and machine learning. *Monthly Notices of the Royal Astronomical Society*, 456(2):2183–2195.

de Meulenaer, P., Carrier, F., Miglio, A., Bedding, T. R., Campante, T. L., Eggenberger, P., Kjeldsen, H., and Montalbán, J. (2010). Core properties of $\alpha$ Centauri A using asteroseismology. *Astronomy and Astrophysics*, 523:A54.

Degl'Innoccenti, S., Dziembowski, W. A., Fiorentini, G., and Ricci, B. (1997). Helioseismology and standard solar models. *Astroparticle Physics*, 7:77–95.

Dodelson, S. (2003). *Modern cosmology*. Academic press, 1st edition.

Eisenstein, D. J., Weinberg, D. H., Agol, E., Aihara, H., Allende Prieto, C., Anderson, S. F., Arns, J. A., Aubourg, É., Bailey, S., Balbinot, E., Barkhouser, R., Beers, T. C., Berlind, A. A., Bickerton, S. J., Bizyaev, D., Blanton, M. R., Bochanski, J. J., Bolton, A. S., Bosman, C. T., Bovy, J., Brandt, W. N., Breslauer, B., Brewington, H. J., Brinkmann, J., Brown, P. J., Brownstein, J. R., Burger, D., Busca, N. G., Campbell, H., Cargile, P. A., Carithers, W. C., Carlberg, J. K., Carr, M. A., Chang, L., Chen, Y., Chiappini, C., Comparat, J., Connolly, N., Cortes, M., Croft, R. A. C., Cunha, K., da Costa, L. N., Davenport, J. R. A., Dawson, K., De Lee, N., Porto de Mello, G. F., de Simoni, F. o., Dean, J., Dhital, S., Ealet, A., Ebelke, G. L., Edmondson, E. M., Eiting, J. M., Escoffier, S., Esposito, M., Evans, M. L., Fan, X., Femenía Castellá, B., Dutra Ferreira, L., Fitzgerald, G., Fleming, S. W., Font-Ribera, A., Ford, E. B., Frinchaboy, P. M., García

Pérez, A. E., Gaudi, B. S., Ge, J., Ghezzi, L., Gillespie, B. A., Gilmore, G., Girardi, L., Gott, J. R., Gould, A., Grebel, E. K., Gunn, J. E., Hamilton, J.-C., Harding, P., Harris, D. W., Hawley, S. L., Hearty, F. R., Hennawi, J. F., González Hernández, J. I., Ho, S., Hogg, D. W., Holtzman, J. A., Honscheid, K., Inada, N., Ivans, I. I., Jiang, L., Jiang, P., Johnson, J. A., Jordan, C., Jordan, W. P., Kauffmann, G., Kazin, E., Kirkby, D., Klaene, M. A., Knapp, G. R., Kneib, J.-P., Kochanek, C. S., Koesterke, L., Kollmeier, J. A., Kron, R. G., Lampeitl, H., Lang, D., Lawler, J. E., Le Goff, J.-M., Lee, B. L., Lee, Y. S., Leisenring, J. M., Lin, Y.-T., Liu, J., Long, D. C., Loomis, C. P., Lucatello, S., Lundgren, B., Lupton, R. H., Ma, B., Ma, Z., MacDonald, N., Mack, C., Mahadevan, S., Maia, M. A. G., Majewski, S. R., Makler, M., Malanushenko, E., Malanushenko, V., Mand elbaum, R., Maraston, C., Margala, D., Maseman, P., Masters, K. L., McBride, C. K., McDonald, P., McGreer, I. D., McMahon, R. G., Mena Requejo, O., Ménard, B., Miralda-Escudé, J., Morrison, H. L., Mullally, F., Muna, D., Murayama, H., Myers, A. D., Naugle, T., Neto, A. F., Nguyen, D. C., Nichol, R. C., Nidever, D. L., O'Connell, R. W., Ogando, R. L. C., Olmstead, M. D., Oravetz, D. J., Padmanabhan, N., Paegert, M., Palanque-Delabrouille, N., Pan, K., Pandey, P., Parejko, J. K., Pâris, I., Pellegrini, P., Pepper, J., Percival, W. J., Petitjean, P., Pfaffenberger, R., Pforr, J., Phleps, S., Pichon, C., Pieri, M. M., Prada, F., Price-Whelan, A. M., Raddick, M. J., Ramos, B. H. F., Reid, I. N., Reyle, C., Rich, J., Richards, G. T., Rieke, G. H., Rieke, M. J., Rix, H.-W., Robin, A. C., Rocha-Pinto, H. J., Rockosi, C. M., Roe, N. A., Rollinde, E., Ross, A. J., Ross, N. P., Rossetto, B., Sánchez, A. G., Santiago, B., Sayres, C., Schiavon, R., Schlegel, D. J., Schlesinger, K. J., Schmidt, S. J., Schneider, D. P., Sellgren, K., Shelden, A., Sheldon, E., Shetrone, M., Shu, Y., Silverman, J. D., Simmerer, J., Simmons, A. E., Sivarani, T., Skrutskie, M. F., Slosar, A., Smee, S., Smith, V. V., Snedden, S. A., Stassun, K. G., Steele, O., Steinmetz, M., Stockett, M. H., Stollberg, T., Strauss, M. A., Szalay, A. S., Tanaka, M., Thakar, A. R., Thomas, D., Tinker, J. L., Tofflemire, B. M., Tojeiro, R., Tremonti, C. A., Vargas Magaña, M., Verde, L., Vogt, N. P., Wake, D. A., Wan, X., Wang, J., Weaver, B. A., White, M., White, S. D. M., Wilson, J. C., Wisniewski, J. P., Wood-Vasey, W. M., Yanny, B., Yasuda, N., Yèche, C., York, D. G., Young, E., Zasowski, G., Zehavi, I., and Zhao, B. (2011). SDSS-III: Massive Spectroscopic Surveys of the Distant Universe, the Milky Way, and Extra-Solar Planetary Systems. *Astronomical Journal*, 142(3):72.

Elliott, J. R., Gough, D. O., and Sekii, T. (1998). Helioseismic Determination of the Solar Tachocline Thickness. In Korzennik, S., editor, *Structure and Dynamics of the Interior of the Sun and Sun-like Stars*, volume 418 of *ESA Special Publication*, page 763.

Ferguson, J. W., Alexander, D. R., Allard, F., Barman, T., Bodnarik, J. G., Hauschildt, P. H., Heffner-Wong, A., and Tamanai, A. (2005). Low-Temperature Opacities. *The Astrophysical Journal*, 623:585–596.

Foreman-Mackey, D., Hogg, D. W., Lang, D., and Goodman, J. (2013). emcee: The MCMC Hammer. *Publications of the Astronomical Society of the Pacific*, 125:306.

Fossat, E., Boumier, P., Corbard, T., Provost, J., Salabert, D., Schmider, F., Gabriel, A. H., Grec, G., Renaud, C., Robillot, J. M., Roca-Cortés, T., Turck-Chièze, S., Ulrich, R., and Lazrek, M. (2017). Asymptotic g modes: Evidence for a rapid rotation of the solar core. *Astronomy and Astrophysics1*, 604:A40.

Fossat, E., Regulo, C., Roca Cortes, T., Ekhgamberdiev, S., Gelly, B., Grec, G., Khalikov, S., Khamitov, I., Lazrek, M., and Palle, P. I. (1992). On the acoustic cut-off frequency of the sun. *Astronomy and Astrophysics*, 266(1):532–536.

Freytag, B., Ludwig, H.-G., and Steffen, M. (1996). Hydrodynamical models of stellar convection. The role of overshoot in DA white dwarfs, A-type stars, and the Sun. *Astronomy and Astrophysics*, 313:497–516.

Freytag, B., Steffen, M., Ludwig, H. G., Wedemeyer-Böhm, S., Schaffenberger, W., and Steiner, O. (2012). Simulations of stellar convection with CO5BOLD. *Journal of Computational Physics*, 231(3):919–959.

Fröhlich, C. (2006). Solar Irradiance Variability Since 1978. Revision of the PMOD Composite during Solar Cycle 21. *Space Science Reviews*, 125(1-4):53–65.

Gaia Collaboration, Prusti, T., de Bruijne, J. H. J., Brown, A. G. A., Vallenari, A., Babusiaux, C., Bailer-Jones, C. A. L., Bastian, U., Biermann, M., Evans, D. W., and et al. (2016). The Gaia mission. *Astronomy and Astrophysics*, 595:A1.

Garcia Lopez, R. J. and Spruit, H. C. (1991). Li depletion in F stars by internal gravity waves. *The Astrophysical Journal*, 377:268–277.

Geiss, J. and Gloeckler, G. (1998). Abundances of Deuterium and Helium-3 in the Protosolar Cloud. *Space Science Reviews*, 84:239–250.

Gloeckler, G. and Geiss, J. (1996). Abundance of $^3$He in the local interstellar cloud. *Nature*, 381:210–212.

Goodman, J. and Weare, J. (2010). Ensemble samplers with affine invariance. *Communications in Applied Mathematics and Computational Science, Vol. 5, No. 1, p. 65-80, 2010*, 5:65–80.

Gough, D. O. (1990). Comments on Helioseismic Inference. In Osaki, Y. and Shibahashi, H., editors, *Progress of Seismology of the Sun and Stars*, volume 367 of *Lecture Notes in Physics, Berlin Springer Verlag*, page 283.

Greenstein, J. L. and Richardson, R. S. (1951). Lithium and the Internal Circulation of the Sun. *The Astrophysical Journal*, 113:536.

Gregory, P. C. (2005). *Bayesian Logical Data Analysis for the Physical Sciences: A Comparative Approach with Mathematica Support*. Cambridge University Press, 1st edition.

Grevesse, N. and Noels, A. (1993). La Composition Chimique du Soleil. In Hauck, B., Paltani, S., and Raboud, D., editors, *Perfectionnement de l'Association Vaudoise des Chercheurs en Physique*, pages 205–257.

Grevesse, N. and Sauval, A. J. (1998). Standard Solar Composition.

Griffiths, D. (2005). *Introduction to Quantum Mechanics*. Pearson international edition. Pearson Prentice Hall, 2nd edition.

Gustafsson, B., Edvardsson, B., Eriksson, K., Jørgensen, U. G., Nordlund, Å., and Plez, B. (2008). A grid of MARCS model atmospheres for late-type stars. I. Methods and general properties. *Astronomy and Astrophysics*, 486:951–970.

Handberg, R. and Campante, T. L. (2011). Bayesian peak-bagging of solar-like oscillators using MCMC: a comprehensive guide. *Astronomy and Astrophysics*, 527:A56.

Haxton, W. C., Hamish Robertson, R. G., and Serenelli, A. M. (2013). Solar Neutrinos: Status and Prospects. *Annual Review of Astronomy and Astrophysics*, 51:21–61.

Henyey, L. G., Forbes, J. E., and Gould, N. L. (1964). A New Method of Automatic Computation of Stellar Evolution. *The Astrophysical Journal*, 139:306.

Higl, J. and Weiss, A. (2017). Testing stellar evolution models with detached eclipsing binaries. *Astronomy and Astrophysics*, 608:A62.

Hillebrandt, W. and Niemeyer, J. C. (2000). Type IA Supernova Explosion Models. *Annual Review of Astron and Astrophysics*, 38:191–230.

Houdek, G. and Dupret, M.-A. (2015). Interaction Between Convection and Pulsation. *Living Reviews in Solar Physics*, 12:8.

Houdek, G., Trampedach, R., Aarslev, M. J., and Christensen-Dalsgaard, J. (2017). On the surface physics affecting solar oscillation frequencies. *Monthly Notices of the Royal Astronomical Society: Letters*, 464(1):L124–L128.

Hoyle, F. and Schwarzschild, M. (1955). On the Evolution of Type II Stars. *The Astrophysical Journal*, 121:776–778.

Hummer, D. G. and Mihalas, D. (1988). The equation of state for stellar envelopes. I - an occupation probability formalism for the truncation of internal partition functions. *The Astrophysical Journal*, 331:794.

Iglesias, C. A. and Rogers, F. J. (1996). Updated Opal Opacities. *The Astrophysical Journal*, 464:943.

Janka, H. T., Langanke, K., Marek, A., Martínez-Pinedo, G., and Müller, B. (2007). Theory of core-collapse supernovae. *Physics Reports*, 442(1-6):38–74.

Jasche, J. and Wandelt, B. D. (2013). Bayesian physical reconstruction of initial conditions from large-scale structure surveys. *Monthly Notices of the Royal Astronomical Society*, 432:894–913.

Jiang, Y.-F., Cantiello, M., Bildsten, L., Quataert, E., Blaes, O., and Stone, J. (2018). Three Dimensional Radiation Hydrodynamic Simulations of Massive Star Envelopes. *arXiv e-prints*, page arXiv:1809.10187.

Jiménez, A., García, R. A., and Pallé, P. L. (2011). The Acoustic Cutoff Frequency of the Sun and the Solar Magnetic Activity Cycle. *The Astrophysical Journal*, 743(2):99.

Jimenez, R., Cimatti, A., Verde, L., Moresco, M., and Wandelt, B. (2019). The local and distant Universe: stellar ages and $H_0$. *Journal of Cosmology and Astro-Particle Physics*, 2019(3):043.

Johnson, C. I., Rich, R. M., Fulbright, J. P., Valenti, E., and McWilliam, A. (2011). Alpha Enhancement and the Metallicity Distribution Function of Plaut's Window. *The Astrophysical Journal*, 732(2):108.

Jones, B. F., Fischer, D., Shetrone, M., and Soderblom, D. R. (1997). The Evolution of the Lithium Abundances of Solar-Type Stars.VII.M34 (NGC 1039) and the Role of Rotation in Lithium Depletion. *Astronomical Journal*, 114:352–362.

Jones, B. F., Fischer, D., and Soderblom, D. R. (1999). The Evolution of the Lithium Abundances of Solar-Type Stars. VIII. M67 (NGC 2682). *Astronomical Journal*, 117:330–338.

Jørgensen, A. C. S. and Christensen-Dalsgaard, J. (2017). A semi-analytical computation of the theoretical uncertainties of the solar neutrino flux. *Monthly Notices of the Royal Astronomical Society*, 471:4802–4805.

Jørgensen, A. C. S., Mosumgaard, J. R., Weiss, A., Silva Aguirre, V., and Christensen-Dalsgaard, J. (2018). Coupling 1d stellar evolution with 3d-hydrodynamical simulations on the fly - i. a new standard solar model. *Monthly Notices of the Royal Astronomical Society*, 481:L35.

Jørgensen, A. C. S. and Weiss, A. (2018). Addressing the acoustic tachocline anomaly and the lithium depletion problem at the same time. *Monthly Notices of the Royal Astronomical Society*, 481:4389–4396.

Jørgensen, A. C. S. and Weiss, A. (2019). Overcoming the structural surface effect with a realistic treatment of turbulent convection in 1D stellar models. *Monthly Notices of the Royal Astronomical Society*, 488:3463–3473.

Jørgensen, A. C. S., Weiss, A., Angelou, G., and Silva Aguirre, V. (2019). Mending the structural surface effect of 1D stellar structure models with non-solar metallicities

based on interpolated 3D envelopes. *Monthly Notices of the Royal Astronomical Society*, 484(4):5551–5567.

Jørgensen, A. C. S., Weiss, A., Mosumgaard, J. R., Silva Aguirre, V., and Sahlholdt, C. L. (2017). Theoretical oscillation frequencies for solar-type dwarfs from stellar models with 3D-atmospheres. *Monthly Notices of the Royal Astronomical Society*, 472(3):3264–3276.

Joyce, M. and Chaboyer, B. (2018). Classically and Asteroseismically Constrained 1D Stellar Evolution Models of $\alpha$ Centauri A and B Using Empirical Mixing Length Calibrations. *The Astrophysical Journal*, 864(1):99.

Kawaler, S. D. (1988). Angular momentum loss in low-mass stars. *The Astrophysical Journal*, 333:236–247.

Kervella, P., Bigot, L., Gallenne, A., and Thévenin, F. (2017). The radii and limb darkenings of $\alpha$ Centauri A and B . Interferometric measurements with VLTI/PIONIER. *Astronomy and Astrophysics*, 597:A137.

Kippenhahn, R., Weigert, A., and Weiss, A. (2012). *Stellar structure and evolution*. Springer, 2nd edition.

Kjeldsen, H. and Bedding, T. R. (1995). Amplitudes of stellar oscillations: the implications for asteroseismology. *Astronomy and Astrophysics*, 293:87–106.

Kjeldsen, H., Bedding, T. R., Butler, R. P., Christensen-Dalsgaard, J., Kiss, L. L., McCarthy, C., Marcy, G. W., Tinney, C. G., and Wright, J. T. (2005). Solar-like Oscillations in $\alpha$ Centauri B. *The Astrophysical Journal*, 635:1281–1290.

Kjeldsen, H., Bedding, T. R., and Christensen-Dalsgaard, J. (2008). Correcting Stellar Oscillation Frequencies for Near-Surface Effects. *The Astrophysical Journal*, 683(2):L175–L178.

Krishna Swamy, K. S. (1966). Profiles of Strong Lines in K-Dwarfs. *The Astrophysical Journal*, 145:174.

Kurucz, R. L. (1992a). Atomic and Diatomic Molecular Opacities for Atmospheres and Envelopes. In *American Astronomical Society Meeting Abstracts #180*, volume 24 of *Bulletin of the American Astronomical Society*, page 779.

Kurucz, R. L. (1992b). Remaining Line Opacity Problems for the Solar Spectrum. *Revista Mexicana de Astronomia y Astrofisica*, 23.

Leavitt, H. S. and Pickering, E. C. (1912). Periods of 25 Variable Stars in the Small Magellanic Cloud. *Harvard College Observatory Circular*, 173:1–3.

Lebreton, Y. and Goupil, M. J. (2014). Asteroseismology for "à la carte" stellar age-dating and weighing. Age and mass of the CoRoT exoplanet host HD 52265. *Astronomy and Astrophysics*, 569:A21.

Leighton, R. B. (1960). In Thomas, R. N., editor, *Aerodynamic Phenomena in Stellar Atmospheres*, volume 12 of *IAU Symposium*, pages 321–325.

Ludwig, H. G., Caffau, E., Steffen, M., Freytag, B., Bonifacio, P., and Kučinskas, A. (2009). The CIFIST 3D model atmosphere grid. *Memorie della Società Astronomica Italiana*, 80:711.

Ludwig, H.-G., Freytag, B., and Steffen, M. (1999). A calibration of the mixing-length for solar-type stars based on hydrodynamical simulations. I. Methodical aspects and results for solar metallicity. *Astronomy and Astrophysics*, 346:111–124.

Lund, M. N., Silva Aguirre, V., Davies, G. R., Chaplin, W. J., Christensen-Dalsgaard, J., Houdek, G., White, T. R., Bedding, T. R., Ball, W. H., Huber, D., Antia, H. M., Lebreton, Y., Latham, D. W., Handberg, R., Verma, K., Basu, S., Casagrande, L., Justesen, A. B., Kjeldsen, H., and Mosumgaard, J. R. (2017). Standing on the Shoulders of Dwarfs: the Kepler Asteroseismic LEGACY Sample. I. Oscillation Mode Parameters. *The Astrophysical Journal*, 835(2):172.

Lundkvist, M. S., Huber, D., Silva Aguirre, V., and Chaplin, W. J. (2018). Using asteroseismology to characterise exoplanet host stars. *arXiv e-prints*, page arXiv:1804.02214.

Magic, Z. (2016). Scaling of the asymptotic entropy jump in the superadiabatic layers of stellar atmospheres. *Astronomy and Astrophysics*, 586:A88.

Magic, Z. and Asplund, M. (2014). The Stagger-grid: A grid of 3D stellar atmosphere models - VI. Surface appearance of stellar granulation. *arXiv e-prints*, page arXiv:1405.7628.

Magic, Z., Collet, R., Asplund, M., Trampedach, R., Hayek, W., Chiavassa, A., Stein, R. F., and Nordlund, Å. (2013a). The Stagger-grid: A grid of 3D stellar atmosphere models. I. Methods and general properties. *Astronomy and Astrophysics*, 557(A26):A26.

Magic, Z., Collet, R., Hayek, W., and Asplund, M. (2013b). *Astronomy and Astrophysics*, 560:17 pp.

Magic, Z. and Weiss, A. (2016). Surface-effect corrections for the solar model. *Astronomy and Astrophysics*, 592:A24.

Magic, Z., Weiss, A., and Asplund, M. (2015). The Stagger-grid: A grid of 3D stellar atmosphere models. III. The relation to mixing length convection theory. *Astronomy and Astrophysics*, 573:A89.

Manchon, L., Belkacem, K., Samadi, R., Sonoi, T., Marques, J. P. C., Ludwig, H. G., and Caffau, E. (2018). Influence of metallicity on the near-surface effect on oscillation frequencies. *Astronomy and Astrophysics*, 620:A107.

Meakin, C. A. and Arnett, D. (2007). Turbulent Convection in Stellar Interiors. I. Hydrodynamic Simulation. *The Astrophysical JournalS*, 667(1):448–475.

Metcalfe, T. S., Creevey, O. L., and Davies, G. R. (2015). Asteroseismic Modeling of 16 Cyg A & B using the Complete Kepler Data Set. *The Astrophysical Journal, Letters*, 811(2):L37.

Miglio, A. (2012). Asteroseismology of Red Giants as a Tool for Studying Stellar Populations: First Steps. *Astrophysics and Space Science Proceedings*, 26:11.

Miglio, A., Chiappini, C., Mosser, B., Davies, G. R., Freeman, K., Girardi, L., Jofré, P., Kawata, D., Rendle, B. M., Valentini, M., Casagrande, L., Chaplin, W. J., Gilmore, G., Hawkins, K., Holl, B., Appourchaux, T., Belkacem, K., Bossini, D., Brogaard, K., Goupil, M.-J., Montalbán, J., Noels, A., Anders, F., Rodrigues, T., Piotto, G., Pollacco, D., Rauer, H., Allende Prieto, C., Avelino, P. P., Babusiaux, C., Barban, C., Barbuy, B., Basu, S., Baudin, F., Benomar, O., Bienaymé, O., Binney, J., Bland-Hawthorn, J., Bressan, A., Cacciari, C., Campante, T. L., Cassisi, S., Christensen-Dalsgaard, J., Combes, F., Creevey, O., Cunha, M. S., Jong, R. S., Laverny, P., Degl'Innocenti, S., Deheuvels, S., Depagne, É., Ridder, J., Di Matteo, P., Di Mauro, M. P., Dupret, M.-A., Eggenberger, P., Elsworth, Y., Famaey, B., Feltzing, S., García, R. A., Gerhard, O., Gibson, B. K., Gizon, L., Haywood, M., Handberg, R., Heiter, U., Hekker, S., Huber, D., Ibata, R., Katz, D., Kawaler, S. D., Kjeldsen, H., Kurtz, D. W., Lagarde, N., Lebreton, Y., Lund, M. N., Majewski, S. R., Marigo, P., Martig, M., Mathur, S., Minchev, I., Morel, T., Ortolani, S., Pinsonneault, M. H., Plez, B., Prada Moroni, P. G., Pricopi, D., Recio-Blanco, A., Reylé, C., Robin, A., Roxburgh, I. W., Salaris, M., Santiago, B. X., Schiavon, R., Serenelli, A., Sharma, S., Silva Aguirre, V., Soubiran, C., Steinmetz, M., Stello, D., Strassmeier, K. G., Ventura, P., Ventura, R., Walton, N. A., and Worley, C. C. (2017). PLATO as it is : A legacy mission for Galactic archaeology. *Astronomische Nachrichten*, 338:644–661.

Miglio, A., Montalbán, J., and Maceroni, C. (2007). 12 Boötis: a test-bed for extra-mixing processes in stars. *Monthly Notices of the Royal Astronomical Society*, 377:373–382.

Mosser, B., Pinçon, C., Belkacem, K., Takata, M., and Vrard, M. (2017). Period spacings in red giants (Corrigendum). III. Coupling factors of mixed modes. *Astronomy and Astrophysics*, 607:C2.

Mosumgaard, J. R., Ball, W. H., Silva Aguirre, V., Weiss, A., and Christensen-Dalsgaard, J. (2018). Stellar models with calibrated convection and temperature stratification from 3D hydrodynamics simulations. *Monthly Notices of the Royal Astronomical Society*, 478(4):5650–5659.

Nomoto, K., Iwamoto, K., Nakasato, N., Thielemann, F. K., Brachwitz, F., Tsujimoto, T., Kubo, Y., and Kishimoto, N. (1997). Nucleosynthesis in type Ia supernovae. *Nuclear Physics A*, 621:467–476.

Nsamba, B., Campante, T. L., Monteiro, M. J. P. F. G., Cunha, M. S., Rendle, B. M., Reese, D. R., and Verma, K. (2018a). Asteroseismic modelling of solar-type stars: internal

systematics from input physics and surface correction methods. *Monthly Notices of the Royal Astronomical Society*, 477:5052–5063.

Nsamba, B., Monteiro, M. J. P. F. G., Campante, T. L., Cunha, M. S., and Sousa, S. G. (2018b). $\alpha$ Centauri A as a potential stellar model calibrator: establishing the nature of its core. *Monthly Notices of the Royal Astronomical Society*, 479:L55–L59.

Otí Floranes, H., Christensen-Dalsgaard, J., and Thompson, M. J. (2005). The use of frequency-separation ratios for asteroseismology. *Monthly Notices of the Royal Astronomical Society*, 356:671–679.

Piau, L., Collet, R., Stein, R. F., Trampedach, R., Morel, P., and Turck-Chièze, S. (2014). Models of solar surface dynamics: impact on eigenfrequencies and radius. *Monthly Notices of the Royal Astronomical Society*, 437(1):164–175.

Pijpers, F. P. and Thompson, M. J. (1992). Faster formulations of the optimally localized averages method for helioseismic inversions. *Astronomy and Astrophysics*, 262:L33–L36.

Pinsonneault, M. H., Elsworth, Y., Epstein, C., Hekker, S., Mészáros, S., Chaplin, W. J., and Johnson, J. A. e. a. (2014). The APOKASC Catalog: An Asteroseismic and Spectroscopic Joint Survey of Targets in the Kepler Fields. *The Astrophysical Journal Supplement*, 215:23 pp.

Planck Collaboration, Ade, P. A. R., Aghanim, N., Arnaud, M., Ashdown, M., Aumont, J., Baccigalupi, C., Banday, A. J., Barreiro, R. B., Bartlett, J. G., and et al. (2016). Planck 2015 results. XIII. Cosmological parameters. *Astronomy and Astrophysics*, 594:A13.

Pont, F., Melo, C. H. F., Bouchy, F., Udry, S., Queloz, D., Mayor, M., and Santos, N. C. (2005). A planet-sized transiting star around OGLE-TR-122. Accurate mass and radius near the hydrogen-burning limit. *Astronomy and Astrophysics*, 433:L21–L24.

Porqueres, N., Kodi Ramanah, D., Jasche, J., and Lavaux, G. (2019). Explicit Bayesian treatment of unknown foreground contaminations in galaxy surveys. *Astronomy and Astrophysics*, 624:A115.

Pourbaix, D. and Boffin, H. M. J. (2016). Parallax and masses of $\alpha$ Centauri revisited. *Astronomy and Astrophysics*, 586:A90.

Pourbaix, D., Nidever, D., McCarthy, C., Butler, R. P., Tinney, C. G., Marcy, G. W., Jones, H. R. A., Penny, A. J., Carter, B. D., Bouchy, F., Pepe, F., Hearnshaw, J. B., Skuljan, J., Ramm, D., and Kent, D. (2002). Constraining the difference in convective blueshift between the components of alpha Centauri with precise radial velocities. *Astronomy and Astrophysics*, 386:280–285.

Pratt, J., Baraffe, I., Goffrey, T., Constantino, T., Viallet, M., Popov, M. V., Walder, R., and Folini, D. (2017). Extreme value statistics for two-dimensional convective penetration in a pre-main sequence star. *Astronomy and Astrophysics*, 604:A125.

Pratt, J., Baraffe, I., Goffrey, T., Geroux, C., Viallet, M., Folini, D., Constantino, T., Popov, M., and Walder, R. (2016). Spherical-shell boundaries for two-dimensional compressible convection in a star. *Astronomy and Astrophysics*, 593:A121.

Rabello-Soares, M. C., Basu, S., and Christensen-Dalsgaard, J. (1999). On the choice of parameters in solar-structure inversion. *Monthly Notices of the Royal Astronomical Society*, 309:35–47.

Raffelt, G. G. (1996). *Stars as laboratories for fundamental physics : the astrophysics of neutrinos, axions, and other weakly interacting particles*.

Rauer, H., Catala, C., Aerts, C., Appourchaux, T., Benz, W., Brandeker, A., Christensen-Dalsgaard, J., Deleuil, M., Gizon, L., Goupil, M.-J., Güdel, M., Janot-Pacheco, E., Mas-Hesse, M., Pagano, I., Piotto, G., Pollacco, D., Santos, Ċ., Smith, A., Suárez, J.-C., Szabó, R., Udry, S., Adibekyan, V., Alibert, Y., Almenara, J.-M., Amaro-Seoane, P., Eiff, M. A.-v., Asplund, M., Antonello, E., Barnes, S., Baudin, F., Belkacem, K., Bergemann, M., Bihain, G., Birch, A. C., Bonfils, X., Boisse, I., Bonomo, A. S., Borsa, F., Brandão, I. M., Brocato, E., Brun, S., Burleigh, M., Burston, R., Cabrera, J., Cassisi, S., Chaplin, W., Charpinet, S., Chiappini, C., Church, R. P., Csizmadia, S., Cunha, M., Damasso, M., Davies, M. B., Deeg, H. J., Díaz, R. F., Dreizler, S., Dreyer, C., Eggenberger, P., Ehrenreich, D., Eigmüller, P., Erikson, A., Farmer, R., Feltzing, S., de Oliveira Fialho, F., Figueira, P., Forveille, T., Fridlund, M., García, R. A., Giommi, P., Giuffrida, G., Godolt, M., Gomes da Silva, J., Granzer, T., Grenfell, J. L., Grotsch-Noels, A., Günther, E., Haswell, C. A., Hatzes, A. P., Hébrard, G., Hekker, S., Helled, R., Heng, K., Jenkins, J. M., Johansen, A., Khodachenko, M. L., Kislyakova, K. G., Kley, W., Kolb, U., Krivova, N., Kupka, F., Lammer, H., Lanza, A. F., Lebreton, Y., Magrin, D., Marcos-Arenal, P., Marrese, P. M., Marques, J. P., Martins, J., Mathis, S., Mathur, S., Messina, S., Miglio, A., Montalban, J., Montalto, M., Monteiro, M. J. P. F. G., Moradi, H., Moravveji, E., Mordasini, C., Morel, T., Mortier, A., Nascimbeni, V., Nelson, R. P., Nielsen, M. B., Noack, L., Norton, A. J., Ofir, A., Oshagh, M., Ouazzani, R.-M., Pápics, P., Parro, V. C., Petit, P., Plez, B., Poretti, E., Quirrenbach, A., Ragazzoni, R., Raimondo, G., Rainer, M., Reese, D. R., Redmer, R., Reffert, S., Rojas-Ayala, B., Roxburgh, I. W., Salmon, S., Santerne, A., Schneider, J., Schou, J., Schuh, S., Schunker, H., Silva-Valio, A., Silvotti, R., Skillen, I., Snellen, I., Sohl, F., Sousa, S. G., Sozzetti, A., Stello, D., Strassmeier, K. G., Švanda, M., Szabó, G. M., Tkachenko, A., Valencia, D., Van Grootel, V., Vauclair, S. D., Ventura, P., Wagner, F. W., Walton, N. A., Weingrill, J., Werner, S. C., Wheatley, P. J., and Zwintz, K. (2014). The PLATO 2.0 mission. *Experimental Astronomy*, 38:249–330.

Richard, O., Vauclair, S., Charbonnel, C., and Dziembowski, W. A. (1996). New solar models including helioseismological constraints and light-element depletion. *Astronomy and Astrophysics*, 312:1000–1011.

Ricker, G. R., Winn, J. N., Vanderspek, R., Latham, D. W., Bakos, G. Á., Bean, J. L., Berta-Thompson, Z. K., Brown, T. M., Buchhave, L., Butler, N. R., Butler, R. P.,

Chaplin, W. J., Charbonneau, D., Christensen-Dalsgaard, J., Clampin, M., Deming, D., Doty, J., De Lee, N., Dressing, C., Dunham, E. W., Endl, M., Fressin, F., Ge, J., Henning, T., Holman, M. J., Howard, A. W., Ida, S., Jenkins, J. M., Jernigan, G., Johnson, J. A., Kaltenegger, L., Kawai, N., Kjeldsen, H., Laughlin, G., Levine, A. M., Lin, D., Lissauer, J. J., MacQueen, P., Marcy, G., McCullough, P. R., Morton, T. D., Narita, N., Paegert, M., Palle, E., Pepe, F., Pepper, J., Quirrenbach, A., Rinehart, S. A., Sasselov, D., Sato, B., Seager, S., Sozzetti, A., Stassun, K. G., Sullivan, P., Szentgyorgyi, A., Torres, G., Udry, S., and Villasenor, J. (2015). Transiting Exoplanet Survey Satellite (TESS). *Journal of Astronomical Telescopes, Instruments, and Systems*, 1(1):014003.

Rieutord, M. (2016). Two-dimensional models of early-type fast rotating stars: the ESTER project. *IAU Focus Meeting*, 29B:147–148.

Rogers, F. J. and Nayfonov, A. (2002). Updated and Expanded OPAL Equation-of-State Tables: Implications for Helioseismology. *The Astrophysical Journal*, 576:1064–1074.

Rogers, F. J., Swenson, F. J., and Iglesias, C. A. (1996). OPAL Equation-of-State Tables for Astrophysical Applications. *The Astrophysical Journal*, 456:902.

Rosenthal, C. S., Christensen-Dalsgaard, J., Nordlund, Å., Stein, R. F., and Trampedach, R. (1999). Convective contributions to the frequencies of solar oscillations. *Astronomy and Astrophysics*, 351:689.

Roxburgh, I. W. (2005). The ratio of small to large separations of stellar p-modes. *Astronomy and Astrophysics*, 434(2):665–669.

Roxburgh, I. W. (2018). Overfitting and correlations in model fitting with separation ratios. *arXiv e-prints*, page arXiv:1808.07556.

Roxburgh, I. W. and Vorontsov, S. V. (2003). The ratio of small to large separations of acoustic oscillations as a diagnostic of the interior of solar-like stars. *a&a*, 411:215–220.

Rubin, V. C. and Ford, W. Kent, J. (1970). Rotation of the Andromeda Nebula from a Spectroscopic Survey of Emission Regions. *The Astophysical Journal*, 159:379.

Ryden, B. (2003). *Introduction to cosmology*. Addison-Wesley, 1st edition.

Schlattl, H. and Weiss, A. (1999). On an overshooting approach to the solar Li problem. *Astronomy and Astrophysics*, 347:272–276.

Schlattl, H. and Weiss, A. (2016). *Documentation for Garstec10*.

Schlattl, H., Weiss, A., and Ludwig, H.-G. (1997). A solar model with improved subatmospheric stratification. *Astronomy and Astrophysics*, 322:646.

Schwarzschild, M. (1975). On the scale of photospheric convection in red giants and supergiants. *Astrophysical Journal*, 195:137–144.

Seager, S. and Lissauer, J. J. (2010). *Introduction to Exoplanets*, pages 3–13.

Serenelli, A. M., Basu, S., Ferguson, J. W., and Asplund, M. (2009). New Solar Composition: The Problem with Solar Models Revisited. *The Astrophysical Journal; Letters*, 705:L123–L127.

Serenelli, A. M., Haxton, W. C., and Peña-Garay, C. (2011). Solar Models with Accretion. I. Application to the Solar Abundance Problem. *The Astrophysical Journal*, 743(1):24.

Silva Aguirre, V., Basu, S., Brandão, I. M., Christensen-Dalsgaard, J., Deheuvels, S., Doan, G., Metcalfe, T. S., Serenelli, A. M., Ballot, J., Chaplin, W. J., Cunha, M. S., Weiss, A., Appourchaux, T., Casagrande, L., Cassisi, S., Creevey, O. L., García, R. A., Lebreton, Y., Noels, A., Sousa, S. G., Stello, D., White, T. R., Kawaler, S. D., and Kjeldsen, H. (2013). Stellar Ages and Convective Cores in Field Main-sequence Stars: First Asteroseismic Application to Two Kepler Targets. *The Astrophysical Journal*, 769:141 (17pp).

Silva Aguirre, V., Bojsen-Hansen, M., Slumstrup, D., Casagrande, L., Kawata, D., Ciucă, I., Hand berg, R., Lund, M. N., Mosumgaard, J. R., and Huber, D. (2018). Confirming chemical clocks: asteroseismic age dissection of the Milky Way disc(s). *Monthly Notices of the Royal Astronomical Society*, 475(4):5487–5500.

Silva Aguirre, V., Davies, G. R., Basu, S., Christensen-Dalsgaard, J., Creevey, O. L., Metcalfe, T. S., Bedding, T. R., Casagrande, L., Handberg, R., Lund, M. N., Nissen, P. E., Chaplin, W. J., Huber, D., Serenelli, A. M., Stello, D., Van Eylen, V., Campante, T. L., Elsworth, Y., Gilliland, R. L., Hekker, S., Karoff, C., Kawaler, S. D., Kjeldsen, H., and Lundkvist, M. S. (2015). Ages and fundamental properties of Kepler exoplanet host stars from asteroseismology. *Monthly Notices of the Royal Astronomical Society*, 452:2127–2148.

Silva Aguirre, V., Lund, M. N., Antia, H. M., Ball, W. H., Basu, S., Christensen-Dalsgaard, J., Lebreton, Y., Reese, D. R., Verma, K., Casagrande, L., Justesen, A. B., Mosumgaard, J. R., Chaplin, W. J., Bedding, T. R., Davies, G. R., Handberg, R., Houdek, G., Huber, D., Kjeldsen, H., Latham, D. W., White, T. R., Coelho, H. R., Miglio, A., and Rendle, B. (2017). Standing on the Shoulders of Dwarfs: the Kepler Asteroseismic LEGACY Sample. II. Radii, Masses, and Ages. *The Astrophysical Journal*, 835(2):173.

Solanki, S. K., Inhester, B., and Schüssler, M. (2006). The solar magnetic field. *Reports on Progress in Physics*, 69(3):563–668.

Sonoi, T., Samadi, R., Belkacem, K., Ludwig, H.-G., Caffau, E., and Mosser, B. (2015). Surface-effect corrections for solar-like oscillations using 3D hydrodynamical simulations. *Astronomy and Astrophysics*, 583:A112.

Spada, F., Demarque, P., Basu, S., and Tanner, J. D. (2018). Improved Calibration of the Radii of Cool Stars Based on 3D Simulations of Convection: Implications for the Solar Model. *The Astrophysical Journal*, 869(2):135.

Spiegel, E. A. and Zahn, J.-P. (1992). The solar tachocline. *Astronomy and Astrophysics*, 265:106–114.

Spruit, H. (1997). Convection in stellar envelopes: a changing paradigm. *Mem. Societa Astronomica Italiana*, 68:397.

Stein, R. F. and Nordlund, Å. (1998). Simulations of Solar Granulation. I. General Properties. *The Astrophysical Journal*, 499(2):914–933.

Tayar, J., Somers, G., Pinsonneault, M. H., Stello, D., Mints, A., Johnson, J. A., Zamora, O., García-Hernández, D. A., Maraston, C., Serenelli, A., Prieto, C. A., Bastien, F. A., Basu, S., Bird, J. C., Cohen, R. E., Cunha, K., Elsworth, Y., García, R. A., Girardi, L., Hekker, S., Holtzman, J., Huber, D., Mathur, S., Mészáros, S., Mosser, B., Shetrone, M., Silva Aguirre, V., Stassun, K., Stringfellow, G. S., Zasowski, G., and Roman-Lopes, A. (2017). The Correlation between Mixing Length and Metallicity on the Giant Branch: Implications for Ages in the Gaia Era. *The Astrophysical Journal*, 840(1):17.

Thévenin, F., Provost, J., Morel, P., Berthomieu, G., Bouchy, F., and Carrier, F. (2002). Asteroseismology and calibration of alpha Cen binary system. *Astronomy and Astrophysics*, 392:L9–L12.

Thygesen, A. O., Frandsen, S., Bruntt, H., Kallinger, T., Andersen, M. F., Elsworth, Y. P., Hekker, S., Karoff, C., Stello, D., and Brogaard, K. (2012). Atmospheric parameters of 82 red giants in the Kepler field. *Astronomy and Astrophysics*, 543:A160.

Tinsley, B. M. (1979). Stellar lifetimes and abundance ratios in chemical evolution. *The Astrophysical Journal*, 229:1046–1056.

Torres, G., Andersen, J., and Giménez, A. (2010). Accurate masses and radii of normal stars: modern results and applications. *Astronomy and Astrophysics Reviews*, 18(1-2):67–126.

Trampedach, R., Aarslev, M. J., Houdek, G., Collet, R., Christensen-Dalsgaard, J., Stein, R. F., and Asplund, M. (2017). The asteroseismic surface effect from a grid of 3D convection simulations. I. Frequency shifts from convective expansion of stellar atmospheres. *Monthly Notices of the Royal Astronomical Society*, 466:L43–L47.

Trampedach, R., Asplund, M., Collet, R., Nordlund, Å., and Stein, R. F. (2013). A Grid of Three-Dimensional Stellar Atmosphere Models of Solar Metallicity. I. General Properties, Granulation, and Atmospheric Expansion. *The Astrophysical Journal*, 769(1):18.

Trampedach, R. and Stein, R. F. (2011). The Mass Mixing Length in Convective Stellar Envelopes. *The Astrophysical Journal*, 731:78.

Trampedach, R., Stein, R. F., Christensen-Dalsgaard, J., Nordlund, Å., and Asplund, M. (2014a). Improvements to stellar structure models, based on a grid of 3D convection simulations - I. T($\tau$) relations. *Monthly Notices of the Royal Astronomical Society*, 442(1):805–820.

Trampedach, R., Stein, R. F., Christensen-Dalsgaard, J., Nordlund, Å., and Asplund, M. (2014b). Improvements to stellar structure models, based on a grid of 3D convection simulations - II. Calibrating the mixing-length formulation. *Monthly Notices of the Royal Astronomical Society*, 445(1):4366–4384.

Tumlinson, J. and Shull, J. M. (2000). Zero-Metallicity Stars and the Effects of the First Stars on Reionization. *The Astrophysical Journal, Letters*, 528(2):L65–L68.

Ulrich, R. K. (1970). The Five-Minute Oscillations on the Solar Surface. *The Astrophysical Journal*, 162:993.

Van Eylen, V., Dai, F., Mathur, S., Gandolfi, D., Albrecht, S., Fridlund, M., García, R. A., Guenther, E., Hjorth, M., and Justesen, A. B. (2018). HD 89345: a bright oscillating star hosting a transiting warm Saturn-sized planet observed by K2. *Monthly Notices of the Royal Astronomical Society*, 478(4):4866–4880.

Van Eylen, V., Kjeldsen, H., Christensen-Dalsgaard, J., and Aerts, C. (2012). Properties of extrasolar planets and their host stars: A case study of HAT-P-7. *Astronomische Nachrichten*, 333(10):1088.

Van Eylen, V., Lindholm Nielsen, M., Hinrup, B., Tingley, B., and Kjeldsen, H. (2013). Investigation of Systematic Effects in Kepler Data: Seasonal Variations in the Light Curve of HAT-P-7b. *The Astrophysical Journal, Letters*, 774(2):L19.

Vauclair, S. (2000). Helioseismology and the Solar Interior Dynamics. *Journal of Astrophysics and Astronomy*, 21:323.

Ventura, P., Zeppieri, A., Mazzitelli, I., and D'Antona, F. (1998). Pre-main sequence Lithium burning: the quest for a new structural parameter. *Astronomy and Astrophysics*, 331:1011–1021.

Vernazza, J. E., Avrett, E. H., and Loeser, R. (1981). Structure of the solar chromosphere. III - Models of the EUV brightness components of the quiet-sun. *The Astrophysical Journal Supplement Series*, 45:635.

Viallet, M. and Baraffe, I. (2012). Scenarios to explain extreme Be depletion in solar-like stars: accretion or rotation effects? *Astronomy and Astrophysics*, 546:A113.

Vinyoles, N., Serenelli, A. M., Villante, F. L., Basu, S., Bergström, J., Gonzalez-Garcia, M. C., Maltoni, M., Peña-Garay, C., and Song, N. (2017). A New Generation of Standard Solar Models. *The Astrophysical Journal*, 835:202.

Vögler, A., Shelyag, S., Schüssler, M., Cattaneo, F., Emonet, T., and Linde, T. (2005). Simulations of magneto-convection in the solar photosphere. Equations, methods, and results of the MURaM code. *Astronomy and Astrophysics*, 429:335–351.

Weiss, A. and Schlattl, H. (2008). GARSTEC - The Garching Stellar Evolution Code: The direct descendant of the legendary Kippenhahn code. *Astrophysics and Space Science*, 316(1-4):99–106.

Whittle, P. (1951). *Hypothesis testing in time series analyses*. PhD thesis, Uppsala, Almqvist & Wiksell.

Zahn, J.-P. (1991). Convective penetration in stellar interiors. *Astronomy and Astrophysics*, 252:179–188.

Ziegler, U. and Rüdiger, G. (2003). Box simulations of rotating magnetoconvection. Effects of penetration and turbulent pumping. *Astronomy and Astrophysics*, 401:433–442.

Zwicky, F. (1937). On the Masses of Nebulae and of Clusters of Nebulae. *Astrophysical Journal*, 86:217.

# Acknowledgement

First and foremost, I would like to express my sincere gratitude to my advisor, Achim Weiss, for giving me the opportunity to study stellar physics at the Max Planck Institute for Astrophysics. His supervision, expertise, and helpful insights have played a key role in the research presented in this thesis. By giving me the freedom to pursue my own ideas, by respecting and valuing my opinions, by promoting my work, and by helping me to establish collaborations, he made it a pleasure to work with him. I highly value the advice and feedback that he has given me through the years.

The whole stellar group deserves a special mention for creating a warm, enthusiastic, and professional working environment at group meetings and in seminars. My years at the Max Planck Institute have been inspiring and cheerful. In this connection, special thanks also go to my office mates for creating a good and pleasant atmosphere.

Furthermore, I would like to thank Jørgen Christensen-Dalsgaard, who kindly provided his inversion tool for inferring the solar sound speed. This tool was employed in connection with the results presented in Chapter 4. I also appreciate his indispensable guidance on the Aarhus adiabatic pulsation code (ADIPLS) and would like to thank him for inviting me to and welcoming me in Aarhus on several occasions.

The interface between GARSTEC and the MCMC algorithm used in Chapter 9 was developed by George Angelou, to whom I am indebted for providing his framework. I appreciate the fruitful and friendly discussions with him as well as his engaged collaboration and useful advice. With his assistance, it was possible to effortlessly adapt the interface and the output files of GARSTEC, in order to perform the required sampling of the parameter space. It has been a delightful experience to work with him.

I would like to extend my sincere thanks to both Zazralt Magic and Regner Trampedach for their advice and for giving access to their grids of RHD simulations of stellar envelopes. Moreover, I record my gratitude to Remo Collet for providing his expertise, for all his thoughtful comments, and for his assistance in running the Stagger code: during my research, I ran 3D simulations of convective stellar envelopes and analyzed the resulting output. Constructing such models is an intricate business, and while (nearly) none of the results has entered this thesis, I would like to express my appreciation for his tremendous effort.

I would also like to acknowledge Jakob R. Mosumgaard, Víctor Silva Aguirre, and Christian L. Sahlholdt for their collaboration. In particular, I would like to thank them for providing best-fitting stellar models for the *Kepler* targets presented in Chapter 6 and

for their contributions to the work presented in Chapter 8. Many of our exchanges and discussions have been both intriguing and fruitful.

It goes without saying that special thanks go to Andi Weiss and the entire IT department for their persistent computational support.

Finally, I deeply thank my partner, Natalia, and my parents, Anna Maria and Ove, for their support, encouragement, patience, understanding, and motivation. They often expressed their unwavering belief in my capabilities, for which I am forever grateful. With their kindness and support, both my parents and Natalia have played a vital role that cannot be overstated. In this connection, I am extremely thankful for Natalia's ingenious, practical advice: with useful and warmly phrased constructive criticism, she greatly improved the quality of my scientific talks — she often patiently listened to several trials. The same holds true for written work that she carefully read and commented upon — again often iteratively.

The successful completion of this dissertation in its present form would not have been possible without the people mentioned above.